MAGNETIC RESONANCE INVESTIGATIONS OF ION TRANSPORT

MAGNETIC RESONANCE INVESTIGATIONS OF TRANSPORT PHENOMENA IN LITHIUM-ION BATTERY ELECTROLYTE MATERIALS

By J. DAVID BAZAK, B.Sc.F.S., B.Sc., M.Sc.

A Thesis Submitted to the School of Graduate Studies in Partial Fulfillment of the Requirements for the Degree Doctor of Philosophy

McMaster University DOCTOR OF PHILOSOPHY (2019) Hamilton, Ontario (Chemistry)

TITLE: Magnetic Resonance Investigations of Transport Phenomena in Lithium-Ion Battery Electrolyte Materials

AUTHOR: J. David Bazak

SUPERVISOR: Professor Gillian R. Goward

PAGES: xxxvi, 304

Lay Abstract

Lithium-ion batteries are a critical component of the ongoing efforts to transition the global automobile fleet to electric vehicles and integrate renewable energy sources into the electricity grid. An important aspect of designing and optimizing lithium-ion batteries is a comprehensive understanding of the factors which impact the ability of the electrolyte in the battery to ferry the lithium ions from one electrode to the other, the process which enables them to release energy into the circuit to power a device. This thesis describes results obtained from measuring the diffusion of the ions within the electrolyte for both conventional liquid-state electrolytes, and emerging solid-state electrolyte materials. It also includes studies which make use of MRI to image the flow of ions within the liquid-state electrolyte of an operating battery mimic, and monitor the concentration changes of the ions across the electrolyte as a current is applied to it.

Abstract

The subject of this thesis is the application of magnetic resonance methods to the characterization and quantification of lithium-ion transport in a wide range of lithium-ion battery electrolyte materials relevant to the electromobility and energy storage sectors. In particular, field-gradient magnetic resonance techniques, in the form of PFG-NMR diffusivity measurements of both liquid- and solid-state electrolytes and *in situ* MRI of electrochemical cells, comprise the core means by which these characterizations were realized. PFG-NMR and ionic conductivity studies of a range of liquid-state electrolyte mixtures were performed, as a function of temperature, to assess how key mass and charge transport properties reflect differences in composition. *In situ* MRI was used to study the effect of temperature on steady-state concentration gradient formation in polarized liquid electrolytes, with the results quantitatively compared to model predictions. This approach was then extended, using a combination of MRI and spatially-resolved PFG-NMR, to study the interlinked effects of temperature and current density on concentration gradient formation, and to attempt a comprehensive characterization of the ion transport parameters with spatial resolution. Finally, PFG-NMR and MAS-NMR were applied in a solid-state electrolyte context to investigate compositional effects on ion transport in the argyrodite family of lithium-sulphide ion conductors, and the influence of macroscopic sample format (glass, crystalline powder, compressed crystalline pellet) on micro-scale ion transport in a thio-LISICON ion conductor. Taken together, the studies demonstrate the effectiveness of magnetic resonance methods for the robust elucidation of the means by which material properties impact ion transport in technologically-relevant lithium-ion electrolyte systems.

Acknowledgments

I would like to sincerely thank my supervisor, Prof. Gillian Goward, for, nearly five years before the time of this writing, taking a chance on a struggling theoretical physicist who wanted to join an experimental chemistry group to "learn NMR and work on something relevant to green energy." The opportunity has been transformative for me, both in terms of research ability and personal self-belief, and I am immensely grateful to have been granted it, along with all of the helpful support and mentorship over the years. I would also like to thank my original co-supervisor (and current committee member), Prof. Saeid R. Habibi, for agreeing to incorporate me into his group's research efforts when I was starting out, and for his patience and guidance with my attempts to link my own research to those efforts. While it did not ultimately come to fruition, much valuable learning took place in the course of these experiences, and they had a significant effect on how I think about my research. Much sincere thanks also goes to the other members of my supervisory committee, Prof. Michael Noseworthy and Prof. Randall Dumont, for all of their helpful feedback and encouragement in committee meetings and the comprehensive exam – it was absolutely fantastic to have them both on my committee. I would also like to sincerely thank Prof. Dany Carlier for all of her help throughout my time as a visiting scholar in Bordeaux – it made the daunting prospect of completing my thesis abroad so much more manageable.

I am also grateful to have had the opportunity to work very closely with Dr. Sergey Krachkovskiy, who was indispensable in helping me get started with many of the NMR techniques that were used in this thesis, and whose prodigious research acumen was both

extremely helpful and inspiring. It was also wonderful having his companionship at the many conferences we attended together. I am similarly indebted to Dr. Kris Harris for all of the instruction on solid-state NMR, all of the great conversations – about NMR and (mostly) otherwise and from which I invariably learned something new – his friendship over the years, and his kindness in always thinking of me when he had prepared too much food. I am also very fortunate to have coincided with so many great 'colleagues,' both within the Goward group and in the department at large during my time in Chemistry, many of whom are also very good friends. There are simply too many to name without risk of inadvertent admission, but if the preceding stilted phrasing strikes you as something that I would be likely to say out loud, then you are probably one of them.

I would be negligent if I did not sincerely thank my family for all of the help, support, and encouragement over the years, particularly my sisters, Steff and Callie. Thank you as well to Laura, for all of the lovely times we shared together during my years of study, for the unwavering affection, and for reminding me that there is more to life than the lab. Finally, I would most especially like to thank my mother. Words cannot adequately capture my appreciation, but I am grateful to the very depths of my being for her unceasing support, unerring guidance, and unlimited encouragement. Without her, I would be a shadow of the person I am today… and would never have started PhD studies in the first place!

Table of Contents

List of Tables

List of Figures

Figure 2.4 – T_1 measurement via the inversion recovery method for ^{7}Li in $Li_{5.80}Ca_{0.10}PS_5Cl$ at 40°C and static conditions, using a 20 T Bruker 850HD spectrometer. a) Variable-τ, pseudo-two-dimensional inversion recovery spectrum. b) Fit of the integrated intensity at each τ (which is proportional to the total sample magnetization for τ) using equation (2.13) to determine that $T_1 = (367 \pm 5)$ ms.

Figure 2.5 – T_2 measurement via the CPMG method for ^{7}Li in $Li_{3.30}Al_{0.15}P_{0.85}S_4$ at 30°C and static conditions, using a 7 T Bruker Avance III 300WB spectrometer. a) Variable-echo-number, pseudo-two-dimensional CPMG spectrum. b) Fit of the integrated intensity versus accumulated τ_{echo} (which is proportional to the total sample magnetization for the accumulated τ_{echo}) using equation (2.14) to determine that $T_2 = (4.78 \pm 0.08)$ ms.

Figure 2.6 – Pictorial illustration of a spatially-varying precessional frequency, $\omega(\vec{\boldsymbol{r}}, t)$, induced by deliberately inducing a spatial variation in the longitudinal magnetic field.

Figure 2.7 – A schematic of Fourier-imaging, wherein a test sample with some specific spatial arrangement (in the literature, commonly vials containing H_2O, with ^{1}H being the most receptive NMR nucleus) is probed in the presence of a longitudinal field gradient, illustrating the correspondence of time-domain signal and $\vec{\boldsymbol{k}}$-space spin density to frequency-domain signal and real-space spin density. Adapted with modification from Callaghan, 1991.

Figure 2.8 – a) Two-dimensional frequency-encoding MRI pulse sequence, with slice-selection in the z-direction, which samples the (x, y)-plane. b) A Cartesian raster for the acquisition of $\vec{\boldsymbol{k}}$-space trajectories, wherein a series of phase-encode periods are conducted to sample the y-direction, and then the x-direction of the y-modulated signal is sampled with a frequency-encoding readout gradient. Adapted with modification from Price, 2009,[21] and Callaghan, 1991.

Figure 2.9 – Comparison of a) the regular rotating frame for off-resonance spins, and b) the gradient-based rotating frame, for the analysis of slice-selective MRI. Adapted with modification from Callaghan, 1991.

Figure 2.10 – A simple, one-dimensional CSI pulse sequence with slice-selective excitation for rapid and smooth MRI of the *in situ* cell active volume during concentration polarization. Explanation of the parameters can be found in **Section 4.3**.

Figure 2.11 – Pulse sequence for multiple-FID-point, DHK-SPRITE. The use of multiple FID points following each RF excitation on every step in the ramp allows for a signal-to-noise enhancement by treating each as an individual phase-encoding time and compositing the images produced by each using the chirp-z transform. Explanations for all of the parameters can be found in **Section 4.3**.

Figure 2.12 – Pulse sequence for a PGSTE experiment involving BPP field gradients and an LED period for eddy current compensation. The τ_i here are simply spacing delays between the gradient and RF pulses, p_1 and p_2 are the $\pi/2$ and π RF pulse lengths, $g_1 = \delta/2$, g_2 is the spoiler gradient duration, τ_D is the difference between Δ and all of the other time intervals from the start of the first BPP g_1 to the start of the second, and τ_L is the difference between the targeted LED duration and the sum of τ_3 and g_2.

Figure 2.13 – Schematic illustration of the output of a pseudo-two-dimensional PFG-NMR experiment, showing a slice along the spectral dimension, and the integrated intensity across the spectral dimension plotted against the linearly-varied gradient strength, g, producing a Gaussian attenuation curve. A depiction of the phase-helix along the gradient direction is also included at left.

Figure 2.14 – Graphical solution of the intermediate-time approximation to the Kärger equations for two-compartment PFG-NMR attenuation in the case $p_1 \ll p_2$ and $D_1 \gg D_2$. Using the value of p_1 obtained from solid-state NMR lineshape fitting, and a limiting-slope regression method described in **6.4.5**, the four parameters $\{D_1, D_2, \tau_1, \tau_2\}$ can be extracted from the linearized diffusivity attenuation curve. Adapted with modification from Kärger, 1988.

Figure 2.15 – Incomplete MAS-NMR averaging of the ^{11}B quadrupolar interaction for a series of lithium-iodothioborosilicate ion-conducting glasses (compositions listed in the plot legend) where evidently $C_Q \gg \text{MAS Rate}$, leaving a spinning sideband manifold which would partially trace out the original, static lineshape.

Figure 2.16 – Galvanostatic impedance spectra for the *in situ* cell used in **Chapters 4-5** after polarization to produce a steady-state electrolyte concentration gradient at room temperature, using a 100 μA applied current. DC biases of both 100 μA (*i.e.* measuring while maintaining the steady state) and 0 μA (*i.e.* measuring immediately after current interruption) were conducted, both with a 15 μA rms AC amplitude, to assess the difference in response depending on whether or not the DC current was running.

Figure 2.17 – Kramers-Kronig compliance verification for the galvanostatic impedance spectra of **Figure 2.16**, with a) $I_{\text{DC}} = 100$ μA and b) $I_{\text{DC}} = 0$ μA, using LIN_KK. The respective residual plots as a function of AC frequency are provided in c) and d), demonstrating that the reconstruction is sound, and therefore that the data are in the linear regime.

Figure 3.1 – Representative Nyquist plots over a range of temperatures for the three-electrode cell used to make ionic conductivity measurements of the CMHT1 mixture.

Figure 3.2 – Representative Nyquist plots over a range of temperatures for the two-electrode cell used to make ionic conductivity measurements of the CMHT2 mixture.

overall charge transport) for all four electrolyte mixtures.

Figure 4.1 – Schematic illustration of the tension between migration fluxes (along the electric potential gradient in opposite directions for each ion) and diffusive fluxes (against the concentration gradient for both ions) which ultimately generate a steady-state concentration gradient under constant-current operation of a cell.

Figure 4.2 – A schematic overview of the *in situ* cell used to polarize the electrolyte under applied current (inset: photograph of the *in situ* cell sitting in the RF insert). The cell consists of an active volume containing the electrolyte bored from a PEEK rod (tan colour), encapsulated by Li metal and Cu foil-mounted graphite electrodes seated on Cu current collectors and sealed with PEEK ferrules (green) and PEEK nuts (red). ^{19}F CS images taken at regular intervals visualize the formation of the steady-state concentration gradient of PF_6^- anions (and by electroneutrality, Li^+ cations) across the inter-electrode spacing.

Figure 4.3 – A plot of normalized ^{19}F CS images of the concentration gradient buildup for 1.0 M $LiPF_6$ in EC/DEC, 1:1 (v/v) at 10℃ and 7.2 $A \cdot m^{-2}$. In the left series of images, the polarization proceeds as expected, with increasing concentration at the Li electrode (left) of the image while lithium cations are inserted into the graphite electrode (at right). After 35 minutes, the concentration begins decreasing on the Li side as well as the graphite side, as opposed to converging into a steady-state, until cell failure at 75 minutes. This signal decrease on the concentrated side of the cell while it is operating at a low temperature points towards salt precipitation. The inter-electrode spacing for this cell was nominally 1.9 mm, with estimated dead-space indicated by the dashed green lines.

Figure 4.4 – The blue curve corresponds to the initial (non-normalized) ^{19}F signal intensity profile prior to charging the graphite at 7.2 $A \cdot m^{-2}$ and 10℃ with the 1.0 M $LiPF_6$ in EC/DEC equal parts electrolyte mixture, while the red curve corresponds to the signal profile measured after cell failure from the polarization imaged in **Figure 4.3** and 150 minutes of subsequent relaxation without applied current. The reduction in signal intensity between the two profiles is evidence for the loss of fluorine nuclei from solution in the active volume, indicating that salt precipitation is responsible for the decreasing signal intensity on the concentrated side of the inter-electrode spacing in **Figure 4.3**.

Figure 4.5 – A: Comparison of the baseline and steady-state signal intensity profiles of 1.00 M $LiPF_6$ in EC/PC/DMC, 5:2:3 (v/v) measured by CSI and DHK SPRITE, at 10℃ and with a nominal cell length of 2.43 mm, charging the graphite electrode at 7.2 $A \cdot m^{-2}$. The horizontal compression and translation of the FOV has been applied for the CS images, illustrating the dead-space which DHK SPRITE captures but CSI does not. B: Matching of the steady-state concentration profile measured by CSI with the cubic fit (dashed green line) of that obtained via DHK SPRITE, which produces the effective FOV and alignment for CSI. The fitting region where linear regression is used to compare between cells is indicated.

Figure 4.6 – Comparison of ^{1}H CS images employing two different gradient shapes, 100-point sine and smooth-square, with ^{1}H DHK SPRITE for a 10 mm active volume filled with Mn-doped water in a symmetric NMR tube, illustrating that the discrepancy in concentration gradient measurement for the in situ cell is a result of the conductive parts of the cell distorting the B_0 field gradient, rather than an issue inherent in the CS pulse sequence parameters, since all three imaging experiments accurately measure the standard. Images have been vertically scaled to facilitate simultaneous plotting.

Figure 4.7 – Polarization of the in situ cell in the linear region with $1.00\ \mathrm{M}\ \mathrm{LiPF_6}$ in EC/PC/DMC, 5:2:3 (v/v) solvent mixture at 10℃ (panel A), 25℃ (B), and 40℃ (C). In each case, the concentration gradient builds until converging to a steady state (arrows indicate the direction of evolution), but with decreasing slope as the cell temperature is increased. Nominal cell length is 2.43 mm and in all cases the charging current corresponds to $7.2\ \mathrm{A \cdot m^{-2}}$.

Figure 4.8 – Steady-state concentration profiles at each of the three temperatures, illustrating a decreasing slope as the temperature at which the cell is held is increased. Nominal cell length and current are the same as in **Figure 4.7**.

Figure 4.9 – A comparison of the fitted CSI regression slopes for the concentration gradient magnitudes at three temperatures (10℃, 25℃, and 40℃), and between the two nominal cell lengths (1.45 mm, versus 2.43 mm and a 2.32 mm replicate), demonstrating the difference in the amount of steady-state polarization in the $1.00\ \mathrm{M}\ \mathrm{LiPF_6}$ in EC/PC/DMC electrolyte with temperature, and the constancy in the polarization irrespective of inter-electrode spacing for a given temperature. All polarizations were achieved with a charging current of $7.2\ \mathrm{A \cdot m^{-2}}$, transferring Li ions to the graphite electrode. Error bars correspond to 3σ confidence intervals for the regression slopes for the *in situ* experiments.

Figure 5.1 – Schematic illustration of the flow of variables, from raw measurements, to transformed electrochemical variables, and finally to derived transport parameters.

Figure 5.2 – P3D PFG-MRI pulse sequence, constructed by fusing a one-shot BPP stimulated echo PFG-NMR sequence with a CSI experiment, including initial selective excitation. An explanation of the various blocks and salient parameters is provided in the text.

Figure 5.3 – Mass density as a function of salt mass fraction for $\mathrm{LiPF_6}$ in EC/PC/DMC, 5:2:3 (v/v) at glove box temperature (31°C).

Figure 5.4 – a) Interpolated, baseline-normalized steady-state raw 19F CSI signal intensity profiles illustrating both the reduction in achievable current density with temperature, and the decrease in magnitude of the final formed concentration gradient. b) Schematic of the grid of operating conditions that were attempted, along with the phenomenological fit for the limiting current density. Green dots are successfully formed steady-state gradients,

yellow dots were marginally results (*i.e.* the concentration gradient revealed by the images was relatively steady, but the overpotential was steadily increasing over the same time), and red dots indicate current staircase increments where the current interrupted well before steady-state conditions were achieved.

Figure 5.5 – Time series of raw ^{19}F CS images for the evolution to the steady state for 40°C and -5°C. Note the drastic difference in polarization relative to the applied current density.

Figure 5.6 – Contrasting the steady-state ^{19}F DHK-SPRITE images for 40°C and -5°C, illustrating the greater edge encroachment in the former (marked by the closed red circles, for the identified edges) and the smaller overall polarization in the latter. The inset provides a design schematic of the *in situ* cell used in the measurements. The feature marked with the single asterisk is leftover electrolyte from the filling process trapped behind the lithium metal electrode (which sits in the ~1 mm region of no signal, between 4-5 mm in the FOV) and surrounding the ferrule (green component in the inset). For the -5°C image series, the double asterisk is excess electrolyte that was squeezed behind the graphite electrode during the refilling process after the formation cycle.

Figure 5.7 – a) The signal calibration and fitting region identification of the steady-state ^{19}F DHK-SPRITE images for the 40°C current staircase used to align all other MRI techniques and properly calibrate their FOVs in light of the gradient distortions to which they are susceptible but DHK-SPRITE is immune. b) The result of the alignment procedure for ^{19}F CSI (purple dots), the imaging dimension for ^{7}Li P3D PFG-MRI (green dots), and the imaging dimension for ^{19}F P3D PFG-MRI (cyan dots).

Figure 5.8 – The distribution of cation and anion self-diffusivities, D_+^* and D_-^*, along with the salt diffusivity, across the inter-electrode spacing as a function of driving current density at 40°C. Note the closure of the gap between the higher D_-^* and the lower D_+^* on both sides of the cell at extreme polarization.

Figure 5.9 – a) Resulting uncertainty on $\bar{c}_s(x)$ from the curvature-constrained Monte Carlo estimation of $\overline{\partial c_s}/\partial x$, at 40℃. b) The curvature-constrained estimates of $\overline{\partial c_s}/\partial x$, computed with the aim of reducing numerical instability in the subsequent estimates of t_+^0 and κ. c) The computed $\bar{c}_0(x)$ and $\bar{c}_T(x)$ profiles, demonstrating modest solvent displacement from the anodic side of the cell, relative to the overall changes in total concentration across the cell due to the salt concentration polarization.

Figure 5.10 – a) The spatial distribution of the transference number, t_+^0, and the transport number, τ_+, across the inter-electrode spacing as a function of applied current density at 40℃, showing a dramatic decrease in t_+^0 at high polarization, with little effect on τ_+. b) Comparison of ionic conductivity values derived from the *in situ* measurements and a mapping of the bulk, *ex situ* values onto the concentration profile, again signaling departure at large concentration polarizations.

Figure 6.4 – a) Li^+-ion diffusivity in $Li_{6-x}PS_{5-x}Cl_{1-x}$ obtained from ^7Li PFG NMR measurements for x = 0, 0.25 and 0.5; b) Arrhenius plots of the diffusivity and conductivity values for x = 0 and x = 0.5 from PFG-NMR and EIS.

Figure 6.5 – a) ^7Li MAS NMR for $Li_{6-x}PS_{5-x}Cl_{1-x}$ $(x = 0, 0.25, 0.375, 0.5)$; b) correlation of the activation energies from both techniques with the ^7Li isotropic chemical shift and the Haven ratio for all values of x under study.

Figure 6.6 – Variable-temperature stack plot of static ^7Li spectra for the $x = 0$ argyrodite at 300 MHz, demonstrating the absence of significant quadrupole coupling, in terms of the lack of satellite transitions, broadening of the central transition, and a shift in its position over the entire temperature range, which points to a change in the shielding properties as the primary source of the shift trend in **Figure 6.5a**.

Figure 6.7 – Haven ratios versus temperature, for all four halide-enriched phases examined in the study, demonstrating the relative temperature insensitivity. The flat lines are the average values, and dashed lines indicate the standard error interval.

Figure 6.8 – Comparison of ^7Li MAS spectra for the y-series and dual-doped series (upper panel), demonstrating the strong halide-enrichment shift trend (which is paralleled in the lower panel with the original x-series covered in **6.4.1**), and no major change in chemical shift associated with Ca^{2+}-doping. The inset reveals the secondary peak associated with a Ca^{2+} dopant modifying the local electronic environment of a subset of the Li ions, confirming the proximity of the two cation species.

Figure 6.9 – Secondary peak deconvolutions of ^7Li MAS spectra for the compositions where the halide-enrichment shift trend did not obscure them. In all cases, the blue lineshape is the spectrum, the orange lineshape is the primary resonance, the green lineshape is the secondary resonance, and the black lineshape is the fit sum (the additional purple lineshape for $(x = 0.25, y = 0.10)$ is to account for the halide disorder chemical shift dispersion).

Figure 6.10 – Selected ^7Li 2D EXSY spectra for $y = 0.10$ at 20℃, at 850 MHz field strength and 30 kHz MAS rate. Red brackets indicate cross-peak regions for secondary signals associated with the presence of Ca^{2+} dopants in the Li^+ cages. The 100 ms mixing time is on the order of T_1 for this sample.

Figure 6.11 – a) Nyquist impedance plots of y = 0, 0.1, 0.15, and (x = 0.5, y = 0.1) at 298 K, normalized to the pellet thickness. Figure inset illustrates the enlarged view at high frequencies. b) Diffusivity plots for the same samples, from the PFG-NMR data, illustrating the significantly different effects on the two types of transport measurement from the two doping strategies.

Figure 6.12 – Correlation of activation energies from both EIS and PFG-NMR, as well as ^{7}Li isotropic chemical shift, with lithium vacancy concentration ($x + 2y$).

Figure 6.13 – ^{7}Li MAS-NMR spectrum for the so-called mixed-phase sample, $Li_{5.35}Ca_{0.10}PS_{4.50}Cl_{1.55}$. The resonance at 0.98 ppm is consistent with $x = 0.5$, as determined in **6.4.1**, and consistent with the minimal shift modification of the Ca^{2+}-doping relative to that of Cl^{-} (**Figure 6.8**), while the resonance at 0.83 ppm appears to be a much more halide-rich environment as per the established shift trend for increased Cl^{-} substitution. An example of a $(x = 0.5, y = 0.1)$ sample that also exhibited mixed-phase behaviour, which prompted the synthesis of the $Li_{5.35}Ca_{0.10}PS_{4.50}Cl_{1.55}$ mixed-phase sample with a deliberate LiCl excess, is overlaid for comparison. There is negligible (< 0.5% of integrated signal intensity) LiCl (s) in both samples.

Figure 6.14 – ^{31}P MAS NMR spectrum for the so-called mixed-phase sample, $Li_{5.35}Ca_{0.10}PS_{4.50}Cl_{1.55}$. The cascading pattern of nearly evenly-spaced resonances is indicative of a distribution of phosphorus environments with progressively increasing Cl^{-} substitution in the surrounding anion shells. Note that the resonance at 86.5 ppm is indicative of isolated $[PS_4]^{3-}$ tetrahedra, and overlays the shift distribution pattern (with the peak in this region expected, from the remainder of the pattern, to appear at ~86 ppm). It potentially arises from a small amount of Li_3PS_4-like impurity, which would appear in the tail of the ^{7}Li MAS-NMR spectrum at 0.5-0.6 ppm (and is definitely present in the sample $(x = 0.5, y = 0.1)$ sample provided there, as well as here, for comparison).

Figure 6.15 – a) Diffusivity Arrhenius plot from variable-temperature ^{7}Li PFG-NMR measurements on powder and pellet-pressed versions of the mixed-phase $Li_{5.35}Ca_{0.10}PS_{4.50}Cl_{1.55}$ sample, showing non-ideal Arrhenius behaviour with a cross-over in slopes from low to high temperature which is significantly reduced in the pellet version of the sample. b) NMR relaxation rates compared between the powder and pellet mixed-phase samples. Note the presence of two inflection points in the T_2 curve, indicating the presence of two distinct motional correlation times.

Figure 6.16 – Two-component activation energy fits to the Arrhenius plots for the ^{7}Li PFG-NMR data for the powder (a) and pellet (b) versions of the mixed-phase sample $Li_{5.35}Ca_{0.10}PS_{4.50}Cl_{1.55}$. The non-ideal Arrhenius behaviour is indicative of competing grain and grain-boundary contributions to the overall lithium-ion transport, with the latter having greater influence at lower temperature. That influence is reduced by the compression of the sample into a pellet (**Figure 6.15**).

Figure 6.17 – Comparison of powder and pellet activation energies in the "low"- and "high-temperature" regions of the ^{7}Li PFG-NMR diffusivity Arrhenius plots from **Figure 6.15** for the mixed-phase sample $Li_{5.35}Ca_{0.10}PS_{4.50}Cl_{1.55}$. (See **Figure 6.16** for explicit delineations for the limiting slopes.) The high-temperature region is the same between samples and is associated with grain contributions, while the compression to form the pellet

enhances transport across grain dislocations in multi-crystallite particles, which is the source of the lower activation energy in the pellet sample for the low-temperature region, associated with grain boundary contributions.

Figure 6.18 – Comparison of ^{7}Li PFG-NMR Arrhenius plots for the main y-series and (x, y)-series of compositions. Evident is the small amount of non-ideal behaviour – the slight curvature – even over the relatively restricted temperature range (268 K – 343 K) from which the activation energies in **Table 6.2** were calculated.

Figure 6.19 – ^{7}Li MAS-NMR of crystalline LAPS, $Li_{3.30}Al_{0.15}P_{0.85}S_4$, at 850 MHz and 30 kHz MAS rate, with deconvolution under the assumption of complete MAS averaging of the quadrupolar broadening.

Figure 6.20 – ^{7}Li MAS-NMR of a) β-Li_3PS_4, and b) glass-phase LAPS, both at 850 MHz and 30 kHz MAS rate, to contrast with **Figure 6.19** for the crystalline LAPS. Note that the chemical shift scale is a factor of ten larger in b).

Figure 6.21 – ^{31}P MAS spectrum of crystalline LAPS at 850 MHz and 30 kHz MAS rate. The primary signal is at 81.5 ppm, with a shoulder centred at ~84 ppm and a secondary signal at 89.3 ppm.

Figure 6.22 – Static ^{7}Li quadrupolar NMR spectra collected at 300 MHz, 500 MHz, and 850 MHz for crystalline LAPS, to obtain estimates of the quadrupole parameters and residual amorphous phase signal content.

Figure 6.23 – Czjzek fit to the ^{7}Li MAS-NMR lineshape at 850 MHz and 30 kHz, originally presented as a Lorentzian deconvolution in **Figure 6.19**. The Czjzek model evidently cannot explain the lineshape on the basis of 3 sites + amorphous content.

Figure 6.24 – Attempted single-component diffusivity fit to the crystalline powder LAPS sample PFG-NMR attenuation curve at 358 K, showing that slower diffusion at high gradient values is not well captured. (Note that the confidence interval for the fit decreases at high gradient strength because the model approaches zero asymptotically here.)

Figure 6.25 – Two-component, limiting-slope fit under the intermediate-time approximation to the linearized version of the attenuation curve in **Figure 6.24**, with $q = \gamma\delta g$.

Figure 6.26 – The breakpoint-dependence of the component diffusivities from the limiting-slope intermediate-time approximation to the two-component diffusivity fit of the crystalline powder LAPS sample for a) the amorphous, and b) the bulk component. c) The combined correlation coefficient – the fitting metric – as a function of the location of the two breakpoints along the attenuation curve.

Figure 6.27 – Comparison of the single-component diffusivity Arrhenius plot (a) for the glass-phase, crystalline powder, and crystalline pellet LAPS samples with the two-component Arrhenius plots for (b) the powder, and (c) the pellet. The amorphous components of the powder and pellet samples are approximately similar, but the slope of the bulk component in the pellet sample is significantly reduced, indicating a reduced activation energy for the long-range transport.

Figure 6.28 – Summary of the activation energies obtained from the Arrhenius plots of **Figure 6.27** for all sample treatments, with the amorphous and bulk compartment contributions for the crystalline samples separately extracted by the two-component fitting method.

Figure 6.29 – The extracted bulk and amorphous residence times for the two-component diffusivity fits for the crystalline powder and crystalline pellet LAPS samples, demonstrating the exponential decrease in residence time with increasing temperature.

Figure 6.30 – Comparison of the NMR relaxation times as a function of temperature for all three sample preparations of LAPS: a) the glass-phase, b) the crystalline powder, and c) the crystalline pellet. In particular, note the similarity of the magnitude of the amorphous compartment branch in the crystalline samples to the glass-phase, and the shorter magnitude of the bulk compartment branch for the pellet sample compared with the powder sample.

List of Abbreviations and Symbols

List of Abbreviations

A.U. – Arbitrary Units for intensity or integral intensity axes

AC – Alternating Current

ASSB – All-Solid-State Battery

BMS – Battery Management System

BPP – Bloembergen-Pound-Purcell theory of NMR relaxation (Section 2.1)

BPP – Bipolar Pulse Pair PFG-NMR gradient encoding technique (Section 2.3)

CMHTx – Centre for Mechantronics and Hybrid Technologies electrolyte nomenclature, where $x = \{1,2,3,4\}$ (refer to Table 3.1)

CPE – Constant-Phase Element

CPMG – Carr-Purcell-Meiboom-Gill method for T_2 measurement

CS – Chemical Shift (precedes 'images' or 'imaging')

CSI – Chemical Shift Imaging

CST – Concentrated Solution Theory

DC – Direct Current

DHK-SPRITE – Double-Half-K-space, Single-Point-Ramped-Imaging-with-T_1-Enhancement MRI method

DMC – Dimethyl Carbonate

DST – Dilute Solution Theory

EA – Ethyl Acetate

EC – Ethylene Carbonate

EFG – Electric Field Gradient (tensor)

EIS – Electrochemical Impedance Spectroscopy

EMC – Ethylmethyl Carbonate

EV – Electric Vehicle

EXSY – EXchange SpectroscopY

FEC – Fluoroethylene Carbonate

FID – Free Induction Decay

FOV – Field Of View

FT – Fourier Transform

FWHM – Full Width at Half Maximum

HPLC – High-Performance Liquid Chromatography

LAPS – Al-doped thio-LISICON with formula $Li_{3.30}Al_{0.15}P_{0.85}S_4$

LATP – NASICON-type solid-state electrolyte with formula $Li_{1.3}Al_{0.3}Ti_{1.7}PO_4$

LC – inductor-capacitor block circuit element

LED – Longitudinal Eddy current Delay

LGPS – thio-LISICON solid-state electrolyte with formula $Li_{10}GeP_2S_{12}$

LiFSI – Lithium bis(fluorosulfonyl)imide

LiPON – solid-state electrolyte consisting of a solid-solution of γ-Li_3PO_4 and N

LiTFSI – Lithium bis(trifluoromethanesulfonyl)imide

LISICON – LIthium SuperIonic CONductor

LLTO – lithium lanthanum titanate solid-state electrolyte

LLZTO – a garnet-type solid-state electrolyte with formula $Li_{6.75}La_3Zr_{1.75}Ta_{0.25}O_{12}$

LP30 – common benchmark liquid-state electrolyte, 1.00 M $LiPF_6$ in EC/DMC, 1:1 (v/v)

LSiPS – thio-LISICON solid-state electrolyte with formula $Li_{10}Si_2PS_{12}$

LSnPS – thio-LISICON solid-state electrolyte with formula $Li_{10}SnP_2S_{12}$

MAS-NMR – Magic-Angle-Spinning NMR

MR – Magnetic Resonance

MRI – Magnetic Resonance Imaging

NASICON – NAtrium SuperIonic CONductor

NMR – Nuclear Magnetic Resonance

NPD – Neutron Powder Diffraction

OCV – Open-Circuit Voltage

P3D PFG-MRI – Pseudo-3-Dimensional Pulsed-Field-Gradient-Magnetic Resonance Imaging

PC – Propylene Carbonate

PDE – Partial Differential Equation

PEEK – PolyEther Ether Ketone

PFG-NMR – Pulsed-Field-Gradient NMR

PGSE – Pulsed-Gradient Spin Echo approach to PFG-NMR

PGSTE – Pulsed-Gradient STimulated Echo approach to PFG-NMR

PHEV – Plug-in Hybrid Electric Vehicle

RARE - Rapid Acquisition with Relaxation Enhancement MRI method

RF – Radio Frequency

RMSE – Root Mean Square Error

SEI – Solid-Electrolyte Interface

SOC – State-of-Charge

SOH – State-of-Health

SPM – Single-Particle Model

TDF – ThermoDynamic Factor

TPPI – Time-Proportional Phase Incrementation

XRD – X-Ray Diffraction

List of Symbols – Latin Alphabet

a – guest ion sublattice inter-site distance (Chapter 1)

a_ϵ – temperature-dependent permittivity linear fitting coefficient

A – electrode-electrolyte interfacial area

A_j – j^{th}-order fitting coefficient for *ex situ* ionic conductivity measurements as a function of c_s

An (s) – anode at 0% SOC; fully-delithiated anode

b – attenuating power for PFG-NMR in the Stejskal-Tanner equation

b_ϵ – temperature-dependent permittivity quadratic fitting coefficient

$\vec{\boldsymbol{B}}_0$ – longitudinal magnetic induction field

$\vec{\boldsymbol{B}}_1$ – magnetic induction field for RF excitation

$\vec{\boldsymbol{B}}_{\text{eff}}$ – net magnetic induction field for off-resonance precession in the rotating frame

c_i – concentration of species $i = \{+, -, 0\}$

c_0 – solvent concentration (Chapter 1, Chapter 5)

$\bar{c}_0$ – steady-state solvent concentration

$c_0(x)$ – initial concentration profile (Chapter 4)

c_O – concentration of the oxidized species (Chapter 2)

c_R – concentration of the reduced species (Chapter 2)

c_s – salt concentration

$\bar{c}_s$ – steady-state salt concentration

$c_{s,j}(x)$ – salt concentration at current step j and position x

c_T – total concentration

$\bar{c}_T$ – total concentration in the steady-state

C_{dl} – double-layer capacitance

C_Q – quadrupolar coupling constant

C. C. – complex conjugate

d – dimensionality (Chapter 1)

d – number of independent EFG tensor components in a Czjzek fit (Chapter 2)

d – electrode diameter in the two-electrode conductivity cell (Chapter 3, Chapter 5)

dM – differential of spin-ensemble magnetization

dV – volume differential

D – Fickian diffusion coefficient

$\vec{\boldsymbol{D}}$ – electric displacement

$D(\vec{\boldsymbol{r}})$ – spatially-varying RF coil sensitivity (Chapter 2)

D_i – intrinsic diffusivity of species i

D_i^* – self-diffusivity of species i

$\overline{D}_i^*$ - steady-state self-diffusivity of species i

D_i^{eff} – effective diffusivity of species $i = \{+, -, p\}$, explicitly accounting for contact ion pairing

$\widetilde{D}_i$ – chemical diffusion coefficient of species i

D_s – salt diffusivity

D_κ – charge diffusivity of the ionic conductivity

e – fundamental unit of charge, 1.6022×10^{-19} C

e^- – electron

$\vec{\boldsymbol{E}}$ – electric field

$E(t)$ – time-varying potential for EIS

$\tilde{E}$ – potential phasor

E_{DC} – DC voltage bias for potentiostatic EIS

$E[\text{An (s)}]$ – potential of fully-delithiated anode

$E[\text{Li}_x\text{An (s)}]$ – potential of partially-delithiated anode

$E[\text{Li}_n\text{Cat (s)}]$ – potential of fully-lithiated cathode

$E[\text{Li}_{n-x}\text{Cat (s)}]$ – potential of partially-lithiated cathode

$E_{I,m}$ – eigenvalue of the Zeeman-splitting Hamiltonian for eigenstate $|I, m\rangle$

E_n – generic spin state energy

f – ion hopping correlation factor

$f(C_Q, \eta_Q)$ – Czjzek probability distribution function for quadrupolar coupling parameters

$f_\pm$ – mean molar activity coefficient

F – Faraday's constant, $96485\ \text{C} \cdot \text{mol}^{-1}$

g – variable gradient strength parameter for PFG-NMR

g_i – gradient duration intervals in pulse sequences

$\vec{\boldsymbol{G}}$ – longitudinal field gradient function

h – ion hopping rate (Chapter 1)

h – Planck constant, 6.6261×10^{-34} J · s

H_R – the Haven ratio

I – nuclear spin quantum number (Chapter 2)

I – applied current magnitude (Chapter 4)

I_{DC} – DC current bias for galvanostatic EIS

$\tilde{I}$ – current phasor

$\vec{\boldsymbol{I}}$ – nuclear spin operator

I_{ch} – charge current magnitude

I_{dis} – discharge current magnitude

I_z – z-component projection nuclear spin operator

j^{Li} – Butler-Volmer exchange current density

J – magnitude of the current density per unit area

$\vec{\boldsymbol{J}}$ – current density per unit area

$J_{\mathrm{Lim}}(T)$ – temperature-dependent limiting current density

$\vec{\boldsymbol{k}}$ – reciprocal space coordinate, conjugate to $\vec{\boldsymbol{r}}$, for MRI

k_B – Boltzmann constant, 8.6173×10^{-5} eV · K^{-1}

K_{ij} – CST drag coefficient for species j on species i

L – inter-electrode spacing (for both the two-electrode conductivity cell, and the *in situ* cell)

$\mathrm{Li}_x\mathrm{An}$ (s) – anode at $\mathrm{SOC} > 0\%$; partially-lithiated anode

$\mathrm{Li}_n\mathrm{Cat}$ (s) – cathode at 0% SOC; fully-lithiated cathode

$\mathrm{Li}_{n-x}\mathrm{Cat}$ (s) – cathode at $\mathrm{SOC} > 0\%$; partially-lithiated cathode

m – nuclear spin state quantum number, with $2I + 1$ values ranging from $[-I, I]$ in integer steps

m_0 – mass of the solvent

m_s – mass of the salt

$\vec{\boldsymbol{M}}$ **–** spin-ensemble magnetization

M_0 – molar mass of the solvent (Chapter 5)

M_0 – magnitude of the equilibrium spin-ensemble magnetization (Chapter 2)

M_s – molar mass of the salt (Chapter 5)

$M_{x,y}$ – transverse component of the spin-ensemble magnetization

M_z – longitudinal component of the spin-ensemble magnetization

$M_{x',y'}$ – transverse component of the spin-ensemble magnetization in the rotating frame

$M_{z'}$ – longitudinal component of the spin-ensemble magnetization in the rotating frame

$M_{+'}$ - alternative representation for tranverse-plane magnetization, equivalent to $M_{x'} + iM_{y'}$

N_A – Avogadro's number, 6.0221×10^{23} mol^{-1}

$\vec{\boldsymbol{N}}_i$ – total flux of species i

$O[\,]$ – "order of"

p_i – RF pulse durations in pulse sequences

p_i – occupation fraction for species i in the two-compartment diffusivity analysis scheme of Kärger (Chapter 6)

$\vec{\boldsymbol{P}}$ – polarization field

$P_{D,i}$ – component dielectric polarization for species i in a mixture

q – charge on a carrier (Chapter 1, Chapter 6)

q – magnitude of reciprocal-space length scale, $q = \gamma g \delta$

$\vec{\boldsymbol{q}}$ – reciprocal space coordinate, conjugate to $\vec{\boldsymbol{r}}$, for PFG-NMR

q_{ij} – Bjerrum critical distance between ions i and j

Q – nuclear quadrupole moment

r – disk electrode radius

$\vec{\boldsymbol{r}}$ – position vector in three-dimensional space

$\vec{\boldsymbol{r}}_{ij}$ – the displacement of spin j from spin i

R – universal gas constant, $8.3145\ \mathrm{J \cdot K^{-1} \cdot mol^{-1}}$

R_{ct} – charge-transfer resistance

R_s – cell contact resistance (Chapter 1)

R_s – electrolyte solution resistance (Chapter 3, Chapter 5)

RC – resistor-capacitor block circuit element with resistance R and capacitance C

s – Laplace domain frequency, $s = \sigma + i\omega$, with real part σ and imaginary part ω

$s_{1\mathrm{M}}$ – signal equivalent to 1 M concentration

$s_j(x)$ – signal for current step j at position x

S_0 – NMR signal after initial excitation

$S(0)$ – PFG-NMR signal in the absence of a field gradient

$S(g, \delta, \Delta)$ – PFG-NMR signal

$S(q, \Delta)$ – equivalent notation to $S(g, \delta, \Delta)$

$S(t)$ – NMR signal in the time domain; the FID

$S(\omega)$ – NMR signal in the frequency domain; the spectrum

t – time coordinate

t_p – phase-encoding time

t_+ – DST cationic transference number

t_+^0 – CST cationic transference number, in the solvent reference frame

t_-^0 – CST anionic transference number, in the solvent reference frame

T – temperature

T – half-interval for a selective excitation pulse (Chapter 2)

T_1 – spin-lattice (longitudinal) NMR relaxation time

T_2 – spin-spin (transverse) NMR relaxation time

T_2^* - effective spin-spin (transverse) NMR relaxation time, including field inhomogeneity

T_2^{ih} – transverse relaxation due to field inhomogeneity

T_R – repetition time for RF pulses in DHK-SPRITE

u_i – mobility of species i

$\vec{v}$ – solvent velocity

$\vec{v}_i$ – CST average velocity for species i

$\mathbf{V}$ – EFG tensor

V_{ch} – charge voltage magnitude

V_{dis} – discharge voltage magnitude

V_{ii} – principal-axis-frame components of the EFG tensor

$V_{m,i}$ – partial molar volume of species i

V_{oc} – open-circuit voltage magnitude

W_{nm} – transition rate between spin states with energies E_n and E_m

x – unidimensional spatial coordinate

x – argyrodite halide enrichment stoichiometry (Chapter 6)

(x', y', z') - rotating frame coordinate system

x_0 – mole fraction of the solvent

x_i – mole fraction of species i

$\bar{x}_i$ – steady-state mole fraction of species i

y – argyrodite Ca^{2+} doping stoichiometry (Chapter 6)

y_s – mass fraction of the salt

z – unidimensional spatial coordinate

z_D – dipole coordination number

z_i – charge number of species i

z_{Li} – the lithium stoichiometry in dual-doped argyrodites; $z_{\mathrm{Li}} = 6 - x - 2y$

Z – impedance

(Z', Z'') or $\left(Z_{\mathrm{real}}, Z_{\mathrm{imag}}\right)$ – real and complex parts of impedance

Z_W – Warburg impedance

List of Symbols – Greek Alphabet

α – DHK-SPRITE tip angle (Chapter 2, Figure 2.11)

α – imbalance factor for oneshot PFG-NMR pulse sequence (Chapter 5)

α – least-squares regression confidence level (Chapter 6)

α_p – contact ion-pairing fraction

α_D – dielectric polarizability

γ – gyromagnetic ratio

$\gamma_\pm$ – specific molal activity coefficient

δ – PFG-NMR gradient encoding duration

$\delta\ ^7$Li – chemical shift of ^{7}Li, in ppm

$\delta\ ^{11}$B – chemical shift of ^{11}B, in ppm

$\delta\ ^{31}$P – chemical shift of ^{31}P, in ppm

δ_{iso} – isotropic chemical shift

Δ – diffusion time for PFG-NMR

Δ' - net diffusion time delay in PFG-NMR pulse sequences

$\Delta[\ ]$ - uncertainty in [ ]

Δt – discrete time increment

Δx – discrete, unidimensional spatial increment

$\Delta\omega$ – offset frequency

$\Delta\omega_{\text{eff}}$ – offset frequency in the rotating frame

ϵ_0 – the permittivity of free space, $8.8542 \times 10^{-12}\ \text{F} \cdot \text{m}^{-1}$

$\epsilon_i(0)$ – temperature-dependent permittivity constant fit coefficient (not to be confused with ϵ_0)

$\epsilon_i(T)$ – temperature-dependent permittivity of species i

$\epsilon_{\text{mix}}(T)$ – temperature-dependent mixture permittivity

η – overpotential

η_Q – quadrupolar asymmetry parameter

θ – tip-angle for the RF excitation pulse

(θ, ϕ) – spherical polar coordinates for the interconversion between principal-axis and laboratory frames for the quadrupolar Hamiltonian

κ – ionic conductivity

κ_{diff} – diffusivity-conductivity (contrast D_κ)

$\kappa_{\mathrm{Ex}}(c_s)$ – *ex situ* ionic conductivity as a function of salt concentration

κ_g – first moment of the PFG-NMR non-rectangular gradient shape

λ_g – second moment of the PFG-NMR non-rectangular gradient shape

$\vec{\boldsymbol{\mu}}$ – nuclear magnetic moment

μ_0 – the permeability of free space, $1.2566 \times 10^{-6}\ \mathrm{N \cdot A^{-2}}$

μ_i – electrochemical potential of species i

μ_D – molecular electric dipole moment

ξ – degree of electrode lithiation/delithiation

ρ – mass density

$\rho(\vec{\boldsymbol{r}}, t)$ – local spin density (Chapter 2)

$\rho_D(\vec{\boldsymbol{k}}, t)$ – local spin density, incorporating RF coil sensitivity variation, in reciprocal space

$\rho_D(\vec{\boldsymbol{r}}, t)$ – local spin density, incorporating RF coil sensitivity variation, in real space

σ – electrical conductivity

σ_g – PFG-NMR gradient shape parameter

τ_C – correlation time for NMR relaxation

τ_{echo} – spin echo duration for a CPMG experiment

τ_E – net spin echo delay in spin-echo-based MRI pulse sequences

τ_g – interval for bipolar gradient pulse pairs

τ_i – pulse sequence delay intervals

τ_i – residence time for species i in the two-compartment diffusivity analysis scheme of Kärger (Chapter 6)

τ_L – net delay for LED in PFG-NMR pulse sequences

τ_{RF} – RF pulse duration

τ_+ – cationic transport number

$\phi(\vec{\boldsymbol{r}}, t)$ – spatially-varying NMR phase factor (Chapter 2)

Φ – electric potential

Φ_i – thermodynamic factor (TDF) for species i

ψ – mutual phase shift between input and response phasors for EIS

ω_0 – Larmor precessional frequency about longitudinal field direction

ω_1 – precessional frequency about RF excitation field direction

$\omega_{\mathrm{eff}}(\vec{\boldsymbol{r}}, t)$ – spatially-varying, rotating-frame precessional frequency

ω_Q – frequency describing the quadrupolar splitting

ω_{rf} – frequency of the irradiating RF excitation field

ω' – frequency of rotation for the rotating frame

List of Symbols – Miscellaneous

$\overline{\partial c_s}/\partial x$ – steady-state salt concentration gradient

$\langle \cos(\gamma_D) \rangle$ – angular average over all pairwise combinations of dipole moments in the coordination sphere

$\mathcal{D}$ – Onsager-Maxwell-Stefan electrolyte diffusion coefficient

$\mathcal{D}_{ij}$ – Onsager-Maxwell-Stefan diffusivity of species i relative to species j in CST, $i, j = \{+, -, 0\}$

$\mathcal{F}$ – Fourier transform operator

$\hbar$ – reduced Planck constant, 1.0546×10^{-34} J · s

$\mathcal{H}_0$ – Zeeman-splitting Hamiltonian

$\mathcal{H}_D$ – Dipolar-coupling Hamiltonian

$\mathcal{H}_Q$ – Quadrupolar-coupling Hamiltonian

$\mathbb{R}^+$ – the positive real-number line

$\forall$ – “for all”

$\in$ – “in”

$\vec{\nabla}$ – gradient operator

Declaration of Academic Achievement

Dr. Sergey Krachkovskiy provided instruction on the PFG-NMR and EIS measurements in **Chapter 3** and the associated analysis method, and the initial experiments were conducted with his direct assistance. The MRI experiments used in **Chapter 4** and **Chapter 5** were also initially implemented on the spectrometer by him, he constructed the *in situ* cell, and he suggested the use of DHK-SPRITE as an image calibration tool. The solid-state electrolyte samples investigated in **Chapter 6** were synthesized by P. Adeli and E. P. Ramos at the University of Waterloo, in the group of Prof. Linda F. Nazar. They also performed the ionic conductivity and diffraction measurements, and refined the structures. All other experiments and analysis was performed by J. David Bazak.

Chapter 1 – Transport in Lithium-Ion Batteries

1.1 Overview of Lithium-Ion Energy Storage

Lithium-ion batteries have become a mainstay in energy storage for modern electronic devices, but their importance in the automotive and energy generation sectors is rapidly expanding as part of the burgeoning quest for sustainable energy sources and electrification of the transportation industry, both to avert catastrophic climate change and to mitigate the looming problem of dwindling fossil fuel reserves.[1,2] The International Energy Association estimates a fleet on the order of 5.1 million passenger electric vehicles (EV) worldwide in 2018, with sales of 2 million EVs in that year almost doubling over the previous year.[3] Lithium-ion chemistries dominate the fully EV and plug-in hybrid EV (PHEV) powertrains presently on the market.[2,3] They are also expected to play a significant role in peak-shaving and load management of an electrical grid increasingly dependent on renewable energy sources, with their attendant intermittency issues.[4] Volumes of research have been conducted on the design and optimization of materials for these lithium-ion chemistries, which are simple to conceptualize – two intercalating electrodes with an electrolyte to ferry the ions between the surfaces where they undergo redox reactions – but involve the simultaneous interaction of many physical and chemical processes at the microscopic level.[5,6]

In all battery systems,[7] lithium-ion or otherwise, the core concept is that on discharge, ions are ejected from the negative electrode via the anodic (oxidative) half-

reaction into the electrolyte, which contains a salt of the so-called "working ion" that is transferred between the electrodes. The electrons created by the formation of these ions in the anodic half-reaction do not (ordinarily) enter the electrolyte, and are instead gathered by current collectors to be distributed into the external circuit, where they can do work. The electrons then flow to the positive electrode where they undergo the cathodic (reductive) half-reaction with working ions which have migrated from the bulk of the electrolyte to the surface of the positive electrode, causing the incorporation of the reduced ions into the electrode. This whole process is spontaneous upon the completion of the external circuit with an electrical load provided that there is a potential energy drop for the working ions on transferring from the negative to the positive electrode, which, by conservation of energy, is how the electrons are able to do work in the external circuit. All of the above is (essentially, and ideally) reversed for the charging process, where the supplying of excess energy to the system via the external circuit is used to drive the ions back into the higher-potential negative electrode. Under these circumstances, the negative electrode is the cathode – in the electrochemical sense – and the positive electrode is the anode. However, when referring to electrode chemistries in the literature it is typical to denote them by their redox roles during the discharge process (so "negative electrode" and "anode" become synonymous). The discharge and charge voltages, V_{dis} and V_{ch} respectively, are described by the equations[8]

$$V_{\mathrm{dis}} = V_{\mathrm{oc}} - \eta(\mathrm{SOC}, I_{\mathrm{dis}}), \tag{1.1}$$

$$V_{\mathrm{ch}} = V_{\mathrm{oc}} + \eta(\mathrm{SOC}, I_{\mathrm{ch}}), \tag{1.2}$$

where V_{oc} is the so-called "open circuit" voltage of the disconnected cell, and η is the overpotential which results from internal resistance of the cell toward the ionic current. This overpotential is a complicated function of the many interacting physical and chemical processes internal to the cell mentioned above, but at the cell level, can be primarily associated with the state-of-charge (SOC) of the cell – that is, the balance of charge stored in the anode relative to the cathode – and the magnitude of the current at which the cell is discharging or charging. The study of several of the factors which directly affect this internal resistance to the ionic current, and how they depend on the operating conditions of the cell, will constitute the bulk of the results in this thesis (**Chapter 3-5**), however, the connection of these factors to cell-level voltages is itself a complicated subject (to be briefly surveyed in **Section 1.2**) which will not be covered in depth in the thesis.

A key difference for most lithium-ion chemistries – and all of those presently commercialized[9] – is that the anodic and cathodic reactions take place in porous intercalation electrodes, and do not (ideally) involve the direct electrodeposition and stripping of metallic lithium (as would occur with the lead working ion in a lead-acid system typical of those found in internal combustion engine vehicles, for example); rather, the electrodes consist of host materials into and out of which the lithium ions intercalate/de-intercalate. The net redox reaction and the constituent anodic and cathodic half-reactions for a lithium-ion host-guest intercalating system are:[10]

$$\mathrm{Li}_{n-\xi}\mathrm{Cat\ (s)} + \mathrm{Li}_{\xi}\mathrm{An\ (s)} \rightleftharpoons \mathrm{Li}_{n}\mathrm{Cat\ (s)} + \mathrm{An\ (s)}, \tag{1.3}$$

$$\text{Cathode Half-Cell: } \mathrm{Li}_{n-\xi}\mathrm{Cat\ (s)} + \xi\mathrm{Li}^{+}\ (\mathrm{solv}) + \xi\mathrm{e}^{-} \rightleftharpoons \mathrm{Li}_{n}\mathrm{Cat\ (s)}, \tag{1.4}$$

$$\text{Anode Half-Cell: } \mathrm{Li}_{\xi}\mathrm{An\ (s)} \rightleftharpoons \xi\mathrm{Li}^{+}\ (\mathrm{solv}) + \xi\mathrm{e}^{-} + \mathrm{An\ (s)}, \tag{1.5}$$

where ξ Li^+ ions are ejected from the partially-lithiated anode, $\mathrm{Li}_\xi\mathrm{An\ (s)}$, along with ξ electrons (e^-), solvated in the electrolyte as $\xi\mathrm{Li}^+\ \mathrm{(solv)}$, and then reduced by the electrons from the external circuit at the cathode to change its lithium stoichiometry from $\mathrm{Li}_{n-\xi}\mathrm{Cat\ (s)}$ to $\mathrm{Li}_n\mathrm{Cat\ (s)}$, the fully-lithiated cathode. With these redox reaction equations (1.3-1.5), the (average) open-circuit voltage in equation (1.2) can be approximated by the potentials of the two electrodes and the total amount of charge transferred, ξ (since lithium ions are univalent):[11]

$$V_{\mathrm{oc}} = -\frac{\left(E[\mathrm{Li}_n\mathrm{Cat\ (s)}] - E\left[\mathrm{Li}_{n-\xi}\mathrm{Cat\ (s)}\right]\right) - \left(E[\mathrm{An\ (s)}] - E\left[\mathrm{Li}_\xi\mathrm{An\ (s)}\right]\right)}{\xi e}, \qquad (1.6)$$

with e as the fundamental unit of charge. The electrodes are fashioned as highly porous networks of micro- and nanoscale particles with the electrolyte suffusing the pores to facilitate the ejection/insertion reaction kinetics to and from solvated ions with a very high electrode surface area.[8] The region between the electrodes contains an electrically-insulating separator – typically a highly porous polymer[1] – which prevents short circuiting between the electrodes and forces the liberated electrons to traverse the path through the external circuit in order to achieve the potential energy drop that results from recombining with the working ions at the positive electrode. The choice of metals for the current collectors is largely dictated by the combination of low cost and immunity from parasitic side-reactions with the electrolyte.[12] The structure and operation of a conventional lithium-ion cell is depicted in **Figure 1.1**.

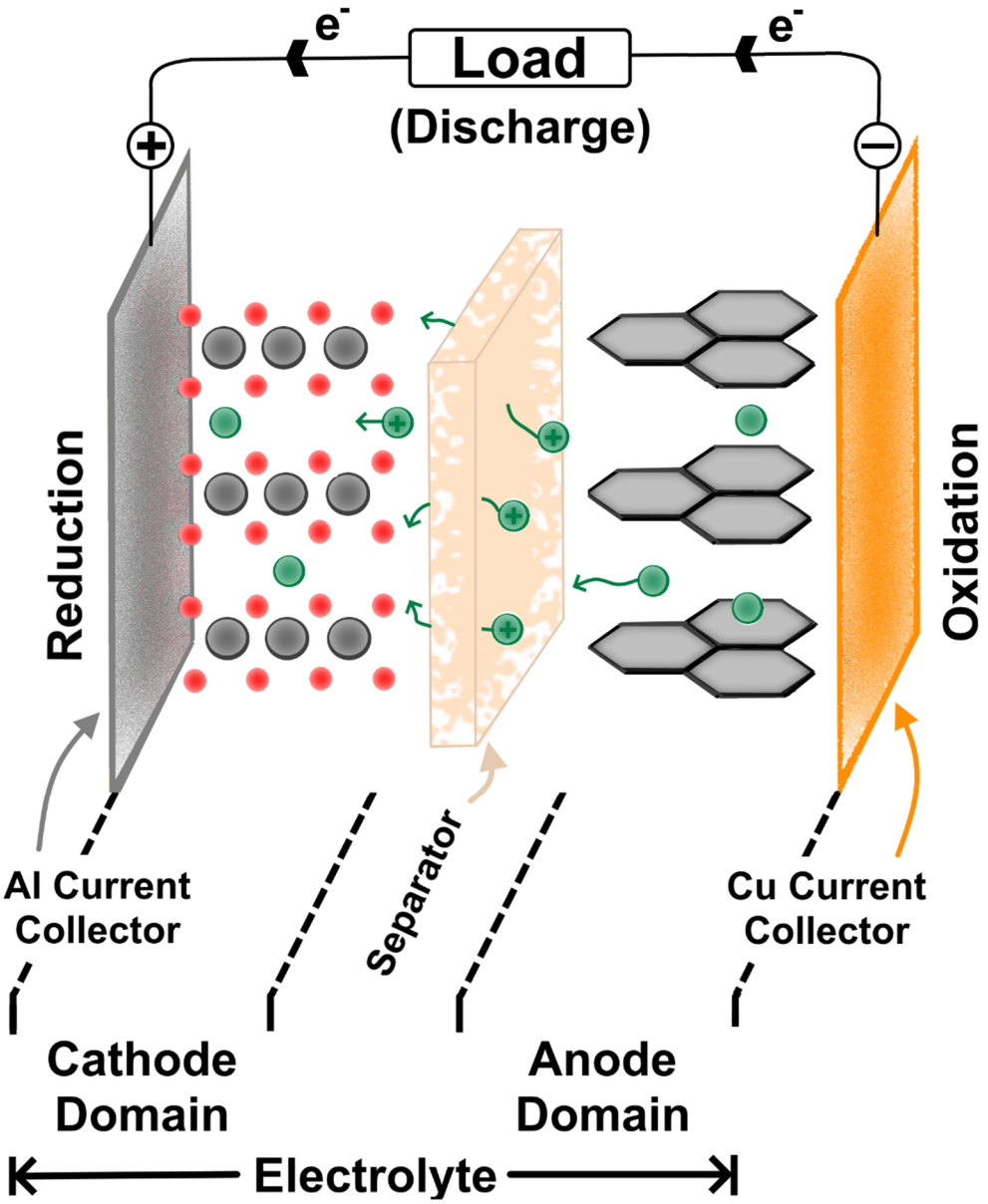

Figure 1.1 – The structure and operation of a conventional lithium-ion cell on discharge. The oxidation of the guest lithium into ions at the surface of the anode produces electric and ionic currents which travel separately through the external circuit and the electrolyte domain to recombine at the cathode. Lithium-ion battery anodes are typically primarily graphitic carbon, whereas the cathode composition ranges from layered metal-oxides (more commonly) to nano-sized polyanionic inorganic compounds which can host lithium.

The cathode material in lithium-ion chemistries can take a variety of compositions, depending to some extent on the application, with commercial varieties essentially falling into three structural families: layered oxides, spinel manganese oxides, and polyanionic phosphates. The commonality is that all feature a rigid anion framework with transition metal centres where redox reactions can take place. The layered oxides include the foremost commercial lithium-ion battery cathodes,[5] $LiCoO_2$, or LCO,[13] $Li[Ni_xMn_yCo_z]O_2$, or NMC (with $x + y + z = 1$),[14] and $LiNi_{0.8}Co_{0.15}Al_{0.05}O_2$, or NCA.[15] These materials feature high energy densities (or analogously, capacities) and operating voltages, but tend to be more expensive because of the incorporation of cobalt.[9] Indeed, recent NMC-related research has focused on maintaining the high performance of the original $x = y = z = 1/3$ composition while lowering the relative ratio of cobalt to the much less expensive nickel and manganese, although there are stability and performance trade-offs associated with this approach.[16] Spinel manganese oxides such as $LiMn_2O_4$ (typically abbreviated as LMO, although including several related structures connected through phase transitions), on the other hand, possess no such resource limitation concerns, but have long-term capacity-fade issues connected with manganese dissolution and migration to the anode (where it catalyzes electrolyte decomposition, forming a resistive film on the surface of the electrode) and oxygen evolution.[6] Polyanionic materials, of which $LiFePO_4$ (or LFP) is the most prominent example,[17] combine the lack of resource limitation (and relative inexpensiveness) of LMO with an extremely durable structure, making them amenable to high-power applications if properly nanosized and conductively coated (the bulk materials being poor electronic conductors),[18] at the downside of possessing relatively low energy

densities. In an EV context, this dichotomy between energy density and power density can be viewed roughly as a "range versus acceleration" conundrum, which is why layered oxide cathodes are preferred for electric vehicles, while LFP is more amenable to compact, high-power density applications (such as power tools).[6] The use of (cheap) elemental sulphur as a lithium-ion battery cathode, where it is reversibly electrochemically converted to Li_2S, has also received significant attention recently, but the ongoing challenges with this chemistry are low sulphur utilization, volume expansion on charge (leading to electrode cracking and loss of electrical contact), and the dissolution of Li-polysulphides which creates a shuttle mechanism to the anode, reducing coulombic efficiency.[4]

In contrast to the variety of materials employed in various applications as cathodes for lithium-ion batteries, there is one clear stand-out material for the anode side: graphite anodes are expected to retain the primacy they have been enjoying in commercial lithium-ion batteries[9,12] since the electrochemical intercalation of lithium was first demonstrated in the early 1980s.[19] In fact, lithium storage is possible in many carbonaceous structures by addition reactions, but the electrical conductivity, intra-layer ion diffusivity, rate capability, and significant storage capacity of graphite are the source of its ubiquity.[20] The ideal anode on both capacity and cell potential grounds would be lithium metal itself, but it poses safety and cyclability challenges, requiring a mechanism for plating/stripping regulation and the prevention of lithium morphological instability (principally, the formation of dendritic structures which can penetrate the separator and generate short circuit conditions, leading to thermal runaway – that is, a fire).[21] Significant development of silicon as an anode material has also been undertaken, owing to its significant capacity to alloy lithium as a

conversion electrode, but a volume expansion problem analogous to that of the sulphur cathodes described above limits the degree of silicon incorporation into anodes, or requires nanoscale architecture (*i.e.* nanowires) and compositing, which complicates the fabrication process.[22]

While the utility of graphite as an anode in state-of-the-art lithium-ion cell chemistries is unrivalled, it is not without complications of its own. Chief amongst these is that at the highly reducing potentials at which the bulk of the intercalation of Li^+ between the graphene layers occurs, typical electrolyte solvents are not stable against reduction, generating a passivating layer known as the solid-electrolyte interphase (SEI).[23] On the one hand, SEI formation is initially self-limiting and, since it is permeable to lithium ions for typical electrolyte formations, essential to the sustained operation of the cell. However, long-term cycling and cycling under abuse conditions will cause slow, continued SEI growth, which reduces lithium inventory (producing capacity fade) and results in the build-up of a resistive film that increases the overpotential (of equations 1.1 and 1.2) and reduces the rate capability (*i.e.* the achievable power) of the cell.[24] Therefore, engineering of the electrolyte composition through both solvent design and the use of sacrificial additives to the blend is a vast and critically important field of lithium-ion battery research and development.[25]

The development of liquid-state lithium-ion battery electrolytes was a long and convoluted process, and proceeded to some extent in concert with the development of anodes, in accord with the aforementioned interlink with SEI formation.[26] The essential ingredients were fully realized only in the 1990s, with the development of the non-aqueous

ethylene carbonate (EC)/dimethyl carbonate (DMC) solvent formulation for a lithium hexafluorophosphate salt, $LiPF_6$.[27] Owing to the low potential for the electrolysis of water relative to the potentials generated by lithium-ion electrodes, and the resulting evolution of flammable gases (H_2 and O_2) building pressure inside the cell, aqueous electrolytes are thoroughly incompatible with typical lithium-ion cell chemistries. (Although recent work has shown that ultra-concentrated aqueous electrolytes may actually provide a much-enhanced stability, and thereby provide a route to the elimination of non-aqueous solvents, although this development is still quite nascent.[28]) Given that a non-aqueous solvent is therefore required, and that a high polarizability is necessary to actually solvate most lithium salts, the search for viable solvents centred on small organic molecules with carbonyl, ether, nitrile, and sulfonyl moieties.[26] Cyclic carbonates – EC and the related propylene carbonate (PC) – offered the best performance, but their viscosity and in particular, the high melting point of EC ($\sim 35℃$), meant that co-solvents were necessary to achieve reasonable ionic conductivity; linear carbonates like DMC, which has a much lower viscosity but a poorer permittivity (meaning that it is not as strong a solvent – refer to **Chapter 3**), being a natural choice.[29] The $LiPF_6$ salt has become the default choice for electrolytes from a limited range of possibilities not on account of any one particularly strong property – $LiBF_4$ and $LiClO_4$ have higher mobility; $LiAsF_6$ and LiTFSI have higher degrees of dissociation in polar solvents – but rather by being the optimal compromise between these competing characteristics, as well as not causing destructive corrosion of the Al current collectors (like LiTFSI, which is otherwise much more stable than all of the other aforementioned candidates).[30] An additional major downside of using organic solvents is

their inherent flammability, especially in light of the massive energy density concentrated into lithium-ion cells. To ameliorate this concern – amongst other potential benefits – increasing attention is turning to solid-state electrolytes. These materials are the subject of **Section 1.4**.

With the electrochemical constraints described above on the electrolyte formulation, a central question for the performance and modelling of electrochemical cells is how these mixtures perform with regard to their primary function: the transport of ions between the electrodes, particularly with regard to cell-level operating variables such as temperature and applied current magnitude. In essence, this can be viewed as the central question of this thesis as well. Electrochemical models, which describe the mass and charge transport throughout the cell and connect it to the formal equations for the charging/discharging potentials of equations (1.1) and (1.2), require physicochemical transport parameters which must be obtained from experiment. These models are introduced in **Sections 1.2** and **1.3**, and **Chapters 3-5** describe results obtained using various magnetic resonance measurement techniques to quantify the transport and relate it to the models. **Chapter 2** provides an introduction to these magnetic resonance methods. **Chapter 6** then switches the focus to ion transport in solid-state electrolytes, introduced in **Section 1.4**, with the aim of elucidating how various structure-property relationships impact the transport. **Chapter 7** then provides a summary of the major findings, and an outlook on future work that would extend the results presented in this thesis. The objective throughout is to characterize and quantify ion transport phenomena in lithium-ion

electrolyte materials, but also to glean as much insight as possible on the inner workings of the materials from experiments on fundamental properties.

1.2 Mathematical Models of Conventional Lithium-Ion Batteries

An important component in the implementation of lithium-ion batteries in automotive applications is the battery management system (BMS), which provides control and monitoring of the battery pack during operation. Accurate models of the dynamical processes occurring within the battery, on a wide variety of timescales, are crucial for successful BMS operation. The BMS objectives broadly divide into short-term control of the state-of-charge (SOC) and longer-term monitoring of the state-of-health (SOH), in addition to thermal management. Owing to the complexity of the physical and chemical processes occurring in the lithium-ion system, state-of-the-art modelling approaches are aiming to employ realistic electrochemical models,[31,32] as opposed to the phenomenological models that have conventionally been implemented in the past.[33] Electrochemical models can provide not only enhanced prediction ability, but retain physical insight about the microscopic processes occurring within the battery and furnish a natural means of incorporating aging phenomena into the model, toward the longer-term SOH monitoring of the battery pack.[34,35]

There is a complex hierarchy of length- and time-scales in battery systems[36] – particularly when intercalation electrodes are involved – which has correspondingly yielded a hierarchy of modelling strategies that balance predictive ability and computational intensity to varying degrees.[37,38] Perhaps the simplest approach is that of the behavioural model, which is a lumped-parameter method for phenomenologically

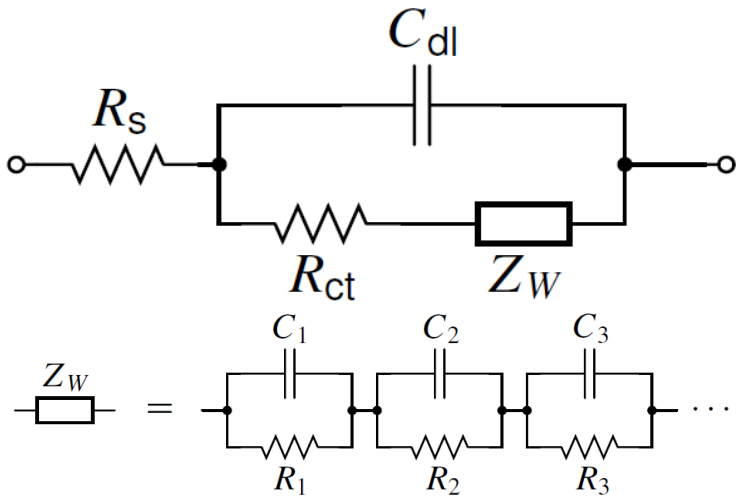

Figure 1.2 – Randles equivalent circuit model of a battery, including a contact resistance for the cell (R_s), a charge-transfer resistance to and from the electrolyte domain from the electrode domains (R_{ct}), an electrochemical double-layer capacitance (C_{dl}) which forms in the electrolyte at the electrode surfaces, and a Warburg impedance (Z_W) which mimics the diffusive response of the electrodes as a series of RC blocks with progressively increasing time constants. Adapted from Plett, 2015.[38]

describing whole-cell dynamics in terms of measured terminal voltage response and an internal state – the SOC level – that is estimated online in the BMS.[39] A somewhat more sophisticated approach, albeit still phenomenological, is the equivalent circuit model, which reduces the intricate dynamics of the battery to a collection of circuit elements; a minimal model incorporating no SOH parameterization, the Randles equivalent circuit,[40] is depicted in **Figure 1.2**. The Warburg element in **Figure 1.2**, Z_W, is a nonlinear element, which must be reduced to a series of RC blocks[38] in order to be compatible with linear state-space representations frequently encountered in control systems engineering.[41] For the equivalent circuit model approach, this at least provides a clear delineation of the relevant timescales in the battery, which can be linked to physicochemical processes.[42] Nevertheless, the drawbacks common to both methods are that they have limited

adaptability, despite their computational simplicity, and largely obfuscate the physical significance of the parameters which govern their response to the inputs, which, as mentioned above, makes the incorporation of aging effects difficult.[34] Additionally, they are predicated on linear response of the state-space model to the inputs; for so-called microcycling, common to portable electronics BMS, this is readily fulfilled, but the frequent occurrence of "deep cycling" episodes which an automotive BMS must account for there is no such guarantee.[32]

This is where realistic electrochemical models enter the frame. Formulated from governing equations for the mass- and charge-transport in each of the domains in **Figure 1.1**, along with Butler-Volmer kinetics to describe the charge transfer to and from the electrolyte domain from the electrode domains and constitutive relations among the parameters, these microscopic models aim to largely capture the dynamics of the battery as they exist *in operando*.[38] The prototypical Doyle-Fuller-Newman model[43] is the platform upon which many electrochemical models are constructed; a summary of the necessary equations is provided in **Figure 1.3**, although the full description of all of the parameters is omitted here, as this thesis will focus exclusively on the electrolyte domain, described in **Section 1.3** (these definitions can be found in the excellent texts on electrochemical systems by Newman[7] and battery modelling and estimation by Plett[38]). As can be surmised by inspection of **Figure 1.3**, the full-order model is computationally intractable for online estimation in BMS applications, so a reduced-order model based on the single-particle formulation (SPM) is often utilized, which reduces the electrode geometry from a porous collection of particles with electrolyte occupying the pores to a single sphere of electrode

particle surrounded by electrolyte.[31,44–47] In any event, owing to the vast parameter space, these studies frequently draw from the experimental physicochemical literature to assign the model parameters[48–52] – particularly as regards their temperature-dependence, which is becoming an increasingly important focus of improved BMS estimation capability.[42,47] Additionally, many reduced-order formulations of electrochemical models neglect the electrolyte transport dynamics altogether, treating the electrolyte domain in a volume-

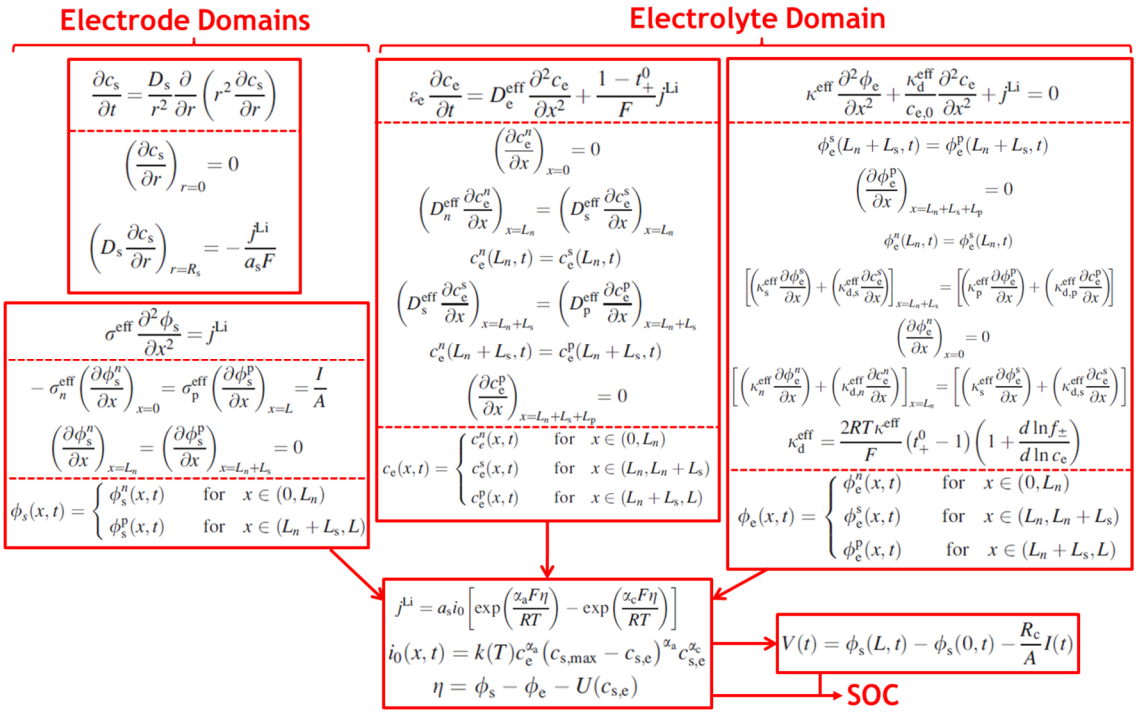

Figure 1.3 – Mathematical formulation of the Doyle-Fuller-Newman model for mass- and charge-transport in the electrode and electrolyte domains with Butler-Volmer charge transfer kinetics, including all boundary conditions (below first set of dashed lines in each domain) and constitutive relations (below second set of dashed lines). This model can be used for SOC estimation in an automotive BMS. A full description of the parameters can be found in the texts of Newman[7] and Plett.[38] Adapted from Plett, 2015,[38] and Tanim *et al.*, 2015.[47]

averaged sense, which, as will be the focus of **Chapter 4**, is demonstrably unsound at low-temperature, and at high C-rate,[1] as the results of **Chapter 5** will emphasize.

1.3 Theory of Ion Transport in Liquid-State Electrolytes

As mentioned in **Section 1.2**, the basic theory for quantitatively modelling transport in electrolyte solutions has been primarily established in its canonical form by Newman, and forms the basis for the widely used Doyle-Fuller-Newman electrochemical model frequently deployed in state-estimation algorithms for battery control systems.[43] The discussion in this section will therefore largely parallel that of chapters 11 and 12 in Newman's book.[7] The concentrated solution theory (CST) component of the Doyle-Fuller-Newman model is best understood with reference to the simpler and more familiar theory of dilute solutions (DST), wherein the motions of solute molecules are not correlated and the solvent can be viewed as a passive medium. With that stipulation, the total ionic flux in DST can simply be written down as a combination of diffusion, migration and convective fluxes:

$$\underbrace{\vec{\boldsymbol{N}}_i}_{\text{flux}} = \underbrace{-z_i u_i c_i F \vec{\nabla}\Phi}_{\text{migration}} - \underbrace{D_i \vec{\nabla} c_i}_{\text{diffusion}} + \underbrace{c_i \vec{\boldsymbol{v}}}_{\text{convection}} \quad , \tag{1.7}$$

where $\vec{\boldsymbol{N}}_i$ is the total flux of ion i, $-\vec{\nabla}\Phi$ is the electric field, $\vec{\boldsymbol{v}}$ is the solvent velocity (if nonzero), and c_i, z_i, u_i and D_i are the concentration, charge number, mobility, and intrinsic diffusivity, respectively, of ion $i = \{+, -\}$ (with F as Faraday's constant; additional discussion of the precise meaning of intrinsic diffusivity, along with all of the various types of diffusivity discussed in this thesis, can be found in **Section 3.1**). Convection is generally

[1] C-rate describes rate of charge/discharge for a cell in terms of units of its own capacity.

considered to be negligible in electrolyte systems, although a careful consideration of its impacts may be necessary in high C-rate conditions.[53] Mobility is only well-defined in the DST context, where it is related to the diffusivity via the Nernst-Einstein equation:

$$D_i = RTu_i, \tag{1.8}$$

with R as the universal gas constant, and T as the temperature of the system. The diffusion is driven by the ion concentration gradient, so the mobility is a sort of thermal "flow inertia" which is necessary to connect the electric field to a coherent flow of ions – the migration. This term in equation (1.7) is very similar in form to Ohm's law ($\vec{\boldsymbol{J}} = -\sigma\vec{\nabla}\Phi$, with $\vec{\boldsymbol{J}}$ as the current density and σ as the electrical conductivity). Conservation of mass in the form of the continuity equation,

$$\frac{\partial c_i}{\partial t} = -\vec{\nabla} \cdot \vec{\boldsymbol{N}}_i, \tag{1.9}$$

then yields the evolution of the ion concentration gradient. The continuity equation enforces conservation of mass by implying that any local accumulation is due solely to the net input from the fluxes, with the absence of production and depletion of species within the electrolyte bulk proscribed by its electroneutrality and the inertness of the solvent medium. In conjunction with the explicit statement of this electroneutrality condition,

$$\sum_i z_i c_i = 0, \tag{1.10}$$

the conservation of current, $\vec{\nabla} \cdot \vec{\boldsymbol{J}} = 0$, where $\vec{\boldsymbol{J}}$ in this context becomes the sum of the ionic fluxes ($\vec{\boldsymbol{J}} = F\sum_i z_i\vec{\boldsymbol{N}}_i$), defines the charge transport of the electrolyte:

$$\vec{\boldsymbol{J}} = -F^2\vec{\nabla}\Phi\sum_i z_i^2 u_i c_i - F\sum_i z_i D_i\vec{\nabla}c_i + F\vec{\boldsymbol{v}}\sum_i z_i c_i. \tag{1.11}$$

Isolating the electric field in analogy with Ohm's law defines the ionic conductivity, κ, in the dilute-solution limit (where the solvent reference frame is assumed, or equivalently, that convection is absent):

$$-\vec{\nabla}\Phi = \frac{1}{\kappa}\vec{J} + \frac{F}{\kappa}\sum_i z_i D_i \vec{\nabla} c_i \quad \Longrightarrow \quad \frac{1}{\kappa} = -\frac{RT}{z_+ z_- F^2}\frac{(1-t_+)}{c_+ D_-}. \tag{1.12}$$

The second step in equation (1.12) is a specialization to the common case of a binary electrolyte salt. When this is the case, the fraction of current carried by the cationic species of charge is defined by the cation transference number, t_+:

$$t_+ = \frac{z_+ D_+}{z_+ D_+ - z_- D_-}. \tag{1.13}$$

The net mass transport in a binary electrolyte, where electroneutrality is assumed, is defined by the salt diffusivity:

$$D_s = \frac{(z_+ - z_-) D_+ D_-}{z_+ D_+ - z_- D_-}. \tag{1.14}$$

With D_s and electroneutrality, equation (1.9) can be written in terms of the neutral salt concentration, $c_s \equiv c_+ = c_-$. Collectively, the parameters κ, t_+, and D_s completely characterize the electrolyte transport.

On the other hand, when the solution is concentrated, the solvent motions become correlated with the salt, as do the motions of the ions with each other. The most feasible means of treating this strongly interacting morass of molecules is via the formalism of CST, which specifies that $n(n-1)/2$ measurable parameters are necessary to fully describe the ionic and solvent fluxes of an n-component mixture. For a binary, univalent salt, the components are the cation (denoted with a '+'), the anion (denoted with a '−'), and the

solvent (commonly considered a uniform, uncharged medium, and therefore denoted with a '0'). The resulting three parameters to describe the transport in the binary, univalent electrolyte mixture in CST mirror those of the DST case: D_s, κ, and the transference number, t_+^0, which has updated notation now representing the transference of the cation with respect to the solvent velocity (all governing equations could equivalently be formulated with respect to the transference of the anion, t_-^0, of course, via the inherent electroneutrality of the electrolyte). However, as will be outlined below, the forms of these parameters are substantially altered under CST relative to the DST equations (1.12-14) given above.

The origin of the $n(n-1)/2$ parameters in CST traces to the fundamental governing equations, which describe the electrochemical potential gradients, $\vec{\nabla}\mu_i$, of each species ($i = \{+,-,0\}$ for a binary, univalent electrolyte) as being driven by what amount to drag forces for the velocities of each component with respect to another:

$$c_i\vec{\nabla}\mu_i = \sum_j K_{ij}\left(\vec{\boldsymbol{v}}_j - \vec{\boldsymbol{v}}_i\right) = RT\sum_j \frac{c_i c_j}{c_T \mathcal{D}_{ij}}\left(\vec{\boldsymbol{v}}_j - \vec{\boldsymbol{v}}_i\right), \tag{1.15}$$

where the $\vec{\boldsymbol{v}}_i$ are the *average* species velocities, and the K_{ij} are the drag coefficients (R is the universal gas constant and T is the temperature). The quantity c_T is the total concentration:

$$c_T = \sum_i c_i. \tag{1.16}$$

The equations represented by (1.15) essentially put the solvent and the ions on 'equal footing' in the treatment of the electrolyte transport. By factoring K_{ij} into the component concentrations, normalized by the total concentration, and separating out RT, what remains

is a quantity with dimensions of mutual diffusivity, $\mathcal{D}_{ij}$, occasionally termed 'the Onsager-Maxwell-Stefan (OSM) diffusivity.' (This quantity can also be interpreted as a friction coefficient, by continuing the analogy with drag force, but diffusivity is a more natural setting for the description of transport processes.) Additionally, by Newton's third law, $K_{ij} = K_{ji}$ trivially, and hence, $\mathcal{D}_{ij} = \mathcal{D}_{ji}$. Therefore, the $\mathcal{D}_{ij}$ constitute the most fundamental description of the $n(n-1)/2$ parameters to describe the CST system, and the mutual nature of their description is the origin of this necessary number of parameters.

The electrochemical potentials are essentially abstract, being a hybrid of the usual thermodynamic chemical potentials and electrical potentials, to side-step the complications of reference potentials for these quantities in solution and the intertwined processes of diffusion (against the chemical potential gradient) and migration (against the electrical potential gradient). As a result, the primary means of operationalizing the governing equations is to isolate the $\vec{\boldsymbol{v}}_i$ and define the fluxes of each species, $\vec{\boldsymbol{N}}_i = c_i\vec{\boldsymbol{v}}_i$. The fluxes can then be interpreted through the lens of conservation laws – namely, conservation of mass and charge – since the total current density, $\vec{\boldsymbol{J}}$, is proportional to the sum of the fluxes in CST in the same way that equation (1.11) was developed for DST, and conservation of current ($\vec{\nabla} \cdot \vec{\boldsymbol{J}} = 0$) and mass (the continuity equation, 1.9) carry over as always. The algebra is involved, but by combining the governing equations as fluxes with the conservation laws and making use of the Gibbs-Duhem relation (that is, $\sum_i \vec{\boldsymbol{N}}_i \cdot \vec{\nabla}\mu_i = 0$ at constant temperature and pressure), they can be reconstituted as the following mass- and charge-balance partial differential equations, specific to a binary, univalent electrolyte:

$$\frac{\partial c_s}{\partial t} = \vec{\nabla} \cdot \left[D_s \left(1 - \frac{\partial \ln(c_0)}{\partial \ln(c_s)} \right) \vec{\nabla} c_s \right] - \frac{\vec{\boldsymbol{J}} \cdot \vec{\nabla} t_+^0}{F}, \tag{1.17}$$

$$\vec{\nabla} \cdot \vec{\boldsymbol{J}} = \vec{\nabla} \cdot \left[-\kappa \vec{\nabla} \Phi - \frac{2\kappa RT}{F} \left(1 + \frac{\partial \ln(f_\pm)}{\partial \ln(c_s)} \right) (t_+^0 - 1) \vec{\nabla} \ln(c_s) \right] = 0. \tag{1.18}$$

The parameters involved in equations (1.17) and (1.18) are either intrinsic to the salt (its concentration, c_s, and mean molar activity coefficient, $f_\pm$, which describes its tendency to dissociation in solution), the solvent (c_0), or are comprised of combinations of these and the OSM diffusivities previously introduced. The operating conditions of the system are defined by the current density ($\vec{\boldsymbol{J}}$) – and by extension, the resulting internal electrical potential gradient, $\vec{\nabla}\Phi$ – as well as the temperature.

The further development of equations (1.15), (1.17), and (1.18) into expressions for D_s, κ, and t_+^0 – and the ramifications for measuring them – are elaborated in **Chapter 5**, in the context of *in situ* transport parameter measurements in a highly polarized cell, and so will not be reproduced here. However, it is fruitful to conclude the discussion of CST as Newman does,[7] by comparing the DST and CST equations in parallel, as presented in **Table 1.1**. The forms of the salt diffusivity and transference number are appealingly similar, but the switch from intrinsic to OSM diffusivities on going from the DST to the CST context represents a deceptively significant increase in the complexity of the interactions which the parameters represent, since the motions of the ions are no longer considered independently of the solvent in the CST case. Related to this, the form of the ionic conductivity equation in CST bears out the other additional complication: the appearance of a new term involving $\mathcal{D}_{+-}$, which takes into account the diffusion of the cations and anions with respect to each

other, quantifying the mutual drag in both their diffusion and migration as a result of interactions between them that are considered negligible in the DST case.

The theoretical development above is used heavily, as mentioned, in **Chapter 5**, with the aim of attempting to evaluate the expressions in the CST column of **Table 1.1** using *in situ*, spatially-resolved magnetic resonance measurements of the ion diffusivities in a polarized electrolyte, coupled with *in situ* magnetic resonance images of the electrolyte concentration gradient itself in the steady-state of equation (1.17). The aim of **Chapter 4** is to determine the influence of temperature on this steady-state of equation (1.17), and also confirm that the measured steady-state concentration gradient does indeed correspond to the Newman model predictions for it, again primarily making use of *in situ* magnetic resonance imaging. **Chapter 3**, meanwhile, examines a method for evaluating t_+^0 from the magnetic resonance diffusivity measurements taking account of the fact that these measurements are not sensitive to the charge state of the nuclei being probed – that is, they include contributions from aggregate species, and in particular, neutral ion pairs which can form transiently in non-dilute solutions. This technique is again called into action for the

Table 1.1 – Comparison of electrolyte transport parameter expressions between dilute and concentrated solution theory.

Concentrated Solution Theory	**Dilute Solution Theory**
$D_s = \frac{(z_+ - z_-)\mathcal{D}_{0+}\mathcal{D}_{0-}}{z_+\mathcal{D}_{0+} - z_-\mathcal{D}_{0-}}$	$D_s = \frac{(z_+ - z_-)D_+D_-}{z_+D_+ - z_-D_-}$
$t_+^0 = \frac{z_+\mathcal{D}_{0+}}{z_+\mathcal{D}_{0+} - z_-\mathcal{D}_{0-}}$	$t_+ = \frac{z_+D_+}{z_+D_+ - z_-D_-}$
$\frac{1}{\kappa} = -\frac{RT}{c_T z_+ z_- F^2}\left(\frac{1}{\mathcal{D}_{+-}} + \frac{c_0}{c_+}(1 - t_+^0)\frac{1}{\mathcal{D}_{0-}}\right)$	$\frac{1}{\kappa} = -\frac{RT}{c_0 z_+ z_- F^2}\frac{c_0}{c_+}(1 - t_+)\frac{1}{D_-}$

analysis in **Chapter 5**. More specific background information for all three chapters is provided in their corresponding introductory sections.

1.4 Solid-State Electrolytes and Ion Transport

While much of the research in this thesis is focused on conventional liquid-state lithium-ion battery electrolytes, recent policy momentum by both governments[54,55] and automakers[56,57] in the electromobility sector has underscored their interest in long-term development strategies that will ultimately encompass all-solid-state batteries (ASSBs). The recent large-scale and multi-billion dollar recall of Samsung smartphones with "exploding" batteries has illustrated the volatility of the lithium-ion system when either poorly manufactured or subject to abuse, and there are considerable transportation safety issues associated with lithium-ion batteries as well.[58] As alluded to in **Section 1.1**, particularly problematic is the flammable solvent used in the electrolyte, the need for which is obviated in ASSBs. Solid-state electrolytes for ASSBs, in addition to realizing a solvent-free system, have as their virtues improved shock-resistance, large electrochemical windows, thermal stability, amenability to miniaturization, and environmental friendliness.[59,60] Additionally, several promising cathode materials have voltage windows extending above 4.5 V, and certain alternative pyrophosphate cathodes[61] have intercalation potentials as high as ∼5 V, which exceeds the electrochemical stability of many common electrolyte solvents,[12,25] so solid-state electrolytes may also enable high-power-density energy storage applications not presently accessible to liquid electrolytes.[62] The emergence of so-called "micro-mechatronics" has also established an arena where thin-film batteries (i.e. containing a solid-state electrolyte) would be indispensable.[63] Therefore, given the

momentum towards the development of ASSB with solid-state electrolytes in the current industrial development cycle, and the major potential safety benefits and novel applications, it is an opportune period of time to study the fundamental dynamics and structural properties of solid-state electrolytes, with an eye toward a more complete understanding of how they work on a microscopic level and how to develop versions with optimal properties.

Ion conductors tend to be similar in conceptual function to cathode materials – voids in the host framework for guest ions – but have cation transference numbers close to unity; there is no electrical conduction (and there are, of course, no mobile anions as with conventional liquid electrolytes), so they are not electrochemically active.[60] The conduction mechanism is hopping between potential wells – voids in the host crystal structure which coordinate the ions, either consisting of unoccupied crystallographic sites or interstitial sites which the guest ion may occupy – mediated by phonon motion of the framework itself, which provides the activation energy for the hop.[64] Void sites are typically only partially occupied, which is what enables the relatively fast ion conduction.[65]

Many types of oxide lithium ion conductors have been identified: garnet-type materials with $A_3B_3C_2O_{12}$ frameworks (with $A, B,$ and C denoting cations, which can be a variety of elements, that are, respectively, 8-fold, 4-fold, and 6-fold coordinated),[62] NAtrium SuperIonic CONductor (NASICON)-type frameworks (with formula $A_xM_2(XO_4)_3$, where A is an alkali metal, M is a transition metal, and X is silicon or a pnictogen, notably LATP),[66] LIthium SuperIonic CONductor (LISICON)-type frameworks (e.g. $Li_{14}ZnGe_4O_{16}$),[59] amorphous LiPON (a solid solution of Li_3PO_4 with N, in essence),[67]

perovskite (ABO_3)-type lithium lanthanum titanate (LLTO),[68] amongst many others. However, interfacing with electrodes is an ongoing challenge,[69] and the poor ductility, high grain-boundary resistance,[70] and propensity toward mechanical strain (leading to cracking) of oxide-based ion conductors somewhat limits their upside.[71]

One increasingly prominent strategy for both ameliorating the ductility and grain-boundary resistance issues of oxides and simultaneously boosting their conductivity is to simply replace O^{2-} with the much more polarizable S^{2-}.[72] This idea really gathered steam in 2011, with the publication of the thio-LISICON $Li_{10}GeP_2S_{12}$ (LGPS), which exhibited a room-temperature conductivity higher than what is attainable in most *liquid* electrolytes, let alone oxide ion conductors.[73] Following on the heels of this discovery, many other fast-conducting thio-LISICON variants – $Li_{10}SnP_2S_{12}$ (LSnPS)[74] and $Li_{11}Si_2PS_{12}$ (LSiPS),[75] for example – were rapidly reported. In parallel with the development of thio-LISICONs, the argyrodite family of lithium-sulphide ion conductors was also discovered and steadily refined.[76] While sulphides almost uniformly exceed their oxide variants in terms of ionic conductivity, they do possess downsides in the form of poorer electrochemical windows – requiring the generation of fortuitous or synthetic interfaces – and limited thermodynamic stability in the presence of moisture, issues which are presently the subject of intense research.[63,77] Concurrently to these more materials engineering-oriented challenges, much effort is also presently being directed toward unravelling the key structural and chemical features that enable fast ion conduction in sulphides, with the aim of uncovering universal design principles for this class of materials which might spur further discovery of materials families which are not afflicted by these limitations.[78,79]

Pursuant to this objective, experimental characterizations of the lithium ion dynamics within lithium-sulphide frameworks are presently highly topical. Owing to the obviated necessity of a mobile counter-ion, since the framework itself performs this role in solid-state electrolytes,[71] lithium-ion conduction in these materials does not produce the concentration gradients that are discussed in **Section 1.3**, and studied in **Chapters 4-5** of this thesis. This at once makes lithium-ion transport simpler *and* horrendously more complicated in solid-state electrolytes, depending on the level of characterization; the discrete translational symmetry and multi-ion correlations leading to concerted hopping processes is very computationally intensive to accurately calculate, especially given that the high vacancy populations of these materials necessitate large supercells to accurate reflect the macroscopic stoichiometries.[78,80] An analogous difficulty afflicts experimental measurements of solid-state transport: it is very difficult to connect the experimentally measured length- and time-scales of the diffusion process with atomic-scale properties of the structure, because of the strong correlations in the hopping.[81]

Starting from the most fundamental description, on the macroscopic scale, and irrespective of the microscopic hopping mechanism – interstitial, vacancy-mediated, substitutional, and so forth[64] – the diffusion adopts, or can be reasonably approximated to, a Fickian diffusion process.[82–84] Schematically, this can be envisioned as in **Figure 1.4**,[85] where the flow of density to and from a position on the grid, x, within a time interval Δt

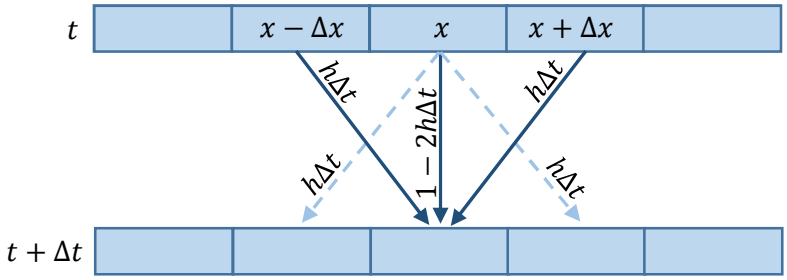

Figure 1.4 – Schematic overview of Fickian diffusion, illustrating the flow of density to and from position x between frames t and $t + \Delta t$, with hopping rate h. Adapted from Strauss, W. A. *Partial Differential Equations*, John Wiley and Sons, 2008.

can be described by a probability of hopping per unit time, h. Denoting this density (be it a concentration, occupation fraction, *etc*.) by ρ, then

$$\rho(x, t + \Delta t) = h\Delta t\rho(x - \Delta x, t) + (1 - 2h\Delta t)\rho(x, t) + h\Delta t\rho(x + \Delta x, t). \quad (1.19)$$

Rearranging, and moving to the continuum limit:

$$\frac{\rho(x, t + \Delta t) - \rho(x, t)}{\Delta t} \xrightarrow{\Delta t \to 0}$$

$$\frac{\partial \rho}{\partial t} = h[\rho(x - \Delta x, t) + \rho(x + \Delta x, t) - 2h\Delta t\rho(x, t)] \xrightarrow{\Delta x \to a} ha^2 \frac{\partial^2 \rho}{\partial x^2}, \quad (1.20)$$

where a is taken as the lattice spacing. Equation (1.20) is the canonical Fickian diffusion equation, with $D = ha^2$. Generalizing to an arbitrary number of dimensions,

$$\frac{\partial \rho}{\partial t} = D\nabla^2 \rho. \quad (1.21)$$

which is identical to the DST mass-transport equation in the absence of migration (*i.e.* the electric potential is zero) and convection (which can be seen from the CST result in equation (1.17), for which the first term reduces to the DST result when the solvent concentration does not vary with the local salt concentration). Solutions to (1.21) have the form of a Gaussian function in position from the origin, $\vec{\boldsymbol{r}}$, with a spread (variance) which

increases with increasing diffusion time, t. This equation can be modified, as necessary, with source/sink terms and convection in a straightforward fashion, but as presented, equation (1.21) can be used to readily derive the Einstein relation,

$$\langle|\vec{\boldsymbol{r}}|^2(t)\rangle = 2dDt, \tag{1.22}$$

by multiplying through $|\vec{\boldsymbol{r}}|^2$ and integrating over space, where d is the number of dimensions (in principle, this is only valid as $t \to \infty$). This relation is of fundamental importance: on the left-hand side is the ensemble average of microscopic displacement after a time t has elapsed, and on the right-hand side is the macroscopic diffusion coefficient. It is a highly general result – and essentially the definition of the diffusion coefficient[84] – which provides a crucial micro-macro interconnection that is often exploited in first-principles studies.[78]

However, diffusion in solid-state ion conductors is decidedly *not* Fickian at the microscopic scale, because of the aforementioned inter-ionic correlations. The Einstein relation is therefore often modified with the introduction of a correlation factor, $0 < f \leq 1$,[86] with $f = 1$ implying isotropic, purely random-walk (that is, Fickian) diffusion of the type described by equation (1.21). It is also important to delineate between measurements which capture *self-diffusion* of a species i – purely thermal, equilibrium motion, denoted D_i^* – and *chemical diffusion*, $\widetilde{D}_i$, which occurs against a concentration gradient (a non-equilibrium, irreversible process if uncompensated by other competing processes), with the two related by a "thermodynamic factor" $\widetilde{D}_i = D_i^*\Phi_i$ that incorporates counter-charge interactions (the salt diffusivity D_s of equation (1.17) and **Table 1.1** is synonymous with this chemical diffusion coefficient, as can be seen in **Section 5.3**). Since concentration

gradients are minimal in solid-state ion conductors (at least, on the bulk scale), a measurement of self-diffusivity for these materials is, for all practical purposes, a measurement of the diffusivity of the ions in the material (in sharp contrast with the approach in **Chapter 3** for liquid electrolytes). This type of self-diffusivity measurement is precisely what is furnished by pulsed-field gradient magnetic resonance techniques,[87] which are introduced in **Chapter 2** and encountered throughout the remainder of the thesis.

While the correlation factor, f, is very difficult to determine (properly) experimentally,[81] it is possible to develop a direct measure of the correlation in the ion transport via the Haven ratio,

$$H_R = \frac{D^*}{D_\kappa}, \tag{1.23}$$

where D_κ is the charge-diffusivity, computed via the Nernst-Einstein equation:

$$D_\kappa = \frac{k_B T}{cq^2}\kappa, \tag{1.24}$$

with c as the charge carrier concentration, q as the charge per carrier, k_B and the Boltzmann constant, and T as the temperature. For solid-state electrolytes, $H_R = 1$ corresponds to purely thermal motion – all conductive motion is diffusive motion – which essentially corresponds to the dilute charge carrier limit (and incidentally, this is the only case when $H_R = f = 1$). At the other limit, $H_R = 0$, it would imply that *all* motion is concerted; the ion conductor is essentially behaving as a 'conveyor belt.' In practice, most ion conductors exhibit values of H_R between these extremes.[88] H_R can thus serve as a useful probe of factors which enhance the ionic conductivity on an atomic scale – most significantly, the vacancy population of the ion sublattice in the ion conducting framework.

The measurement and analysis of solid-state ion diffusivity is not grappled with in this thesis until **Chapter 6**, following, as outlined in **Sections 1.1** and **1.3**, the results on liquid-state electrolytes presented in **Chapters 3-5**. The aim of **Chapter 6** is to apply solid-state diffusivity measurements to the elucidation of several structure-property relationships in two different lithium-sulphide ion conductor families: the argyrodites and a thio-LISICON, $Li_{3.30}Al_{0.15}P_{0.85}S_4$ (LAPS). The Haven ratio performs a central role in the interpretation of the diffusivity measurements for the first of these, providing an experimental probe of the influence of progressively increasing halide-enrichment of the argyrodites, correlated against the activation energies of the corresponding phases. Diffusivity – and its associated activation energy – is again used to correlate with structural modifications in the argyrodites in the form of aliovalent Ca^{2+}-ion doping; it is also used to examine the influence of pellet compression on microscopic ion transport for one of these phases. This approach is then taken a step further for the transport characterization of the LAPS sample, with the glass, crystalline powder, and crystalline pellet forms of the sample all examined. Here, a second diffusivity component – attributed to the residual amorphous phase – is found for the powder and pellet samples, with the remaining bulk diffusivity component the only one exhibiting the influence of the pellet compression. The aim of all three studies was to gain as much insight as possible about the fundamental factors affecting lithium-ion transport in the studied solid-state ion conductors, rather than merely quantifying it.

1.5 References

(1) Tarascon, J.-M.; Armand, M. Issues and Challenges Facing Rechargeable Lithium Batteries. *Nature* **2001**, *414* (6861), 359–367.

(2) Thackeray, M. M.; Wolverton, C.; Isaacs, E. D. Electrical Energy Storage for Transportation—Approaching the Limits of, and Going beyond, Lithium-Ion Batteries. *Energy Environ. Sci.* **2012**, *5* (7), 7854.

(3) IEA. *Global EV Outlook 2019*; Paris, 2019.

(4) Nazar, L. F.; Cuisinier, M.; Pang, Q. Lithium-Sulfur Batteries. *MRS Bull.* **2014**, *39* (05), 436–442.

(5) Croy, J. R.; Abouimrane, A.; Zhang, Z. Next-Generation Lithium-Ion Batteries: The Promise of near-Term Advancements. *MRS Bull.* **2014**, *39* (05), 407–415.

(6) Doeff, M. M. Battery Cathodes. In *Encyclopedia of Sustainability Science and Technology*; Springer New York: New York, NY, 2012; pp 708–739.

(7) Newman, J.; Thomas-Alyea, K. E. *Electrochemical Systems*, 3rd ed.; John Wiley & Sons, 2004.

(8) Goodenough, J. B. Evolution of Strategies for Modern Rechargeable Batteries. *Acc. Chem. Res.* **2013**, *46* (5), 1053–1061.

(9) Nitta, N.; Wu, F.; Lee, J. T.; Yushin, G. Li-Ion Battery Materials: Present and Future. *Mater. Today* **2015**, *18* (5), 252–264.

(10) Ong, S. P.; Mo, Y.; Richards, W. D.; Miara, L. J.; Lee, H. S.; Ceder, G. Phase Stability, Electrochemical Stability and Ionic Conductivity of the Li 10±1 MP 2 X 12 (M = Ge, Si, Sn, Al or P, and X = O, S or Se) Family of Superionic Conductors. *Energy Environ. Sci.* **2013**, *6* (1), 148–156.

(11) Islam, M. S.; Fisher, C. A. J. Lithium and Sodium Battery Cathode Materials: Computational Insights into Voltage, Diffusion and Nanostructural Properties. *Chem. Soc. Rev.* **2014**, *43* (1), 185–204.

(12) Marom, R.; Amalraj, S. F.; Leifer, N.; Jacob, D.; Aurbach, D. A Review of Advanced and Practical Lithium Battery Materials. *J. Mater. Chem.* **2011**, *21* (27), 9938.

(13) Mizushima, K.; Jones, P. C.; Wiseman, P. J.; Goodenough, J. B. LixCoO2 (0<x<-1): A New Cathode Material for Batteries of High Energy Density. *Mater. Res. Bull.* **1980**, *15* (6), 783–789.

(14) Ohzuku, T.; Makimura, Y. Layered Lithium Insertion Material of LiCo1/3Ni1/3Mn1/3O2. *Chem. Lett.* **2001**, *30* (7), 642–643.

(15) Mayer, S. T. Mixed Lithium Manganese Oxide and Lithium Nickel Cobalt Oxide Positive Electrodes. 6,007,947, 1999.

(16) Blomgren, G. E. The Development and Future of Lithium Ion Batteries. *J. Electrochem. Soc.* **2017**, *164* (1), A5019–A5025.

(17) Padhi, A. K.; Nanjundaswamy, K. S.; Goodenough, J. B. Phospho-Olivines as Positive-Electrode Materials for Rechargeable Lithium Batteries. *J. Electrochem. Soc.* **1997**, *144* (4), 1188.

(18) Guo, Y.-G.; Hu, J.-S.; Wan, L.-J. Nanostructured Materials for Electrochemical Energy Conversion and Storage Devices. *Adv. Mater.* **2008**, *20* (15), 2287–2878.

(19) Yazami, R.; Touzain, P. A Reversible Graphite-Lithium Negative Electrode for Electrochemical Generators. *J. Power Sources* **1983**, *9* (3), 365–371.

(20) Kaskhedikar, N. A.; Maier, J. Lithium Storage in Carbon Nanostructures. *Adv. Mater.* **2009**, *21* (25–26), 2664–2680.

(21) Li, S.; Jiang, M.; Xie, Y.; Xu, H.; Jia, J.; Li, J. Developing High-Performance Lithium Metal Anode in Liquid Electrolytes: Challenges and Progress. *Adv. Mater.* **2018**, *30* (17), 1–29.

(22) Manthiram, A. Materials Challenges and Opportunities of Lithium Ion Batteries. *J. Phys. Chem. Lett.* **2011**, *2* (3), 176–184.

(23) Goodenough, J. B.; Kim, Y. Challenges for Rechargeable Li Batteries †. *Chem. Mater.* **2010**, *22* (3), 587–603.

(24) Vetter, J.; Novák, P.; Wagner, M. R.; Veit, C.; Möller, K. C.; Besenhard, J. O.; Winter, M.; Wohlfahrt-Mehrens, M.; Vogler, C.; Hammouche, A. Ageing Mechanisms in Lithium-Ion Batteries. *J. Power Sources* **2005**, *147* (1–2), 269–281.

(25) Xu, K. Electrolytes and Interphases in Li-Ion Batteries and Beyond. *Chem. Rev.*

2014, *114* (23), 11503–11618.

(26) Xu, K. Nonaqueous Liquid Electrolytes for Lithium-Based Rechargeable Batteries. *Chem. Rev.* **2004**, *104* (10), 4303–4418.

(27) Tarascon, J.-M.; Guyomard, D. New Electrolyte Compositions Stable over the 0 to 5 V Voltage Range and Compatible with the Li1+xMn2O4/Carbon Li-Ion Cells. *Solid State Ionics* **1994**, *69* (3–4), 293–305.

(28) Suo, L.; Borodin, O.; Sun, W.; Fan, X.; Yang, C.; Wang, F.; Gao, T.; Ma, Z.; Schroeder, M.; von Cresce, A.; et al. Advanced High-Voltage Aqueous Lithium-Ion Battery Enabled by "Water-in-Bisalt" Electrolyte. *Angew. Chemie - Int. Ed.* **2016**, *85287*, 7136–7141.

(29) Ue, M.; Sasaki, Y.; Tanaka, Y.; Morita, M. Nonaqueous Electrolytes with Advances in Solvents. In *Modern Aspects of Electrochemistry*; 2014; Vol. 58, pp 93–165.

(30) Younesi, R.; Veith, G. M.; Johansson, P.; Edström, K.; Vegge, T. Lithium Salts for Advanced Lithium Batteries: Li–Metal, Li–O 2 , and Li–S. *Energy Environ. Sci.* **2015**, *8* (7), 1905–1922.

(31) Ahmed, R.; El Sayed, M.; Arasaratnam, I.; Tjong, J.; Habibi, S. R. Reduced-Order Electrochemical Model Parameters Identification and SOC Estimation for Healthy and Aged Li-Ion Batteries Part I: Parameterization Model Development for Healthy Batteries. *IEEE J. Emerg. Sel. Top. Power Electron.* **2014**, *2* (3), 659–677.

(32) Chaturvedi, N. A.; Klein, R.; Christensen, J.; Ahmed, J.; Kojic, A. Algorithms for Advanced Battery-Management Systems. *IEEE Control Syst.* **2010**, *30* (3), 49–68.

(33) Plett, G. L. Extended Kalman Filtering for Battery Management Systems of LiPB-Based HEV Battery Packs - Part 3. State and Parameter Estimation. *J. Power Sources* **2004**, *134* (2), 277–292.

(34) Barré, A.; Deguilhem, B.; Grolleau, S.; Gérard, M.; Suard, F.; Riu, D. A Review on Lithium-Ion Battery Ageing Mechanisms and Estimations for Automotive Applications. *J. Power Sources* **2013**, *241*, 680–689.

(35) Hannan, M. A.; Lipu, M. S. H.; Hussain, A.; Mohamed, A. A Review of Lithium-

Ion Battery State of Charge Estimation and Management System in Electric Vehicle Applications: Challenges and Recommendations. *Renew. Sustain. Energy Rev.* **2017**, *78* (May), 834–854.

(36) Miranda, D.; Costa, C. M.; Lanceros-Mendez, S. Lithium Ion Rechargeable Batteries: State of the Art and Future Needs of Microscopic Theoretical Models and Simulations. *J. Electroanal. Chem.* **2015**, *739*, 97–110.

(37) Ramadesigan, V.; Northrop, P. W. C.; De, S.; Santhanagopalan, S.; Braatz, R. D.; Subramanian, V. R. Modeling and Simulation of Lithium-Ion Batteries from a Systems Engineering Perspective. *J. Electrochem. Soc.* **2012**, *159* (3), R31–R45.

(38) Plett, G. L. *Battery Management Systems, Volume I: Battery Modeling*; Artech House Publishers, 2015.

(39) Plett, G. L. Extended Kalman Filtering for Battery Management Systems of LiPB-Based HEV Battery Packs - Part 1. Background. *J. Power Sources* **2004**, *134* (2), 252–261.

(40) Lasia, A. *Electrochemical Impedance Spectroscopy and Its Applications*; 2005.

(41) Bar-Shalom, Y.; Li, X.-R.; Kirubarajan, T. *Estimation with Applications to Tracking & Navigation*, Revised Ed.; Danvers, Maryland, 2001.

(42) Seaman, A.; Dao, T. S.; McPhee, J. A Survey of Mathematics-Based Equivalent-Circuit and Electrochemical Battery Models for Hybrid and Electric Vehicle Simulation. *J. Power Sources* **2014**, *256*, 410–423.

(43) Doyle, M.; Fuller, T. F.; Newman, J. Modeling of Galvanostatic Charge and Discharge of the Lithium/Polymer/Insertion Cell. *J. Electrochem. Soc.* **1993**, *140* (6), 1526.

(44) Santhanagopalan, S.; Guo, Q.; Ramadass, P.; White, R. E. Review of Models for Predicting the Cycling Performance of Lithium Ion Batteries. *J. Power Sources* **2006**, *156* (2), 620–628.

(45) Di Domenico, D.; Fiengo, G.; Stefanopoulou, A. Lithium-Ion Battery State of Charge Estimation with a Kalman Filter Based on a Electrochemical Model. *Control Appl. 2008. CCA 2008. IEEE Int. Conf.* **2008**, 702–707.

(46) Li, S. E.; Wang, B.; Peng, H.; Hu, X. An Electrochemistry-Based Impedance Model for Lithium-Ion Batteries. *J. Power Sources* **2014**, *258*, 9–18.

(47) Tanim, T. R.; Rahn, C. D.; Wang, C.-Y. A Temperature Dependent, Single Particle, Lithium Ion Cell Model Including Electrolyte Diffusion. *J. Dyn. Syst. Meas. Control* **2015**, *137* (1), 011005.

(48) Ramadesigan, V.; Chen, K.; Burns, N. A.; Boovaragavan, V.; Braatz, R. D.; Subramanian, V. R. Parameter Estimation and Capacity Fade Analysis of Lithium-Ion Batteries Using Reformulated Models. *J. Electrochem. Soc.* **2011**, *158* (9), A1048.

(49) Forman, J. C.; Bashash, S.; Stein, J. L.; Fathy, H. K. Reduction of an Electrochemistry-Based Li-Ion Battery Model via Quasi-Linearization and Padé Approximation. *J. Electrochem. Soc.* **2011**, *158* (2), A93–A101.

(50) Luo, W.; Lyu, C.; Wang, L.; Zhang, L. A New Extension of Physics-Based Single Particle Model for Higher Charge–Discharge Rates. *J. Power Sources* **2013**, *241*, 295–310.

(51) Luo, W.; Lyu, C.; Wang, L.; Zhang, L. An Approximate Solution for Electrolyte Concentration Distribution in Physics-Based Lithium-Ion Cell Models. *Microelectron. Reliab.* **2013**, *53* (6), 797–804.

(52) Mastali Majdabadi, M.; Farhad, S.; Farkhondeh, M.; Fraser, R. A.; Fowler, M. Simplified Electrochemical Multi-Particle Model for LiFePO4 Cathodes in Lithium-Ion Batteries. *J. Power Sources* **2015**, *275*, 633–643.

(53) Xue, K.-H.; Plett, G. L. A Convective Transport Theory for High Rate Discharge in Lithium Ion Cells. *Electrochim. Acta* **2013**, *87*, 575–590.

(54) Zeisel, H. Energy Transition and Electric Mobility: A Challenge for German Ecosystem between Science and Industry. In *IMLB Japan*; 2018.

(55) Ishikawa, H. Japan's Policy of Promoting Next Generation Vehicle and Battery Technologies. In *IMLB Japan*; 2018.

(56) Lamp, P. Next Generation of Automotive Batteries – Requirements and Challenges. In *IMLB Japan*; 2018.

(57) Toriumi, M. Electrification Strategy of Nissan. In *IMLB Japan*; 2018.

(58) Barai, A.; Uddin, K.; Chevalier, J.; Chouchelamane, G. H.; McGordon, A.; Low, J.; Jennings, P. Transportation Safety of Lithium Iron Phosphate Batteries - A Feasibility Study of Storing at Very Low States of Charge. *Sci. Rep.* **2017**, *7* (1), 5128.

(59) Knauth, P. Inorganic Solid Li Ion Conductors: An Overview. *Solid State Ionics* **2009**, *180* (14–16), 911–916.

(60) Thangadurai, V.; Narayanan, S.; Pinzaru, D. Garnet-Type Solid-State Fast Li Ion Conductors for Li Batteries: Critical Review. *Chem. Soc. Rev.* **2014**, *43* (13), 4714.

(61) Kundu, D.; Tripathi, R.; Popov, G.; Makahnouk, W. R. M.; Nazar, L. F. Synthesis, Structure, and Na-Ion Migration in Na 4 NiP 2 O 7 F 2 : A Prospective High Voltage Positive Electrode Material for the Na-Ion Battery. *Chem. Mater.* **2015**, *27* (3), 885–891.

(62) Murugan, R.; Thangadurai, V.; Weppner, W. Fast Lithium Ion Conduction in Garnet-Type Li7La3Zr2O12. *Angew. Chemie Int. Ed.* **2007**, *46* (41), 7778–7781.

(63) Takada, K. Progress in Solid Electrolytes toward Realizing Solid-State Lithium Batteries. *J. Power Sources* **2018**, *394*, 74–85.

(64) Park, M.; Zhang, X.; Chung, M.; Less, G. B.; Sastry, A. M. A Review of Conduction Phenomena in Li-Ion Batteries. *J. Power Sources* **2010**, *195* (24), 7904–7929.

(65) Xie, H.; Alonso, J. A.; Li, Y.; Fernández-Díaz, M. T.; Goodenough, J. B. Lithium Distribution in Aluminum-Free Cubic Li 7 La 3 Zr 2 O 12. *Chem. Mater.* **2011**, *23* (16), 3587–3589.

(66) Anantharamulu, N.; Koteswara Rao, K.; Rambabu, G.; Vijaya Kumar, B.; Radha, V.; Vithal, M. A Wide-Ranging Review on Nasicon Type Materials. *J. Mater. Sci.* **2011**, *46* (9), 2821–2837.

(67) Manthiram, A.; Yu, X.; Wang, S. Lithium Battery Chemistries Enabled by Solid-State Electrolytes. *Nat. Rev. Mater.* **2017**, *2* (4), 16103.

(68) Rivera, A.; Sanz, J. Lithium Dynamics in the Fast Ionic Conductor

Li0.18La0.61TiO3 Probed by 7Li NMR Spectroscopy. *Phys. Rev. B* **2004**, *70* (9), 094301.

(69) Hou, W.; Guo, X.; Shen, X.; Amine, K.; Yu, H.; Lu, J. Solid Electrolytes and Interfaces in All-Solid-State Sodium Batteries: Progress and Perspective. *Nano Energy* **2018**, *52*, 279–291.

(70) Dawson, J. A.; Canepa, P.; Famprikis, T.; Masquelier, C.; Islam, M. S. Atomic-Scale Influence of Grain Boundaries on Li-Ion Conduction in Solid Electrolytes for All-Solid-State Batteries. *J. Am. Chem. Soc.* **2018**, *140*, 362–368.

(71) Janek, J.; Zeier, W. G. A Solid Future for Battery Development. *Nat. Energy* **2016**, *1* (9), 16141.

(72) Zhang, Z.; Shao, Y.; Lotsch, B.; Hu, Y.-S.; Li, H.; Janek, J.; Nazar, L. F.; Nan, C.-W.; Maier, J.; Armand, M.; et al. New Horizons for Inorganic Solid State Ion Conductors. *Energy Environ. Sci.* **2018**, *11* (8), 1945–1976.

(73) Kamaya, N.; Homma, K.; Yamakawa, Y.; Hirayama, M.; Kanno, R.; Yonemura, M.; Kamiyama, T.; Kato, Y.; Hama, S.; Kawamoto, K.; et al. A Lithium Superionic Conductor. *Nat. Mater.* **2011**, *10* (9), 682–686.

(74) Bron, P.; Johansson, S.; Zick, K.; Schmedt auf der Günne, J.; Dehnen, S.; Roling, B. Li 10 SnP 2 S 12 : An Affordable Lithium Superionic Conductor. *J. Am. Chem. Soc.* **2013**, *135* (42), 15694–15697.

(75) Kuhn, A.; Gerbig, O.; Zhu, C.; Falkenberg, F.; Maier, J.; Lotsch, B. V. A New Ultrafast Superionic Li-Conductor: Ion Dynamics in Li11Si2PS12and Comparison with Other Tetragonal LGPS-Type Electrolytes. *Phys. Chem. Chem. Phys.* **2014**, *16* (28), 14669–14674.

(76) Deiseroth, H.-J.; Kong, S.-T.; Eckert, H.; Vannahme, J.; Reiner, C.; Zaiß, T.; Schlosser, M. Li6PS5X: A Class of Crystalline Li-Rich Solids With an Unusually High Li+ Mobility. *Angew. Chemie Int. Ed.* **2008**, *47* (4), 755–758.

(77) Xu, R. C.; Xia, X. H.; Zhang, S. Z.; Xie, D.; Wang, X. L.; Tu, J. P. Interfacial Challenges and Progress for Inorganic All-Solid-State Lithium Batteries. *Electrochim. Acta* **2018**, *284*, 177–187.

(78) He, X.; Zhu, Y.; Mo, Y. Origin of Fast Ion Diffusion in Super-Ionic Conductors. *Nat. Commun.* **2017**, *8* (May), 15893.

(79) Wang, Y.; Richards, W. D.; Ong, S. P.; Miara, L. J.; Kim, J. C.; Mo, Y.; Ceder, G. Design Principles for Solid-State Lithium Superionic Conductors. *Nat. Mater.* **2015**, *14* (10), 1026–1031.

(80) Rao, R. P.; Adams, S. Studies of Lithium Argyrodite Solid Electrolytes for All-Solid-State Batteries. *Phys. status solidi* **2011**, *208* (8), 1804–1807.

(81) Vargas-Barbosa, N. M.; Roling, B. "Dynamic Ion Correlations in Solid and Liquid Electrolytes: How Do They Affect Charge and Mass Transport? *ChemElectroChem* **2019**, *13* (3), celc.201901627.

(82) Van der Ven, A.; Thomas, J. C.; Xu, Q.; Bhattacharya, J. Linking the Electronic Structure of Solids to Their Thermodynamic and Kinetic Properties. *Math. Comput. Simul.* **2010**, *80* (7), 1393–1410.

(83) Van der Ven, A.; Thomas, J. C.; Xu, Q.; Swoboda, B.; Morgan, D. Nondilute Diffusion from First Principles: Li Diffusion in LixTiS2. *Phys. Rev. B* **2008**, *78* (10), 104306.

(84) Toyoura, K.; Koyama, Y.; Kuwabara, A.; Tanaka, I. Effects of Off-Stoichiometry of LiC 6 on the Lithium Diffusion Mechanism and Diffusivity by First Principles Calculations. *J. Phys. Chem. C* **2010**, *114* (5), 2375–2379.

(85) Giordano, N. J.; Nakanishi, H. *Computational Physics*, 2nd ed.; Pearson Education, Inc.: Upper Saddle River, NJ, 2006.

(86) Kizilyalli, M.; Corish, J.; Metselaar, R. Definitions of Terms for Diffusion in the Solid State. *Pure Appl. Chem.* **1999**, *71* (7), 1307–1325.

(87) Heitjans, P.; Indris, S. Diffusion and Ionic Conduction in Nanocrystalline Ceramics. *J. Phys. Condens. Matter* **2003**, *15* (30), R1257–R1289.

(88) Murch, G. E. The Haven Ratio in Fast Ionic Conductors. *Solid State Ionics* **1982**, *7*, 177–198.

Chapter 2 – Methods for Transport Measurement and Electrolyte Materials Characterization

2.1 Nuclear Magnetic Resonance Phenomena

The majority of the experiments presented in this thesis are underpinned by nuclear magnetic resonance. Broadly speaking, these can be viewed as falling under two distinct umbrellas: nuclear magnetic resonance spectroscopy (NMR), and field-gradient methods – pulsed-field gradient NMR (PFG-NMR) and magnetic resonance imaging (MRI). As will be explained in **Sections 2.2** and **2.3** below, the essential distinction for the latter is that the field gradient provides a means of spatial localization of the nuclei in the sample, but the core principle of magnetic resonance is identical between the two umbrellas. Many excellent introductory texts exist on the fundamentals of magnetic resonance methods; the discussion in this section therefore largely parallels and fuses several of these,[1–3] with the sole aim of simply documenting the necessary lexicon for more specific methodological overviews in **Sections 2.2-2.4**.

Glibly speaking, the entirety of NMR spectroscopy can be summarized as the perturbation of magnetic-field-induced spin-symmetry breaking ('Zeeman splitting') from equilibrium and the subsequent observation of the system's recovery. Yet this exceedingly simple concept unlocks an astounding range of phenomena which has rendered it central to chemistry as an entire discipline, and a significant contributor in physics and materials science as well.[1] Zeeman splitting arises from the coupling of the magnetic moment of the

nucleus, $\vec{\boldsymbol{\mu}}$, to the external magnetic induction field, $\vec{\boldsymbol{B}}_0$, yielding an interaction Hamiltonian:[4]

$$\mathcal{H}_0 = -\vec{\boldsymbol{\mu}} \cdot \vec{\boldsymbol{B}}_0. \tag{2.1}$$

To maximize the splitting, in magnetic resonance experiments the external field is large (on the order of a few Tesla to 20+ Tesla, or at least several thousand times that of the Earth's field) and designed to be as unidirectional as possible – it is therefore frequently termed 'the longitudinal field,' and the energy differences in equation 2.1 are proportional to the component of the nuclear magnetic moment along this direction, typically denoted as the z-direction. After the discovery of electron spin by Uhlenbeck and Goudsmit some years following the original discovery of Zeeman splitting,[5] it was realized that the original of the nuclear magnetic moment was indeed its own nuclear spin, $\vec{\boldsymbol{I}}$, which is an inherently quantum mechanical quantity described by the state vector $|I, m\rangle$. Here I is the nuclear spin quantum number (an intrinsic property of a given atomic isotope), and m spans $\{-I, I\}$ with integer separation, describing the $2I + 1$ possible spin states of the nucleus relative to a symmetry axis – which is conveniently set by the external field direction, z. The nuclear magnetic moment along this direction is then set by the gyromagnetic ratio, γ, another inherent property of a given isotope, as[3]

$$\mu_z = \gamma \hbar I_z, \tag{2.2}$$

with $\hbar$ as the reduced Planck constant. Combining equations (2.1) and (2.2), the result is that the eigenvalues of $\mathcal{H}_0$ are

$$\mathcal{H}_0|I, m\rangle = E_{I,m}|I, m\rangle = -(\gamma \hbar B_0) I_z |I, m\rangle = -(\gamma \hbar B_0) m |I, m\rangle, \tag{2.3}$$

or, upon dividing out $\hbar$,

$$\omega_0 = -\gamma B_0, \tag{2.4}$$

with ω_0 as the characteristic frequency of Zeeman transitions between nuclear spin states.

Equation (2.4) is in some sense the 'fundamental equation' of NMR spectroscopy.[1] The frequency ω_0, named the Larmor frequency, is most readily interpreted as a precessional frequency, with the precession induced by the torque exerted on the nuclear magnetic moment by the external field:

$$\frac{d\vec{\boldsymbol{M}}}{dt} = \gamma\vec{\boldsymbol{M}} \times \vec{\boldsymbol{B}}, \tag{2.5}$$

where $\vec{\boldsymbol{M}}$ is a magnetization vector representing the ensemble of nuclear magnetic moments in a sample, for which the derivative in time on the left-hand side of (2.5) – the precession – is generated by the torque $\vec{\boldsymbol{M}} \times \vec{\boldsymbol{B}}$.[3] The advantage of moving to this semiclassical, ensemble-based description is that it provides a simple means of describing the recovery of the equilibrium polarization of spin states described by (2.1): relaxation. Equation (2.5) can be unpacked into a differential form of the well-known Bloch equations that describe the evolution of the signal back to equilibrium after an initial perturbation:[2]

$$\frac{dM_z}{dt} = -\frac{(M_z - M_0)}{T_1}, \tag{2.6}$$

$$\frac{dM_{x,y}}{dt} = -\frac{M_{x,y}}{T_2}, \tag{2.7}$$

where M_0 is the magnitude of the sample magnetization associated with the equilibrium magnetic field B_0. The time constants T_1 and T_2 describe the relaxation of the magnetization in the longitudinal (z) and transverse (x, y) directions, respectively, which will be further elaborated below, but a general fact is that $T_2 \leq T_1$. The perturbation from equilibrium is

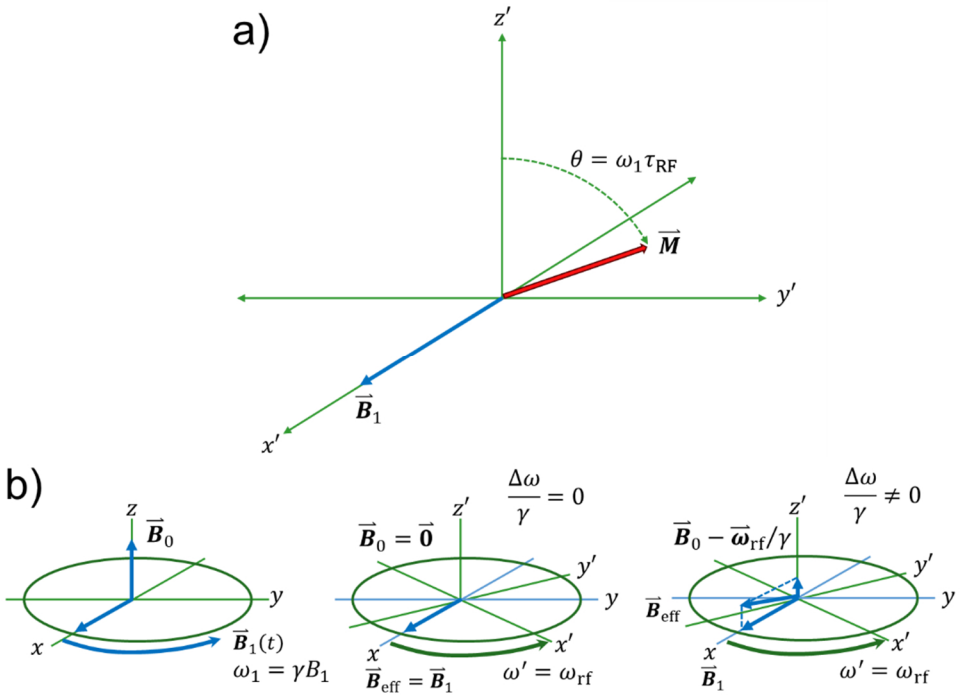

Figure 2.1 – a) The geometry of excitation for an ensemble of on-resonance spins with magnetization $\vec{M}$ in the rotating frame (coordinates x', y', z', rotating at $\omega' = \omega_{rf}$), excited through an angle of $\theta = \omega_1 \tau_{RF}$ by an irradiating RF field $\vec{B}_1$. b) Comparison of the Cartesian frame, rotating frame on-resonance ($\omega_{rf} = \omega_0$), and rotating frame off-resonance ($\omega_{rf} \neq \omega_0$) excitation scenarios.

accomplished by supplying the energy to overcome the Zeeman splitting – equivalent to irradiating the magnetized sample with radio-frequency (RF)-spectrum radiation for the magnetic field strengths and gyromagnetic ratios typically encountered in NMR applications.[1] This $\vec{B}_1$ field is itself oscillating near ω_0 – perturbing the equilibrium magnetization means transferring some of the longitudinal magnitude into transverse magnitude, thereby causing the reaction torque of the magnetization against $\vec{B}_0$ – so it is commonly described in a rotating frame (x', y', z') with $\omega' = \omega_{rf}$ such that $\vec{B}_1$ is stationary, as depicted in **Figure 2.1**. With this alternate description, the RF excitation pulse can be

viewed as a simple rotation of $\overrightarrow{\boldsymbol{M}}$ by an angle $\theta = \omega_1 \tau_{\mathrm{RF}}$ when it is applied *on-resonance.* That is, the frame rate is at the Larmor frequency itself, $\Delta\omega \equiv \omega_0 - \omega_{\mathrm{rf}} = 0$, resulting in the static $\overrightarrow{\boldsymbol{B}}_0$ field effectively cancelling and precession occurring solely about the now-stationary $\overrightarrow{\boldsymbol{B}}_1$ with frequency $\omega_1 = \gamma B_1$, where the exact value of the angle (in radians) is determined by the duration of the pulse, τ_{RF} (**Figure 2.1a**).[2] When $\omega_{\mathrm{rf}} \neq \omega_0$, the excitation is said to be *off-resonance* ($\Delta\omega \neq 0$), and the precession will occur about a net magnetic field $\overrightarrow{\boldsymbol{B}}_{\mathrm{eff}}$ formed by the stationary $\overrightarrow{\boldsymbol{B}}_1$ and the residual longitudinal component $\overrightarrow{\boldsymbol{B}}_0 - \overrightarrow{\boldsymbol{\omega}}_{\mathrm{rf}}/\gamma$, as in the third scenario illustrated in **Figure 2.1b**.[3]

Following the application of the pulse – the rotation of $\overrightarrow{\boldsymbol{M}}$ by θ – the RF coil which produces $\overrightarrow{\boldsymbol{B}}_1$ to perform the excitation functions as a receiver antenna for the decay of the transverse magnetization; the sample emits RF radiation as it relaxes back to equilibrium. The resulting electromagnetic signal is recorded in the time domain as a so-called free induction decay (FID), and for an ensemble of isolated, non-interacting spins, the signal equation takes the form:[2]

$$S(t) = S_0 \exp(i\Delta\omega) \exp(-t/T_2), \tag{2.8}$$

with $S_0 \propto M_0$ and $\Delta\omega$ as the *offset* of the frequency of the excited spins from the "on-resonance" condition, $\omega = \omega_0$, which is the precessional frequency of the rotating reference frame (with the rotating frame corresponding to the carrier wave frequency at which the signal received by the RF coil is recorded; these frequency differences are small, and are therefore typically reported in ppm). As mentioned above, since $T_2 \leq T_1$, and since T_2 reflects the transverse relaxation which produces the signal, T_2 will set the decay envelope of the signal (the reasons for which will, again, be elaborated later in this section).

A loosely similar FID to that represented by equation (2.8) is provided in **Figure 2.2a**, from the single-pulse excitation of ^{7}Li nuclei in a 1 M LiCl (aq) sample (using a 20 T, Bruker 850HD spectrometer at 25℃). However, signals in NMR spectroscopy are almost universally analyzed not in the time domain in which they are acquired, but rather in the frequency domain, $S(\omega)$, by Fourier-transformation (FT):[1]

$$S(\omega) \equiv \mathcal{F}[S(t)] = \frac{S_0}{2\pi} \int_{-\infty}^{\infty} dt \exp(-i\omega t) \exp(i\Delta\omega) \exp(-t/T_2)$$

$$= \frac{T_2}{1 + (\omega - \Delta\omega)^2 T_2^2}, \tag{2.9}$$

where $\mathcal{F}$ represents the Fourier transformation operation, which corresponds to decomposing a function of a certain variable into an infinite sum of component harmonics in its conjugate variable (with the conjugate variable having reciprocal dimensions to the original variable – the reason for the use of a very general definition, not restricted to time-frequency transformation, will become apparent in **Section 2.2**). The resulting frequency function in the second line of (2.9) – a *lineshape* known as a Lorentzian – is sharply peaked at the signal offset, $\Delta\omega$ (the signal offset is not to be confused with the *transmitter offset*, which is the difference between the frequency at which the carrier wave for signal reception is synthesized and the natural Larmor frequency of the nucleus in question at the given field strength). This FT-NMR spectroscopy approach provides a highly sensitive and highly diagnostic probe of local nuclear environments (and is so prevalent in modern NMR spectroscopy that the 'FT' is typically omitted),[1–3] and yet the simple one-pulse experiment described above does not even come close to exhausting the possibilities of magnetic resonance methods, some of which will be the subjects of **Sections 2.2-2.4**. Many ancillary

details of this experiment – *e.g.* phasing, referencing, digitization/sampling, apodization, acquisition hardware – are not described here, for the sake of brevity, but the interested reader can find detailed summaries in any introductory NMR text.[1–3] The frequency-

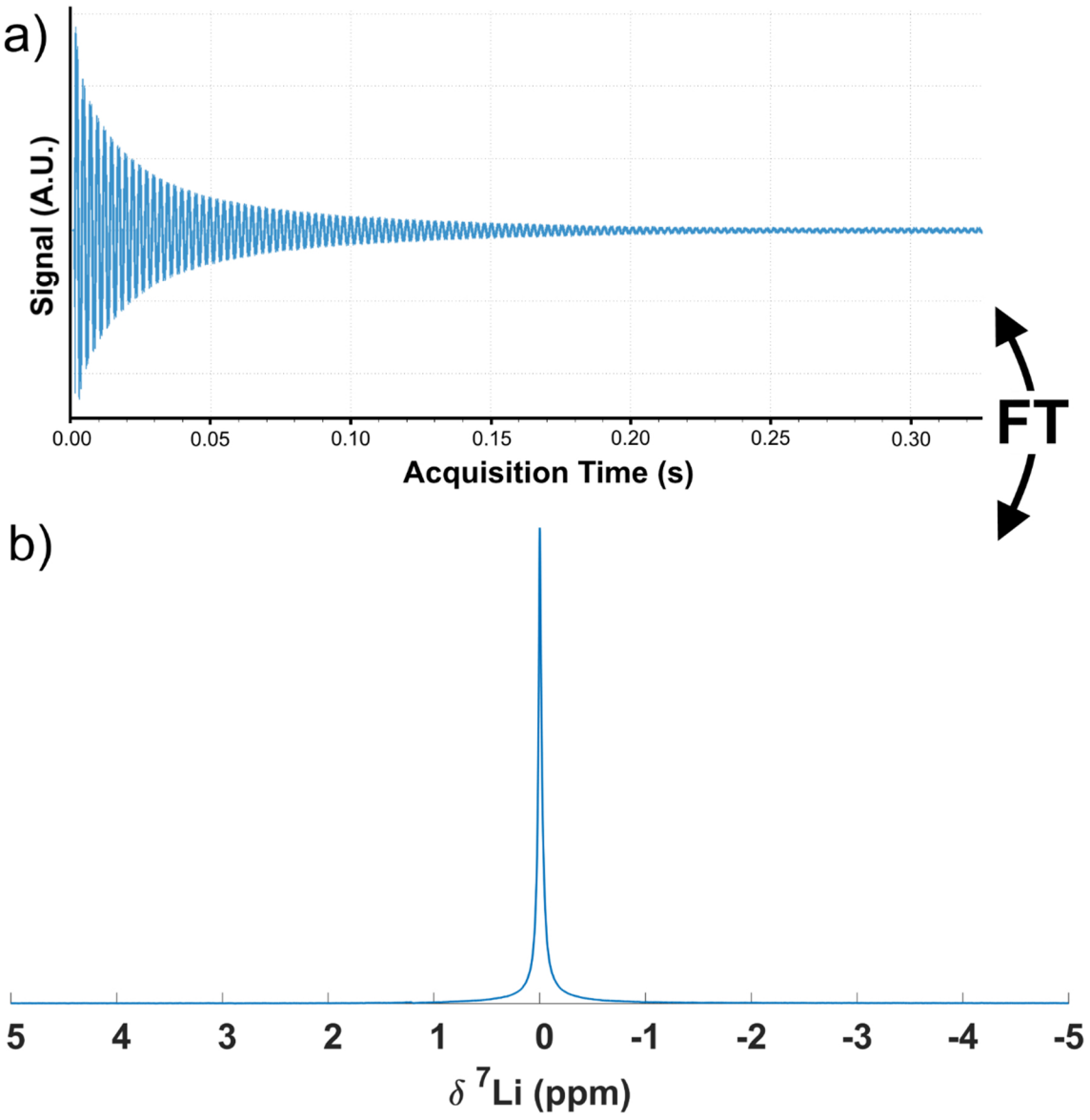

Figure 2.2 – a) Time-domain FID of the ^{7}Li signal from 1 M LiCl (aq) acquired at 20 T on a Bruker 850HD spectrometer, roughly corresponding to the signal equation of (2.9). b) The frequency-domain spectrum of a), obtained by Fourier transformation of the FID.

domain spectrum, $S(\omega)$, of the time-domain FID, $S(t)$, from **Figure 2.2a** is provided in **Figure 2.2b**.

Relaxation of the perturbed ensemble of nuclear magnetic moments is described phenomenologically in equations (2.6) and (2.7), but a proper treatment requires incorporation of the distribution of interactions which mediate the thermalization of the spin populations, and the distribution of the fluctuations in these interactions as well.[2] The simplest approach for this incorporation is the prescription developed in the Bloembergen-Purcell-Pound (BPP) theory of relaxation,[6] wherein the relaxation is driven primarily by the dipolar coupling, with Hamiltonian:

$$\mathcal{H}_D = \frac{\mu_0}{4\pi}\sum_{i<j}\gamma_i\gamma_j\hbar\frac{1}{r_{ij}^3}\left[\vec{\boldsymbol{I}}_i\cdot\vec{\boldsymbol{I}}_j - \frac{3\left(\vec{\boldsymbol{I}}_i\cdot\vec{\boldsymbol{r}}_{ij}\right)\left(\vec{\boldsymbol{I}}_j\cdot\vec{\boldsymbol{r}}_{ij}\right)}{r_{ij}^2}\right], \tag{2.10}$$

where μ_0 is the permeability of free space, and $\vec{\boldsymbol{r}}_{ij}$ is the displacement of spin j relative to spin i (the sum is over all pairwise combinations, counted only once). For rapidly tumbling spins, $\langle\mathcal{H}_D\rangle = 0$ on the time-scale of the NMR experiment, so it is the fluctuations of $\mathcal{H}_D$ between the spins which generate the relaxation. In the case of spin-lattice dipolar coupling, where "the lattice" is the surrounding bath of nuclei whose magnetizations are unperturbed by the pulse – their precessional frequencies in most cases being orders of magnitude larger in separation from ω_0 than the bandwidth of the excitation pulse in the frequency domain – this thermalizes the longitudinal magnetization, which as per equation (2.6), occurs on the time-scale quantified by T_1. A foundational result in NMR theory due to Hebel and Schlichter[7] proposes that the transition rates W_{nm} between any given pair of spin states, $|n\rangle$

and $|m\rangle$ with energies E_n and E_m, can give the ensemble rate of spin-lattice relaxation, $1/T_1$, as an energy-weighted average:

$$\frac{1}{T_1} = \frac{1}{2}\frac{\sum_{n,m} W_{nm}(E_n - E_m)^2}{\sum_n E_n^2}. \tag{2.11}$$

The transition rates W_{nm} can be computed via standard quantum-mechanical time-dependent perturbation theory methods:[4]

$$W_{nm} = \frac{1}{\hbar^2}\int_0^t dt' \exp\left[\frac{i(E_n - E_m)(t-t')}{\hbar}\right]\overline{\langle n|\hbar\mathcal{H}_D(t')|m\rangle\langle m|\hbar\mathcal{H}_D(t)|n\rangle} + \text{C. C.} \tag{2.12}$$

Here, C. C. is the complex conjugate of the preceding expression, and time-dependent perturbation theory describes the evolution of the states in the limit where the differences between the E_n and E_m is much less than the Zeeman splitting of equation (2.1), which is virtually always fulfilled. On the NMR time-scale, $t \gg \hbar/(E_n - E_m)$, so the evaluation of (2.12) centres on the evaluation of the time-averaged products of the matrix elements, $\overline{\langle n|\hbar\mathcal{H}_D(t')|m\rangle\langle m|\hbar\mathcal{H}_D(t)|n\rangle}$. Any expression of this form is denoted as a *correlation function*, and can often be replaced with a suitable ansatz, such as exponential decay with a characteristic time τ_C in the case of rapid tumbling.[8] It is also possible (though cumbersome) to factor this correlation function into spatial and spin parts for the matrix elements $\langle m|\hbar\mathcal{H}_D(t)|n\rangle$, and introduce so-called *spectral density functions* which are the Fourier-transformed analogues of the correlation function.[2]

In either case, the correlation time τ_C partitions the fluctuation time-scales for spin-lattice relaxation into "slow" and "fast" regimes, with a T_1 minimum occurring when $\omega_0\tau_C = 1$ serving as the approximate dividing line. Heuristically, when fluctuations are

"fast", the transition probabilities for a dipolar-coupling-induced spin flip are low because the time window for interactions to occur is short (τ_C is small), so the relaxation is slow; when fluctuations are "slow", the thermal oscillations between geometric configurations of the spins where interactions are maximized are gradual, and the relaxation is consequently again slow (τ_C is long, so it takes longer for unfavourable configurations for transitions to change). The regulation of the fluctuations in a thermodynamic system is, of course, accomplished by temperature; therefore, an Arrhenius plot of $1/T_1$ against reciprocal temperature will exhibit a maximum (*i.e.* the T_1 minimum), which may or may not be accessible by the experimental apparatus, for which there is an associated τ_C for spin-lattice

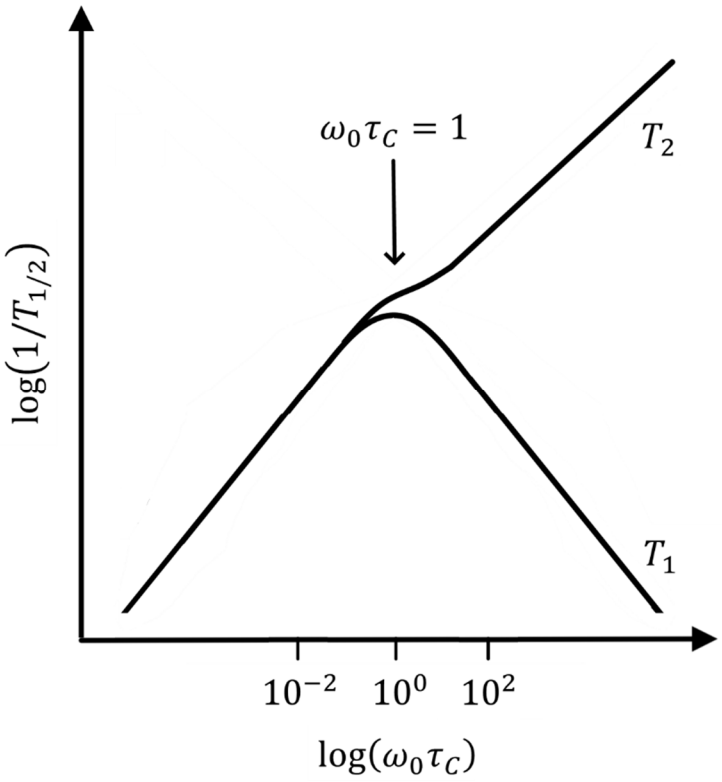

Figure 2.3 – Schematic description of the longitudinal (T_1) and transverse (T_2) relaxation as a function of correlation time, τ_C, at fixed Larmor frequency ω_0. τ_C is, roughly speaking, inversely related to temperature, so this figure is approximately an Arrhenius plot of the relaxation rates. Adapted with modification from Callaghan, 1991.[2]

relaxation (longitudinal magnetization decay). The logic for the construction of a fluctuation-induced decay of the transverse magnetization also ultimately leads to the introduction of a correlation function, although the energy scale for transverse relaxation is no longer set by the large Zeeman splitting as was the case for longitudinal relaxation – the states of the perturbed spins are rendered degenerate by the excitation – so the development requires solving the time-evolution of the density operator for $\mathcal{H}_D$, which is a much more involved process and necessitates somewhat more opaque approximations.[9] Owing to this degeneracy, T_2 is termed the "spin-spin" relaxation, and more accurately describes a loss of signal coherence than a true "returning of the system to equilibrium." Here again, with short correlation times, the relaxation is long, and for the same logic as with T_1 (indeed, at sufficiently high temperature, the equality condition for $T_2 \leq T_1$ is approached). However, the key difference is that long correlation times between pairs of spins *which are both perturbed to energetic degeneracy* means that mutual spin flips are "easy," and so the signal thermalizes rapidly and T_2 is short. The behaviour of both forms of relaxation is summarized schematically as a function of correlation time at fixed Larmor frequency in **Figure 2.3**, which is adapted with modification from Callaghan, 1991.[2] A key point to emphasize is that, regardless of the interaction mechanism which is leading-order for T_1 and T_2, whether or not it is dipolar coupling, the same phenomenological features as appear in **Figure 2.3** will manifest in an Arrhenius plot of the relaxation rates.

The actual measurement of T_1 and T_2 is best understood via the solutions to the differential Bloch equations, (2.6) and (2.7):

$$M_z(t) = M_0 - \big(M_0 - M_z(0)\big)\exp(-t/T_1), \tag{2.13}$$

$$M_{x,y}(t) = M_0 \exp(-t/T_2). \tag{2.14}$$

For T_1, taking $M_z(0) = -M_0$, or in other words, performing an excitation of $\theta = \pi$ radians, completely inverts the sample magnetization. Immediately observing this inverted magnetization with a $\pi/2$ pulse, which corresponds to maximum transverse-plane excitation, would essentially flip the spectrum in **Figure 2.2b** "upside-down" relative to the baseline. If, instead, an interval τ is waited prior to the application of the second $\pi/2$ pulse, some degree of longitudinal relaxation for the inverted magnetization will have occurred in the interim, and the observable signal is now only generated from some fraction of the total sample magnetization. In particular, there will be a value of τ at which the inverted magnetization is "halfway" recovered along the longitudinal direction when the $\pi/2$ pulse is transmitted, in which case there will be nothing to excite, since there is no net component of the magnetization along the longitudinal axis at this time. Some algebra in equation (2.13) readily shows that this "null point" in the inversion recovery occurs at $T_1/\ln(2)$, from which an estimate of T_1 can be arrived at simply by varying τ to find the null point. A more systematic approach is to perform a series of inversion recovery experiments with variable τ and then fit the series of partially-recovered magnetizations to equation (2.13). This process for T_1 measurement is depicted in **Figure 2.4**, for a sample of $Li_{5.80}Ca_{0.10}PS_5Cl$ argyrodite solid-state ion conductor at 40°C, measured on a 20 T Bruker 850HD spectrometer at 40°C, without sample spinning (which is to be discussed in **Section 2.4**).

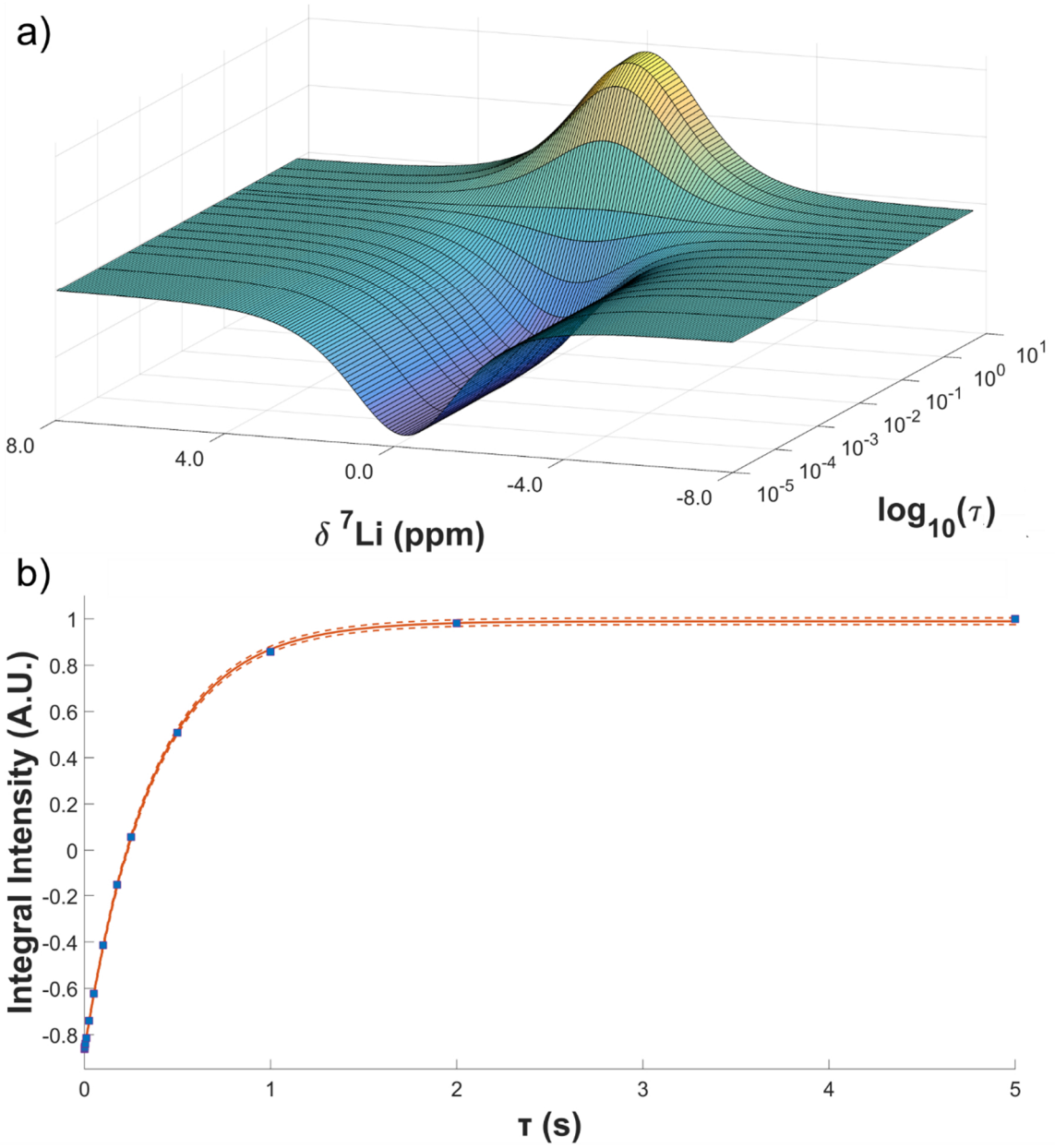

Figure 2.4 – T_1 measurement via the inversion recovery method for ^{7}Li in $Li_{5.80}Ca_{0.10}PS_5Cl$ at 40°C and static conditions, using a 20 T Bruker 850HD spectrometer. a) Variable-τ, pseudo-two-dimensional inversion recovery spectrum. b) Fit of the integrated intensity at each τ (which is proportional to the total sample magnetization for τ) using equation (2.13) to determine that $T_1 = (367 \pm 5)$ ms.

The measurement of T_2 is slightly more complicated; spin-spin interactions are not the only experimentally relevant factor which can contribute to the decay of signal coherence: local field inhomogeneity will alter nuclear precession rates, resulting in a dephasing of the signal that appears as though it was caused by transverse-plane relaxation.[1] Therefore, adding the different transverse-plane decay rates together gives:

$$\frac{1}{T_2^*} = \frac{1}{T_2} + \frac{1}{T_2^{\mathrm{ih}}}, \tag{2.15}$$

where T_2^* is the effective time constant including all transverse-plane signal decay effects (and would, in reality, be the time constant in equation (2.9) broadening the idealized Lorentzian lineshape for frequency-domain NMR signal), and T_2^{ih} represents the added contribution from the inhomogeneity, over top of the leading-order spin-spin interaction causing the inherent sample T_2. Fortunately, it is possible to "re-synchronize" the signal dephasing from the T_2^{ih} time scale, since it is not inherent to the sample, using the Carr-Purcell-Meiboom-Gill (CPMG) pulse sequence.[10,11] This pulse sequence has at its core a *spin echo*, wherein, after a set delay τ_{echo}, the transverse signal is refocused using a π pulse that, rather than inverting the magnetization *across* the transverse plane, as with the inversion recovery experiment for the measurement of T_1, inverts it *within* the transverse plane, by simply changing the axis of rotation for the angle θ. The net effect is that the order of precession between the fastest- and slowest-precessing spins is reversed, so that, by symmetry about the time at which the π pulse occurs, everything will (ideally) once again be in phase. However, the inherent T_2 process is a thermalization – an irreversible diffusion of the signal coherence produced by the sample itself – so T_2 decay itself is not

refocused by the spin echo; only broadening from the inhomogeneity. By performing a series of experiments, each with progressively greater numbers of spin echoes chained in

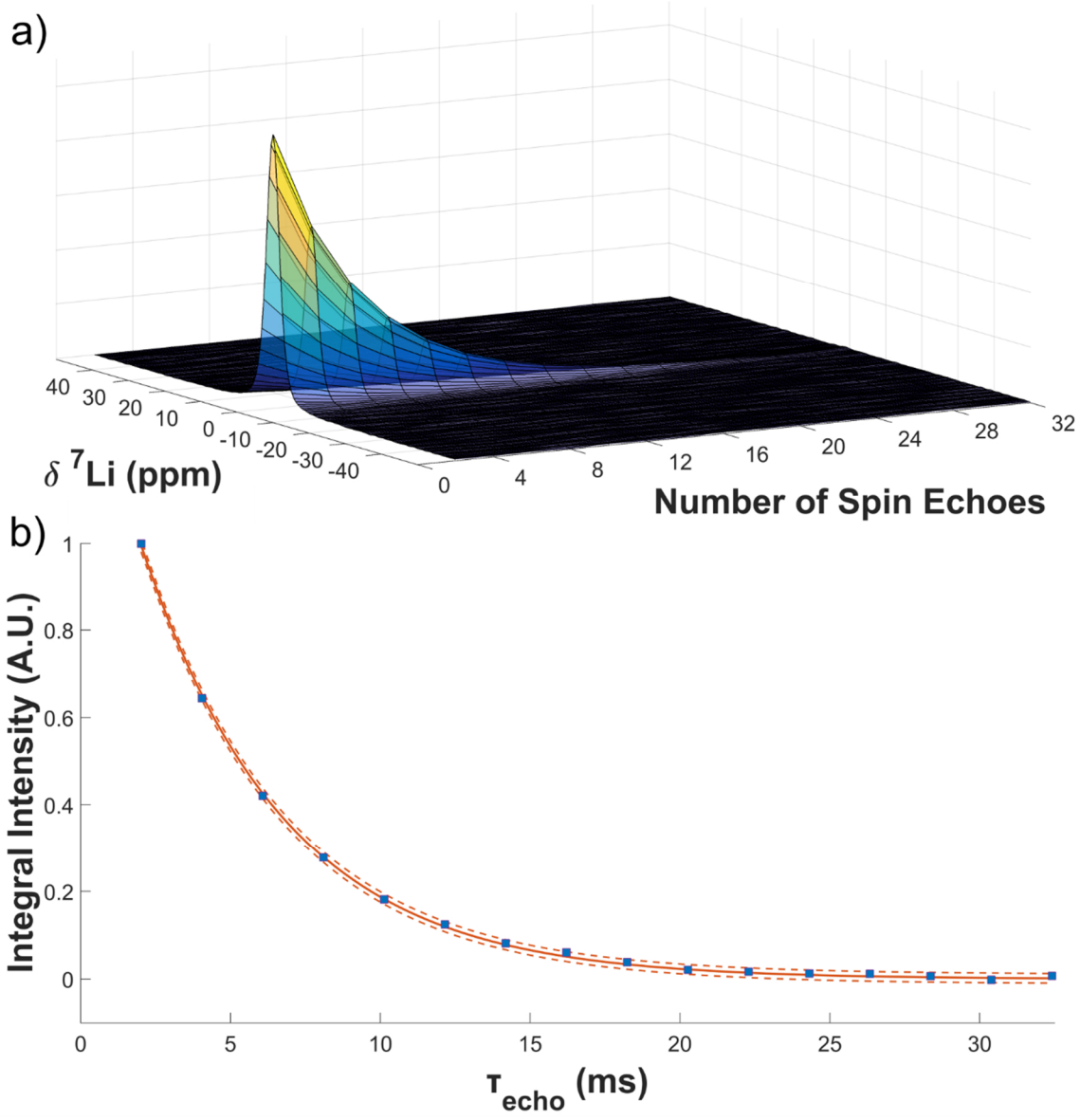

Figure 2.5 – T_2 measurement via the CPMG method for ^{7}Li in $Li_{3.30}Al_{0.15}P_{0.85}S_4$ at 30°C and static conditions, using a 7 T Bruker Avance III 300WB spectrometer. a) Variable-echo-number, pseudo-two-dimensional CPMG spectrum. b) Fit of the integrated intensity versus accumulated τ_{echo} (which is proportional to the total sample magnetization for the accumulated τ_{echo}) using equation (2.14) to determine that $T_2 = (4.78 \pm 0.08)$ ms.

sequence, one after another, the T_2 decay can be traced out in the gradually reduced integrated spectral intensity as a function of echo number, and then fit to equation (2.14) to determine the time constant itself. The echo duration, τ_{echo}, is twice the spacing interval between the initial $\pi/2$ excitation pulse and the refocusing π pulse (again, by symmetry), plus the width of the π pulse itself, so the number of echoes can be readily converted to a time axis in order to perform the fit. The result of this process for a $Li_{3.30}Al_{0.15}P_{0.85}S_4$ glass sample measured at 7 T on a Bruker Avance III 300WB spectrometer at 30°C, without sample spinning, is presented in **Figure 2.5**.

2.2 Theory and Methods of Magnetic Resonance Imaging

The concepts in **Section 2.1** were concerned with conventional NMR spectroscopy, which can provide a wealth of structural and dynamical information about the various nuclear environments in the sample, but cannot spatially localize them; to accomplish this end, a means is required for correlating spin density, $\rho(\vec{r}, t)$, with position in the active volume of the sample (that is, the portion of the sample volume which can be successfully probed with the apparatus). Equation (2.4) hints at how this might be realized: if the longitudinal field were to vary in space, then the precessional rate would also become a function of position, and the resulting spectrum would encode spatial information – a sort of "spin labelling." This idea of encoding spatial information in the phase of the nuclear precession is demonstrated pictorially in **Figure 2.6**, and forms the essence of the fundamental theorem of NMR localization. Much of the content in this section is again sourced from the excellent text of Callaghan, 1991, with a review article on chemical-shift

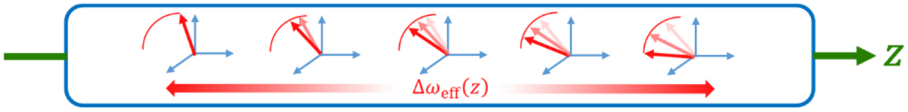

Figure 2.6 – Pictorial illustration of a spatially-varying precessional frequency, $\omega(\vec{\boldsymbol{r}}, t)$, induced by deliberately inducing a spatial variation in the longitudinal magnetic field.

imaging by one of its inventors, T. Brown (2007),[12] serving as an additional helpful resource.

The origin of the fundamental theorem comes from considering the magnitude of the net magnetization, dM, of a small element of volume in the sample, dV, located at position $\vec{\boldsymbol{r}}$ at time t, which can be written in terms of the spin density at $(\vec{\boldsymbol{r}}, t)$:

$$dM(\vec{\boldsymbol{r}}, t) = \rho(\vec{\boldsymbol{r}}, t)dV. \tag{2.16}$$

Just as with NMR spectroscopy, the signal corresponding to this small element of volume will be proportional to its net magnetization, provided it is properly accounted for that, when no longer considering a bulk response, the RF coil may have spatially-varying sensitivity, $D(\vec{\boldsymbol{r}})$:[12]

$$S(t) = \iiint_V d\vec{\boldsymbol{r}}\, \rho(\vec{\boldsymbol{r}}, t) D(\vec{\boldsymbol{r}}) \exp\big(i\phi(\vec{\boldsymbol{r}}, t)\big) = \iiint_V d\vec{\boldsymbol{r}}\, \rho_D(\vec{\boldsymbol{r}}, t) \exp\big(i\phi(\vec{\boldsymbol{r}}, t)\big), \tag{2.17}$$

where $\rho_D(\vec{\boldsymbol{r}}, t)$ simply notates the fact that the detectable spin density as a function of position can be affected by the RF coil sensitivity. The phase factor $\phi(\vec{\boldsymbol{r}}, t)$ records how much a particular volume element contributes to the overall signal, weighted by the spin density there, and is the means by which the spatially-varying precessional frequencies enter the signal equation. Formally, the time-evolution of the phase factor can be written:[13]

$$\frac{d\phi}{dt} \equiv \omega_{\mathrm{eff}}(\vec{\boldsymbol{r}}, t) = \gamma B_{\mathrm{eff}}(\vec{\boldsymbol{r}}, t), \tag{2.18}$$

that is to say, one can still use equation (2.4) for the Larmor frequency for an individual volume element (and under the same rotating-frame picture for the spin evolution as with NMR spectroscopy, described in **Section 2.1**), provided that the precise variation of the magnetic field there is known:

$$\phi(\vec{\boldsymbol{r}}, t) = \gamma \int_0^t dt' \, B_{\text{eff}}(\vec{\boldsymbol{r}}, t'). \tag{2.19}$$

To operationalize the formal solution for the phase factor in equation (2.19), a specific spatial modulation of the longitudinal field is needed; the simplest solution is to merely make it linearly varying across the dimension of the active volume to be imaged:

$$B_{\text{eff}}(\vec{\boldsymbol{r}}, t') = B_0 - (\omega_0 - \omega_{\text{rf}})/\gamma + \vec{\boldsymbol{G}}(t') \cdot \vec{\boldsymbol{r}}, \tag{2.20}$$

where $\vec{\boldsymbol{G}}$ has constant magnitude and direction for the duration of the spin labelling, and is otherwise zero at all other times, which picks out a linear variation in the field strength along the direction of $\vec{\boldsymbol{G}}$ for the entire local field. (It is important to note that $\vec{\boldsymbol{B}}$ itself is always oriented along the usual longitudinal direction; the linear variation in magnitude in other imaging directions is still just a variation in the z-component of the longitudinal field there, with the imaging direction dictated by the sense in which this z-component variation occurs across the sample.) With a specific form of spatial modulation for the longitudinal field to insert into equation (2.19), on returning to the signal equation (2.17), the result is that:

$$S(t) = e^{i\gamma\Delta\omega_{\text{eff}}} \iiint_V d\vec{\boldsymbol{r}} \, \rho_D(\vec{\boldsymbol{r}}, t) e^{i\gamma \int_0^t dt' B_{\text{eff}}(\vec{\boldsymbol{r}}, t')} \tag{2.21}$$

$$= e^{i\gamma\Delta\omega_{\text{eff}}} \iiint_V d\vec{\boldsymbol{r}}\, \rho_D(\vec{\boldsymbol{r}}, t) e^{i\vec{\boldsymbol{k}}(t)\cdot\vec{\boldsymbol{r}}}$$

where the usual, spatially-independent offset is factored out of the volume integral, and the definition has been made that:

$$\vec{\boldsymbol{k}}(t) = \gamma \int_0^t dt'\, \vec{\boldsymbol{G}}(t') \tag{2.22}$$

since $\vec{\boldsymbol{r}}$ itself in equation (2.20) is not part of the time-variable integration. The reason for making the definition (2.22) is that the form of equation (2.21) reveals something quite remarkable about $\rho_D(\vec{\boldsymbol{r}}, t)$: it is the Fourier transform of $S(t)$, with $\vec{\boldsymbol{k}}$ as the conjugate variable to $\vec{\boldsymbol{r}}$! Absorbing the pre-factor for the offset, this is the succinct mathematical statement of the fundamental theorem of NMR localization:

$$S(t) \equiv \rho_D(\vec{\boldsymbol{k}}, t); \tag{2.23}$$

a spatially-modulated signal in the time domain is identical to the spin density map in a reciprocal space, conjugate to $\vec{\boldsymbol{r}}$. Since the Fourier transform is invertible, this means that measuring the time-domain signal and Fourier-transforming is equivalent to measuring the real-space map of the spin density – the localization of the NMR signal. A schematic illustration of the foregoing discussion is provided in **Figure 2.7**.

The major outcome of the analysis of the fundamental theorem of NMR localization and the pictorial demonstration in **Figure 2.7** is that sampling a spatially-modulated FID is tantamount to sampling along a trajectory in $\vec{\boldsymbol{k}}$-space. These $\vec{\boldsymbol{k}}$-space trajectories can be created in several ways: i) by generating or propagating an excitation and then sampling in the time-domain while a field gradient is active, known as frequency-encoding, or ii) by again forming an excitation, applying a gradient with magnitude $G(t)$ for duration T_0, and then acquiring the signal after the conclusion of the gradient pulse, corresponding to a single point in $\vec{\boldsymbol{k}}$-space (for a rectangular gradient, this is simply $\gamma G T_0$), known as phase-encoding.[12] In praxis, a combination of the two approaches may be used, and they can, of course, be coupled to a variety of contrast/filtering mechanisms (for example, based on the relaxation properties of the spins being sampled) and other signal enhancement

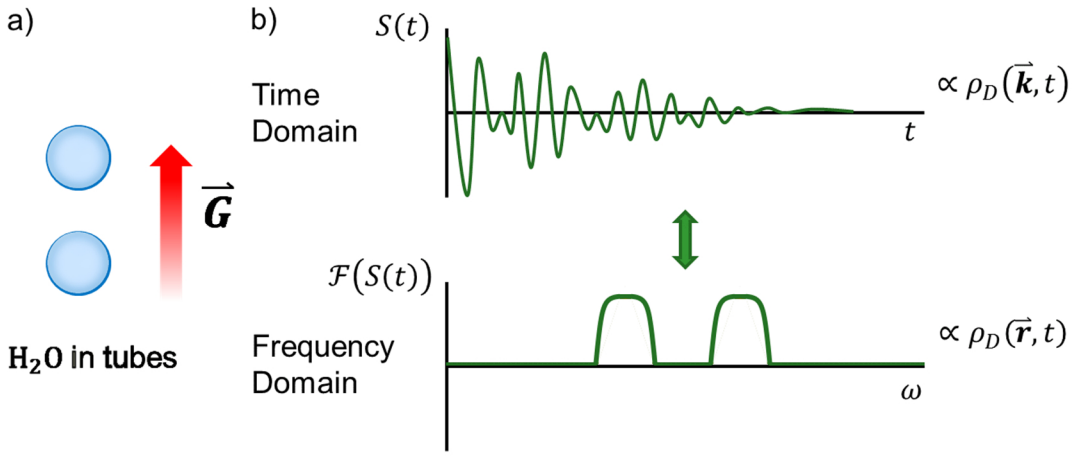

Figure 2.7 – A schematic of Fourier-imaging, wherein a test sample with some specific spatial arrangement (in the literature, commonly vials containing H_2O, with ^1H being the most receptive NMR nucleus) is probed in the presence of a longitudinal field gradient, illustrating the correspondence of time-domain signal and $\vec{\boldsymbol{k}}$-space spin density to frequency-domain signal and real-space spin density. Adapted with modification from Callaghan, 1991.[2]

approaches.[2] A simple two-dimensional frequency-encoding experiment is illustrated in **Figure 2.8**, in terms of both its pulse sequence, and the $\vec{\boldsymbol{k}}$-space sampling method (known as a *raster*). In order to reconstruct an image with the desired *resolution*, the extent of the sampling in $\vec{\boldsymbol{k}}$-space must be regulated – for example, by adjusting the phase-encoding duration or the gradient strength – with resolution being roughly a function of the largest-magnitude $\vec{\boldsymbol{k}}$-space points under a uniform raster. Then to achieve the desired *field-of-view* (FOV), it is necessary to ensure that sufficient numbers of $\vec{\boldsymbol{k}}$-points are acquired, since FOV is simply the product of the number of sample points at the set resolution (it is also possible to have independent resolutions and FOVs in each imaging direction).

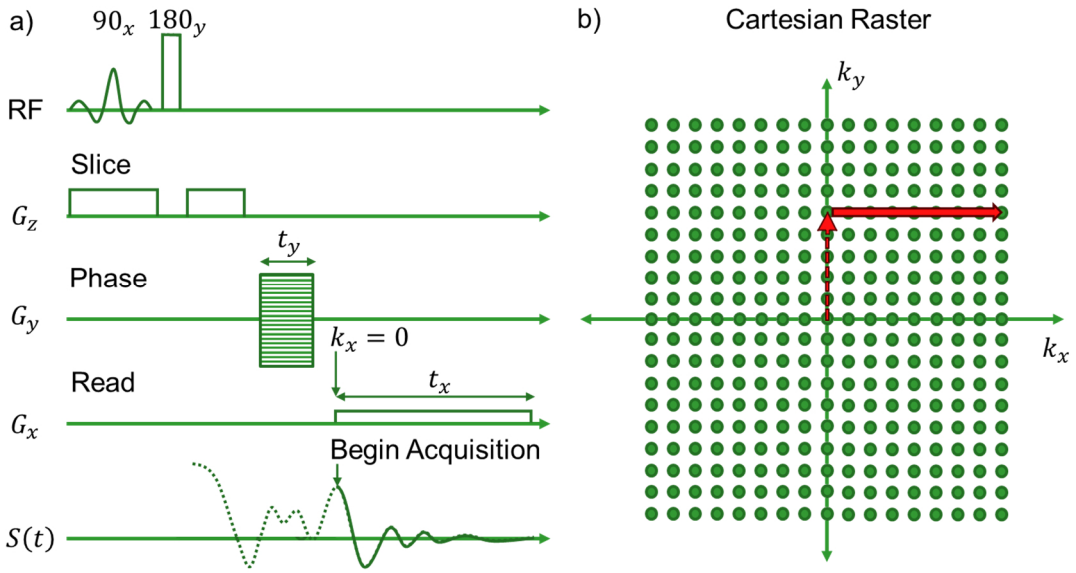

Figure 2.8 – a) Two-dimensional frequency-encoding MRI pulse sequence, with slice-selection in the z-direction, which samples the (x, y)-plane. b) A Cartesian raster for the acquisition of $\vec{\boldsymbol{k}}$-space trajectories, wherein a series of phase-encode periods are conducted to sample the y-direction, and then the x-direction of the y-modulated signal is sampled with a frequency-encoding readout gradient. Adapted with modification from Price, 2009,[21] and Callaghan, 1991.[2]

One additional feature in the pulse sequence of **Figure 2.8** is the use of *selective excitation*, wherein the initial excitation itself has a spatial component, in this case corresponding to *slice-selection*, or the excitation of only those spins situated within some layer of the sample. It is also possible to perform *chemical-selective* excitation, which makes use of a shaped RF pulse to alter the bandwidth of the frequency domain that is actually sampled in the experiment. For example, limiting the excitation in the frequency domain to a narrow band is equivalent to multiplying the spectrum by a "hat function." The Fourier transform of a hat function is a sinc-function ($\mathrm{sinc}(x) = \sin(x)/x$), so a sinc-shape must be convolved into the regular *broadband* rectangular RF pulse to achieve this selectivity.[1] As a general rule based on the conjugate-variable relationship between the time and frequency domains, a narrow bandwidth in the frequency domain will require a lengthy pulse duration in the time domain. Shaped-pulse excitation is also an element of many slice-selective schemes, where the application of the shaped pulse during a gradient encoding period essentially targets only a narrow section of the frequency spread produced by the gradient.[2] To understand the form of the slice-selective pulse in **Figure 2.8**, it is necessary to move to a modified rotating frame (focusing on a particular z value) where the frame rate is dictated by $\gamma G_z z$ (and the spins at z are consequently on-resonance). This produces the modified rotating-frame Bloch equations:[2]

$$\begin{aligned}
\frac{dM_{x'}}{dt} &= -\gamma M_{z'} B_{y'} = -\gamma M_{z'} B_1(t) \sin[\gamma G_z z(t+T)] \\
\frac{dM_{y'}}{dt} &= \gamma M_{z'} B_{x'} = \gamma M_{z'} B_1(t) \cos[\gamma G_z z(t+T)] \\
\frac{dM_{z'}}{dt} &= \gamma\left(M_{x'} B_{y'} - M_{y'} B_{x'}\right)
\end{aligned} \tag{2.24}$$

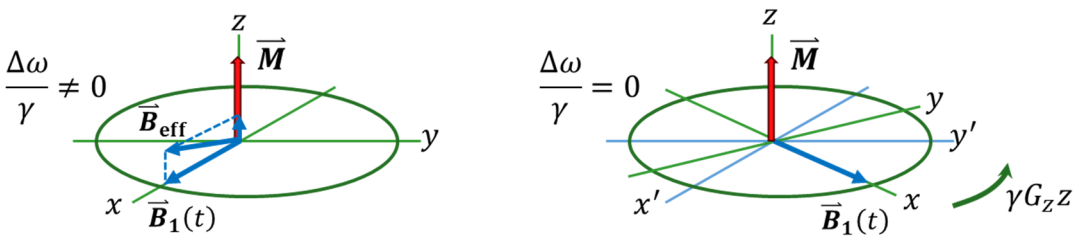

Figure 2.9 – Comparison of a) the regular rotating frame for off-resonance spins, and b) the gradient-based rotating frame, for the analysis of slice-selective MRI. Adapted with modification from Callaghan, 1991.[2]

where the selective RF pulse is centred at $t = 0$, and superimposed on a gradient that is turned on over $[-T, T]$, with $2T$ greater than the duration of the selective RF pulse. The two rotating frames are contrasted in **Figure 2.9**. Combining the $M_{x'}$ and $M_{y'}$ Bloch equations in the customary way to form $M_{+'}$,[1] and making the assumption $dM_{z'}/dt \approx 0$, which corresponds to assuming a linear response to the excitation pulse within the slice,[2] the result is that the differential equation for the time-evolution of the transverse-plane magnetization during the slice-selection is:

$$\frac{dM_{+'}}{dt} = i\gamma M_0 B_1(t) e^{i\gamma G_z z(t+T)}. \tag{2.25}$$

This produces a phase factor, $\exp(i\gamma G_z z T)$, on integration which varies across the slice, and therefore needs to be cancelled. This can be accomplished either with a compensating, oppositely-signed gradient following the slice-selective pulse (as is done in **Figure 2.10** below), or by inserting a non-selective π pulse with a gradient pulse in the same sense as the slice gradient, as occurs in **Figure 2.8**.

MRI is used in two chapters of this thesis for the *in situ* experimental determination of the ion concentration gradients formed in liquid electrolytes during constant-current

cycling. In **Chapter 4**, the effect of temperature on the concentration gradients was quantitatively investigated. Details of the methodology used in that study are explained in **Section 4.3**, particularly as it pertains to the complications associated with the acquisition of MR images in the presence of conductive surfaces. It has previously been found that frequency-encoding MRI strategies suffer from significant distortions under these conditions,[14] so the preferred method of image acquisition is a pure-phase-encoding approach.[15] Reasonably fast acquisitions – necessary for quasi-real-time monitoring of the concentration gradient buildup – were realized using Chemical Shift Imaging (CSI; so-named because it is a pure-phase-encode method which retains a spectral dimension). The pulse sequence is provided in **Figure 2.10**. The imaging direction was along the *in situ* cell axis, aligned with the longitudinal field, and therefore a z-direction phase-encoding

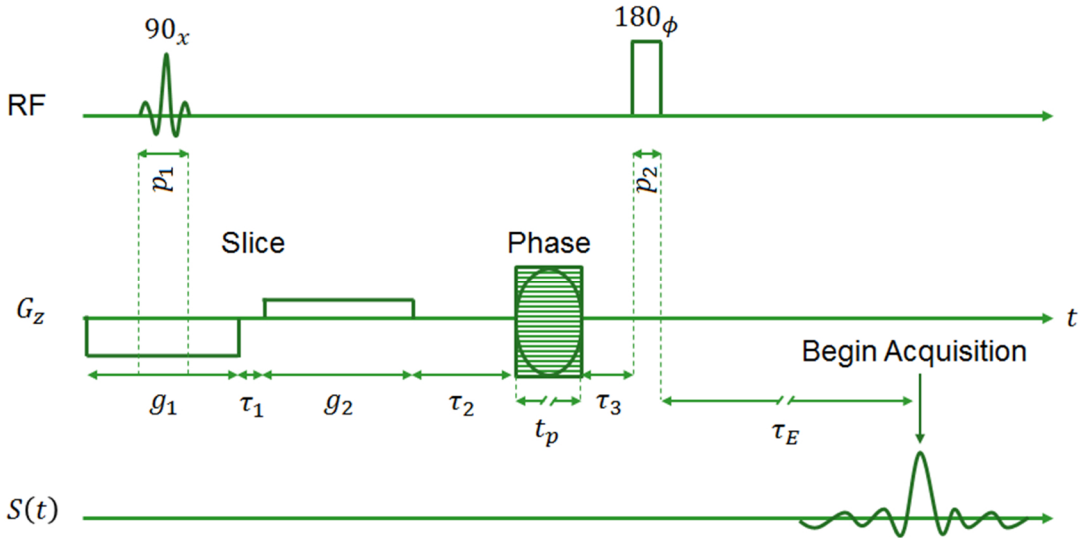

Figure 2.10 – A simple, one-dimensional CSI pulse sequence with slice-selective excitation for rapid and smooth MRI of the *in situ* cell active volume during concentration polarization. Explanation of the parameters can be found in **Section 4.3**.

gradient was used. The sinusoidal shape of the gradient pulses, which are incremented in a series of experiments to acquire all of the k-points necessary to achieve suitable resolution of the electrolyte active volume, are utilized because the smoother ramping relative to rectangular pulses helps to mitigate eddy currents in the probe which can distort and contribute significant noise to the signal during acquisition. The sequence is constructed around a spin echo in order to refocus latent field inhomogeneity, and a relatively narrow slice-selective excitation along z has been added to eliminate signal from residual electrolyte trapped inside the *in situ* cell, but outside the active volume where the concentration polarization is taking place.

While the pure-phase-encode approach outperforms frequency-encoding MRI in the *in situ* cell imaging context, it is not entirely immune to the distortions which plague the quantitative analysis of MR images for the latter either. Two tactics which can also make the imaging process more robust are the use of pre-stabilized gradients and small-tip-angle excitation (using $\theta \ll \pi/2$, in the nomenclature above). These can be realized with the Double-Half-K-space, Single-Point-Ramped-Imaging-with-T_1-Enhancement (DHK-SPRITE) imaging modality.[16] As the name would suggest, DHK-SPRITE employs an incremental ramping of the gradient strength for phase-encoding, not between successive excitations where a single k-point is collected, which will generate progressively larger eddy currents as the rise-time of the gradient needs to increase to reach the highest magnitudes, but rather all at once, with a "staircase-like" pattern (the DHK refers to the fact that the negative and positive k values are acquired on separate ramps, again to avoid

any large, sudden gradient magnitude increases). The pulse sequence for DHK-SPRITE is provided in **Figure 2.11**.

The T_1 enhancement property originates from the DHK-SPRITE signal equation:[16]

$$S(t_p) = M_0 e^{-\frac{t_p}{T_2^*}} \left| \frac{1 - e^{-\frac{T_R}{T_1}}}{1 - \cos(\theta)\, e^{-\frac{T_R}{T_1}}} \right| \sin(\theta), \tag{2.26}$$

which favours small θ because of the denominator, particularly when T_R, the repetition time between the RF pulses on each step of the staircase, is significantly less than T_1. Also, because the gradient is pre-stabilized, there is no signal decay prior to the start of the phase-encoding time, t_p – it begins with the RF excitation. As a result, this pulse sequence is also very amenable to MRI applications in fast-relaxing and highly field-inhomogeneous samples (which is certainly the case for the *in situ* cell near the electrodes, in the region

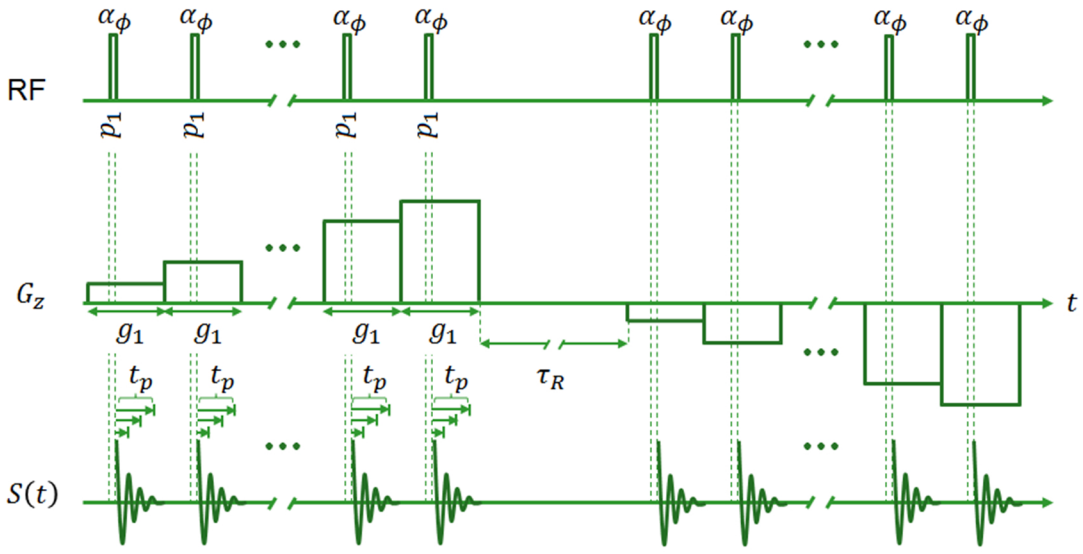

Figure 2.11 – Pulse sequence for multiple-FID-point, DHK-SPRITE. The use of multiple FID points following each RF excitation on every step in the ramp allows for a signal-to-noise enhancement by treating each as an individual phase-encoding time and compositing the images produced by each using the chirp-z transform. Explanations for all of the parameters can be found in **Section 4.3**.

called the "dead space" – a region which DHK-SPRITE captures but CSI does not). Therefore, comparison of the concentration gradients between DHK-SPRITE (which is only feasible in the steady-state due to poor signal-to-noise, originating from the small θ) and CSI allows the former to be used as a "yardstick" for calibrating the FOV of the latter and properly aligning it relative to the actual axial dimension of the *in situ* cell, thereby enabling accurate quantification of the concentration gradients with the faster and smoother CS images. The large signal-to-noise gap between DHK-SPRITE and CSI can be somewhat rectified by a further enhancement of the former (also included in **Figure 2.11**): multi-FID point acquisition, as opposed to the strictly single-point imaging approach with which DHK-SPRITE was originally intended. By acquiring multiple FID points at each step in the ramp, each FID point can be treated as a distinct phase-encoding time, provided that the image reconstruction takes this variable-t_p factor into account via the use of the chirp-z transform,[17] as opposed to simple Fourier transformation that is normally used in the application of the fundamental theorem of NMR localization.

This calibration approach, covered in depth in **Chapter 4**, was published in *The Journal of Physical Chemistry C*,[18] and was also in variable-current *in situ* MRI experiments to provide justification for a dendrite-growth model used for inverse-modelling analysis of *in situ* MRI results, in the form of accurate measurement of the edge-encroachment into the cell under lithium plating conditions.[19] It was also used heavily in **Chapter 5**, analogously as in **Chapter 4**, where a considerably larger range of experimental conditions was analyzed, which will be published in a forthcoming paper.

2.3 Theory and Methods of Pulsed-Field Gradient NMR

Section 2.2 dealt with one application of gradient magnetic resonance: the localization of NMR signal in order to form magnetic resonance images. However, there is another application which is even more prevalently utilized in this thesis, which is PFG-NMR. PFG-NMR is a technique for the measurement of diffusivity, which uses the field gradient to detect displacement of the nuclei, rather than identify their precise location, and was pioneered by Stejskal and Tanner in the 1960s.[20] The gradient-encoding ideas are much the same as for MRI, and as described in **Section 2.2**, but the premise of PFG-NMR is to instead "decode" the phase information after a suitable waiting period. The extent to which this "decoding" is not recovered – the signal attenuation – is a measure of the thermal motion of the nuclear species being probed. The discussion in this section is drawn primarily from the texts of Price[21] and Kärger,[22] which both include highly comprehensive coverage of the theory and practical application of the method.

There are many forms of PFG-NMR experiment, but the basic structure has commonality across all of them.[21] As with MRI, phase-encoding in PFG-NMR is accomplished via the application of a linear field gradient across the sample, of the same form as equations (2.18-20), though in the PFG-NMR context frequently denoted g. This gradient is applied for a brief duration δ, and then a period Δ is allowed to pass, called the diffusion time, during which the spins undergo translational diffusion, carrying their associated gradient phases with them. The gradient decoding then takes place, again with duration δ, and the signal is observed. If decoding was successful, then the same signal should be observed regardless of the gradient strength applied, for fixed δ and Δ. However,

in the event of translational motion, the spins will have been displaced from the positions that they occupied during the gradient encoding, and so will not receive the proper phase shift cancellation from the decoding gradient. The *degree* of this signal attenuation, as a function of the attenuating power (to be discussed below), can be related to the magnitude of the self-diffusivity (equilibrium thermal motion) of the probed nuclei within the sample.

Most PFG-NMR sequences, regardless of their complexity, have at their core an echo to bring about the decoding event. The simplest case employs a spin echo (PGSE) of the type described in **Section 2.1**, where half-way through Δ, following the conclusion of δ, a π refocusing pulse is applied, which works in exactly the same way as described for the refocusing of field inhomogeneity, but in this case the spreading of the precessional frequencies induced by the gradient causes significantly greater dephasing than mere longitudinal field inhomogeneity does. This PGSE approach has the virtue of simplicity, but it requires transverse signal to persist for the entirety of Δ, which will typically need to be much greater than δ, so it is completely unsuited to samples with short T_2. The other major disadvantage is that for large gradients, ramping and ringdown – with the associated signal-disrupting eddy currents cascading through the probe circuitry – can artificially attenuate the signal, causing an overestimate of the diffusivity, and there is no natural mechanism for compensation, or preservation of the signal.

The first difficulty can be overcome by instead constructing the sequence around a stimulated echo (PGSTE). In this case, the signal is excited and the gradient is encoded, as with the spin echo sequence, but instead of a π refocusing pulse eventually arriving at $\Delta/2$, the magnetization is (more or less) immediately rotated back onto the longitudinal axis with

a second $\pi/2$ pulse, putting it into what is termed "z-storage," after the fact that z is the preferred designation for the longitudinal axis, as discussed in **Section 2.1**. With no transverse magnetization component, there is no transverse relaxation; the signal coherence is effectively "frozen" provided that the longitudinal magnetization of the sample persists. This manipulation switches the relaxation time-scale controlling the length of Δ from T_2 to T_1, which, as **Figure 2.3** illustrates, is likely to be more amenable to suitably lengthy diffusion times for most samples, at most experimentally accessible temperatures. Once Δ has transpired, a third $\pi/2$ RF pulse is supplied to the sample, to recall the magnetization to the transverse plane. This is done with the phasing of the pulses such that the net effect of the two $\pi/2$ pulses is equivalent to the single π pulse of the spin echo formulation. The gradient can then be decoded, and the signal acquired once the stimulated echo refocuses.

The other major difficulty for PFG-NMR experiments is the potential overestimation of the diffusivity as a consequence of eddy current ringdown. This can be ameliorated in several ways through pulse sequence design. One very prevalent approach is that of bipolar gradients[23] – essentially, splitting one large gradient pulse of duration δ into two shorter gradient pulses of length $\delta/2$, oppositely signed, and with a π RF pulse between them (this is often referred to – somewhat confusingly in light of relaxation theory – as a Bipolar Pulse Pair, or BPP). From the NMR signal perspective, this can be viewed as a "double negative" – the net effect is the sum of the two phase contributions from the individual $\delta/2$ pulses of the bipolar gradient pulse. However, the eddy currents are generated with opposite signs (or more precisely, the amplitude envelopes[24] of the eddy currents, which are turbulent, are), allowing for considerable cancellation/compensation. A

further development of this approach was the "oneshot" sequence,[25] which deliberately unbalances the bipolar gradient pulses, and then moves the remainder into the z-storage period, to function as a *spoiler gradient*, which again, compensates against existing eddy current ringdown (spoiler gradients can also themselves be added to a regular stimulated echo PFG-NMR experiment with the same aim, and indeed are used in conventional NMR spectroscopy as well to "erase," by dephasing, unwanted signal coherences). The addition of an extra waiting period of z-storage after the application of the decoding gradient (with or without a spoiler gradient), again to allow eddy currents to clear prior to the beginning of acquisition, is termed a Longitudinal Eddy current Delay (LED), and is also a common

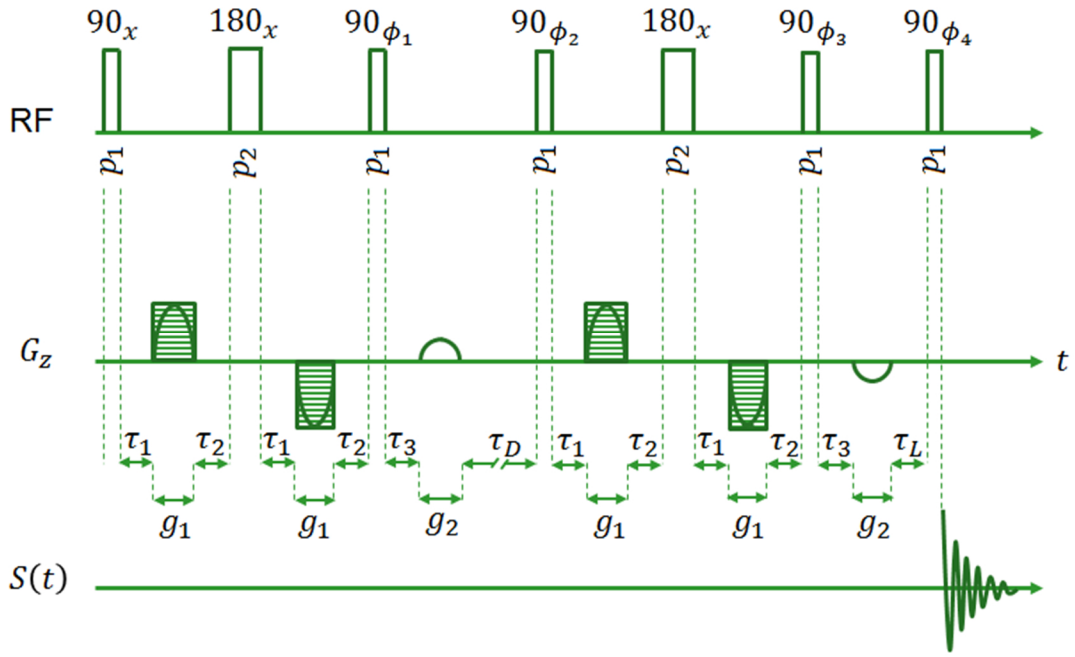

Figure 2.12 – Pulse sequence for a PGSTE experiment involving BPP field gradients and an LED period for eddy current compensation. The τ_i here are simply spacing delays between the gradient and RF pulses, p_1 and p_2 are the $\pi/2$ and π RF pulse lengths, $g_1 = \delta/2$, g_2 is the spoiler gradient duration, τ_D is the difference between Δ and all of the other time intervals from the start of the first BPP g_1 to the start of the second, and τ_L is the difference between the targeted LED duration and the sum of τ_3 and g_2.

feature in modern PFG-NMR experiments.[24] The pulse sequence for a BPPLEDPGSTE[2] experiment is presented in **Figure 2.12**. This experiment was heavily used in **Chapter 6** of this thesis for argyrodite solid-state ion conductors, and was also used for the *ex situ* diffusivity measurements of liquid-state electrolytes which are a component of **Chapter 3**. A oneshot version of this experiment, which was coupled to a CSI experiment for spatial resolution of the measured diffusivities to form a pseudo-three-dimensional experiment, was used in **Chapter 5**, with the pulse sequence presented in **Figure 5.2**.

A schematic illustrating the output of a PFG-NMR experiment is provided in **Figure 2.13**. It is a pseudo-two-dimensional experiment, with a spectral dimension and a dimension constructed by performing the experiment with an incrementally increasing attenuating power, which can be realized in several ways, though is most commonly done by incrementing the magnitude of the field gradient.[26] The most common method for arriving at the signal equation for the PFG-NMR experiment is convolution of the propagator for the diffusion equation with the initial condition for the Bloch equations governing the magnetization, with incorporation of gradient dephasing.[21,27,28] This gradient dephasing takes the form of a "helix" of phases along the sample in the direction of the gradient, with the pitch of the helix related to the characteristic length scale[29] $q^{-1} = (\gamma g \delta)^{-1}$ (here q is the conjugate variable to z, much the same as $\vec{\boldsymbol{k}}$ and $\vec{\boldsymbol{r}}$ in the MRI context of **Section 2.**2). It is an involved calculation, but the result is the famed Stejskal-Tanner equation[20] for the signal attenuation by diffusivity in a PFG-NMR experiment:

$$S(g, \delta, \Delta) = S(0) \exp\left(-D^* \gamma^2 g^2 \delta^2 (\Delta - \delta/3)\right), \tag{2.27}$$

[2] No one actually uses the entire compound acronym; verified by Google.

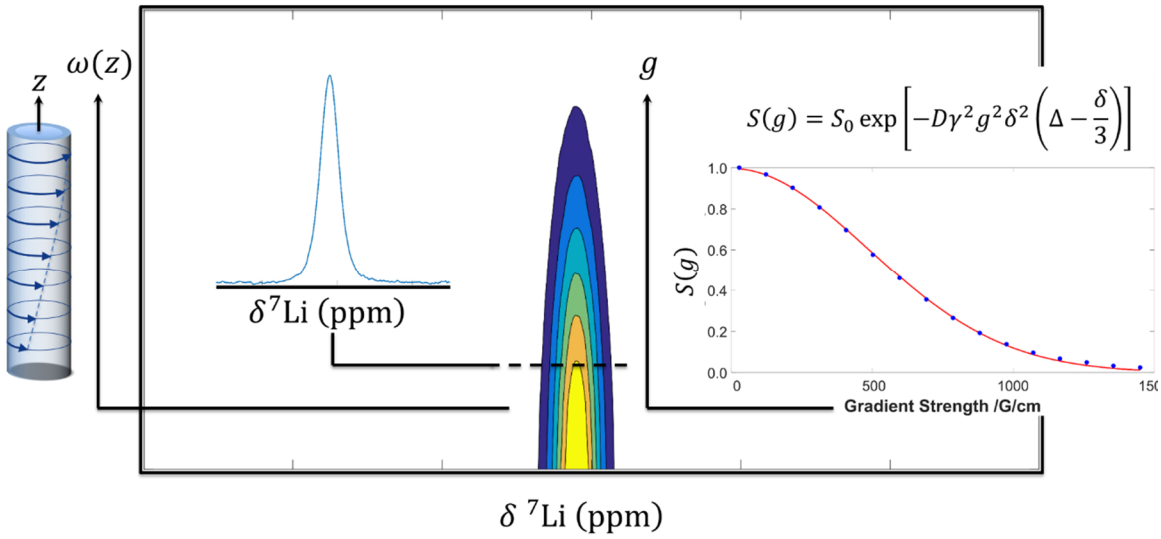

Figure 2.13 – Schematic illustration of the output of a pseudo-two-dimensional PFG-NMR experiment, showing a slice along the spectral dimension, and the integrated intensity across the spectral dimension plotted against the linearly-varied gradient strength, g, producing a Gaussian attenuation curve. A depiction of the phase-helix along the gradient direction is also included at left.

where $S(0)$ is the signal in the absence of a gradient, D^* is the self-diffusivity coefficient, and the other parameters have the meanings initially described above. From equation (2.27), it can be seen that under fixed conditions where D^* is constant, the attenuating power given by $b = \gamma^2 g^2 \delta^2 (\Delta - \delta/3)$ will cause an exponential decay in the signal with increasing b, provided that b is sufficiently large relative to D^* to register significant attenuation. When g is the independent variable, with δ and Δ held constant, then $S(g)$ will have a Gaussian-type decay, as is illustrated in the inset of **Figure 2.13**. For PFG-NMR sequence with extensions beyond the simple PGSTE experiment for which the attenuation is described by equation (2.27), and including shaped (*i.e.* non-rectangular) gradient pulses, it is necessary to modify the Stejskal-Tanner equation. For example, the general form of b

for the signal attenuation of the bipolar gradient PGSTE experiment depicted in **Figure 2.12** is:[30]

$$b = q^2\sigma_g^2\left[\Delta + \frac{2\kappa_g - 2\lambda_g - 1}{4} - \frac{\tau_g}{2}\right], \tag{2.28}$$

where σ_g is the gradient shape parameter (equal to $2/\pi$ for a sine shape), κ_g and λ_g describe the normalized first and second moments of the gradient (and are $1/2$ and $3/8$, respectively, for a sine shape), and τ_g is the interval between the bipolar pulse pair. In any event, the integrated signal intensity, such as the example in the inset of **Figure 2.13**, is fit in a least-squares sense to the applied gradient strengths in order to determine D^*, the sole fitting parameter.

One additional complexity pertains to the measurement of multi-component diffusivity attenuation curves, such as would be encountered in an ion-conducting sample consisting of bulk crystalline and amorphous compartments where there is exchange of ions between the compartments (which is the case for the crystalline $Li_{3.30}Al_{0.15}P_{0.85}S_4$ samples in **Section 6.4.5**). These can be treated with the Kärger equations, which are a specialization of the ubiquitous Chapman-Kolmogoroff equations for the joint probability distributions of interconnected stochastic processes, and take the differential form:[22,31]

$$\begin{aligned}
\dot{S_1} &= -\gamma^2 g^2 \delta^2 D_1 S_1 - \frac{1}{\tau_1} S_1 + \frac{p_{21}}{\tau_2} S_2 + \cdots + \frac{p_{n1}}{\tau_n} S_n \\
\dot{S_2} &= \frac{p_{12}}{\tau_1} S_1 - \gamma^2 g^2 \delta^2 D_2 S_2 - \frac{1}{\tau_2} S_2 + \cdots + \frac{p_{n2}}{\tau_n} S_n \\
&\vdots \\
\dot{S_n} &= \frac{p_{1n}}{\tau_1} S_1 + \frac{p_{2n}}{\tau_2} S_2 + \cdots - \gamma^2 g^2 \delta^2 D_2 S_2 - \frac{1}{\tau_2} S_2
\end{aligned} \tag{2.29}$$

where the p_{ij} are occupation fractions, and the τ_i are the residence times for the diffusing species in the various compartments. For the case of two compartments, there is an analytic solution:[2,22]

$$\begin{aligned} S(q,\Delta) &= S_1(q,\Delta) + S_2(q,\Delta) \\ &= p_1' \exp(-q^2 D_1' \Delta) + p_2' \exp(-q^2 D_2' \Delta) \end{aligned} \tag{2.30}$$

with:

$$D_{1(2)}' = \frac{1}{2}\left(D_1 + D_2 + \frac{1}{q^2}\left(\frac{1}{\tau_1} + \frac{1}{\tau_2}\right) \mp \sqrt{\left[D_2 - D_1 + \frac{1}{q^2}\left(\frac{1}{\tau_2} - \frac{1}{\tau_1}\right)\right]^2 + \frac{4}{q^4 \tau_1 \tau_2}} \right) \tag{2.31}$$

$$p_1' = 1 - p_2{}' \tag{2.32}$$

$$p_2' = \frac{1}{D_2' - D_1'}(p_1 D_1 + p_2 D_2 - D_1') \tag{2.33}$$

These equations can be analyzed further under three different scenarios: the long-time approximation, the short-time approximation, and the so-called intermediate-time approximation.[2,22] In the long-time approximation, the diffusion paths are considered as being sufficiently long that $D_{\mathrm{lr}} \approx p_1 D_1 + p_2 D_2$; that is, Δ encompasses many residence times for both of the compartments, so the diffusivity is the occupation-weighted average of the individual diffusivities for the compartments. Conversely, in the short-time approximation, provided that $D_1 \gg D_2$, there will be clear separation of the two diffusion rates in the attenuation curve, and a linearized version of it (with $\ln(S(q,\Delta))$ versus q^2, assuming fixed Δ) can be fit with limiting slopes in the usual manner that D^* is fit from a single-component attenuation curve, the two diffusion regimes treated as essentially

independent on the time-scale set by Δ. The interesting case is that of the intermediate-time approximation, where the cross-over between the regimes is relevant, but Δ is not sufficiently long that two distinct regimes are not still evident in the attenuation curve. Here, provided that $p_1 \ll p_2$ and $D_1 \gg D_2$, equations (2.31-33) reduce to the following:[2,22]

$$S(q,\Delta) = \exp\left[-q^2\left(D_2 + \frac{p_1 D_1}{q^2 \tau_2 p_1 D_1 + 1}\right)\Delta\right] \tag{2.34}$$

This form is tractable, with D_2, $p_1 D_1$, and τ_2 being determinable from the asymptotes and their intercepts on the linearized signal attenuation plot. If information about the relative occupancies is known from independent experiments (of course, $p_1 + p_2 = 1$), then the

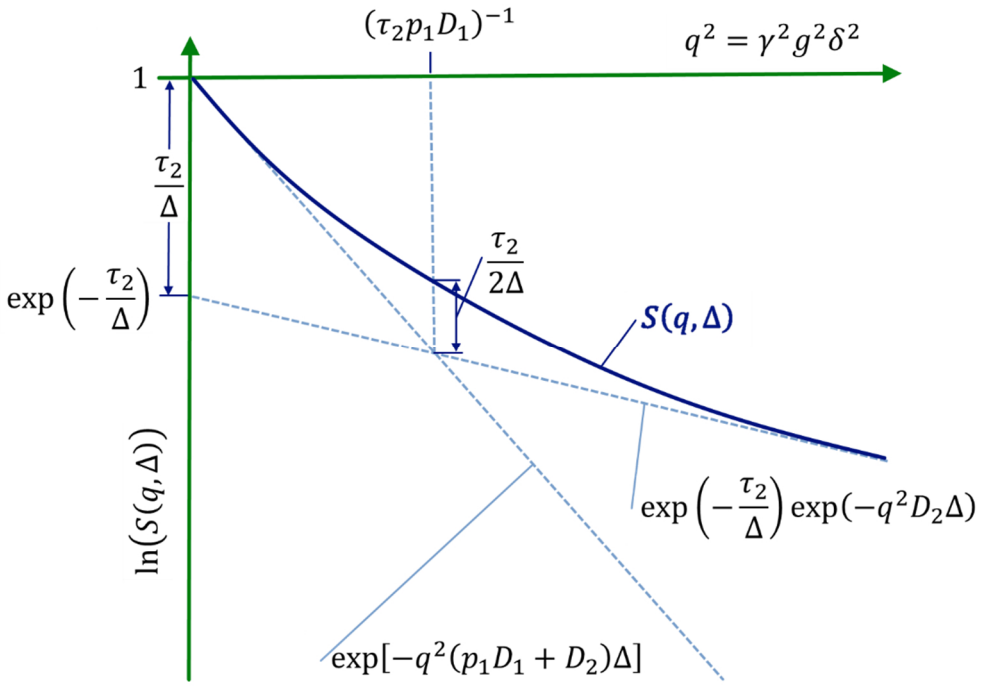

Figure 2.14 – Graphical solution of the intermediate-time approximation to the Kärger equations for two-compartment PFG-NMR attenuation in the case $p_1 \ll p_2$ and $D_1 \gg D_2$. Using the value of p_1 obtained from solid-state NMR lineshape fitting, and a limiting-slope regression method described in **6.4.5**, the four parameters $\{D_1, D_2, \tau_1, \tau_2\}$ can be extracted from the linearized diffusivity attenuation curve. Adapted with modification from Kärger, 1988.[22]

system is completely soluble. The graphical solution is depicted in **Figure 2.14**. This method was applied to the analysis of crystalline and amorphous diffusivity in $Li_{3.30}Al_{0.15}P_{0.85}S_4$ samples in **Section 6.4.5**, using occupancies deduced from magic-angle spinning NMR lineshapes (with the latter technique a subject of the subsequent section).

2.4 Solid-State NMR

The NMR spectroscopy principles discussed in **Section 2.1** are focussed on solution-state samples. Many of the same concepts carry over to the solid-state case, but there are several notable differences. In particular, the rapid tumbling of ions and molecules in the solution state results in an expectation value for their interaction Hamiltonians (*e.g.* equation (2.10) for the dipolar coupling) of approximately zero.[1] With the more rigid motions encountered in solids, this is typically no longer the case, although as **Figure 2.3** illustrates, species with a sufficiently short correlation time τ_C will exhibit solution-like relaxation, which is termed the *motional narrowing limit*[2] (and applies, for example, to spectra of the argyrodite ion conductors in an electrochemically relevant temperature range – refer to **Figure 6.6**).

Of particular relevance for **Chapter 6** in this thesis is the quadrupolar interaction, which describes transitions between states induced by the electric field gradient tensor, $\mathbf{V}$:[3]

$$\mathcal{H}_Q = \frac{eQ}{6I(2I-1)\hbar}\vec{\boldsymbol{I}} \cdot e\mathbf{V} \cdot \vec{\boldsymbol{I}}, \tag{2.35}$$

where $\mathcal{H}_Q$ is the quadrupolar Hamiltonian, e is the fundamental unit of charge, and Q is the nuclear quadrupole moment, intrinsic to a particular isotope (and identically zero for spin-0 and spin-1/2 nuclei). $\mathbf{V}$ is a rank-2 tensor, and permits a description in terms of a principal

axis frame (X, Y, Z) in which it is diagonal, with components $\mathrm{V}_{XX}, \mathrm{V}_{YY}, \mathrm{V}_{ZZ}$, which are typically described in terms of the quadrupolar coupling constant, C_Q and the quadrupolar asymmetry parameter, η_Q:[32]

$$C_Q = \frac{eQ\mathrm{V}_{ZZ}}{h}, \qquad \eta_Q = \frac{(\mathrm{V}_{XX} - \mathrm{V}_{YY})}{\mathrm{V}_{ZZ}}, \tag{2.36}$$

where h is Planck's constant. C_Q has dimensions of frequency in Hz, while $0 \leq \eta_Q \leq 1$. $\mathcal{H}_Q$ embodies considerable complexity, especially as the nuclear spin quantum number I increases. However, for the primary nucleus investigated in **Chapter 6**, ^{7}Li, $I = 3/2$, and indeed, C_Q is typically not large either, owing to the comparatively small size of the nucleus.[32] This will typically limit the influence of quadrupolar broadening on spectra.

The static quadrupolar lineshape can be described by the secular approximation for $\mathcal{H}_Q$, in which off-diagonal terms of small magnitude relative to the Zeeman splitting are neglected (which, again, is not unreasonable for ^{7}Li):[33]

$$\mathcal{H}_Q = \frac{eQV_{ZZ}}{4I(2I-1)}\left(3I_z^2 - I(I+1)\right) \cdot \left[\frac{3\cos^2\theta - 1}{2} + \eta_Q \cos(2\phi)\,(\cos^2(\theta) - 1)\right], \tag{2.37}$$

where (θ, ϕ) are spherical polar coordinates describing the rotation of the principal-axis frame into the laboratory frame. This expression defines a quadrupole splitting, ω_Q, from which the spacing between the $2I + 1$ states for m in the spectrum is obtained, with the gap relative to the Larmor frequency for each state defined by $(2m - 1)\omega_Q$.[3] For the spectrum of a powder sample, with its myriad site orientations and therefore intricate interaction geometry, this can produce an elaborate lineshape; for $I = 3/2$, the most prominent

features will be the large *central transition*, between the $m = 1/2$ and $m = -1/2$ states (just as with the spin-1/2 nuclei for which the discussion in this chapter preceding this section was largely predicated on, governed by ω_0), and a series of singularity-like features which are the perturbed satellite transitions, $|3/2, +3/2\rangle \leftrightarrow |3/2, +1/2\rangle$ and $|3/2, -1/2\rangle \leftrightarrow |3/2, -3/2\rangle$.[32] Fitting lineshapes of this complexity is challenging, but it can provide significant insight concerning the local nuclear environments – in terms of both symmetry and electronic structure – and enable comparisons with diffraction-based structural refinement techniques.[32]

However, it is possible to "average out" a considerable amount of this lineshape complexity by mimicking the tumbling of molecules in solution. The major interactions which can contribute to various order in the solid-state NMR spectrum – the quadrupolar coupling, the dipolar coupling, and the anisotropy of the chemical shift – all contain a term which has associated Legendre P_2^0 symmetry (*i.e.* the first term in equation (2.37) for the quadrupolar coupling). Rapidly spinning the sample about an angle such that the rotational average for these terms approaches zero – *magic-angle spinning* (MAS-NMR) – can achieve this spectral simplification. For the quadrupolar interaction in particular, it turns out that MAS-NMR cannot fully accomplish this averaging, but as long as the MAS rate exceeds the characteristic frequency of the interaction in question - C_Q for the quadrupolar interaction – MAS-NMR will reduce the spectrum to an isotropic resonance (which contains zeroth-order terms for the interactions that did not originally possess orientational dependence), and perhaps a series of *spinning side bands*, where any incomplete averaging due to an insufficient MAS rate manifests. **Figure 2.15** demonstrates this for several

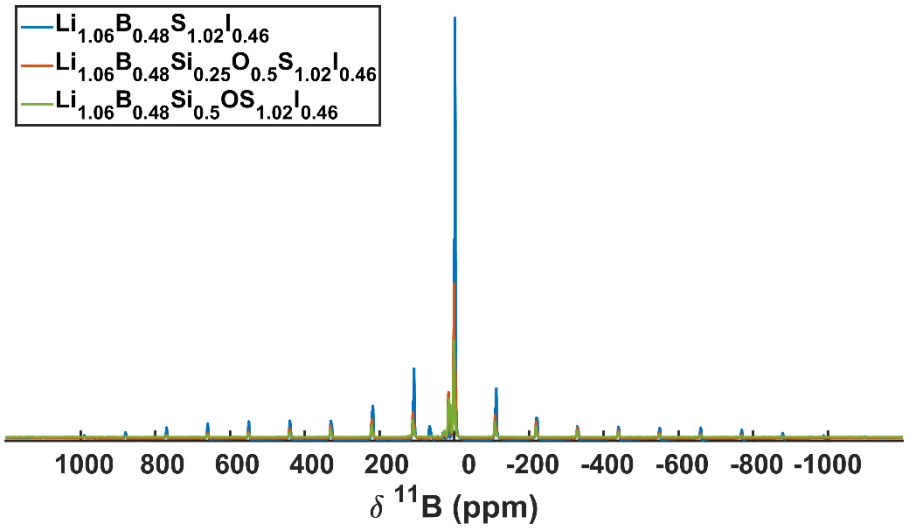

Figure 2.15 – Incomplete MAS-NMR averaging of the ^{11}B quadrupolar interaction for a series of lithium-iodothioborosilicate ion-conducting glasses (compositions listed in the plot legend) where evidently $C_Q \gg$ MAS Rate, leaving a spinning sideband manifold which would partially trace out the original, static lineshape.

lithium-iodothioborosilicate ion-conducting glasses, where the ^{11}B quadrupole interaction is much greater than the achievable spinning speed. MAS-NMR also cannot average out a distribution of C_Q and η_Q parameters, as would occur in a disordered sample. This can be accounted for in the lineshape fitting process by allowing the V_{ii} to be normally distributed, producing a probability distribution function for C_Q and η_Q:[34]

$$f(C_Q, \eta_Q) = \frac{C_Q^{d-1}\eta_Q}{\sqrt{2\pi}\sigma^d}\left(1 - \frac{\eta_Q^2}{9}\right)\exp\left(\frac{C_Q^2}{2\sigma^2}\left(1 + \frac{\eta^2}{3}\right)\right), \qquad (2.38)$$

where σ is the standard deviation of the multi-variate Gaussian V_{ii} distribution, and d is the number of independent V_{ii} components. Fitting to MAS-NMR lineshapes using equation (2.38) can be accomplished using ssNake v1.1,[35] which generates a library of (C_Q, η_Q) configurations prior to attempting the fit to the MAS-NMR lineshape.

The Czjzek model was tested (**Fig. 6.23**) against ^{7}Li MAS-NMR lineshapes for the $Li_{3.30}Al_{0.15}P_{0.85}S_4$ crystalline samples (**Fig. 6.19**), which are known to have a high degree of partial occupancy for lithium sites, from diffraction measurements, and which contain a significant amorphous fraction. The intention was to see whether this may indeed have been a more appropriate model to account for the lineshape than a fit model containing more Lorentzian resonances than resolvable sites in the diffraction studies. The other major application of MAS-NMR in this thesis was to characterize a wide range of argyrodite compositions. Here, the value of high-field, fast MAS was highly evident; minute chemical shift differences between different doping levels were measured, and correlated against the other ion transport properties of the compositions to gain insight about the ion conduction mechanism (**Figure 6.5** and **Figure 6.8**).[36]

2.5 Electrochemical Impedance Spectroscopy

While the majority of the experimental techniques involved in this thesis centre around magnetic resonance (**Sections 2.2-2.4**), electrochemical impedance spectroscopy (EIS) also underpins the results and analysis of **Chapters 3-5**, and is a component of **Chapter 6**, although in that case, the measurements themselves were conducted by the Nazar group at the University of Waterloo. EIS is a versatile tool with utility across a wide range of disciplines and applications,[37–40] with particular applications in lithium-ion battery materials relating to liquid-[41,42] and solid-state electrolyte characterization,[43–45] analysis of electrodes,[46] and modelling of full-cell performance.[47] It offers a fast, non-invasive, relatively inexpensive, and information-rich means of interrogating diverse samples, but with the potential downsides of complicated data interpretation and high

sensitivity to noise.[37] The introductory material on the technique itself is largely drawn from the text of Lasia,[37] while Plett[48] provides a good supplemental overview of equivalent circuit modelling as part of the development of battery modelling theory.

Impedance can be defined as the transfer function between AC input current, $I(t)$, and its voltage response, $E(t)$, with both typically analyzed in the Laplace domain to reduce functions containing derivatives and integrals with respect to time to rational functions:

$$Z(s) \equiv \frac{E(s)}{I(s)}, \tag{2.39}$$

where $s = \sigma + i\omega$ defines the Laplace domain frequency with real part σ and imaginary part ω. The technique is perturbative, and can actually be configured in terms of either an oscillating current or oscillating voltage input signal, despite the definition of impedance being in terms of an input AC current. Within this regime, the dispersive real component of the Laplace domain can be neglected, and the output is analyzed in terms of Fourier transformation of the time-domain input signal, typically acquired over a few periods at a given frequency:

$$Z(i\omega) = \frac{\mathcal{F}[E(t)]}{\mathcal{F}[I(t)]} = \frac{\Delta E}{\Delta I} = \frac{\tilde{E}e^{i\omega t}}{\tilde{I}e^{i\omega t}} = \frac{\tilde{E}}{\tilde{I}} = \frac{|E|}{|I|}e^{i\psi}, \tag{2.40}$$

where ΔE and ΔI represent the voltage and current AC perturbations superimposed atop the DC biases for voltage and current of E_{DC} and I_{DC}, $\tilde{E}$ and $\tilde{I}$ are the phasor descriptions with the ω oscillatory component separated out, and ψ is the mutual phase shift induced between the input and the response at ω. Provided that $\sigma \approx 0$, the perturbation can be understood to be non-energy-dispersive, meaning that it does not disrupt the steady-state

response of the system by depositing energy – the "linear" regime. It becomes a spectroscopic technique when the frequency of the perturbation is incrementally stepped, typically over the frequency decades spanning MHz to sub-Hz, although the necessary range will be a function of the characteristic time scales which define all of the dynamical processes underway in the system.

The measured impedances are complex (equation 2.40), and are therefore typically represented via either Nyquist plots, where the real and imaginary parts are the abscissa and ordinate, respectively, and the frequency dependence is implicit, or Bode plots, where separate plots of the magnitude and phase angle are each given against a logarithmic frequency axis. An example Nyquist plot is given in **Figure 2.16** for the *in situ* cell used in **Chapters 4-5** polarized to the steady-state with a 100 μA current at room temperature to form a concentration gradient, using both a $I_{\mathrm{DC}} = 100$ μA bias while the steady-state is maintained, and a $I_{\mathrm{DC}} = 0$ μA bias immediately after the current is interrupted, both with $\Delta I = 15$ μA rms (that is, operating the impedance analyzer in galvanostatic mode, where an AC current perturbation is superimposed on a DC current). Additional examples can be found in **Figures 3.2** and **5.11** for two-electrode blocking conductivity cells, which were performed in potentiostatic mode about the OCV. The semi-circular regions resemble the impedance response of a parallel RC block circuit element,[48] and can therefore be associated to specific characteristic time scales in the system – modelling of impedance spectra in real electrochemical systems using this equivalent circuit paradigm is an oft-encountered means of extracting information from them.[41,44]

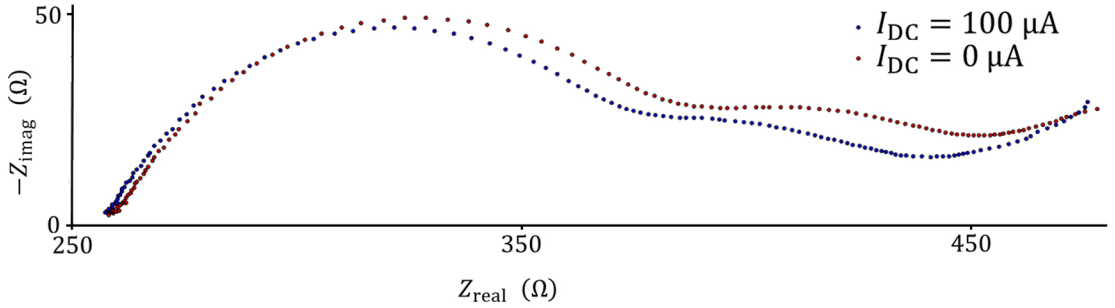

Figure 2.16 – Galvanostatic impedance spectra for the *in situ* cell used in **Chapters 4-5** after polarization to produce a steady-state electrolyte concentration gradient at room temperature, using a 100 μA applied current. DC biases of both 100 μA (*i.e.* measuring while maintaining the steady state) and 0 μA (*i.e.* measuring immediately after current interruption) were conducted, both with a 15 μA rms AC amplitude, to assess the difference in response depending on whether or not the DC current was running.

However, the model equations describing the underlying physicochemical processes typically require linearization in order to make contact with the perturbative regime of the EIS measurement. For example, the Butler-Volmer current $j^{\text{Li}}(t)$ which describes the ion exchange current density at an electrode-electrolyte interface for intercalation/de-intercalation (**Figure 1.3**) depends on the cell potential and the concentrations of the oxidized (c_O) and reduced (c_R) species at the interface, so the resulting perturbation for its perturbation, Δj^{Li}, would take the form:[37]

$$\Delta j^{\text{Li}} = \left(\frac{\partial j^{\text{Li}}}{\partial E}\right)\Delta E + \left(\frac{\partial j^{\text{Li}}}{\partial c_O}\right)\Delta c_O + \left(\frac{\partial j^{\text{Li}}}{\partial c_R}\right)\Delta c_R. \qquad (2.41)$$

The partial derivatives would be evaluated analytically from the model equation for the Butler-Volmer exchange current in **Figure 1.3**, while the voltage perturbation ΔE would be directly measured and the perturbations for the species concentrations, Δc_O and Δc_R, would have to be obtained from linearizations of the c_O and c_R mass transport equations, introducing additional phasors to the current and voltage ones in equation (2.40) which

would have to then be connected to these. It is these modelling complications which require that EIS is essentially not usable as a "stand-alone technique" for the extraction of dynamical information from real systems.[37] One particular exception is the measurement of ionic conductivities from electrochemical cells with blocking electrodes;[49] here, the inherent cell geometry, perhaps in conjunction with simple equivalent circuit modelling appropriate to the spectrum,[41,44] can be readily employed to find the value of the impedance where the response is purely real. The resulting *resistance* (a real impedance is equivalent to resistance by analogy with Ohm's Law in equation 2.39) is synonymous with the charge transport resistance, itself connected to the inherent conductivity of the material between the electrodes via the cell geometry parameters (refer to **Sections 3.3.2** and **5.4.2** for details of implementation).

An important consideration for all EIS experiments – especially when linearized model equations are to be employed – is whether the response is truly in the so-called linear regime. *Linearity* implies that the response is independent of the perturbation amplitude, and correspondingly that the sum of the responses to individual input signals is equivalent to the sum of the individual responses, but also that the system obeys *causality* (it does not generate noise independent of the input signal) and exhibits *stability* (equilibrium exists prior to the measurement, and recurs after a sufficiently long period following the perturbation).[37] Colloquially: the measurement is not altering the state of the system – particularly that the state is not different between initial and final perturbation frequencies as the frequency incrementation which generates the spectrum proceeds.

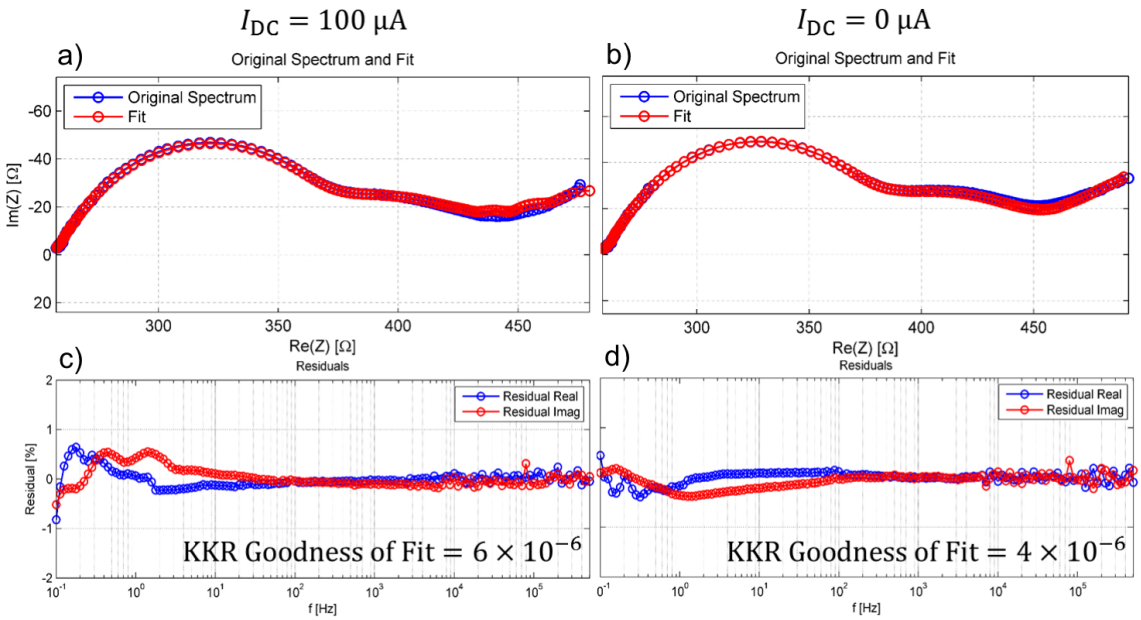

Figure 2.17 – Kramers-Kronig compliance verification for the galvanostatic impedance spectra of **Figure 2.16**, with a) $I_{DC} = 100$ µA and b) $I_{DC} = 0$ µA, using LIN_KK. The respective residual plots as a function of AC frequency are provided in c) and d), demonstrating that the reconstruction is sound, and therefore that the data are in the linear regime.

Obviously, a simple test is to merely confirm that reducing the perturbation amplitude yields an identical Nyquist plot. However, a quantitative test is to evaluate the Kramers-Kronig relations for the impedance as a function of the perturbing frequency:

$$Z_{\text{real}}(\omega) = Z_{\text{real}}(\infty) + \frac{2}{\pi}\int_0^\infty dx\, \frac{xZ_{\text{imag}}(x) - \omega Z_{\text{imag}}(\omega)}{x^2 - \omega^2} \tag{2.42}$$

$$Z_{\text{imag}}(\omega) = -\frac{2\omega}{\pi}\int_0^\infty dx\, \frac{xZ_{\text{real}}(x) - \omega Z_{\text{real}}(\omega)}{x^2 - \omega^2} \tag{2.43}$$

Equations (2.42) and (2.43) imply that one can reconstruct, *e.g.*, the imaginary impedance response from the real response, and this reconstruction can then be compared against the measured imaginary response, functioning as an internal self-consistency check for the

data, which would have to satisfy a specified goodness of fit threshold in order to be considered reliable. The numerical integrations of equations (2.42) and (2.43) using the discrete spectral data is a non-trivial problem, but robust schemes for accomplishing this have been developed, such as LIN_KK.[50] The Kramers-Kronig compliance assessment using LIN_KK for the impedance spectra in **Figure 2.16** is provided in **Figure 2.17**. The small goodness of fit values imply that reconstructions are highly unlikely to be realized by chance, and the residuals of considerably less than 1% relative magnitude over most of the frequency decades further support the conclusion of linear, stable, and causal response to the perturbing AC current. Kramers-Kronig compliance was verified for all of the EIS measurements performed in this thesis.

2.6 References

(1) Levitt, M. H. *Spin Dynamics*, 2nd Editio.; John Wiley & Sons, Ltd: Chichester, UK, 2008.

(2) Callaghan, P. T. *Principles of Nuclear Magnetic Resonance Microscopy*; Oxford University Press: Oxford, UK, 1991.

(3) Duer, M. J. *Solid-State NMR Spectroscopy*; Blackwell Publishing Ltd.: Oxford, UK, 2004.

(4) Sakurai, J. J.; Napolitano, J. *Modern Quantum Mechanics*, 2nd Editio.; Pearson Education, Inc., 2010.

(5) McQuarrie, D. A. *Quantum Chemistry*, 2nd Editio.; University Science Books, 2007.

(6) Bloembergen, N.; Purcell, E. M.; Pound, R. V. Relaxation Effects in Nuclear Magnetic Resonance Absorption. *Phys. Rev.* **1948**, *73* (7), 679–712.

(7) Hebel, L. C.; Slichter, C. P. Nuclear Spin Relaxation in Normal and Superconducting Aluminum. *Phys. Rev.* **1959**, *113* (6), 1504–1519.

(8) Wilkening, M.; Heitjans, P. From Micro to Macro: Access to Long-Range Li+

Diffusion Parameters in Solids via Microscopic 6, 7Li Spin-Alignment Echo NMR Spectroscopy. *ChemPhysChem* **2012**, *13* (1), 53–65.

(9) Cheung, T. T. P. Spin Diffusion in NMR in Solids. *Phys. Rev. B* **1981**, *23* (3), 1404–1418.

(10) Carr, H. Y.; Purcell, E. M. Effects of Diffusion on Free Precession in Nuclear Magnetic Resonance Experiments. *Phys. Rev.* **1954**, *94* (3), 630–638.

(11) Meiboom, S.; Gill, D. Modified Spin□Echo Method for Measuring Nuclear Relaxation Times. *Rev. Sci. Instrum.* **1958**, *29* (8), 688–691.

(12) Brown, T. R. Chemical Shift Imaging. In *Encyclopedia of Magnetic Resonance*; John Wiley & Sons, Ltd: Chichester, UK, 2007; pp 1–12.

(13) Brateman, L. Chemical Shift Imaging: A Review. *Am. J. Roentgenol.* **1986**, *146* (5), 971–980.

(14) Sethurajan, A. K.; Krachkovskiy, S. A.; Halalay, I. C.; Goward, G. R.; Protas, B. Accurate Characterization of Ion Transport Properties in Binary Symmetric Electrolytes Using In Situ NMR Imaging and Inverse Modeling. *J. Phys. Chem. B* **2015**, *119* (37), 12238–12248.

(15) Krachkovskiy, S. A.; Bazak, J. D.; Werhun, P.; Balcom, B. J.; Halalay, I. C.; Goward, G. R. Visualization of Steady-State Ionic Concentration Profiles Formed in Electrolytes during Li-Ion Battery Operation and Determination of Mass-Transport Properties by in Situ Magnetic Resonance Imaging. *J. Am. Chem. Soc.* **2016**, *138* (25), 7992–7999.

(16) Halse, M.; Goodyear, D. J.; MacMillan, B.; Szomolanyi, P.; Matheson, D.; Balcom, B. J. Centric Scan SPRITE Magnetic Resonance Imaging. *J. Magn. Reson.* **2003**, *165* (2), 219–229.

(17) Halse, M.; Rioux, J.; Romanzetti, S.; Kaffanke, J.; MacMillan, B.; Mastikhin, I.; Shah, N. J.; Aubanel, E.; Balcom, B. J. Centric Scan SPRITE Magnetic Resonance Imaging: Optimization of SNR, Resolution, and Relaxation Time Mapping. *J. Magn. Reson.* **2004**, *169* (1), 102–117.

(18) Bazak, J. D.; Krachkovskiy, S. A.; Goward, G. R. Multi-Temperature in Situ

Magnetic Resonance Imaging of Polarization and Salt Precipitation in Lithium-Ion Battery Electrolytes. *J. Phys. Chem. C* **2017**, *121* (38), 20704–20713.

(19) Sethurajan, A. K.; Foster, J. M.; Richardson, G.; Krachkovskiy, S. A.; Bazak, J. D.; Goward, G. R.; Protas, B. Incorporating Dendrite Growth into Continuum Models of Electrolytes: Insights from NMR Measurements and Inverse Modeling. *J. Electrochem. Soc.* **2019**, *166* (8), A1591–A1602.

(20) Stejskal, E. O.; Tanner, J. E. Spin Diffusion Measurements: Spin Echoes in the Presence of a Time□Dependent Field Gradient. *J. Chem. Phys.* **1965**, *42* (1), 288–292.

(21) Price, W. S. *NMR Studies of Translational Motion*; 2009.

(22) Karger, J.; Pfeifer, H.; Heink, W. Principles and Application of Self-Diffusion Measurements by Nuclear Magnetic Resonance. In *Advances in Magnetic Resonance*; Waugh, J. S., Ed.; Academic Press, Inc.: San Diego, 1988; p 438.

(23) Wu, D. H.; Chen, A. D.; Johnson, C. S. An Improved Diffusion-Ordered Spectroscopy Experiment Incorporating Bipolar-Gradient Pulses. *J. Magn. Reson. Ser. A* **1995**, *115* (2), 260–264.

(24) Gibbs, S. J.; Johnson, C. S. A PFG NMR Experiment for Accurate Diffusion and Flow Studies in the Presence of Eddy Currents. *J. Magn. Reson.* **1991**, *93* (2), 395–402.

(25) Pelta, M. D.; Morris, G. A.; Stchedroff, M. J.; Hammond, S. J. A One-Shot Sequence for High-Resolution Diffusion-Ordered Spectroscopy. *Magn. Reson. Chem.* **2002**, *40* (13), S147–S152.

(26) Kärger, J.; Ruthven, D. M. Diffusion in Nanoporous Materials: Fundamental Principles, Insights and Challenges. *New J. Chem.* **2016**, *40* (5), 4027–4048.

(27) Kärger, J. Diffusion Measurements by NMR Techniques. *Adsorpt. Diffus.* **2008**, No. February, 85–133.

(28) Stallmach, F.; Galvosas, P. Spin Echo NMR Diffusion Studies. In *Annual Reports on NMR Spectroscopy*; 2007; Vol. 61, pp 51–131.

(29) Momot, K. I.; Kuchel, P. W. PFG NMR Diffusion Experiments for Complex

Systems. *Concepts Magn. Reson. Part A* **2006**, *28A* (4), 249–269.

(30) Sinnaeve, D. The Stejskal – Tanner Equation Generalized for Any Gradient Shape — An Overview of Most Pulse Sequences Measuring Free Diffusion. *Concepts Magn. Reson. Part A* **2012**, *40A* (2), 39–65.

(31) Kärger, J.; Kočiřik, M.; Zikánová, A. Molecular Transport through Assemblages of Microporous Particles. *J. Colloid Interface Sci.* **1981**, *84* (1), 240–249.

(32) Ashbrook, S. E.; Sneddon, S. New Methods and Applications in Solid-State NMR Spectroscopy of Quadrupolar Nuclei. *J. Am. Chem. Soc.* **2014**, *136* (44), 15440–15456.

(33) Freude, D. Quadrupolar Nuclei in Solid-State NMR. In *Encyclopedia of Analytical Chemistry*; Meyers, R. A., Ed.; John Wiley & Sons: Chichester, UK, 2000; pp 12188–12224.

(34) Czjzek, G.; Fink, J.; Götz, F.; Schmidt, H.; Coey, J. M. D.; Rebouillat, J.-P.; Liénard, A. Atomic Coordination and the Distribution of Electric Field Gradients in Amorphous Solids. *Phys. Rev. B* **1981**, *23* (6), 2513–2530.

(35) van Meerten, S. G. J.; Franssen, W. M. J.; Kentgens, A. P. M. SsNake: A Cross-Platform Open-Source NMR Data Processing and Fitting Application. *J. Magn. Reson.* **2019**, *301*, 56–66.

(36) Adeli, P.; Bazak, J. D.; Park, K. H.; Kochetkov, I.; Huq, A.; Goward, G. R.; Nazar, L. F. Boosting Solid-State Diffusivity and Conductivity in Lithium Superionic Argyrodites by Halide Substitution. *Angew. Chemie* **2019**, ange.201814222.

(37) Lasia, A. *Electrochemical Impedance Spectroscopy and Its Applications*; 2005.

(38) Chang, B.-Y.; Park, S.-M. Electrochemical Impedance Spectroscopy. *Annu. Rev. Anal. Chem.* **2010**, *3* (1), 207–229.

(39) Park, M.; Zhang, X.; Chung, M.; Less, G. B.; Sastry, A. M. A Review of Conduction Phenomena in Li-Ion Batteries. *J. Power Sources* **2010**, *195* (24), 7904–7929.

(40) Miyano, K.; Yanagida, M.; Shirai, Y. Impedance Spectroscopy Revisited. *Adv. Energy Mater.* **2020**, *1903097*, 1903097.

(41) Brug, G. J.; van den Eeden, A. L. G.; Sluyters-Rehbach, M.; Sluyters, J. H. The Analysis of Electrode Impedances Complicated by the Presence of a Constant Phase Element. *J. Electroanal. Chem. Interfacial Electrochem.* **1984**, *176* (1–2), 275–295.

(42) Halalay, I. C. Versatile Cell for Complex Permittivity Measurements on Liquids. *Rev. Sci. Instrum.* **1999**, *70* (8), 3432–3434.

(43) Winand, J.-M.; Depireux, J. Measurement of Ionic Conductivity in Solid Electrolytes. *Europhys. Lett.* **1989**, *8* (5), 447–452.

(44) Boukamp, B. A. Electrochemical Impedance Spectroscopy in Solid State Ionics: Recent Advances. *Solid State Ionics* **2004**, *169* (1–4), 65–73.

(45) Uddin, M.-J.; Cho, S.-J. Reassessing the Bulk Ionic Conductivity of Solid-State Electrolytes. *Sustain. Energy Fuels* **2018**, *2* (7), 1458–1462.

(46) Dees, D. W.; Abraham, D. P.; Lu, W.; Gallagher, K. G.; Bettge, M.; Jansen, A. N. Electrochemical Modeling and Performance of a Lithium- and Manganese-Rich Layered Transition-Metal Oxide Positive Electrode. *J. Electrochem. Soc.* **2015**, *162* (4), A559–A572.

(47) Xie, Y.; Li, J.; Yuan, C. Mathematical Modeling of the Electrochemical Impedance Spectroscopy in Lithium Ion Battery Cycling. *Electrochim. Acta* **2014**, *127*, 266–275.

(48) Plett, G. L. *Battery Management Systems, Volume I: Battery Modeling*; Artech House Publishers, 2015.

(49) Levi, M. D.; Dargel, V.; Shilina, Y.; Aurbach, D.; Halalay, I. C. Impedance Spectra of Energy-Storage Electrodes Obtained with Commercial Three-Electrode Cells: Some Sources of Measurement Artefacts. *Electrochim. Acta* **2014**, *149*, 126–135.

(50) Boukamp, B. A. A Linear Kronig-Kramers Transform Test for Immittance Data Validation. *J. Electrochem. Soc.* **1995**, *142* (6), 1885.

Chapter 3 – Pulsed-Field Gradient NMR and EIS Investigations of Liquid-State Lithium-Ion Batteries

3.1 Outline and Context in the Thesis

The investigation described in this chapter involves several of the essential techniques and methods that recur throughout this thesis. The aim was to apply a technique for transference number characterization which combined diffusivity measurements from PFG-NMR and conductivity measurements from EIS to compute the transference number while explicitly taking into account the influence of contact ion pairing. Such a modification more completely captures the ion transport in concentrated electrolyte solutions than approximations which rely on PFG-NMR results alone. The study presented here ran in parallel with another investigation in the group of Prof. Gillian R. Goward, headed by Dr. Sergey A. Krachkovskiy, on a more conventional electrolyte formulation, which was published in the *Journal of the Electrochemical Society* (**2017**, *164(6)*, A912-A916) with authorship of S. A. Krachkovskiy, J. David Bazak, S. Fraser, I. C. Halalay, and G. R. Goward. Several of the electrolyte compositions featured here mirror the general properties of those which were the focus of the JES paper; in fact, the idea to use an EC-heavy electrolyte composition for that paper was borne out of the excellent results achieved in this study on the CMHT1 composition (so-named for the Centre for Mechatronics and Hybrid Technologies at McMaster University, where some of the measurements were performed), which also utilized a high proportion of cyclic carbonate solvent. This study

also examines the effect of the popular fluorinated ethylene carbonate additive in a fully solvating role in the electrolyte mixture. The variable-temperature results presented here are intended to both characterize electrolyte transport properties for electrochemical modelling applications, and also provide insight for electrolyte design, in terms of how temperature and composition impact the ion transport.

3.2 Introduction and Context in the Field

Accurate battery management system (BMS) operation for modern lithium-ion batteries requires modelling which captures the fast cell dynamics occurring in electric vehicle applications,[1–3] along with a means of estimating the state of charge (SOC) and describing aging effects.[4–6] A critical component of any battery model, whether at atomic, particulate or continuum length scales, is accurate parameterization of the mass transport of the lithium ions, in the form of liquid- and solid-state diffusivities.[7–9] *Operando* experimental determination of these parameters in a real cell is complicated at any length scale, and in particular, it remains an important challenge to probe lithium ion dynamics within the concentrated electrolyte system, determine how these are influenced by temperature, and determine how this influence might affect macroscopic device performance.[10–12] Similarly, completely rigorous electrochemical models of lithium-ion cells,[13,14] which treat the microscopic dynamics of ion transport and make no simplifications regarding the cell composition and electrode porosity, are essentially intractable for online estimation methods necessary for electric vehicle application.[15] Therein lies the role of *ex situ* characterization methods, like PFG-NMR, to provide supplementary data on the electrolyte transport parameters, which can be taken as inputs

for constructing reduced-order electrochemical models[1,4,16–20] that nevertheless retain all of the essential features of the full model, and have as their basis accurate physicochemical relations between operating conditions and ion transport.

PFG-NMR measurements have been employed as a component of a number of lithium-ion battery liquid- and polymer-electrolyte characterization studies.[21–30] There are many electrochemical techniques[10,31–38] which can provide mass transport information considering the electrolyte as a bulk system, but one of the inherent advantages of NMR-derived diffusion measurements is the nuclear selectivity it confers, allowing for the determination of ion-specific diffusion coefficients even in multicomponent electrolytes beyond simple binary salt mixtures.[39] However, because PFG-NMR probes equilibrium diffusivity based on nuclear identity, and not ion identity, it is important to recognize that the diffusivities it measures are ensemble-weighted averages of the motions of various levels of ion aggregation,[27,28] from solvated ions, to solvent-mediated and contact ion pairs, to larger multi-ion aggregates. Since aggregation can be viewed as effectively reducing the number of charge carriers, care must be taken when translating equilibrium mass transport parameters measured by PFG-NMR into quantities which instead reflect charge transport, namely, the transference number. In Dilute Solution Theory (DST), there is a straightforward connection between the so-called *intrinsic diffusivities* of the ion species in a binary electrolyte, D_i with $i = \{+, -\}$, measured at very low concentration, to the DST cation transference number, t_+:[40]

$$t_+ = \frac{D_+}{D_+ + D_-}, \qquad \text{(DST)} \tag{3.1}$$

However, in Concentrated Solution Theory (CST), the solvent is no longer considered a passive medium, and interactions between it and the ion species, as well as between the ion species themselves, must be factored in. This leads to the CST expression for the transference number in terms of the *Onsager-Stefan-Maxwell diffusivities*, $\mathcal{D}_{ij}$, with $i,j = \{+,-,0\}$ for a binary electrolyte:

$$t_+^0 = \frac{\mathcal{D}_{0+}}{\mathcal{D}_{0+} + \mathcal{D}_{0-}}, \qquad \text{(CST)} \tag{3.2}$$

where t_+^0 is the cationic transference number with respect to the solvent reference frame. The $\mathcal{D}_{ij}$ are explicitly formulated in terms of the mutual drag forces between the mixture components, and thus naturally subsume the ion activities within the model structure.[40] Conversely, PFG-NMR measures *neither* of these two diffusivities; as described above, the PFG-NMR diffusivities are measured at equilibrium – and so are more aptly termed *self-diffusivities*, D_i^* – and over an ensemble of different aggregation states. Formulating a ratio between them for a binary electrolyte in the manner of eqs. (3.1) and (3.2) yields a quantity denoted the transport number,[28]

$$\tau_+ = \frac{D_+^*}{D_+^* + D_-^*}, \tag{3.3}$$

which is purely a measure of the share of the cation in the overall *mass transport*, rather than the proportion of cationic motion contributing to the overall *charge transport* that t_+^0 records.

A simple method for disentangling the PFG-NMR signal contributions stemming from neutral ion pairs and charged ions has been proposed in Stolwijk *et al.*, 2013,[27] and is adopted for the analysis of the series of experiments presented here. The measured mass

and charge diffusivities, D_i^* and D_κ, respectively, are converted into so-called effective diffusivities, can be directly related to t_+^0 and the degree of ion pairing, α_p. The charge diffusivity is arrived at from the measured ionic conductivity, κ, via the Nernst-Einstein equation for a binary electrolyte:

$$D_\kappa = \frac{k_B T}{e^2 c_s} \kappa, \tag{3.4}$$

where k_B is the Boltzmann constant, T is the temperature of the mixture, c_s is the salt concentration, and e is the fundamental unit of charge (this version of the formula assumes a binary, univalent salt).

The process begins with the fundamental interlink between mass transport and charge transport in any conducting system, the Haven ratio H_R,

$$H_R = \frac{(D_+^* + D_-^*)}{D_\kappa} = \frac{\kappa_{\text{diff}}}{\kappa}, \tag{3.5}$$

which is most readily interpreted as the degree of correlation in the ion transport. A value of $H_R = 1$ indicates completely uncorrelated motion, while at the other extreme, $H_R = 0$, the motions of the same species charge carriers are fully interdependent. A fuller picture involves considering *self* versus *distinct* contributions, including both positive correlations and anti-correlations, between both similarly-charged species and oppositely-charged species.[41] In equation (3.5), the term κ_{diff} represents the hypothetical ionic conductivity that one would expect to measure if the (thermal) motion observed by PFG-NMR was completely equivalent to the charge transport motion, given by applying the Nernst-Einstein equation to the numerator of the middle term:

$$\kappa_{\text{diff}} = \frac{e^2 c_s}{k_B T}(D_+^* + D_-^*). \tag{3.6}$$

Since the electric potential that stimulates charge transport will necessarily alter the proportion of correlation and anti-correlation that describes the motion under equilibrium conditions – that probed by PFG-NMR – by driving oppositely-charged species toward opposite electrodes, and since the positive correlations between oppositely-charged species which reduce the charge transport but do not impact the mass transport are not accounted for in κ_{diff}, it stands to reason that $\kappa_{\text{diff}} > \kappa$ under all but the most dilute conditions, and consequently $H_R > 1$ for concentrated electrolytes also.

The Stolwijk method furnishes a relatively straightforward means of estimating the positive correlations between oppositely-charged ions by assuming that a fixed fraction of the mixture at any given time consists of contact ion pairs. Then the self-diffusivities measured by PFG-NMR are "effectively" the sum of fully-solvated ion diffusivity, $D_{+/-}^{\text{eff}}$, and ion pair diffusivity, D_p^{eff}:

$$D_+^* = D_+^{\text{eff}} + D_p^{\text{eff}} \equiv \big(1 - \alpha_p\big)D_+ + \alpha_p D_p \tag{3.7}$$

$$D_-^* = D_-^{\text{eff}} + D_p^{\text{eff}} \equiv \big(1 - \alpha_p\big)D_- + \alpha_p D_p \tag{3.8}$$

where the D_i – the *intrinsic diffusivities* – have the DST interpretation discussed above. It then immediately follows that the sum of the charged contributions in equations (3.7) and (3.8) represents the charge diffusivity of equation (3.4):

$$D_\kappa = D_+^{\text{eff}} + D_-^{\text{eff}} \equiv \big(1 - \alpha_p\big)D_+ + \big(1 - \alpha_p\big)D_-. \tag{3.9}$$

By combining equations (3.7-9) in the definition of H_R in (3.5), the fact that $H_R > 1$ for concentrated electrolytes manifests immediately. Since the system (3.7-9) contains three

unknowns, in the form of the effective diffusivities, and three measurables, in the form of the two self-diffusivities from PFG-NMR and D_κ from EIS, equations (3.7-9) can be solved for the unknown effective diffusivities:

$$D_+^{\text{eff}} = \frac{1}{2}(D_+^* - D_-^* + D_\kappa) \equiv \big(1 - \alpha_p\big)D_+, \tag{3.10}$$

$$D_-^{\text{eff}} = \frac{1}{2}(-D_+^* + D_-^* + D_\kappa) \equiv \big(1 - \alpha_p\big)D_-, \tag{3.11}$$

$$D_p^{\text{eff}} = \frac{1}{2}(D_+^* + D_-^* - D_\kappa) \equiv \alpha_p D_p. \tag{3.12}$$

The cationic transference number and ion pairing fraction can then be calculated as:

$$t_+^0 = \frac{D_+^{\text{eff}}}{D_\kappa} \tag{3.13}$$

$$\alpha_p = \frac{D_p^{\text{eff}}}{D_p^{\text{eff}} + D_+^{\text{eff}}}, \tag{3.14}$$

where in the former case, $\mathcal{D}_{0+} \approx D_+^{\text{eff}}$ and $\mathcal{D}_{0-} \approx D_-^{\text{eff}}$ has been assumed – that is, all deviation from ideal ion activity in solution can be ascribed to the formation of contact ion pairs – and in the latter case, that $D_p \approx D_+$ in the rightmost expressions of equations (3.10-3.12). The basis for the assumption that the intrinsic diffusivity of the contact ion pairs is similar to that of the solvated cations is somewhat specific to $LiPF_6$-based salts with solvents containing cyclic carbonates. It stems from molecular dynamics studies,[42–45] which show that the most probable ion pair formation is replacement of one of the typically 4 cyclic carbonate molecules solvating a lithium cation with a PF_6^- anion, and the observation that the size and molecular mass of PF_6^- and EC/PC are relatively similar. It is further supported by electrochemical microcalorimetry measurements of the lithium solvation

structure in EC/DMC solutions over a wide salt concentration range,[46] which demonstrated that the first coordination sphere of lithium cations does not significantly change between a solvated Li^+ and a contact ion pair.

The analytical machinery in equations (3.10-3.14) is applied first to contrast an electrolyte mixture which has a large fraction of cyclic carbonates (which, as will be discussed below, corresponds to a high relative permittivity) with one where the linear carbonate is predominant by volume (corresponding to a high solvent mobility/lower viscosity). The former electrolyte contains a mixture of the cyclic carbonates ethylene carbonate (EC), a staple of benchmark liquid electrolytes for lithium-ion batteries, and propylene carbonate (PC), which improves low-temperature performance.[47,48] ^{7}Li and ^{19}F PFG-NMR are used to measure cation and anion self-diffusivities, and then these are combined with ionic conductivity measurements from EIS to determine the effective diffusivities, transference number, and ion pairing fraction. This information is used to demonstrate that optimal ion transport – particularly at low temperature – is obtained not with minimally-viscous solvent mixtures, but rather with high cyclic carbonate content. Second, effective diffusivities and transference numbers obtained for several fluoroethylene carbonate (FEC)-containing electrolyte blends with higher salt concentration are evaluated, and contrasted with the more conventional EC-containing blends in terms of their transport properties. The importance of FEC as an additive for electrode passivation in high-voltage lithium-ion batteries[49–53] and thermally-stable interphase formation for low-temperature operation[54] is well-documented, but with increased efforts to improve its low-voltage performance by using it as a co-solvent with

more traditional linear carbonates,[55] the transport performance of electrolyte mixtures which employ it as a major fraction is of increasing interest.

3.3 Experimental

3.3.1 Electrolyte Compositions

The composition of the four electrolytes used in this study are listed in **Table 3.1**. Note that the precise solvent blends for CMHT3 and CMHT4 cannot be disclosed owing to NDA protections required by an industrial collaborator. The electrolyte solutions were prepared using freeze-thaw degassed solvents, consisting of 98% ethylene carbonate (Sigma Aldrich), 99% propylene carbonate (Sigma Aldrich), 99+% dimethyl carbonate (DMC; Sigma Aldrich), 99% ethylmethyl carbonate (EMC; Sigma Aldrich), 98% fluoroethylene carbonate (Alfa Aesar), and battery-grade $LiPF_6$ salt (Sigma Aldrich). All preparations were done under argon atmosphere in a glovebox (1.2 ppm O2 content, < 0:1 ppm H2O). A total of 5 mL of each mixture was made, with 500 µL allocated to the 5 mm NMR tube and the remainder used to fill either a two- or three-electrode cell for the conductivity measurements.

Table 3.1 – Electrolyte compositions and nomenclature.

Mixture Name	Composition
CMHT1	1.00 M $LiPF_6$ in EC/PC/DMC, 5:2:3 (v/v)
CMHT2	1.00 M $LiPF_6$ in EC/EMC, 3:7 (v/v)
CMHT3	1.25 M $LiPF_6$ in High-FEC Content Blend
CMHT4	1.00 M $LiPF_6$ + 0.20 M LiFSI in Low-FEC Content Blend

3.3.2 EIS Measurements of Ionic Conductivity

The three-electrode cell was used for the first series of measurements, on CMHT1 in **Table 3.1**, and consisted of a glassy carbon working electrode, with reference and

counter electrodes fashioned from solid Li, and was constructed in the glovebox. A NESLAB Endocal RTE-220 circulator filled with ethylene glycol was used for temperature control of the conductivity measurements with this cell type, with the cell immersed up to the lid in the fluid, which were obtained via EIS using a Gamry Instruments Interface1000 impedance spectrometer operating in potentiostatic mode at 3 V. At each temperature, measurements were made once the open-circuit voltage was observed to deviate by no more than ± 1 mV over a 120 s interval, which produced precise and repeatable measurements (i.e. reasonable thermal stability). Three experiments were performed per temperature, and this equilibration criterion yielded results which only varied in the fourth significant figure. A sample rate of 10 points per decade was employed, covering the 1 MHz to 10 Hz frequency range examined, with an AC excitation amplitude of 200 mV rms. The value of R_s, the electrolyte resistance of the cell, was obtained from fitting a series resistor-CPE circuit to the diffusion tail of the resulting Nyquist plots,[56] and converted into the conductivity using the standard formula for resistance of current flow to a disk, the surface of the glassy carbon electrode:[57]

$$\kappa = \frac{1}{4R_s r}, \tag{3.15}$$

where $r = 0.15$ cm is the radius of the disc electrode. Equation (3.4) was then used to determinate the charge diffusivity of the mixture at the operating temperature. Representative Nyquist plots for this cell configuration are provided in **Figure 3.1**.

While very precise results were obtainable for CMHT1 with the 3-electrode cell setup, temperature control with the circulator was laborious and the high-frequency impedance response was non-ideal. For these reasons, a change to a portable 2-electrode

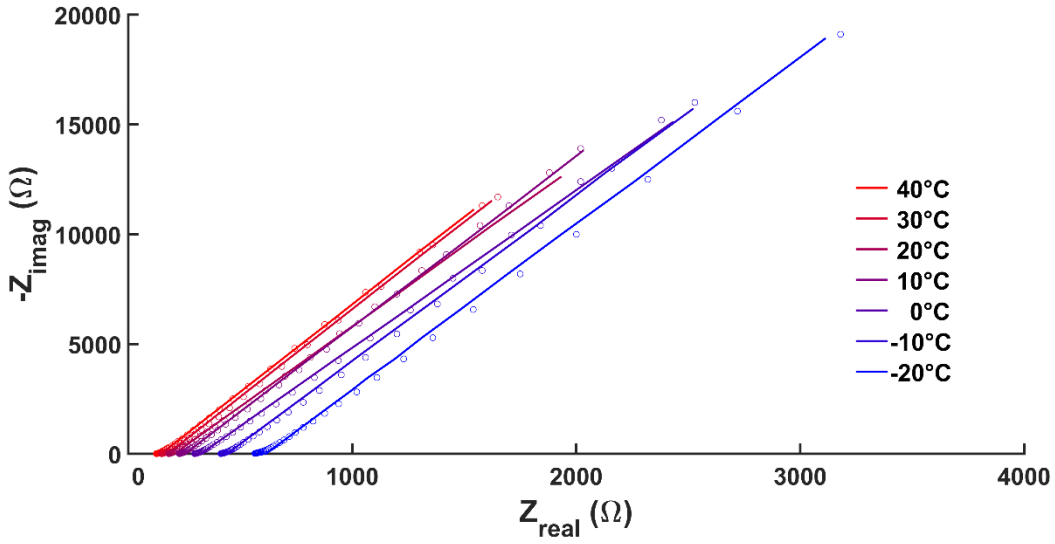

Figure 3.1 – Representative Nyquist plots over a range of temperatures for the three-electrode cell used to make ionic conductivity measurements of the CMHT1 mixture.

cell was made for the remaining electrolyte mixtures, so that temperature regulation could be performed with the Thermotron 8800 thermal chamber at the Centre for Mechatronics and Hybrid Technologies (the acronym for which, incidentally, lends its name to the mixture designators). The two-electrode cell was provided by Dr. Ion Halalay, and is of similar construction to that of Halalay, 1999.[58] Both electrodes in the cell were blocking, comprised of Ni, and so the Interface1000 was operated in potentiostatic mode at 0 V for these sets of measurements, with the same thermal equilibration criterion as for the 3-electrode cell applied. An AC excitation amplitude of 10 mV rms was used for these experiments, with frequencies in the range of 1 MHz to 10 Hz sampled at 20 points per decade. The standard formula for a resistor of uniform cross-section was employed to find the conductivity of the electrolyte in this cell from the R_s values obtained from the Nyquist plot real-axis intercepts (*i.e.* $Z'' = 0$):

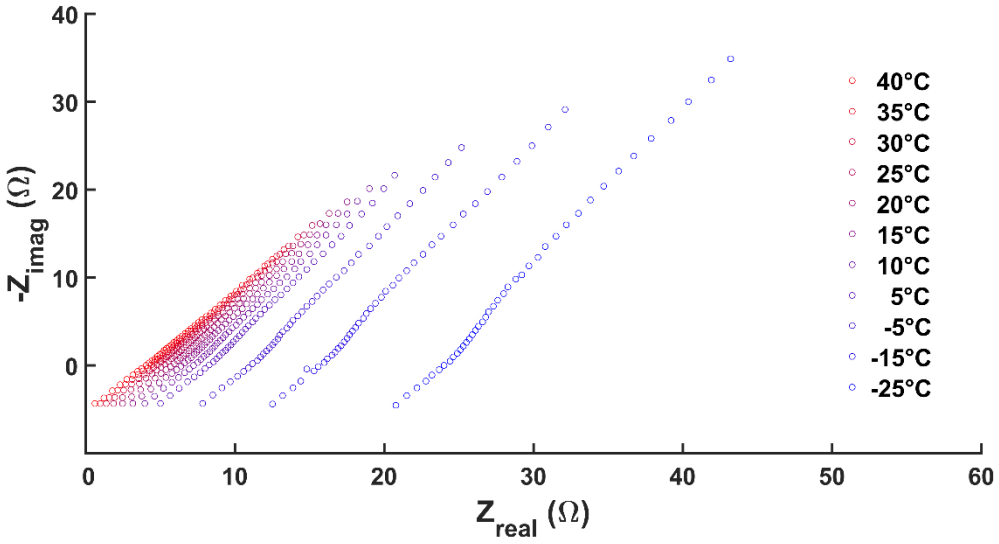

Figure 3.2 – Representative Nyquist plots over a range of temperatures for the two-electrode cell used to make ionic conductivity measurements of the CMHT2 mixture.

$$\kappa = \frac{L}{\pi d^2 R_s}, \tag{3.16}$$

where the separation between the Ni electrodes is $L = 0.2$ cm for this cell, and the electrode area is determined by the cross-sectional diameter of $d = 2.27$ cm. The precise intercept $(R_s, 0)$ was determined via linear interpolation from the points (Z_1', Z_1'') and (Z_2', Z_2'') at the frequencies immediately below and above the real axis, respectively:

$$R_s = \frac{0 - Z_1''}{Z_2'' - Z_1''}(Z_2' - Z_1') + Z_1'. \tag{3.17}$$

Representative Nyquist plots for the CMHT1 mixture over a range of temperatures are provided in **Figure 3.2**.

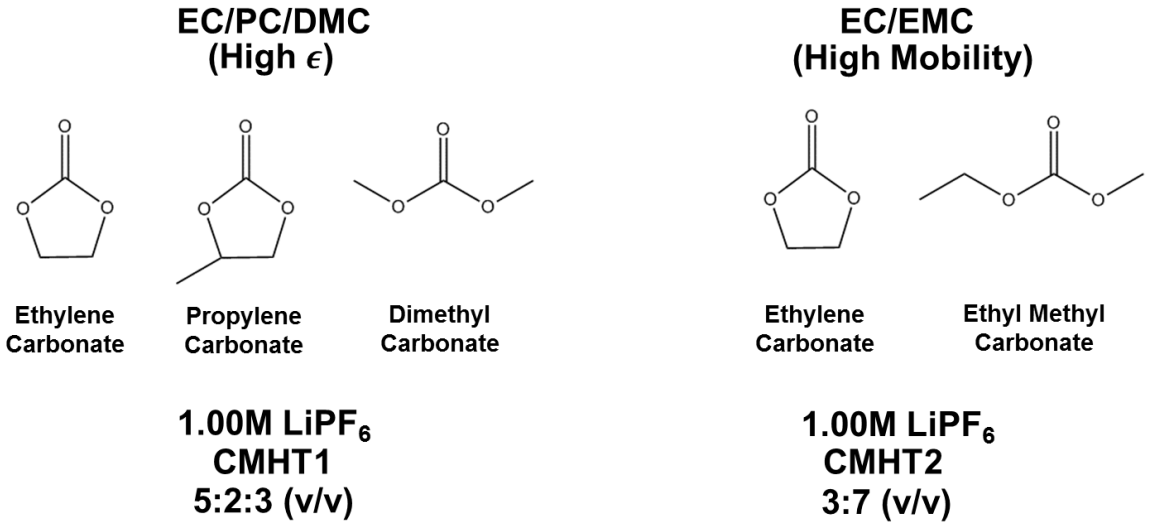

Figure 3.3 – Molecular structures of the component solvent molecules in the CMHT1 and CMHT2 electrolyte mixtures.

3.3.3 PFG-NMR Measurements

PFG-NMR measurements of both ^{7}Li and ^{19}F were made using a Bruker Avance 300WB NMR spectrometer with a Diff50 probe and an 8 mm ^{7}Li/^{19}F RF coil insert, using a bipolar-gradient, stimulated echo with Longitudinal Eddy current Delay (LED) pulse sequence. A total of 8 uniformly spaced gradient steps were used, with maximum gradients ranging up to $\pm 422.7\,\mathrm{G/cm}$ for ^{7}Li and to $\pm 147.6\,\mathrm{G/cm}$ for ^{19}F at the lowest temperatures, taking 8 scans per gradient. The $\pi/2$ excitation pulse was $11.25\,\mu\mathrm{s}$ for ^{7}Li and $36\,\mu\mathrm{s}$ for ^{19}F, both at 40 W. The diffusion time was $\Delta = 200\,\mathrm{ms}$, and the gradient pulse duration was $\delta = 4\,\mathrm{ms}$. A 5 ms LED period was employed prior to acquisition. Fits to the Stejskal-Tanner equation for signal attenuation due to diffusion,[59] with appropriate modifications for the bipolar gradients using SINE.100 gradient shapes,[60] were performed in TopSpin v3.2 based on integrated peak area. Temperature control was obtained using the

onboard BCU II chiller, calibrated with shift thermometer based on methanol according to standard protocols.

3.4 Results and Discussion

3.4.1 PFG-NMR + Conductivity Analysis for EC-Based Electrolytes

The first mixtures to be analyzed, CMHT1 and CMHT2, present a contrast in design trends for standard EC-based electrolytes, both at 1.00 M $LiPF_6$ concentration. The high proportion of cyclic carbonates in CMHT1 is intended to produce a high relative permittivity – leading to improved solvation – at the trade-off of increased solvent viscosity.[61] Conversely, CMHT2, with its low proportion of EC relative to the linear carbonate EMC, is a standard benchmark electrolyte with comparatively low viscosity.[55] The molecular models of the constituent solvent components are presented in **Figure 3.3**. The raw results of the conductivity, ^{7}Li PFG-NMR, and ^{19}F PFG-NMR experiments are presented in **Figure 3.4**. All three curves for both mixtures exhibit monotonic increase with temperature in approximately Arrhenius fashion. The measured cation diffusivity, D_+^*, is the smallest over the bulk of the temperature range, while the measured anion diffusivity, D_-^*, overtakes the charge diffusivity, D_κ, above 40℃ for CMHT1 and is always the largest of the diffusivities for CMHT2. For CMHT1, this overtaking is an indication of increasing ion pair formation with increasing temperature, which can be seen explicitly in **Figure 3.5**.

Here it is apparent that, while the effective anion diffusivity, D_-^{eff}, is always highest, the effective pair diffusivity, D_p^{eff}, indeed begins to exceed the effective cation

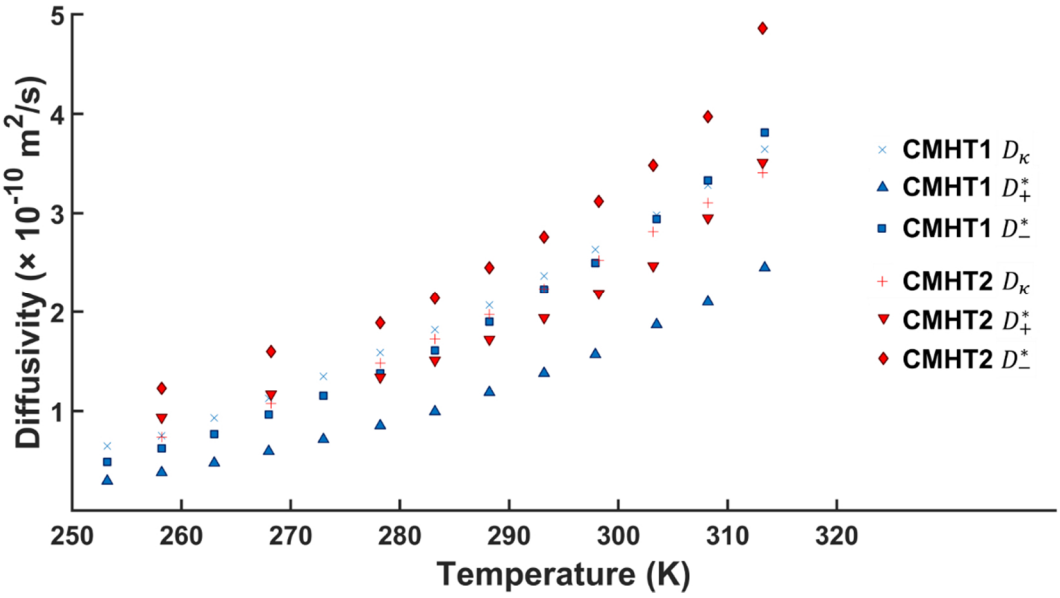

Figure 3.4 – Measured cation, anion, and charge diffusivities versus temperature, for the electrolyte mixtures CMHT1 (EC/PC/DMC) and CMHT2 (EC/EMC).

diffusivity, D_+^{eff}, at 40°C for CMHT1. On the other hand, CMHT2 exhibits a pairing diffusivity which is always larger than the effective cation diffusivity.

As discussed in section **3.2**, in solution, lithium cations are transported with a relatively large attendant solvation shell,[10,42] thus it is unsurprising that the effective anion diffusivity is always greater than that of the cation for these mixtures. This is because the PF_6^- anion molecules are much larger than the Li^+ cations, leading to greater charge delocalization (lower solvation), and are comparable in size to the solvent molecules, resulting in faster diffusion. As a consequence of these geometric factors, it is also possible for the anion to eject a solvent molecule from the Li solvation shell and replace it if the two ions are in sufficient vicinity of each other to interact, generating a contact pairing of the two oppositely-charged ions.[42] This transient pairing phenomenon produces

a type of "drag" on the ions, which has implications for the conductivity of the mixture if the ion pairing is significant.

The effective diffusivities in **Figure 3.5** are designed to be concentration-weighted, relative to the ionic and ion pair contributions to the mass transport, so the increase in D_p^{eff} with temperature signals an increase in the concentration of ion pairs, which, in turn, correlates with D_κ becoming smaller than D_-^* at the highest temperatures. This can be understood from the fact that the relative permittivity, $\epsilon(T)$, of a polar solvent decreases with increasing temperature, which is typically modelled quadratically as:

$$\epsilon(T) = \epsilon(0) + a_\epsilon T + b_\epsilon T^2, \tag{3.18}$$

with $|b_\epsilon| \ll |a_\epsilon|$, $a_\epsilon < 0$, $b_\epsilon < 0$, and $\epsilon(0) = \text{const}$ (to be clear, *not* the permittivity of free space, ϵ_0, as $\epsilon(T)$ is, in fact, defined relative to ϵ_0; *vide infra*).[62] The permittivity is

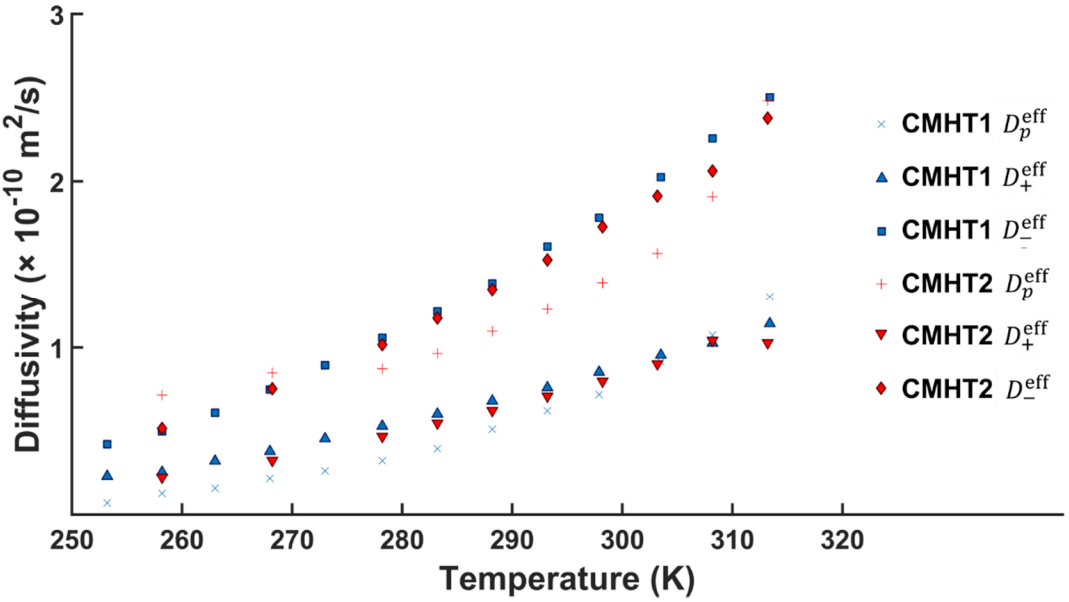

Figure 3.5 – Effective cation, anion and pair diffusivities versus temperature, for the electrolyte mixtures CMHT1 and CMHT2.

used to relate the polarization field, $\vec{\boldsymbol{P}}$, to the electric displacement $\vec{\boldsymbol{D}}$ imposed by the external voltage and the local electric field $\vec{\boldsymbol{E}}$:

$$\vec{\boldsymbol{D}} = \epsilon_0 \vec{\boldsymbol{E}} + \vec{\boldsymbol{P}} = \epsilon_0 \epsilon(T) \vec{\boldsymbol{E}}, \tag{3.19}$$

where ϵ_0 is the permittivity of free space. Clearly, if $\epsilon(T)$ decreases for fixed $\vec{\boldsymbol{D}}$, then the local electric field is less screened by the local polarization of the solvent, and nearby ions of opposite charge experience increased attractive force. This bolsters the ability of the anion to displace a solvent molecule in the Li^+ solvation shell according to the mechanism discussed above.

The effect of ion pairing is manifest in the experimentally obtained conductivities of the electrolyte mixtures. For CMHT1, the largest volume fraction of the solvent consists of the cyclic carbonates EC and PC, which have relatively large ϵ when compared with the linear carbonates DMC and EMC.[61] Following the analysis above, this mixture will therefore be less amenable to ion pairing relative to CMHT2 (since the individual ions are better screened by the solvent), for which the solvent mixture is majority-EMC. As mentioned above, the trade-off for including a higher proportion of high-ϵ solvent in the mixture is that it will tend to be more viscous, and possess a higher freezing point (unmixed EC freezes at ~ 35℃). As is clear in **Figure 3.4**, D_κ^* for CMHT2 is always smaller than that of CMHT1 at each temperature. This is borne out by the calculation of the pairing fractions, α_p, for the two mixtures from the effective diffusivities using equation (3.14).

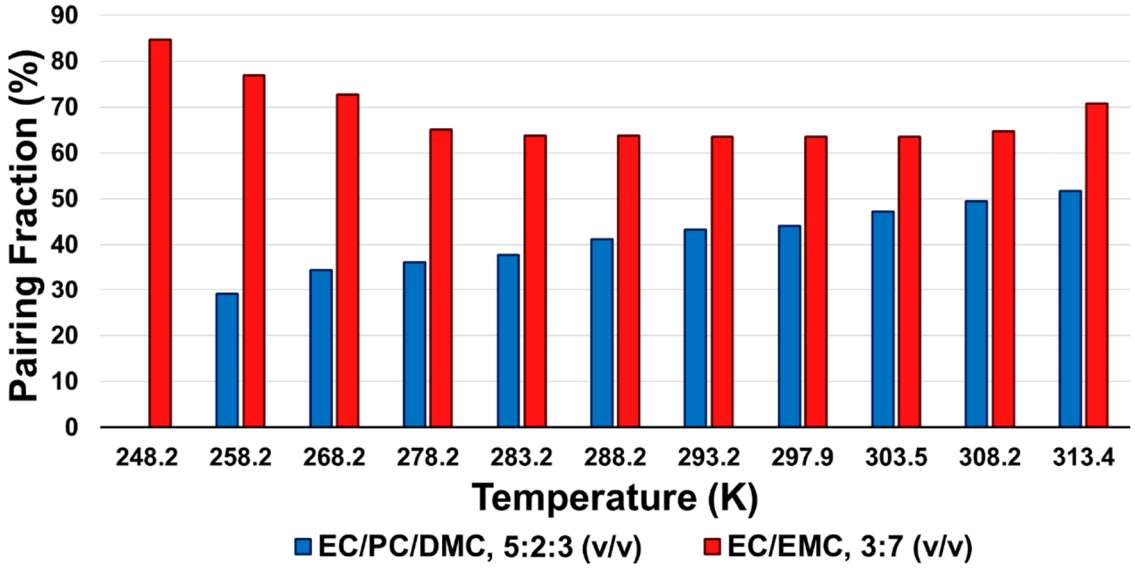

Figure 3.6 – Pairing fraction α_p over a series of temperatures for the mixtures CMHT1 and CMHT2.

As is demonstrated in **Figure 3.6**, the fraction of ions for CMHT2 which are correlated in electrically neutral pairs is consistently higher than for CMHT1 for all temperatures studied. The primary function of the partitioning of the measured diffusivities into effective diffusivities using equations (3.10-12) is to render it possible to determine the transference number for the cation from the data, which reflects the share of the cation in the overall ionic transport of the electrolyte, using equation (3.13) for t_+^0. This will exhibit the decreasing availability of Li cations as ion pairing becomes more competitive at elevated temperatures – as is borne out in **Figure 3.7** for the CMHT1 mixture – in contrast to the behaviour of the transport number, τ_+ from equation (3.3), which reflects the share of the cation in the overall mass transport of the system. The transport number will be enhanced with increasing temperature because higher temperatures lead to higher diffusivities, as in **Figure 3.4**. The observed linearity of both

t_+^0 and τ_+ for CMHT1 is due to the asymptotic behaviour of a ratio of two quadratic functions of T at large T, since both the numerator and denominator of equations (3.3) and (3.13) are quadratic in T (as is clear in **Figures 3.4** and **3.5**). Note that in typical reduced-order model formulations of electrochemical models which include temperature effects, the transference number is presumed temperature-independent.[1]

The curvature in the t_+^0 and τ_+ plots for CMHT2 is a result of the fact, from **Figure 3.6**, that there appears to be a minimum in α_p. While the simple physical picture described above can account for the gradually increasing ion pairing fractions of both CMHT1 and CMHT2 with temperature, the recurrence of high ion pairing in CMHT2 as the temperature decreases beyond the point where the α_p minimum lies is a more

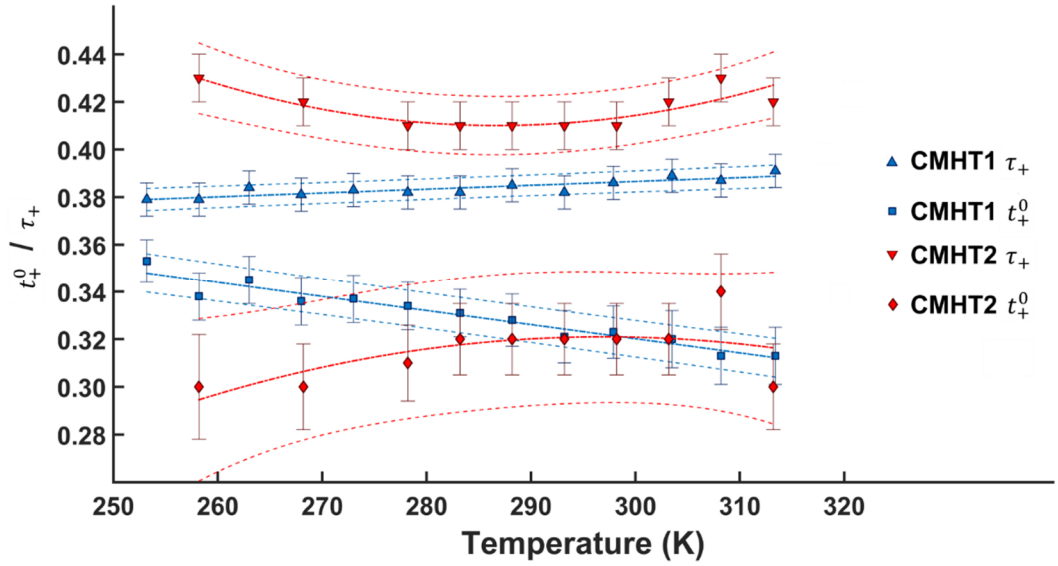

Figure 3.7 – Transference and transport numbers versus temperature for CMHT1 and CMHT2. Both compositions exhibit an increasing trend in τ_+ and a decreasing trend in t_+^0 towards the upper end of the temperature range, which has a straightforward interpretation in terms of increasing anion exchange with the cation solvent shell, which would be thermally activated. The diverging behaviour at temperatures below the α_p minimum for CMHT2 complicates the interpretation, however. Dashed lines constitute 95% confidence interval for the fits.

complicated matter. One metric that can provide some insight – albeit with some approximations for the current study which render it necessary to restrict the interpretations to a qualitative lens – is the Bjerrum critical distance, q_{ij}; essentially, the distance within which two ions, of opposite charge and type i and j, must approach in order to be considered as effectively being a contact pair:[61,63]

$$q_{ij} = \frac{|z_i z_j| e^2}{8\pi\epsilon_0\epsilon(T)k_B T}, \tag{3.20}$$

where z_i and z_j are the (signed or unsigned) charge numbers of the ions. The Bjerrum model is simplistic – that is, hard spheres in a dielectric continuum with a uniform permittivity[64] – but it can successfully capture the ion pairing phenomena under a variety of short-range interaction models,[65] and so is generally applicable as a leading order result in low-permittivity electrolytes. The fundamental role of the solvent in keeping attracted charges screened so that they can migrate under the influence of the electric potential is clear from the presence, again, of $\epsilon(T)$ in equation (3.20). However, returning to equation (3.18) for the phenomenological dependence of $\epsilon(T)$ on T, the presence of multiple powers of T in the denominator means that q_{ij} can have local extrema.

The Bjerrum critical distance can be approximately compared between CMHT1 and CMHT2 by estimating the temperature-dependence of $\epsilon(T)$ for the two solvent compositions. In the case of CMHT2, the temperature-dependence of $\epsilon(T)$ for the 3:7 (v/v) EC/EMC mixture has been directly measured experimentally with a simple cylindrical capacitor setup, along with $\epsilon(T)$ for the EC and PC components of the CMHT1 mixture:[62]

$$\epsilon_{\mathrm{EC/EMC,3:7}}(T) = 20.314 - 0.0736\text{℃}^{-1}T \tag{3.21}$$

$$\epsilon_{\mathrm{EC}}(T) = 105.79 - 0.4361\text{℃}^{-1}T + 4 \times 10^{-4}\text{℃}^{-2}T^2 \tag{3.22}$$

$$\epsilon_{\mathrm{PC}}(T) = 70.76 - 0.2642\text{℃}^{-1}T + 7.5 \times 10^{-4}\text{℃}^{-2}T^2 \tag{3.23}$$

Less information is available on the temperature-dependence of the relative permittivity of DMC in the literature, with values typically only for $25\text{℃} - 40\text{℃}$ which are approximately 3.1.[61,66] Thus, to approximately obtain the temperature-dependence of ϵ_{DMC}, the Kirkwood Theory of Dielectric Polarization of Polar Liquids can be utilized, from which:

$$\epsilon(T) - 1 = 6\pi \frac{N_A}{V_m}\left[\alpha_D + \frac{\mu_D^2}{3k_BT}(1 + z_D\langle\cos(\gamma_D)\rangle)\right], \tag{3.24}$$

where N_A is Avogadro's number, V_m is the partial molar volume, $\alpha_D = 7.7 \times 10^{-24}$ cm^{-3} is the molecular polarizability for DMC,[67] $\mu_D = 0.98D$ is the dipole moment for DMC,[68,69] z_D is the coordination number, and the term $\langle\cos(\gamma_D)\rangle$ denotes an angular average over all pairwise combinations of dipole moments in a given molecule's coordination sphere. Obviously, the latter two terms, z_D and $\langle\cos(\gamma_D)\rangle$, would require extensive molecular dynamics calculations to obtain, but they can be estimated from the scant ϵ_{DMC} data which is available using (3.24) in reverse, arriving at an estimate of $1 + z_D\langle\cos(\gamma_D)\rangle = -0.142$ for DMC from the available 25℃ ϵ measurements. Having retrieved or developed relationships between $\epsilon(T)$ and T for each of the three solvent components of CMHT1, the component polarizations $P_{D,i}$ are computed from the component permittivities:[62]

$$P_{D,i} = \frac{(\epsilon_i(T) - 1)(2\epsilon_i(T) + 1)}{9\epsilon_i(T)}, \tag{3.25}$$

and then the *mixture* permittivity can be approximated by using a partial-molar-volume-weighted version of equation (3.25):

$$\frac{(\epsilon_{\text{mix}}(T) - 1)(2\epsilon_{\text{mix}}(T) + 1)}{9\epsilon_{\text{mix}}(T)} = \frac{\sum_i x_i V_{m,i} P_{D,i}}{\sum_i x_i V_{m,i}}, \tag{3.26}$$

where the x_i are the mole fractions of each component, calculated, along with partial molar volumes, $V_{m,i}$, from the components' densities[67] and molecular masses (under the assumption of minimal density change over the target temperature range, which is not unreasonable[35]).

The results of the Bjerrum critical distance estimate for CMHT1 and CMHT2 are presented in **Figure 3.8**. Since this metric estimates the largest distance between an ion and its counter at which they can be considered a contact pair, the significantly smaller

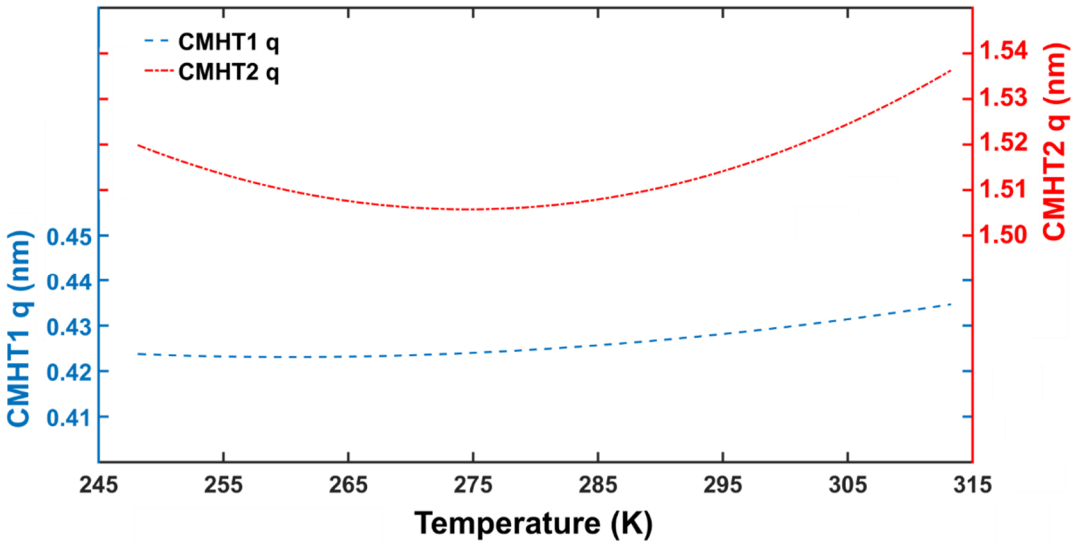

Figure 3.8 – The Bjerrum critical distance, q, estimated for the CMHT1 and CMHT2 mixtures. Note the difference in terms of overall magnitude, shape, and temperature at which the minimum occurs, comparing with **Figure 3.7**.

value for CMHT1 relative to CMHT2 already goes some way to explaining the very different magnitudes for the ion pairing fraction between the two in **Figure 3.6**. The approximately threefold larger critical distance for CMHT2 is largely a consequence of its approximately threefold smaller relative permittivity ($\epsilon_{\mathrm{CMHT2}}(298\ \mathrm{K}) = 18.5$, versus $\epsilon_{\mathrm{CMHT1}}(298\ \mathrm{K}) = 57.6$). The shapes of the two curves and the locations of the minima reflect how the temperature impacts the solvating capability of the mixture through the temperature-dependence of ϵ_{mix}. Evidently, the solvating capability of CMHT2 is optimum over a much narrower range of temperatures than CMHT1, which only approaches its (shallow) minimum near the bottom of the observed temperature range. This accounts for the difference in shape of the α_p temperature curves in **Figure 3.6**, and dramatically demonstrates the importance of optimizing the solvating capability of an

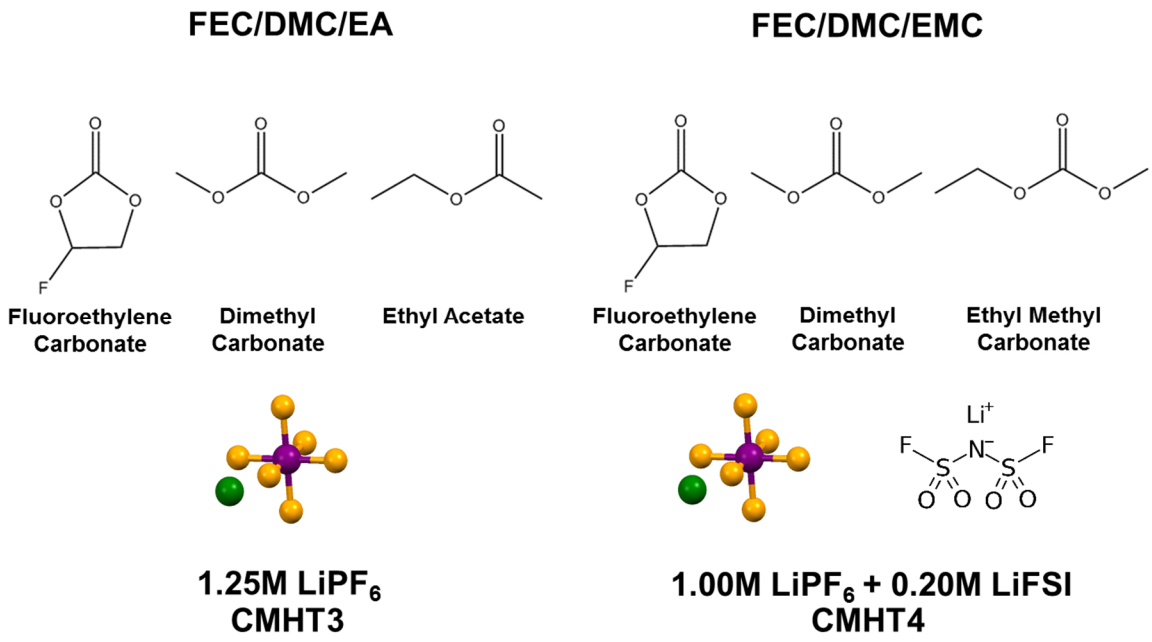

Figure 3.9 – Molecular structures of the component solvent and salt molecules in the CMHT3 and CMHT4 electrolyte mixtures.

electrolyte mixture for low-temperature applications – and, for that matter, of having a directly measurable metric like the ion pairing fraction for comparing "whole-electrolyte" results against solvent mixture properties like the relative permittivity and the viscosity.

3.4.2 The Influence of Fluorinated Ethylene Carbonate

The mixtures CMHT3 and CMHT4 involve the use of fluoroethylene carbonate (FEC), which has one of its hydrogen atoms replaced with an electron-withdrawing fluorine atom for enhanced oxidative stability against high-voltage cathodes, in place of the standard EC component (molecular structures for the components of CMHT3 and CMHT4 are illustrated in **Figure 3.9**). They also have higher salt concentrations than CMHT1 and CMHT2, since the conductivity maximum as a function of salt concentration naturally varies with solvent composition. The measured diffusivities for these mixtures are exhibited in **Figure 3.10**. The same trends are evident as for the EC-based mixtures,

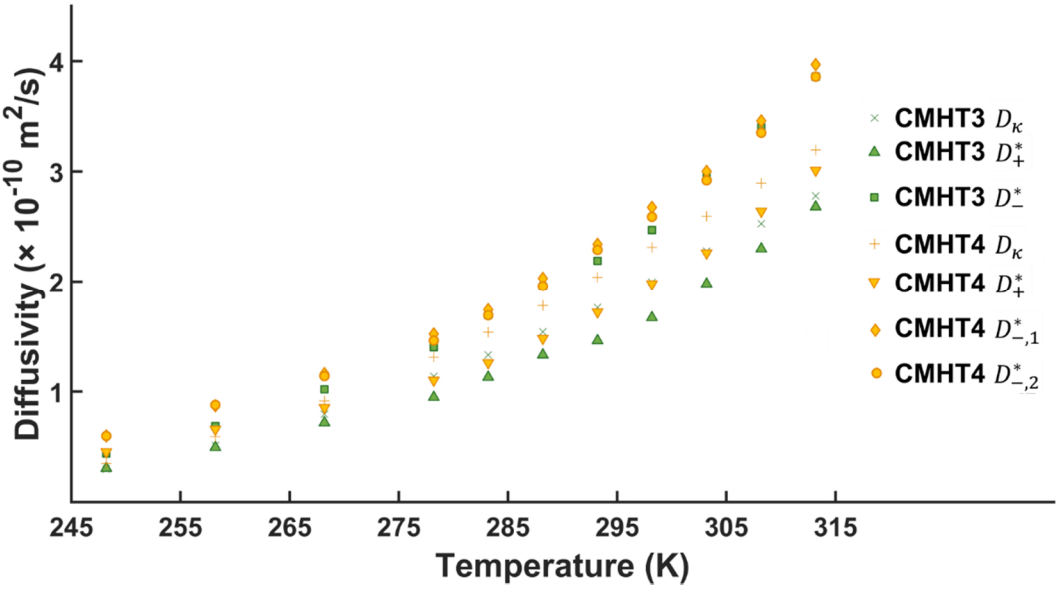

Figure 3.10 – Measured cation and anion diffusivities versus temperature, for electrolyte mixtures CMHT3 and CMHT4. Note the similarity in the magnitude of the diffusivities for both anions in CMHT4.

on comparing with **Figure 3.4**, in terms of both the general mathematical structure of the temperature dependences and the higher relative magnitudes of anionic versus cationic diffusivities (note that the conductivities are presented subsequently, in **Figure 3.12**). Comparison with the measured diffusivities of the EC-based mixtures also reveals that the magnitudes are quite similar, in spite of the increased concentrations of the FEC-based mixtures.

Additionally, the mixture CMHT4 contains two different types of anions: the usual PF_6^- and FSI^-, which demonstrate very similar measured diffusivities across the entire temperature range in **Figure 3.10**. This observation, coupled with the fact that the multicomponent transport number for this mixture was calculated to be identical to the transport number calculated by treating all anions as equivalent, well within uncertainty, justifies assimilating together both types of ion pairs which would result from a rigorous

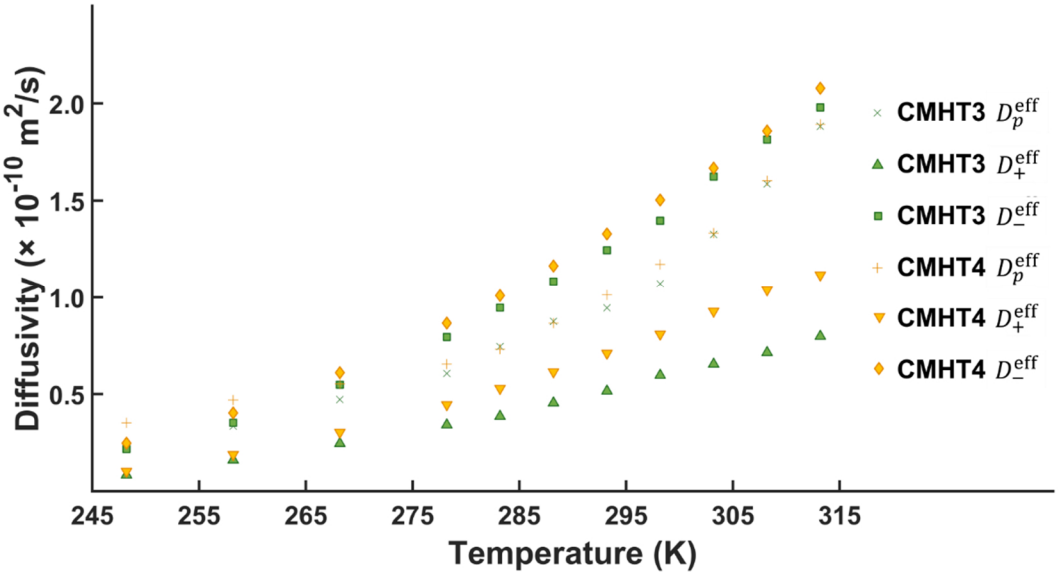

Figure 3.11 – Effective cation, anion and pair diffusivities versus temperature, for electrolyte mixtures CMHT3 and CMHT4.

analysis of the system. This interchangeability makes the application of the Stolwijk *et al.* method applied in section **3.4.1** tractable; a system with two different anions in solution with a common cation would otherwise require a conductivity, three diffusion coefficients, and two transference numbers for complete characterization under CST.[40] This would necessitate performing an additional experiment to fix the second transference number (the conductivity and the three diffusion coefficients obtained via the EIS, ^{7}Li PFG-NMR, and 2 × ^{19}F PFG-NMR measurements can only fix one additional degree of freedom).

In **Figure 3.11**, the temperature-dependences of the effective diffusivities for the FEC-containing mixtures are presented. Both CMHT3 and CMHT4 exhibit very similar effective pair diffusivities across the moderate- and high-temperature parts of the examined range, although at low temperatures, the effective pair diffusivity of the

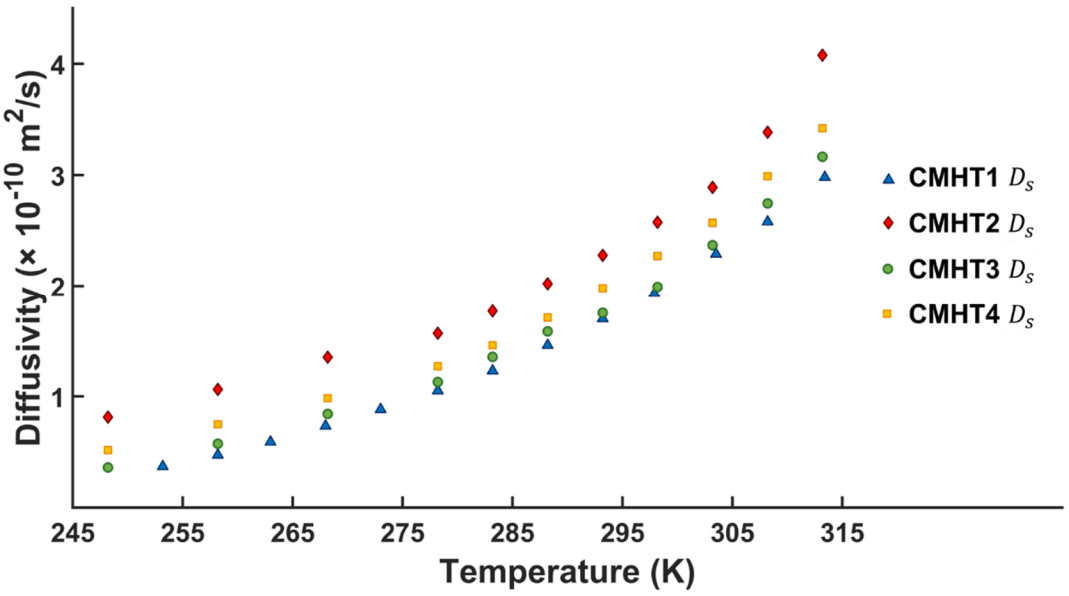

Figure 3.12 – Comparison of the temperature dependence of the salt diffusivity (*i.e.* the harmonic mean of the individual ionic diffusivities) amongst the four electrolyte mixtures.

CMHT4 mixture exceeds even the corresponding effective anion diffusivity (as discussed above, the effective diffusivities are concentration-weighted, and so reflect the relative concentrations of pairs versus isolated ions). This is similar to the behaviour of CMHT2 in **Figure 3.4**. However, the phenomenology is likely different, since FEC is a much larger constituent in CMHT3 than EC and FEC are for CMHT2 and CMHT4, respectively, and its relative permittivity is quite similar to that of EC.[70,71] While the relative reduction in screening in CMHT2, due to its lower EC content, is likely driving pair formation in that instance, the higher-by-volume FEC content in CMHT3 suggests that the high pair diffusivity is a result of the larger salt concentration (refer to **Table 3.1** for mixture compositions).

Comparison between all four electrolyte mixtures can be achieved on the basis of their conductivities, transport and transference numbers, and their salt diffusivities (the harmonic mean of individual ionic self-diffusivities). The latter are presented in **Figure 3.12**, demonstrating, as detailed in section **3.4.1**, how CMHT1 and CMHT2 represent the trade-off between high EC content (and hence, higher viscosity but better solvation) and high mobility through increased proportions of the linear carbonates. The PC fraction in CMHT1 enhances the effect of the EC, as it also possesses a moderately high dielectric constant, with concomitantly increased viscosity.[72] CMHT2 exhibits a consistently higher salt diffusivity at all temperatures relative to CMHT1, but the reverse is true of the conductivity, as can be observed in **Figure 3.13**. Intermediate between these two cases, in terms of salt diffusivity, are the FEC-based mixtures CMHT3 and CMHT4. This balance is achieved in spite of the fact that these mixtures have moderately higher salt

concentrations than CMHT1 and CMHT2. For the case of CMHT4, this is most likely a result of the relatively high proportion of linear carbonates (two-thirds of the total solvent volume) compensating for the increased salt concentration, but CMHT3 has a slightly higher salt diffusivity than CMHT1 at all temperatures, despite being 50% FEC by volume and more concentrated. This can be attributed to the influence of the 30% EA in the mixture, which has a lower viscosity and density than the linear carbonates,[61] allowing for greater still mobility. However, both FEC-based mixtures exhibit lower conductivities (particularly as temperature is decreased; refer to **Figure 3.13**), rendering the gains in mobility with increased salt concentration somewhat diminished, owing to the high ion pairing in these mixtures (**Figure 3.11**). FEC is noted as being less amenable to Li^+ solvation,[70,71] even though it possesses a dielectric constant which is comparable to EC.[72]

Plots of the transport and transference numbers for all four mixtures are also provided in **Figure 3.14** and **Figure 3.15**, respectively. The figures demonstrate that the behaviour of the CMHT3 and CMHT4 mixtures with decreasing temperature is more similar to CMHT2 – in terms of a maximum/minimum in t_+^0 versus τ_+ at moderate temperature – than CMHT1. The τ_+ values at each temperature are comparable for CMHT2-4 – albeit slightly smaller for the more FEC-rich CMHT3 mixture – and uniformly higher than CMHT1. Though it is a small margin, this does suggest higher participation of the Li^+ in the mass transport for CMHT2-4 than CMHT1, likely a consequence of the presumably lower viscosity of these mixtures than CMHT1, despite the higher salt concentrations of CMHT3 and CMHT4, since their proportions of cyclic

carbonates in the solvent are nevertheless lower than that of CMHT1. However, the transference number plots again reinforce that CMHT1 is the best performer at low temperature, purely on charge transport grounds (this can be seen in the conductivities of **Figure 3.13** also, although it is a smaller effect here). Interestingly, CMHT4 surpasses it from 10℃ and above, in terms of both κ and t_+^0. This, despite being only one third FEC by volume, and containing no EC. The τ_+ plots show that CMHT4 has comparable mobility to CMHT3 at all temperatures, but at moderate-to-high temperatures, CMHT4 evidently retains a much better proportion of unpaired charge carriers. The conductivity boost may stem from the extra salt concentration relative to CMHT1, with the added 0.2 M LiFSI perhaps not being as readily able to form an ion pair as $LiPF_6$. It would be interesting to comprehensively study the effect of this secondary salt with PFG-NMR, to determine the concentration range and/or proportion of the total salt concentration at

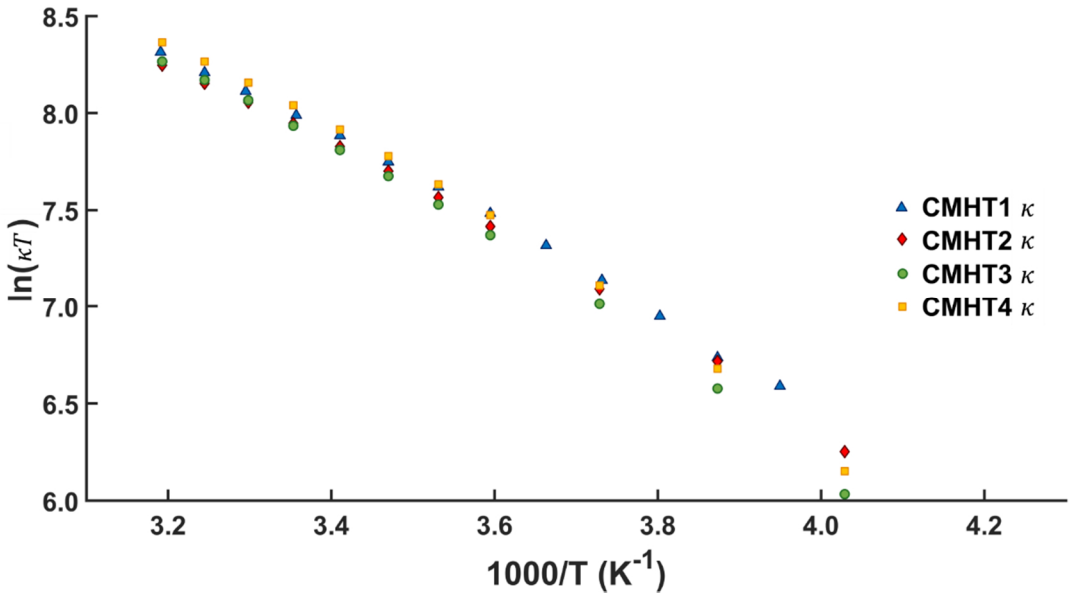

Figure 3.13 – Arrhenius plot of the measured conductivities of all four electrolyte mixtures across the range of examined temperatures.

which it does effectively act as a boost to the ion transport, and to also correlate with the ion pairing and diffusivity trends, since past work indicates that LiFSI will dissociate less than $LiPF_6$ in identical solvent mixtures, albeit at larger salt concentrations.[73]

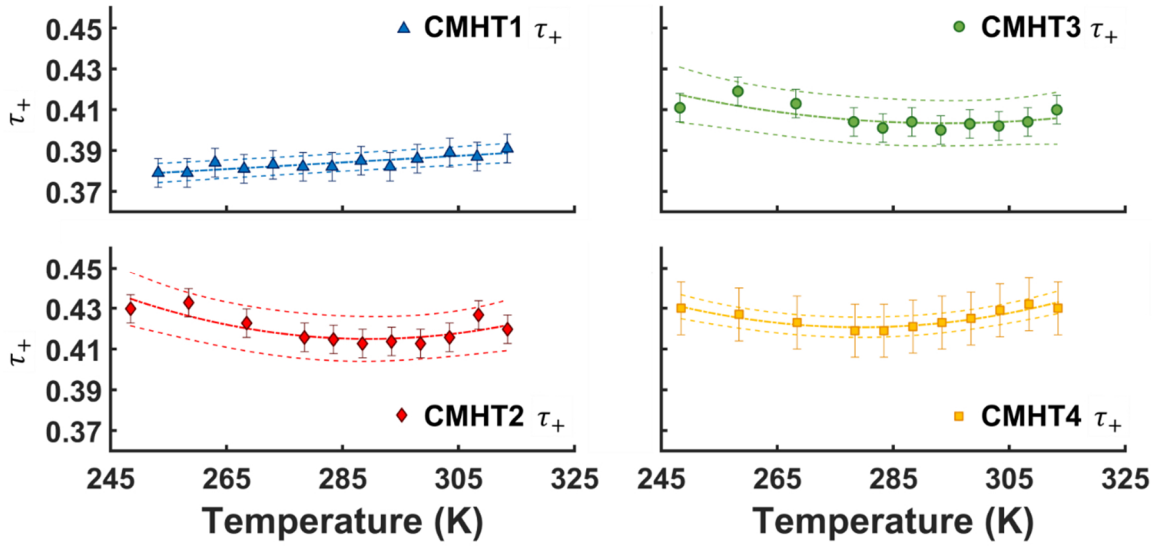

Figure 3.14 – The effect of temperature on transport number (share of the cation in overall mass transport) for all four electrolyte mixtures.

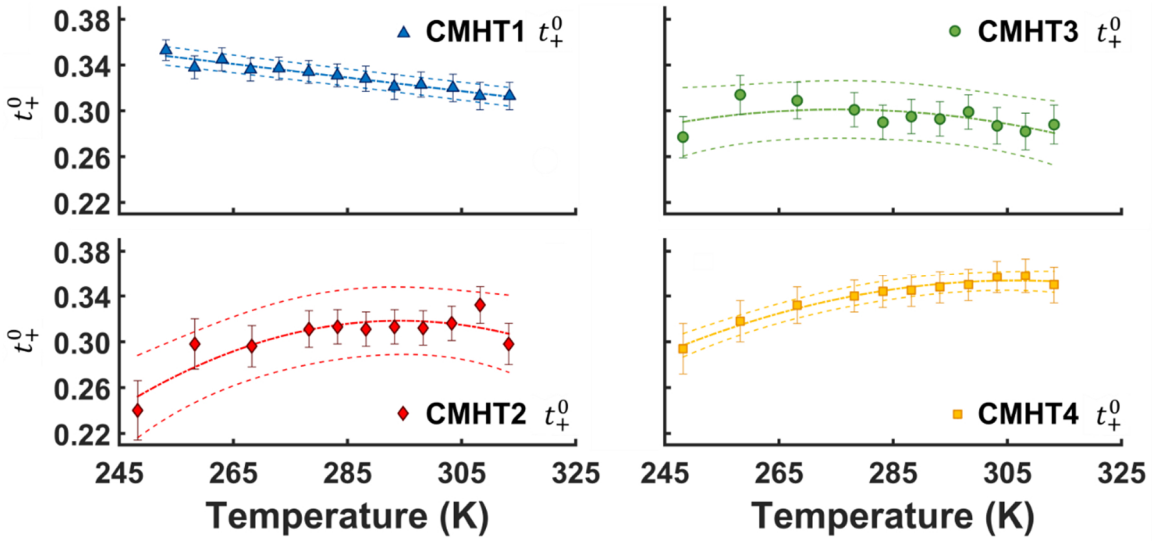

Figure 3.15 – The effect of temperature on transference number (share of the cation in overall charge transport) for all four electrolyte mixtures.

3.5 Summary and Conclusions

This chapter describes an extension of the combined PFG-NMR and EIS method for determining transference numbers and ion pairing fractions from measured self-diffusivities and ionic conductivities to solvent mixtures with compositions that vary significantly from standard benchmark electrolytes like LP30 (*i.e.* $1.00\ \mathrm{M}\ \mathrm{LiPF_6}$ in EC/DMC, 1:1 (v/v)). The better low-temperature performance of cyclic-carbonate-rich electrolyte relative to a high linear-carbonate-fraction electrolyte is analyzed through the lens of the calculated ion pairing fractions and the cationic transference number, and correlated with an estimate of the Bjerrum critical distance to demonstrate the scope of property tuning that could be undertaken purely on the basis of solvent properties – especially with an eye to specializing electrolyte design to low-temperature applications. The cyclic-carbonate-rich and linear-carbonate-rich standard EC-containing electrolytes are then contrasted with mixtures that replace EC with FEC, and also employ a higher salt concentration. One of these mixtures, for which this additional salt concentration beyond $1.00\ \mathrm{M}$ was supplied by LiFSI instead of $\mathrm{LiPF_6}$, was able to outperform the cyclic-carbonate-rich electrolyte at moderate-to-high temperature in terms of both ionic conductivity and transference number, although it exhibited a transference number maximum with temperature similar to the behaviour of the linear-carbonate-rich electrolyte, and at low temperature still underperforms the cyclic-carbonate-rich (and PC-containing) electrolyte mixture.

3.6 References

(1) Tanim, T. R.; Rahn, C. D.; Wang, C.-Y. A Temperature Dependent, Single Particle, Lithium Ion Cell Model Including Electrolyte Diffusion. *J. Dyn. Syst. Meas. Control* **2015**, *137* (1), 011005.

(2) Santhanagopalan, S.; Guo, Q.; Ramadass, P.; White, R. E. Review of Models for Predicting the Cycling Performance of Lithium Ion Batteries. *J. Power Sources* **2006**, *156* (2), 620–628.

(3) Seaman, A.; Dao, T. S.; McPhee, J. A Survey of Mathematics-Based Equivalent-Circuit and Electrochemical Battery Models for Hybrid and Electric Vehicle Simulation. *J. Power Sources* **2014**, *256*, 410–423.

(4) Ahmed, R.; El Sayed, M.; Arasaratnam, I.; Tjong, J.; Habibi, S. R. Reduced-Order Electrochemical Model Parameters Identification and SOC Estimation for Healthy and Aged Li-Ion Batteries Part I: Parameterization Model Development for Healthy Batteries. *IEEE J. Emerg. Sel. Top. Power Electron.* **2014**, *2* (3), 659–677.

(5) Plett, G. L. Extended Kalman Filtering for Battery Management Systems of LiPB-Based HEV Battery Packs - Part 1. Background. *J. Power Sources* **2004**, *134* (2), 252–261.

(6) Jiang, F.; Peng, P. Elucidating the Performance Limitations of Lithium-Ion Batteries Due to Species and Charge Transport through Five Characteristic Parameters. *Sci. Rep.* **2016**, *6* (June), 32639.

(7) Sethurajan, A. K.; Krachkovskiy, S. A.; Halalay, I. C.; Goward, G. R.; Protas, B. Accurate Characterization of Ion Transport Properties in Binary Symmetric Electrolytes Using In Situ NMR Imaging and Inverse Modeling. *J. Phys. Chem. B* **2015**, *119* (37), 12238–12248.

(8) Wilkening, M.; Heitjans, P. From Micro to Macro: Access to Long-Range Li+ Diffusion Parameters in Solids via Microscopic 6, 7Li Spin-Alignment Echo NMR Spectroscopy. *ChemPhysChem* **2012**, *13* (1), 53–65.

(9) Park, M.; Zhang, X.; Chung, M.; Less, G. B.; Sastry, A. M. A Review of Conduction Phenomena in Li-Ion Batteries. *J. Power Sources* **2010**, *195* (24),

7904–7929.

(10) Valøen, L. O.; Reimers, J. N. Transport Properties of LiPF[Sub 6]-Based Li-Ion Battery Electrolytes. *J. Electrochem. Soc.* **2005**, *152* (5), A882.

(11) Krachkovskiy, S. A.; Pauric, A. D.; Halalay, I. C.; Goward, G. R. Slice-Selective NMR Diffusion Measurements: A Robust and Reliable Tool for In Situ Characterization of Ion-Transport Properties in Lithium-Ion Battery Electrolytes. *J. Phys. Chem. Lett.* **2013**, *4* (22), 3940–3944.

(12) Xu, K. Electrolytes and Interphases in Li-Ion Batteries and Beyond. *Chem. Rev.* **2014**, *114* (23), 11503–11618.

(13) Doyle, M.; Fuller, T. F.; Newman, J. Modeling of Galvanostatic Charge and Discharge of the Lithium/Polymer/Insertion Cell. *J. Electrochem. Soc.* **1993**, *140* (6), 1526.

(14) Doyle, M.; Newman, J.; Gozdz, A. S.; Schmutz, C. N.; Tarascon, J.-M. Comparison of Modeling Predictions with Experimental Data from Plastic Lithium Ion Cells. *J. Electrochem. Soc.* **1996**, *143* (6), 1890.

(15) Plett, G. L. *Battery Management Systems, Volume I: Battery Modeling*; Artech House Publishers, 2015.

(16) Chaturvedi, N. A.; Klein, R.; Christensen, J.; Ahmed, J.; Kojic, A. Modeling, Estimation, and Control Challenges for Lithium-Ion Batteries. In *Proceedings of the 2010 American Control Conference*; IEEE, 2010; pp 1997–2002.

(17) Di Domenico, D.; Fiengo, G.; Stefanopoulou, A. Lithium-Ion Battery State of Charge Estimation with a Kalman Filter Based on a Electrochemical Model. *Control Appl. 2008. CCA 2008. IEEE Int. Conf.* **2008**, 702–707.

(18) Speltino, C.; Di Domenico, D.; Fiengo, G.; Stefanopoulou, A. Experimental Identification and Validation of an Electrochemical Model of a Lithium-Ion Battery. *Control Conf. (ECC), 2009 Eur.* **2009**, 1053–1058.

(19) Prada, E.; Di Domenico, D.; Creff, Y.; Bernard, J.; Sauvant-Moynot, V.; Huet, F. Simplified Electrochemical and Thermal Model of LiFePO4-Graphite Li-Ion Batteries for Fast Charge Applications. *J. Electrochem. Soc.* **2012**, *159* (9),

A1508–A1519.

(20) Li, S. E.; Wang, B.; Peng, H.; Hu, X. An Electrochemistry-Based Impedance Model for Lithium-Ion Batteries. *J. Power Sources* **2014**, *258*, 9–18.

(21) Capiglia, C.; Saito, Y.; Kageyama, H.; Mustarelli, P.; Iwamoto, T.; Tabuchi, T.; Tukamoto, H. 7Li and 19F Diffusion Coefficients and Thermal Properties of Non-Aqueous Electrolyte Solutions for Rechargeable Lithium Batteries. *J. Power Sources* **1999**, *81–82*, 859–862.

(22) Aihara, Y.; Bando, T.; Nakagawa, H.; Yoshida, H.; Hayamizu, K.; Akiba, E.; Price, W. S. Ion Transport Properties of Six Lithium Salts Dissolved in γ-Butyrolactone Studied by Self-Diffusion and Ionic Conductivity Measurements. *J. Electrochem. Soc.* **2004**, *151* (1), A119.

(23) Stolwijk, N. A.; Wiencierz, M.; Obeidi, S. Self-Diffusion versus Ion Conduction in Polymer Electrolytes: On the Occurrence of Pairs, Triplets, and Higher-Order Clusters. *Electrochim. Acta* **2007**, *53* (4), 1575–1583.

(24) Zhao, J.; Wang, L.; He, X.; Wan, C.; Jiang, C. Determination of Lithium-Ion Transference Numbers in LiPF6–PC Solutions Based on Electrochemical Polarization and NMR Measurements. *J. Electrochem. Soc.* **2008**, *155* (4), A292.

(25) Stolwijk, N. A.; Obeidi, S. Combined Analysis of Self-Diffusion, Conductivity, and Viscosity Data on Room Temperature Ionic Liquids. *Electrochim. Acta* **2009**, *54* (5), 1645–1653.

(26) Hayamizu, K. Temperature Dependence of Self-Diffusion Coefficients of Ions and Solvents in Ethylene Carbonate, Propylene Carbonate, and Diethyl Carbonate Single Solutions and Ethylene Carbonate + Diethyl Carbonate Binary Solutions of LiPF 6 Studied by NMR. *J. Chem. Eng. Data* **2012**, *57* (7), 2012–2017.

(27) Stolwijk, N. A.; Kösters, J.; Wiencierz, M.; Schönhoff, M. On the Extraction of Ion Association Data and Transference Numbers from Ionic Diffusivity and Conductivity Data in Polymer Electrolytes. *Electrochim. Acta* **2013**, *102*, 451–458.

(28) Krachkovskiy, S. A.; Bazak, J. D.; Fraser, S.; Halalay, I. C.; Goward, G. R. Determination of Mass Transfer Parameters and Ionic Association of LiPF 6 :

Organic Carbonates Solutions. *J. Electrochem. Soc.* **2017**, *164* (4), A912–A916.

(29) Feng, Z.; Higa, K.; Han, K. S.; Srinivasan, V. Evaluating Transport Properties and Ionic Dissociation of $LiPF_6$ in Concentrated Electrolyte. *J. Electrochem. Soc.* **2017**, *164* (12), A2434–A2440.

(30) Villaluenga, I.; Pesko, D. M.; Timachova, K.; Feng, Z.; Newman, J.; Srinivasan, V.; Balsara, N. P. Negative Stefan-Maxwell Diffusion Coefficients and Complete Electrochemical Transport Characterization of Homopolymer and Block Copolymer Electrolytes. *J. Electrochem. Soc.* **2018**, *165* (11), A2766–A2773.

(31) Hafezi, H.; Newman, J. Verification and Analysis of Transference Number Measurements by the Galvanostatic Polarization Method. *J. Electrochem. Soc.* **2000**, *147* (8), 3036.

(32) Zhou, J.; Danilov, D.; Notten, P. H. L. A Novel Method for the In Situ Determination of Concentration Gradients in the Electrolyte of Li-Ion Batteries. *Chem. - A Eur. J.* **2006**, *12* (27), 7125–7132.

(33) Nyman, A.; Behm, M.; Lindbergh, G. Electrochemical Characterisation and Modelling of the Mass Transport Phenomena in LiPF6-EC-EMC Electrolyte. *Electrochim. Acta* **2008**, *53* (22), 6356–6365.

(34) Zugmann, S.; Fleischmann, M.; Amereller, M.; Gschwind, R. M.; Wiemhöfer, H. D.; Gores, H. J. Measurement of Transference Numbers for Lithium Ion Electrolytes via Four Different Methods, a Comparative Study. *Electrochim. Acta* **2011**, *56* (11), 3926–3933.

(35) Lundgren, H.; Behm, M.; Lindbergh, G. Electrochemical Characterization and Temperature Dependency of Mass-Transport Properties of LiPF6 in EC:DEC. *J. Electrochem. Soc.* **2014**, *162* (3), A413–A420.

(36) Wohde, F.; Balabajew, M.; Roling, B. Li + Transference Numbers in Liquid Electrolytes Obtained by Very-Low-Frequency Impedance Spectroscopy at Variable Electrode Distances. *J. Electrochem. Soc.* **2016**, *163* (5), A714–A721.

(37) Ehrl, A.; Landesfeind, J.; Wall, W. A.; Gasteiger, H. A. Determination of Transport Parameters in Liquid Binary Lithium Ion Battery Electrolytes. *J.*

Electrochem. Soc. **2017**, *164* (4), A826–A836.

(38) Landesfeind, J.; Gasteiger, H. A. Temperature and Concentration Dependence of the Ionic Transport Properties of Lithium-Ion Battery Electrolytes. *J. Electrochem. Soc.* **2019**, *166* (14), A3079–A3097.

(39) Kühnel, R.-S.; Balducci, A. Lithium Ion Transport and Solvation in N -Butyl- N -Methylpyrrolidinium Bis(Trifluoromethanesulfonyl)Imide–Propylene Carbonate Mixtures. *J. Phys. Chem. C* **2014**, *118* (11), 5742–5748.

(40) Newman, J.; Thomas-Alyea, K. E. *Electrochemical Systems*, 3rd ed.; John Wiley & Sons, 2004.

(41) Vargas-Barbosa, N. M.; Roling, B. "Dynamic Ion Correlations in Solid and Liquid Electrolytes: How Do They Affect Charge and Mass Transport? *ChemElectroChem* **2019**, *13* (3), celc.201901627.

(42) Borodin, O.; Smith, G. D. Quantum Chemistry and Molecular Dynamics Simulation Study of Dimethyl Carbonate: Ethylene Carbonate Electrolytes Doped with LiPF 6. *J. Phys. Chem. B* **2009**, *113* (6), 1763–1776.

(43) Seo, D. M.; Borodin, O.; Han, S.-D.; Ly, Q.; Boyle, P. D.; Henderson, W. A. Electrolyte Solvation and Ionic Association. *J. Electrochem. Soc.* **2012**, *159* (5), A553–A565.

(44) Ong, M. T.; Verners, O.; Draeger, E. W.; van Duin, A. C. T.; Lordi, V.; Pask, J. E. Lithium Ion Solvation and Diffusion in Bulk Organic Electrolytes from First-Principles and Classical Reactive Molecular Dynamics. *J. Phys. Chem. B* **2015**, *119* (4), 1535–1545.

(45) Borodin, O.; Olguin, M.; Ganesh, P.; Kent, P. R. C.; Allen, J. L.; Henderson, W. A. Competitive Lithium Solvation of Linear and Cyclic Carbonates from Quantum Chemistry. *Phys. Chem. Chem. Phys.* **2016**, *18* (1), 164–175.

(46) Schmid, M. J.; Xu, J.; Lindner, J.; Novák, P.; Schuster, R. Concentration Effects on the Entropy of Electrochemical Lithium Deposition: Implications for Li + Solvation. *J. Phys. Chem. B* **2015**, *119* (42), 13385–13390.

(47) Zhang, S. .; Xu, K.; Allen, J. .; Jow, T. . Effect of Propylene Carbonate on the Low

Temperature Performance of Li-Ion Cells. *J. Power Sources* **2002**, *110* (1), 216–221.

(48) Zhang, S. .; Xu, K.; Jow, T. . A New Approach toward Improved Low Temperature Performance of Li-Ion Battery. *Electrochem. commun.* **2002**, *4* (11), 928–932.

(49) Hu, L.; Zhang, Z.; Amine, K. Fluorinated Electrolytes for Li-Ion Battery: An FEC-Based Electrolyte for High Voltage LiNi0.5Mn1.5O4/Graphite Couple. *Electrochem. commun.* **2013**, *35*, 76–79.

(50) Shkrob, I. A.; Wishart, J. F.; Abraham, D. P. What Makes Fluoroethylene Carbonate Different? *J. Phys. Chem. C* **2015**, *119* (27), 14954–14964.

(51) Xia, J.; Nie, M.; Burns, J. C.; Xiao, A.; Lamanna, W. M.; Dahn, J. R. Fluorinated Electrolyte for 4.5 V Li(Ni0.4Mn0.4Co0.2)O2/Graphite Li-Ion Cells. *J. Power Sources* **2016**, *307*, 340–350.

(52) Wang, L.; Ma, Y.; Qu, Y.; Cheng, X.; Zuo, P.; Du, C.; Gao, Y.; Yin, G. Influence of Fluoroethylene Carbonate as Co-Solvent on the High-Voltage Performance of LiNi1/3Co1/3Mn1/3O2 Cathode for Lithium-Ion Batteries. *Electrochim. Acta* **2016**, *191*, 8–15.

(53) He, M.; Su, C.-C.; Feng, Z.; Zeng, L.; Wu, T.; Bedzyk, M. J.; Fenter, P.; Wang, Y.; Zhang, Z. High Voltage LiNi 0.5 Mn 0.3 Co 0.2 O 2 /Graphite Cell Cycled at 4.6 V with a FEC/HFDEC-Based Electrolyte. *Adv. Energy Mater.* **2017**, *7* (15), 1700109.

(54) Rodrigues, M.-T. F.; Babu, G.; Gullapalli, H.; Kalaga, K.; Sayed, F. N.; Kato, K.; Joyner, J.; Ajayan, P. M. A Materials Perspective on Li-Ion Batteries at Extreme Temperatures. *Nat. Energy* **2017**, *2* (8), 17108.

(55) Glazier, S. L.; Downie, L. E.; Xia, J.; Louli, A. J.; Dahn, J. R. Effects of Fluorinated Carbonate Solvent Blends on High Voltage Parasitic Reactions in Lithium Ion Cells Using OCV Isothermal Microcalorimetry. *J. Electrochem. Soc.* **2016**, *163* (10), A2131–A2138.

(56) Brug, G. J.; van den Eeden, A. L. G.; Sluyters-Rehbach, M.; Sluyters, J. H. The

Analysis of Electrode Impedances Complicated by the Presence of a Constant Phase Element. *J. Electroanal. Chem. Interfacial Electrochem.* **1984**, *176* (1–2), 275–295.

(57) Newman, J. Resistance for Flow of Current to a Disk. *J. Electrochem. Soc.* **1966**, *113* (5), 501.

(58) Halalay, I. C. Versatile Cell for Complex Permittivity Measurements on Liquids. *Rev. Sci. Instrum.* **1999**, *70* (8), 3432–3434.

(59) Stejskal, E. O.; Tanner, J. E. Spin Diffusion Measurements: Spin Echoes in the Presence of a Time-Dependent Field Gradient. *J. Chem. Phys.* **1965**, *42* (1), 288–292.

(60) Sinnaeve, D. The Stejskal – Tanner Equation Generalized for Any Gradient Shape — An Overview of Most Pulse Sequences Measuring Free Diffusion. *Concepts Magn. Reson. Part A* **2012**, *40A* (2), 39–65.

(61) Xu, K. Nonaqueous Liquid Electrolytes for Lithium-Based Rechargeable Batteries. *Chem. Rev.* **2004**, *104* (10), 4303–4418.

(62) Hall, D. S.; Self, J.; Dahn, J. R. Dielectric Constants for Quantum Chemistry and Li-Ion Batteries: Solvent Blends of Ethylene Carbonate and Ethyl Methyl Carbonate. *J. Phys. Chem. C* **2015**, *119* (39), 22322–22330.

(63) Marcus, Y.; Hefter, G. Standard Partial Molar Volumes of Electrolytes and Ions in Nonaqueous Solvents. *Chem. Rev.* **2004**, *104* (7), 3405–3452.

(64) Byberg, J.; Jensen, S. J. K.; Kläning, U. K. Extension of the Bjerrum Theory of Ion Association. *Trans. Faraday Soc.* **1969**, *65*, 3023–3031.

(65) Justice, M.-C.; Justice, J.-C. Ionic Interactions in Solutions. I. The Association Concepts and the McMillan-Mayer Theory. *J. Solution Chem.* **1976**, *5* (8), 543–561.

(66) Rivas, M. A.; Pereira, S. M.; Banerji, N.; Iglesias, T. P. Permittivity and Density of Binary Systems of {dimethyl or Diethyl Carbonate}+n-Dodecane from K. *J. Chem. Thermodyn.* **2004**, *36* (3), 183–191.

(67) Haynes, W. M.; Lide, D. R.; Bruno, T. J. *CRC Handbook of Chemistry and*

Physics: A Ready-Reference Book of Chemical and Physical Data, 97th Editi.; CRC Press: Boca Raton, Florida, 2016; Vol. 10.

(68) Reddy, S. K.; Balasubramanian, S. Liquid Dimethyl Carbonate: A Quantum Chemical and Molecular Dynamics Study. *J. Phys. Chem. B* **2012**, *116* (51), 14892–14902.

(69) Lovas, F. J.; Plusquellic, D. F.; Widicus Weaver, S. L.; McGuire, B. A.; Blake, G. A. Organic Compounds in the C3H6O3 Family: Microwave Spectrum of Cis–Cis Dimethyl Carbonate. *J. Mol. Spectrosc.* **2010**, *264* (1), 10–18.

(70) Nanbu, N.; Takahashi, R.; Kobayashi, D.; Suzuki, K. Physicochemical Properties of Fluoroethylene Carbonate and Performance of Electric Double-Layer Capacitors at High Concentrations of Electrolyte. **2007**, *75*, 2007.

(71) Ohtake, M.; Takimoto, K.; Nanbu, N.; Takehara, M.; Ue, M.; Sasaki, Y. Physical Properties of Fluorinated Cyclic Carbonates for Secondary Lithium Batteries. *ECS Meet.* **2008**, *214* (2002), 2016.

(72) Ue, M.; Sasaki, Y.; Tanaka, Y.; Morita, M. Nonaqueous Electrolytes with Advances in Solvents. In *Modern Aspects of Electrochemistry*; 2014; Vol. 58, pp 93–165.

(73) Takekawa, T.; Kamiguchi, K.; Imai, H.; Hatano, M. Physicochemical and Electrochemical Properties of the Organic Solvent Electrolyte with Lithium Bis(Fluorosulfonyl)Imide (LiFSI) As Lithium-Ion Conducting Salt for Lithium-Ion Batteries. *ECS Trans.* **2015**, *64* (24), 11–16.

Chapter 4 – Multi-Temperature *In Situ* Magnetic Resonance Imaging of Polarization and Salt Precipitation in Lithium-Ion Battery Electrolytes

4.1 Outline and Context in the Thesis

This chapter presents the initial exploration of extending the *in situ* Magnetic Resonance Imaging (MRI) technique developed in the Goward group at McMaster, published in Krachkovskiy *et al., J. Am. Chem. Soc.*, **2016**, *138(25)* (to which the author was also a contributor), to a variable-temperature operational regime. Since comparisons were to be made across different cells under different conditions, it was important to also develop a means of image calibration, to compensate for the known artifacts associated with MR imaging in the presence of conducting surfaces. A surprising outcome of this investigation was that salt precipitation from a common benchmark battery electrolyte at relatively modest low-temperature conditions clearly exhibited salt precipitation, which was detected *in situ* during the imaging process. This observation has ramifications both for design of electrolytes intended for low-temperature applications, and for long-term state-of-health monitoring of lithium-ion batteries. The study then proceeds to measure the extent of the electrolyte concentration polarization increase with decreasing temperature in an electrolyte specifically designed for low-temperature performance, and then quantitatively connects the observations to the model by demonstrating that, at least to lowest-order in the linear region at the centre of the cell, the measured *in situ* concentration

gradients match the model predictions. It was also verified that this prediction was independent of the inter-electrode spacing, which is important because the magnitudes of the inter-electrode spacing used in these experiments is significantly larger than would be desirable in a commercial cell.

All of the work conducted for this chapter was performed at McMaster University, under the supervision of Prof. Gillian R. Goward. The *in situ* cell design and prototyping was performed by Dr. Sergey A. Krachkovskiy, with Dr. Krachkovskiy also being instrumental in training the author on the MRI techniques necessary for the work in this chapter, and implementing them on the spectrometer. The experiments were all conducted by the author, as was all of the analysis, with the notable exception for the latter that the SPRITE image calibration concept was suggested to the author by Dr. Krachkovskiy. The work was published in *Journal of Physical Chemistry C*, with authorship of J. David Bazak, S. A. Krachkovskiy, and G. R. Goward (*J. Phys. Chem. C.*, **2017**, *121(38)*, 20704-20713).

4.2 Introduction and Context in the Field

Lithium-ion batteries have become a mainstay in energy storage for modern electronic devices, and are of increasing importance as part of the burgeoning quest for sustainable energy resources and transportation, both to avert catastrophic climate change and to mitigate the looming problem of dwindling fossil fuel reserves. Central challenges in the widespread deployment of lithium ion batteries in automotive applications are the state of charge (SOC) and state of health (SOH) estimation problems, which both require elaborate electrochemical modelling approaches.[1] In particular, mass transport in the electrolyte has been found to contribute substantially to the overall polarization of a cell

undergoing drive cycle simulation,[2] and at high rates and low temperatures, gradients in the electrolyte concentration must be properly taken into account through the modelling process.[3,4] The microscopic models necessitated by the electrolytes used in lithium-ion battery systems, which derive from concentrated solution theory,[5] contain many free parameters. In order to obtain an accurate description of the dynamics in the battery system, it is therefore necessary to directly assign a large subset of these parameters and determine how they behave over a range of operational regimes.

Recent years have seen a rapid development of *in situ* techniques deployed to study a range of phenomena in operating mimics of energy storage devices.[6] At the forefront of this development are imaging/microscopy techniques, which enable visualization of the dynamics occurring during operation. Raman microscopy has been utilized to observe electrolyte processes in lithium-ion battery mimics,[7,8] and magnetic resonance imaging (MRI) has been applied to a number of electrochemical systems, such as lithium-ion batteries under polarization,[9–17] fuel cells,[18,19] metal-air battery electrolytes,[20] and double-layer capacitors.[21] A number of these MRI studies on lithium-ion battery systems have focused on lithiation and deposition processes associated with the electrodes,[10,12,16,17] but MRI has primarily been leveraged to study transport in the electrolyte domain, which is governed by the salt diffusivity (D_s), cationic transference number (t_+^0), and ionic conductivity (κ) parameters. While a range of conventional electrochemical methods can characterize the required parameters,[22–26] along with less common approaches such as UV/vis absorption,[27] the chief advantage of *in situ* MRI for these measurements is the capability for directly capturing the spatial variation of the obtained data across the

electrolyte domain during polarization, along with gradients in the salt concentration, as opposed to furnishing bulk values averaged across the entire cell.

One of the primary difficulties of applying MRI in a quantitative fashion to *in situ* battery mimics is the presence of conductive components – the current collectors and electrodes – which generate distortions in both the longitudinal, polarizing and transverse, excitation magnetic fields (B_0 and B_1 respectively).[28,29] As a result of these distortions, frequency-encoding MRI techniques, which are often utilized in this type of experiment because of their short total acquisition times, exhibit non-uniform initial concentration profiles[9] and 'dead-space' near the metallic electrodes, where the signal is strongly suppressed.[13] Pure phase-encoding MRI techniques provide a means of circumventing this issue for *in situ* cell designs. Rather than permitting frequency distortions from field inhomogeneity to accrue while the free-induction decay (FID) is acquired with a read-out gradient, spatial information is encoded with incremented gradients for a fixed, brief phase-encode period.[30,31] However, in spite of the additional time required by the higher number of gradient steps, the total acquisition time for pure phase-encoding techniques is competitive with frequency-encoding techniques in practical samples, because acceptable signal-to-noise can be achieved with only a small number of scans relative to frequency-encoding techniques. One of the simplest pure phase-encoding techniques is Chemical Shift Imaging (CSI), which avoids the blurring associated with spins resonating at different frequencies localizing to different pixels,[32] and can be readily coupled with a shift- or slice-selective excitation pulse. In the absence of selective excitation, there will inevitably be 'folded-in' signal from electrolyte behind the electrodes if a flooded *in situ* cell design is

employed. CSI can also be used, in principle, to provide information about the spatial distribution of different species across the active volume.[21]

A complication arises with the computation of the field of view (FOV) with this technique if the shaped gradient pulses are non-ideal and there are extremely fast-relaxing regions of the sample: an imaging method which uses robustly stabilized gradients for phase-encoding, and is simultaneously inert to inhomogeneity from the conductive components, is required to accurately calibrate the CSI FOV. Additionally, a known issue with CSI is that signal acquisition begins quite shortly after the application of the large phase-encoding gradient pulses, so there are also residual eddy currents from the probe itself which can disrupt the first few points of the FID, leading to potential spectral distortion.[33] The Double-Half K-space (DHK) Single-Point Ramped Imaging with T_1 Enhancement (SPRITE)[34] technique combines ramped gradients with single-point, low-tip-angle imaging to capture features near metallic surfaces,[28,29] and can therefore readily perform this function. This approach also avoids the residual eddy current problem. There is a trade-off between these two methods, though: since DHK-SPRITE is a low-tip-angle, single-point imaging technique, the signal-to-noise ratio is poorer than CSI. Many scans are therefore required to achieve clear data, rendering it suitable solely for acquiring baseline and steady-state images, while relatively smooth CS images can be acquired quickly enough to capture the transient behavior of the concentration gradient building up to the steady-state. On the other hand, the robustness of DHK-SPRITE against inhomogeneity variations and field distortions near the electrodes provides a means of accurately measuring the cell, and capturing the dead-space near the electrodes which

impacts CSI. Nevertheless, it is important to note that the dead-space exhibited in frequency-encoding *in situ* MRI experiments[9,13,35] is an order of magnitude larger than what has been found for phase-encoding approaches such as CSI;[14] edge effects of 1.5-2.0 mm are found in the former case, which are comparable in size to the entire axial dimension of the active volume in the latter.

The partial-differential equation (PDE) of mass transport in the electrolyte domain of conventional electrochemical models is typically derived from material balance of the salt species dissolved in the solvent in the dilute-solution limit, under the assumption of unidimensional transport between the surfaces of the electrodes and a binary salt, yielding the Nernst-Planck equation:[36–38]

$$\frac{\partial c(x,t)}{\partial t} = \frac{\partial}{\partial x}\left[D\frac{\partial c(x,t)}{\partial x} + \frac{(1-t_+^0)}{FA}I\right], \tag{4.1}$$

where $c(x,t)$ is the salt concentration at position $x \in (0,L)$ and time $t \in \mathbb{R}^+$, L is the inter-electrode spacing, A is the electrode surface area, I is the applied current, and F is Faraday's constant. A so-called 'effective diffusivity' is often assumed, which phenomenologically incorporates both the tortuosity and porosity of the separator material. This PDE is well-posed provided there is an initial condition on the concentration profile,

$$c(x,0) = c_0(x) \tag{4.2}$$

(assumed to be uniform) and there are boundary conditions on the flux at the electrode surfaces, defined by the expression in the square brackets of (4.1):

$$\left.\frac{\partial c}{\partial x}\right|_{x=0,L} = -\frac{(1-t_+^0)}{DFA}I, \qquad \forall t \in \mathbb{R}^+, \tag{4.3}$$

which specify that the cation flux at the electrodes equals the exchange current density and the anion flux there is zero. It can readily be shown that Eqn. (4.1) has a steady-state solution provided that

$$\frac{\partial c(x,t)}{\partial x} = -\frac{(1-t_+^0)}{DFA} I, \qquad \forall x \in (0,L), \tag{4.4}$$

corresponding to migration flux of the anions to the negative electrode and the cations to the positive electrode (on discharging) being compensated by the diffusion flux of both ion species against the concentration gradient between the electrodes, as depicted schematically in **Figure 4.1**.

This gradient forms because of a mismatch in the timescales of insertion/ejection kinetics at the electrodes and charge transport between the electrodes; as cations are ejected from the negative electrode and the local concentration increases, anions are drawn towards

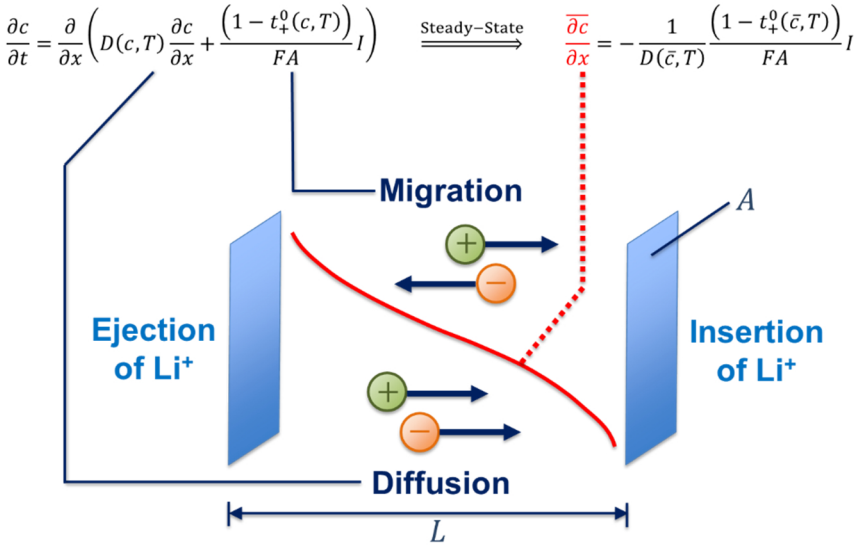

Figure 4.1 – Schematic illustration of the tension between migration fluxes (along the electric potential gradient in opposite directions for each ion) and diffusive fluxes (against the concentration gradient for both ions) which ultimately generate a steady-state concentration gradient under constant-current operation of a cell.

it to maintain local electroneutrality, building up the overall salt concentration nearby. The mirror-image process occurs at the positive electrode, resulting in a strong polarization in salt concentration across the inter-electrode spacing. Consequently, the steepness of this gradient is a function of the ratio in Eqn. (4.4): with increasing applied current (i.e. faster ejection/insertion) for a given D and t_+^0, the larger the polarization. An important corollary of Eqn. (4.4) is that the inter-electrode spacing L is not a relevant length-scale in determining the magnitude of the steady-state concentration gradient in this simplified system, which establishes the relevance of these *in situ* experiments using battery mimics to real battery systems, wherein the inter-electrode spacing is much reduced relative to practical *in situ* cells.

The mass-transport PDE of Eqn. (4.1) and attendant boundary conditions (4.2-4.3) represent a considerable simplification of the concentrated solution theory mass-transport governing equations, based on the Maxwell-Stefan equation. First, local electroneutrality is imposed; $c_+(x,t) = c_-(x,t) \equiv c(x,t)$, which implies that D corresponds to the salt-diffusion coefficient, D_s, defined as the harmonic mean of the individual ion diffusion coefficients with the solvent as the stationary reference frame.[13,39] Second, the mass-transport parameters D and t_+^0 are assumed to be independent of concentration. Third, the system is tacitly assumed to be in thermal equilibrium with a large heat reservoir, so these parameters have no explicit temperature-dependence. The first assumption has been previously found by *in situ* MRI to be a valid one.[14] The second assumption can be readily relaxed by reintroducing concentration-dependence to the mass-transport parameters, $D(c)$ and $t_+^0(c)$, without appealing to a specific analytical form mandated by a treatment with

concentrated solution theory (which introduces considerable complexity and additional, difficult-to-measure transport parameters into the model equations).[13] In this work, the third assumption will also be relaxed, and the temperature-dependence of the concentration gradient under polarization will be investigated, in which case $D(c,T)$ and $t_+^0(c,T)$ necessarily become functions of the cell temperature, T. This will influence the steepness of the steady-state concentration gradient in Eqn. (4.4) at a given level of applied current, and as will be shown, can breach the solubility point of the salt in the electrolyte in operational regimes where there is simultaneous large polarization and low temperature.

The sequence of results presented in this work begins with the demonstration of this salt precipitation phenomenon in a standard 1.00 M $LiPF_6$ electrolyte formulation with an equal parts (v/v) ethylene carbonate (EC) and diethylene carbonate (DEC) solvent mixture using ^{19}F *in situ* MRI to probe the PF_6^- anion. There are three routes around this problem: 1) decreasing the inter-electrode distance to lower the absolute concentration of the salt at the concentrated edge of the polarized electrolyte domain at the same level of applied current (a remedy specific to the experimental design); 2) lowering the initial salt concentration, to commensurately decrease the extent of the concentration polarization, again at the same current level; and 3) employing an electrolyte formulation with improved low-temperature solvation characteristics. The first route was investigated, but the extent of electrode-spacing decrease which was feasible – given the constraints that the presence of the conductive cell components impose on the imaging process – was insufficient to alleviate the salt precipitation (and owing to the fact that it is a design-specific remedy, is not presented here). For the second approach, polarization of a 0.85 M formulation of the

EC/DEC mixture was successfully imaged at the three selected temperatures (corresponding to 'low', 'room', and 'elevated' temperature regimes), with salt precipitation not occurring in the low temperature experimental condition, unlike with the 1.00 M formulation. Previous *ex situ* diffusion and conductivity measurements[40] have suggested that tuning the fraction of the solvent mixture with high dielectric coefficient could enhance the low temperature solvation of standard 1.00 M electrolyte mixtures. To this end, the third route was investigated with an electrolyte mixture consisting of 1.00 M $LiPF_6$ in EC, propylene carbonate (PC), and dimethyl carbonate (DMC), 5:2:3 (v/v). EC and PC both possess relatively large dielectric constants, amongst typical lithium-ion battery electrolyte solvents, while the role of the DMC is to lower the viscosity.[41] Inclusion of a PC fraction of up to 30% can be a successful strategy for ameliorating EC crystallization in low-temperature electrolytes, while balancing the destructive effect of PC on carbonaceous electrodes due to co-insertion.[42] This formulation was also used to quantitatively test the hypothesis, stemming from Eqn. (4.4), that the steady-state concentration gradient is independent of the inter-electrode spacing (to lowest order in an expansion about the centre of the cell) when the second assumption discussed above is relaxed.

4.3 Experimental

The design of the *in situ* cell used in these studies has been previously published.[14] It consists of a polyether ether ketone (PEEK) rod with drilled openings on either side for machined copper current collectors, PEEK HPLC Super Flangeless™ HPLC fittings (ferrules), and PEEK sealing nuts, with metallic lithium adhered to one of the copper

current collectors to serve as the negative electrode, and graphite-cast copper foil (MTI, $60\ \mathrm{g \cdot m^{-2}}$ active material loading) overlaid with a polypropylene separator (Targray) for the other. Two variants were constructed, with the depth of the drill bore into the PEEK rod used to shape the active volume slightly shorter along the vertical axis of the cylinder in one of the variants. In both cases, the diameter of the electrode surface interface with the active volume is approximately $4.2\ \mathrm{mm}$. A diagram of the *in situ* cell is provided in **Figure 4.2**, along with a photograph of the cell sitting in the RF insert and sample output MR images. The size of the active volume was measured under static conditions via MRI, and is reported in conjunction with each result, as the means of measurement differed between experiments. The $1.00\ \mathrm{M\ LiPF_6}$ in EC/DEC, 1:1 (v/v) electrolyte mixture was prepared by Novolyte, while the $0.85\ \mathrm{M}$ variant and the $1.00\ \mathrm{M\ LiPF_6}$ in EC/PC/DMC, 5:2:3 (v/v) mixtures were prepared in-house using 98% EC, 99% DEC, 99+% DMC, and 99.7% PC (all Sigma Aldrich). Cells were assembled, and pre-conditioned to form solid-electrolyte interphase (SEI), under inert atmosphere in an argon-filled glovebox (MBraun; $< 0.1\ \mathrm{ppm\ H_2O}, < 10\ \mathrm{ppm\ O_2}$). The pre-conditioning step, performed with an Arbin BT2000 multi-channel cycler, was necessary to allow gas evolved during the SEI formation to be released prior to performing MRI, and avoid the possibility of bubbles distorting the upper edge of image. Cells for which the EC/PC/DMC mixture was used had an initial pre-conditioning step with the Novolyte electrolyte to form the SEI without the possibility of PC co-insertion into the graphite electrode. In all cases, pre-conditioning consisted of charging the graphite from the Li metal electrode at a current density of $3.6\ \mathrm{A \cdot m^{-2}}$ (corresponding to $\sim C/6$, referenced to a graphite electrode with the active-material loading

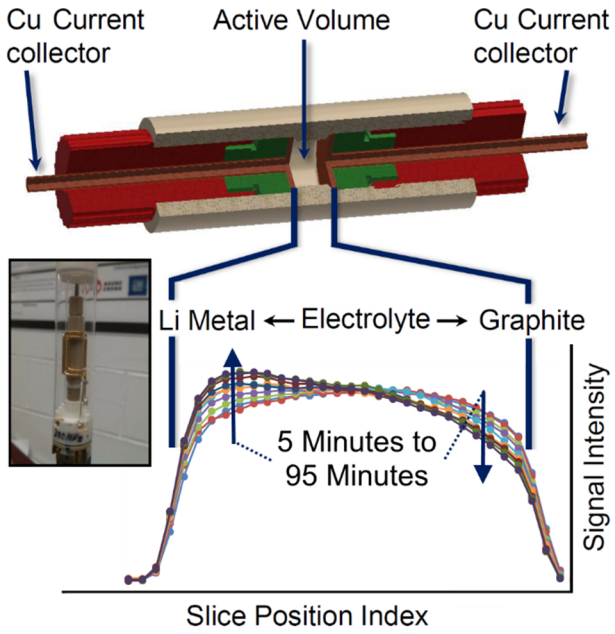

Figure 4.2 – A schematic overview of the *in situ* cell used to polarize the electrolyte under applied current (inset: photograph of the *in situ* cell sitting in the RF insert). The cell consists of an active volume containing the electrolyte bored from a PEEK rod (tan colour), encapsulated by Li metal and Cu foil-mounted graphite electrodes seated on Cu current collectors and sealed with PEEK ferrules (green) and PEEK nuts (red). ^{19}F CS images taken at regular intervals visualize the formation of the steady-state concentration gradient of PF_6^- anions (and by electroneutrality, Li^+ cations) across the inter-electrode spacing.

stated above) for 2 hours, discharging at the same current density until 0.3 V, and charging again at $7.2\ A \cdot m^{-2}$ $(\sim C/3)$ for one additional hour, with 20 minute rests interspersed between each of the current reversals.

During *in situ* imaging, constant currents at the $7.2\ A \cdot m^{-2}$ level were supplied by an Autolab PGStat 30 potentiostat to polarize the cells, with the lithium electrode positioned at the bottom of the cell and the graphite at the top and the current direction assigned such that the graphite was charged from the metallic lithium. The connections were made with grounded, shielded coaxial cables, and a home-made LC low-pass filter with 2.3 MHz cutoff was placed in the circuit to minimize noise pick-up by the

spectrometer. All MRI was performed using a Bruker Avance 300 MHz wide-bore spectrometer, with a Diff50 gradient probe and a dual-tuned 8 mm $^{7}\mathrm{Li}/^{19}\mathrm{F}$ RF insert. The *in situ* cell was positioned vertically in the probe such that the B_0 field was normal to the surface of the electrodes and the B_1 field was parallel to them, to ensure optimal penetration of the electrolyte-filled active volume. Temperature control was achieved indirectly via the water cooling unit for the gradient coil, because the design of the *in situ* cell blocked the chiller gas nozzle for the onboard temperature control unit of the spectrometer. As a result, the target temperatures of 10℃, 25℃, and 40℃ (corresponding to 'low', 'room', and 'elevated' temperature regimes) were not completely realized inside the RF insert. The thermocouple inside the probe gave temperature readings of approximately 12.8℃, 24.3℃, and 36.7℃, respectively, with maximum fluctuations of up to 0.5℃ about these mean values observed. Since this study aims for proof-of-concept results, the nominal target temperatures are used as stand-ins for the actual measured temperatures. More robust temperature control will be the subject of a future *in situ* cell redesign.

^{19}F CSI images were acquired with 32 equally-spaced gradient steps from $-18.2\ \mathrm{G\cdot cm^{-1}}$ to $+19.4\ \mathrm{G\cdot cm^{-1}}$ for the longer cell and $-26.7\ \mathrm{G\cdot cm^{-1}}$ to $+28.5\ \mathrm{G\cdot cm^{-1}}$ for the shorter cell, via the pulse sequence depicted in **Figure 2.10**. A sinc-shaped slice-selective pulse of duration $p_1 = 100$ µs was used for the initial excitation, centred on a slice gradient of $-14.25\ \mathrm{G\cdot cm^{-1}}$ for $g_1 = 300$ µs, with a gradient echo of half that magnitude in the positive direction for the same duration $g_2 = g_1$ following the slice gradient, to remove phase variation across the slice, after a delay $\tau_1 = 50$ µs. A further preparation delay of $\tau_2 = 200$ µs preceded the sine-shaped phase-encoding gradient pulse

of duration 1 ms, corresponding to the phase-encoding time t_p, followed after $\tau_3 = 100$ µs by the refocusing hard π pulse of $p_2 = 58$ µs at 40 W. Digitization was set to begin at the top of the spin echo ($\tau_E = g_1/3 + \tau_1 + g_2 + \tau_2 + t_p + \tau_3$). The recycle delay was chosen as 10 s to allow full relaxation of PF_6^- (which has a ^{19}F longitudinal relaxation time, T_1, of 2 s), leading to a total acquisition time of 10 minutes for a ^{19}F CS image. Intensity profiles were formed by integrating over the spectral dimension. The profiles are then normalized relative to the initial, uniform c_0 intensity profile, to provide a map across the inter-electrode spacing of the concentration deviations from c_0 as the cell is polarized. An analogous approach is used in defining the steady-state concentration profile for the ^{19}F DHK-SPRITE images. The linear gradient ramps for DHK-SPRITE imaging were constructed with 64 points for each half-k-space sequence, ranging in magnitude up to 91.2 $G \cdot cm^{-1}$ for the longer cell, and 165 $G \cdot cm^{-1}$ for the shorter cell. The excitation at each step was achieved with a 2 µs broadband pulse (which corresponds to a tip angle of 6.2 degrees for the PF_6^- signal), and the recycle delay between the gradient ramps was 365 ms. 500 µs of gradient stabilization time was included for each ramp step prior to excitation. The method of multiple FID point acquisition for SPRITE[43] was used, with 8 FID points collected in quadrature with a 1.6 µs dwell time on a 100 µs base phase-encode time yielding a maximum t_p of 122.4 µs. To achieve reasonable signal-to-noise, $2k$ scans were acquired, for a total experimental time of 30 minutes. The DHK-SPRITE pulse sequence is presented in **Figure 2.11**.

4.4 Results and Discussion

4.4.1 *In Situ* MRI of Salt Precipitation at Low Temperature

Figure 4.3 presents the evolution of the concentration gradient of 1.0 M $LiPF_6$ in equal parts EC/DEC solvent mixture under polarization while the graphite electrode is being charged at $7.2\ A \cdot m^{-2}$ and a temperature of 10°C, visualized with normalized ^{19}F CS images. Each image in the sequence, acquired at 10-minute intervals, can be considered as a 'time-lapse' of the distribution of concentrations across the inter-electrode spacing. This is nominally 1.9 mm for this cell, but CSI can only measure between the dead-space regions; the position coordinate in the figure is therefore measured from the *detectable* edge of the active volume, with the average dead-space length for the Li metal side obtained from the DHK-SPRITE images appearing subsequently added to the coordinate in order to centre the detectable region of the cell between the true edges. As the current is applied, the ejection of Li^+ ions at the Li side (left of the image) causes a buildup of concentration, whilst insertion/deposition at the graphite side (right of the image) depletes the electrolyte of Li^+ in this region; the PF_6^- anions migrate in the opposite direction to maintain electroneutrality. As soon as a critical value of the salt concentration has been reached on the Li side of the electrolyte domain, the measured concentration in this region begins to *decrease*, while depletion continues as it should on the graphite side (occurring after approximately 35 minutes in **Figure 4.3**, and indicated by the colour gradient of the cubic fit lines from dark blue to pale red). At around 75 minutes of polarization, this phenomenon results in complete interruption of the ionic current, as the resistance begins rapidly increasing until the cell voltage drops below the allowed threshold of -3 V with respect to

Li/Li^+. Note that the time-scales involved depend strongly on the cell design. Using an estimate for the dead-space indicated by the dashed green lines in **Figure 4.3**, and derived from DHK-SPRITE images presented later in this report, extrapolation of the concentration profiles up to the true edges of the inter-electrode spacing reveals a flattening of the concentration gradient near the Li electrode. This would suggest that a stagnation of the ionic current in the electrolyte on the concentrated side is ultimately triggering the rapid resistance increase.

Upon allowing the cell to fully relax back to uniform salt distribution (approximately 150 minutes post-failure), a new baseline CS image was acquired, and is compared with the initial profile in **Figure 4.4**. Clearly, there is an overall signal reduction of approximately 5% (in a point-to-point comparison in the central region of the active

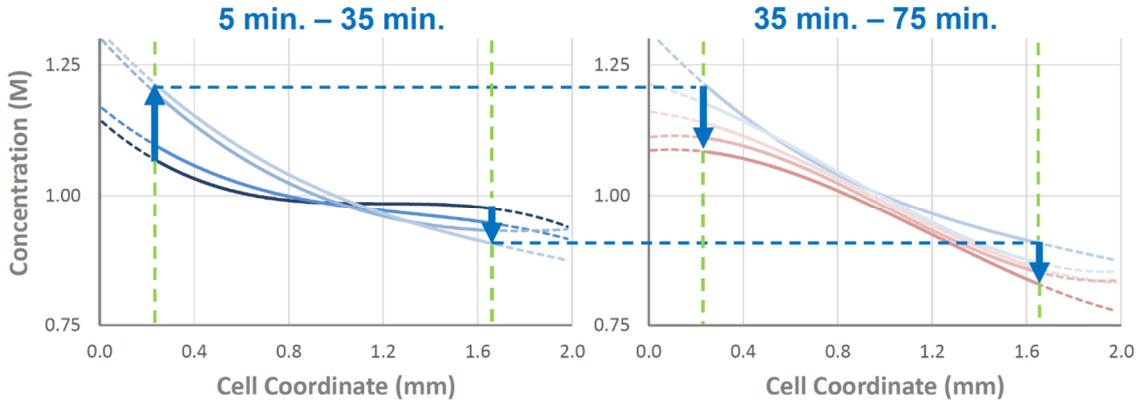

Figure 4.3 – A plot of normalized ^{19}F CS images of the concentration gradient buildup for 1.0 M $LiPF_6$ in EC/DEC, 1:1 (v/v) at 10°C and 7.2 $A \cdot m^{-2}$. In the left series of images, the polarization proceeds as expected, with increasing concentration at the Li electrode (left) of the image while lithium cations are inserted into the graphite electrode (at right). After 35 minutes, the concentration begins decreasing on the Li side as well as the graphite side, as opposed to converging into a steady-state, until cell failure at 75 minutes. This signal decrease on the concentrated side of the cell while it is operating at a low temperature points towards salt precipitation. The inter-electrode spacing for this cell was nominally 1.9 mm, with estimated dead-space indicated by the dashed green lines.

volume), while the shape and edges of the original signal profile are retained. The measurement error for the projected intensities is closer to 1%, based on the comparison of multiple images acquired under identical conditions. Owing to the fact that MRI signal intensity is directly proportional to the local spin density at each pixel, from the fundamental theorem of MR imaging,[32] this is an indication that a fraction of the salt is no longer solvated. The cell filled with this electrolyte mixture polarizes and relaxes back to the original intensity profile at room temperature, and can begin polarization once again with the reduced concentration at 10℃ after relaxing from a failure, so the cell failure is directly related to the disruption of the ionic current, and the 'missing' signal intensity is purely a result of cycling the cell at a reduced temperature.

This indicates that the signal loss is caused by salt precipitation, and the same phenomenology was completely repeatable every time the cell was constructed with this electrolyte formulation and polarized at 10℃. Further, when a 0.85 M variant of the same electrolyte mixture was polarized under the same conditions, the resulting concentration gradient was symmetrical and successfully reached a steady-state, with the initial signal intensity profile recovered on allowing the cell to relax subsequent to the polarization. By slightly reducing the overall initial salt concentration, for the same current density, the absolute concentrations near the electrodes will be less extreme, but with a comparable concentration gradient forming. Salt precipitation was identified as a potential problem at large electrolyte polarization in an influential, early electrochemical modelling study,[44] and

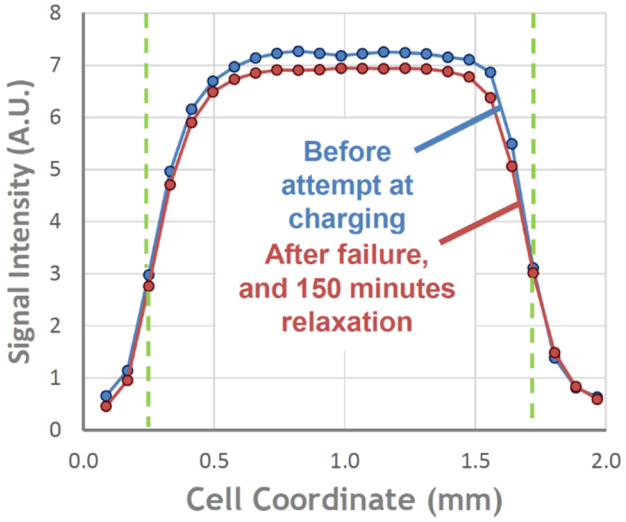

Figure 4.4 – The blue curve corresponds to the initial (non-normalized) ^{19}F signal intensity profile prior to charging the graphite at $7.2\ A \cdot m^{-2}$ and 10°C with the 1.0 M $LiPF_6$ in EC/DEC equal parts electrolyte mixture, while the red curve corresponds to the signal profile measured after cell failure from the polarization imaged in **Figure 4.3** and 150 minutes of subsequent relaxation without applied current. The reduction in signal intensity between the two profiles is evidence for the loss of fluorine nuclei from solution in the active volume, indicating that salt precipitation is responsible for the decreasing signal intensity on the concentrated side of the inter-electrode spacing in **Figure 4.3**.

is a recognized caveat in performance evaluations of electrolytes operating at low temperatures,[45] but insofar as the authors are aware, little subsequent work has addressed this concern. One recent study of the EC/DEC mixture over the same temperature range examined in this study did uncover a significant impairment in electrolyte performance in solutions of concentrations greater than 1.00 M at 10°C, using a combination of *ex situ* electrochemical measurements, concentration cells, and modelling.[46] Those authors suggest that the reason for the abrupt and significant drop in Maxwell-Stefan diffusivities they observed is a consequence of strong EC association with lithium ions coupled with the EC being on the verge of crystallization. However, ^{1}H CS imaging of the *in situ* cell using experimental parameters similar to the ^{19}F CSI experiments employed above (but with an

8 mm ^{1}H RF insert in place of the dual-tuned 8 mm ^{7}Li/^{19}F RF insert) revealed no observable difference between polarization at 25℃ and 10℃ in either the EC chemical shift and peak area in the spectral dimension, nor the overall projected ^{1}H intensity over the entire spectral dimension, in any of the slices on the concentrated side of the polarized cell. This suggests that the observed loss of signal in **Figure 4.4** is a consequence of classic salt precipitation at reduced temperature, rather than a partial change in the physical state of the EC solvent fraction. Nevertheless, the above results illustrate that further study on this phenomenon is warranted, as loss of electrolyte under low-temperature, high-current operational regimes where electrolyte polarization is severe can evidently be a conceivable and unaddressed source of long-term capacity fade for lithium-ion batteries in automotive applications.

4.4.2 Variable-Temperature *In Situ* MRI and Image Calibration

An alternative strategy to avoiding the possibility of salt precipitation at low temperature with a conventional 1.00 M salt concentration is to adopt an electrolyte formulation with enhanced solvation of the salt. Previous studies on ion association using *ex situ* NMR and electrochemical techniques have demonstrated that ion pairing as a function of temperature is lowest when a large fraction of high-dielectric constant solvent is present in the mixture.[40] With this metric in mind, a mixture of 1.00 M $LiPF_6$ in EC/PC/DMC, 5:2:3 (v/v) was adopted for study via the *in situ* MRI method, where EC and PC both possess relatively high dielectric constants. Measurements using *ex situ* methods for the two 1.00 M electrolyte mixtures used in this study are presented in the Supporting Information. In order to obtain quantitatively reliable data, and therefore test the hypothesis

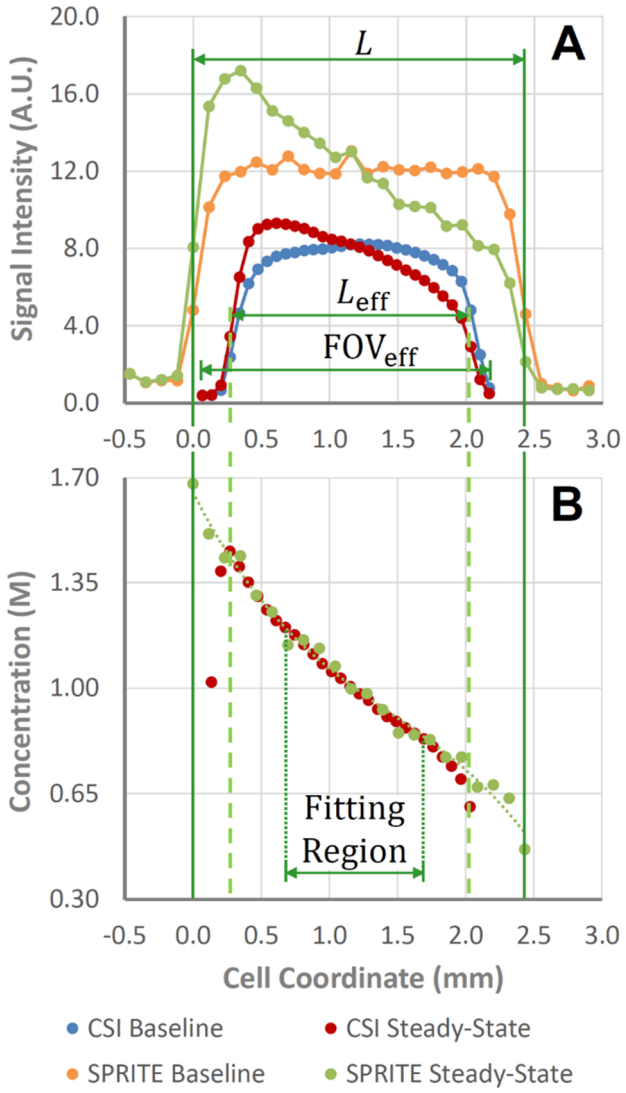

Figure 4.5 – A: Comparison of the baseline and steady-state signal intensity profiles of 1.00 M $LiPF_6$ in EC/PC/DMC, 5:2:3 (v/v) measured by CSI and DHK-SPRITE, at 10℃ and with a nominal cell length of 2.43 mm, charging the graphite electrode at 7.2 $A \cdot m^{-2}$. The horizontal compression and translation of the FOV has been applied for the CS images, illustrating the dead-space which DHK-SPRITE captures but CSI does not. B: Matching of the steady-state concentration profile measured by CSI with the cubic fit (dashed green line) of that obtained via DHK-SPRITE, which produces the effective FOV and alignment for CSI. The linear fitting region used to compare between cells is indicated.

that the steady-state concentration gradient in the modified form of Eqn. (4.4) with $D \rightarrow D(c,T)$ and $t_+^0 \rightarrow t_+^0(c,T)$ is independent of the inter-electrode spacing (to lowest-order in

an expansion about the centre of the cell), the DHK-SPRITE imaging technique was used to accurately measure electrolyte active volume and thereby calibrate the concentration gradients obtained via CSI.

An example of this gradient calibration is provided in **Figure 4.5**. Raw intensity profiles from the two techniques following the alignment procedure are provided in **Figure 4.5A**, demonstrating the dead-space phenomenon for CSI. In **Figure 4.5B**, the normalized, steady-state DHK-SPRITE image of the cell containing 1.00 M $LiPF_6$ in EC/PC/DMC at 10°C and with 7.2 $A \cdot m^{-2}$ applied current charging the graphite electrode is used to align the normalized, steady-state concentration profile obtained from an average of 4 CS images, with the higher-order curvature from a cubic fit to the DHK-SPRITE data (dotted green line in **Figure 4.5B**) assisting with the alignment. There are two fitting parameters in the alignment of the CS images: the effective FOV, which then defines the resolution for a given number of gradient steps (i.e. pixels), and the origin of the coordinate system for the CS images, which is *not* situated at one of the electrodes, but rather at the edge of the dead-space, representing the region of the active volume which can actually be detected by CSI. Both of these parameters are only adjusted in increments of 100 μm, which is the order of magnitude of resolution for CSI with the gradient magnifications used in the experiments. The fitting region where the concentration profile is approximately linear is also indicated in **Figure 4.5B**. Regressions performed over this region of the cell coordinate are used subsequently for quantitative comparisons between experiments. MRI results on a sample without conductive parts, consisting of 10 mm of Mn-doped water in a symmetric NMR tube (Shigemi, Inc.), demonstrate that the disagreement on the size of the cell between CSI

and DHK-SPRITE is not a result of the CSI experimental parameters, but rather a result of the enhanced relaxation in the active volume near the conductive parts of the *in situ* cell and disruption of gradient homogeneity (**Figure 4.6**; all experimental parameters are kept consistent with section **4.3**, but with corresponding adjustments made to the gradient strength in each case to compensate for the larger spatial extent of the sample). It is clear that both DHK-SPRITE and CSI agree on the size and shape of the active volume, for both types of gradient pulse shapes used in the CSI images.

The absolute B_0 gradient strength in the ^{19}F CSI pulse sequence used to monitor the *in situ* cell is much smaller than that of the SPRITE sequence, because there is no selective excitation in the latter sequence to prevent folding-in of electrolyte signal outside

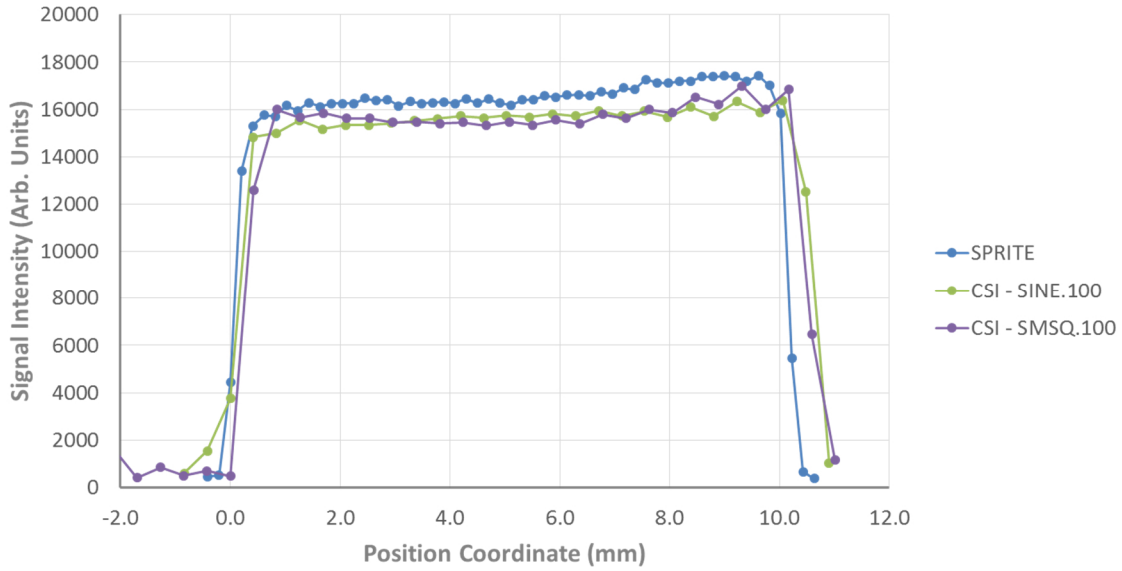

Figure 4.6 – Comparison of ^{1}H CS images employing two different gradient shapes, 100-point sine and smooth-square, with ^{1}H DHK-SPRITE for a 10 mm active volume filled with Mn-doped water in a symmetric NMR tube, illustrating that the discrepancy in concentration gradient measurement for the in situ cell is a result of the conductive parts of the cell distorting the B_0 field gradient, rather than an issue inherent in the CS pulse sequence parameters, since all three imaging experiments accurately measure the standard. Images have been vertically scaled to facilitate simultaneous plotting.

of the active volume (which occurs due to the flooded design of the *in situ* cell). Owing to the fact that there can be no gradient stabilization delay in the CSI sequence (while the SPRITE ramp naturally incorporates this), along with the lower absolute gradient strengths, the smallest phase-encoding gradients in the CSI sequence are particularly susceptible to disruption by the conductive parts of the *in situ* cell. Since these lowest spatial harmonics are most involved in defining the overall breadth of the image, a reduction in their contribution to the Fourier-transformed signal will result in the cell appearing shortened in the image relative to the size of the active volume that would be expected in the absence of conductive parts. An accurate representation of the active volume must therefore compensate for this 'missing' spectral weight. This is the rationale for using the inhomogeneity-robust DHK-SPRITE steady-state concentration profile to calibrate the CSI steady-state concentration profile: the same physical concentration gradient must be represented by both types of image. The calibration produces a compression factor by which the CSI FOV must be multiplied to represent the dead-space near the electrodes, along with a horizontal translation of the image to ensure that the centre of the image (where the concentration is always equal to the initial concentration) coincides with the true centre of the inter-electrode spacing.

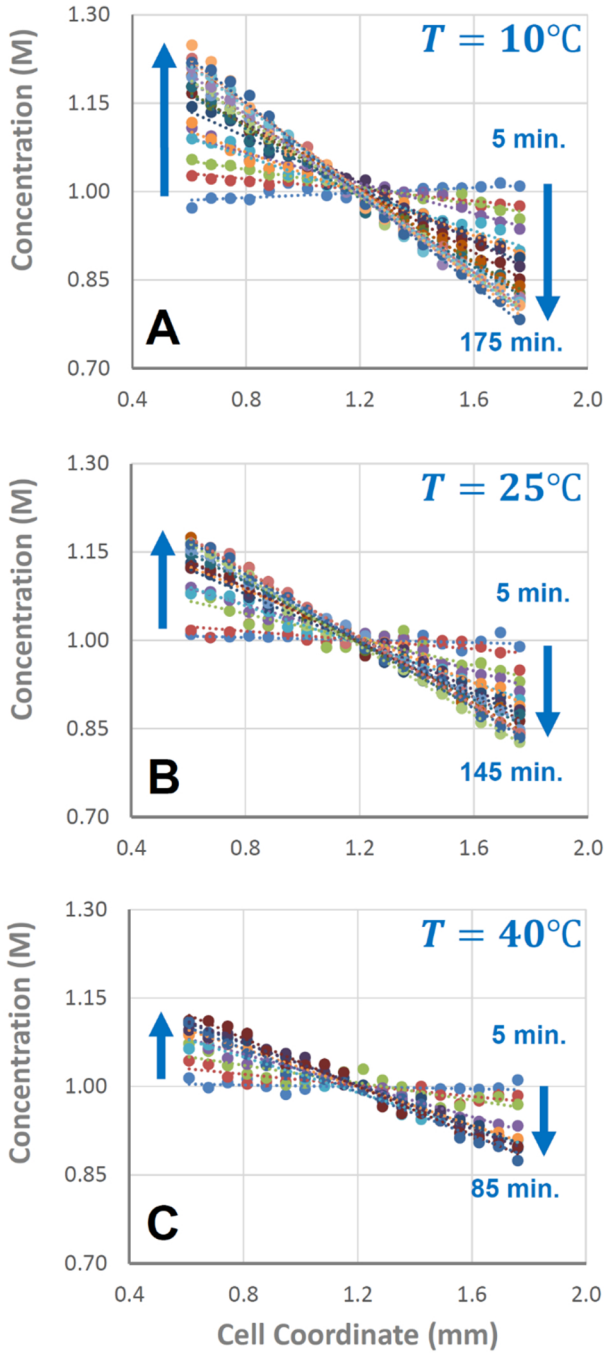

Figure 4.7 – Polarization of the in situ cell in the linear region with 1.00 M $LiPF_6$ in EC/PC/DMC, 5:2:3 (v/v) solvent mixture at 10℃ (panel A), 25℃ (B), and 40℃ (C). In each case, the concentration gradient builds until converging to a steady state (arrows indicate the direction of evolution), but with decreasing slope as the cell temperature is increased. Nominal cell length is 2.43 mm and in all cases the charging current corresponds to 7.2 $A \cdot m^{-2}$.

Principally, however, **Figure 4.5** also demonstrates that the $1.00\ \mathrm{M\ LiPF_6}$ in EC/PC/DMC electrolyte mixture can be successfully polarized to the steady-state at $10℃$ and $7.2\ \mathrm{A \cdot m^{-2}}$ without experiencing the salt precipitation that the $1.00\ \mathrm{M\ LiPF_6}$ in EC/DEC mixture exhibited under the same conditions. **Figure 4.7** presents a sequence of normalized, calibrated $^{19}\mathrm{F}$ CS images illustrating the build-up of the steady-state concentration gradient under polarization at several target temperatures for the EC/PC/DMC mixture, focused on the linear region of the concentration gradient. Steady-state concentration gradients in **Figure 4.8** for all three target temperatures were obtained from averaging 4 of the last normalized CS images in the sequence, which were identical within experimental error. This result demonstrates the extent to which temperature can influence the steady-state concentration gradient, with the deviation from the initial, uniform concentration profile at the edges of the linear region twice as large for $10℃$ as it is for $40℃$. As can be seen in the diffusivity versus temperature plot in the Supporting Information, the salt-diffusion coefficient is dependent on temperature in an approximately quadratic fashion, while the transference number is almost independent of temperature, which is the source of the influence displayed in **Figure 4.8**. Temperature also has a strong influence on the time taken by the cell to reach the steady-state; the slower mass transport that accompanies decreasing the temperature would have to be incorporated in an electrochemical modelling scheme that is based around switching between steady-state profiles in the electrolyte domain. Build-up sequences in **Figure 4.7** for the $10℃$, $25℃$, and $40℃$ experiments reached the steady-state in 175 minutes, 145 minutes, and 85 minutes, respectively.

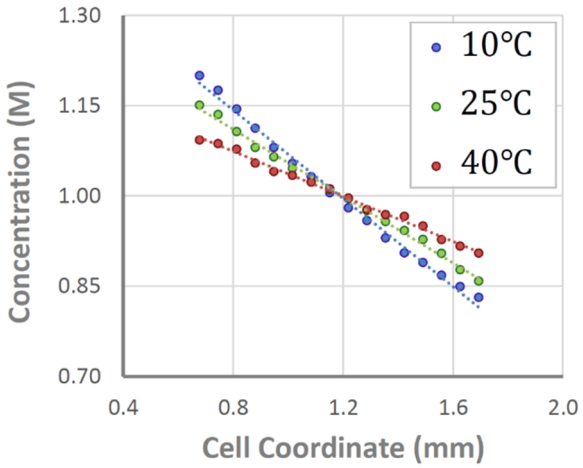

Figure 4.8 – Steady-state concentration profiles at each of the three temperatures, illustrating a decreasing slope as the temperature at which the cell is held is increased. Nominal cell length and current are the same as in **Figure 4.7**.

4.4.3 Assessing the Correspondence Between *In Situ* MRI Results and the Model

The relevance of the above results to electrochemical modelling applications hinges on whether the steady-state concentration gradients measured by *in situ* MRI realistically capture polarization in electrolytes when the inter-electrode spacing is much reduced, as would be the case in authentic battery systems. The length-scale associated with the inter-electrode spacing does not enter into the determination of the steady-state concentration gradient, given by Eqn. (4.4), when the transport parameters are assumed to be independent of the concentration distribution. It *will* alter the time-scale upon which the *steady-state* gradient forms, however, as can be seen by comparing with *in situ* MRI studies where the electrodes are an order of magnitude further apart.[9,13] When that assumption about the concentration-independence is relaxed, Eqn. (4.4) becomes

$$\frac{\overline{\partial c}}{\partial x} = -\frac{\left(1 - t_+^0(\bar{c},T)\right)}{D(\bar{c},T)}\frac{I}{FA} \equiv -f(\bar{c}(x),T)\frac{I}{FA}, \tag{4.5}$$

where the overbars indicate steady-state conditions. The function $f(\bar{c}(x),T)$ can be expanded about the centre of the active volume, where, by symmetry, it must be that $c(L/2,t) = c_0$ (as is borne out in the MR images in **Figures 4.5**, **4.7**, and **4.8**):

$$\begin{aligned} f(\bar{c}(x),T) = f(c_0,T) &+ \left.\frac{\partial f}{\partial \bar{c}}\right|_{c_0,T}\frac{\overline{\partial c}}{\partial x}\left(x - \frac{L}{2}\right) \\ &+ \frac{1}{2}\left[\left.\frac{\partial^2 f}{\partial \bar{c}^2}\right|_{c_0,T}\left(\frac{\overline{\partial c}}{\partial x}\right)^2 + \left.\frac{\partial f}{\partial \bar{c}}\right|_{c_0,T}\frac{\overline{\partial^2 c}}{\partial x^2}\right]\left(x - \frac{L}{2}\right)^2 \\ &+ O\left[\left(x - \frac{L}{2}\right)^3\right], \end{aligned} \tag{4.6}$$

which is a nonlinear function in $\overline{\partial c}/\partial x$ when inserted in Eqn. (4.5). Terms up to quadratic order in $(x - L/2)$ yield the cubic curvature in the steady-state concentration profile exhibited in **Figure 4.5B** on integration. However, in order to demonstrate the applicability of the *in situ* MRI results to realistic systems, it is crucial to confirm that in cells with different inter-electrode spacing, there is quantitative agreement on the magnitude of the steady-state concentration gradient to lowest order in Eqn. (4.6) (to which Eqn. (4.4) is mathematically equivalent, if the T-dependence of D and t_+^0 is explicitly denoted) under identical operational conditions.

To this end, cells with inter-electrode spacing (measured by DHK-SPRITE) of $1.45\ \text{mm}$ and $2.43\ \text{mm}$ were assembled, and the same sequence of experiments was conducted for each, wherein the cell was polarized at each of 10℃, 25℃, and 40℃, all at $7.2\ \text{A} \cdot \text{m}^{-2}$, and the steady-state concentration profiles obtained from CSI and DHK-SPRITE were aligned, along with the CSI buildup images. **Figure 4.9** presents the slope

values from linear regressions to the linear region of the concentration gradient (e.g. the lowest order in Eqn. (4.6), corresponding to the fitting region indicated in **Figure 4.5B**), for each of the temperatures and both of the cell lengths, with 3σ confidence intervals. A replicate of the longer cell is also included, which was measured by DHK-SPRITE to have a spacing of 2.32 mm, to demonstrate the reproducibility of the results. Clearly, there is sound quantitative agreement on the magnitude of the steady-state concentration gradients generated by the cells, in spite of the ~40% difference between their inter-electrode spacing.

The lowest-order term in Eqn. (4.6) can also be computed from *ex situ* PFG-NMR and conductivity measurements of the transport parameters, which are detailed in **Chapter 3**. From the *ex situ* measurements of salt diffusivity as a function of temperature, the diffusivity has an approximately quadratic dependence on temperature. This is reflected in the observed magnitudes of the steady-state concentration gradients by both *in situ* MRI and the *ex situ* experiments in **Figure 4.9**, wherein the difference in magnitude between the 25°C and 40°C concentration gradients is smaller than that of the 10°C and 25°C concentration gradients, given also that the transference number is only weakly influenced by temperature, as determined by the *ex situ* measurements. These *ex situ* measurements additionally exhibit robust agreement with the *in situ* MRI results for the lowest-order term in the concentration gradient, simultaneously providing independent experimental confirmation of the *in situ* MRI results, and illustrating their enhanced usefulness relative to *ex situ* measurements: the coefficients for the higher-order terms in Eqn. (4.6) depend on gradients in the transport parameters with respect to concentration which would be

thoroughly impractical to measure *ex situ*. *In situ* MRI directly obtains the concentration profile – in *both* transient and steady-state regimes – without the need to measure any additional parameters and then integrate Eqn. (4.6).

The importance of these last results is that they demonstrate that carefully measured steady-state concentration gradients by the *in situ* MRI technique can be readily extrapolated to real electrochemical modelling applications, because these are commonly constructed using the Doyle-Fuller-Newman electrolyte-domain PDE, the steady-state

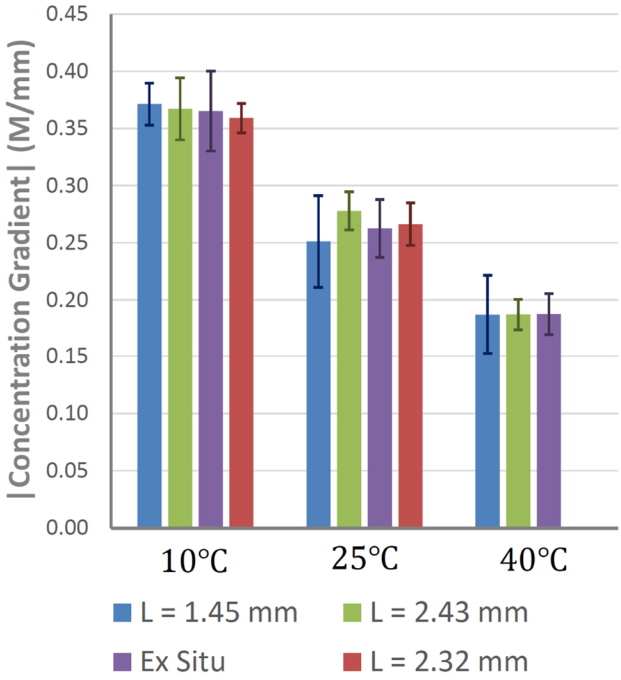

Figure 4.9 – A comparison of the fitted CSI regression slopes for the concentration gradient magnitudes at three temperatures (10°C, 25°C, and 40°C), and between the two nominal cell lengths (1.45 mm, versus 2.43 mm and a 2.32 mm replicate), demonstrating the difference in the amount of steady-state polarization in the $1.00\,\mathrm{M}\,LiPF_6$ in EC/PC/DMC electrolyte with temperature, and the constancy in the polarization irrespective of inter-electrode spacing for a given temperature. All polarizations were achieved with a charging current of $7.2\,\mathrm{A}\cdot\mathrm{m}^{-2}$, transferring Li ions to the graphite electrode. Error bars correspond to 3σ confidence intervals for the regression slopes for the *in situ* experiments.

predictions of which, in Eqn. (4.5), are the basis of the agreement exhibited in **Figure 4.9**. In particular, the inclusion of separator material throughout the active volume (at a trade-off of signal intensity, however), and coupling of the CSI experiment to a single-shot diffusion experiment in a pseudo-3D experiment,[14] would provide access to spatial distributions of effective diffusivities (where the tortuosity is incorporated) and transference numbers in the steady-state, which could be directly employed for model parameterization and validation, with the temperature- and current-dependence systematically investigated. The above results, taken together, demonstrate that it would be possible to completely characterize the transport parameters of the electrolyte over a wide range of temperature and current operating conditions with the *in situ* MRI approach.

4.5 Summary and Conclusions

This study entails the first application of the *in situ* MRI technique to the investigation of variable-temperature electrolyte polarization under applied current. It has been demonstrated that salt precipitation is possible when the electrolyte is polarized at low temperature, which could present a previously unaddressed source of power-density fade in automotive lithium-ion batteries, but that this possibility could be averted by careful engineering of the electrolyte solvation characteristics. Additionally, a quantitative comparison of steady-state concentration gradients at a series of temperatures for cells with different inter-electrode spacing has illustrated that steady-state concentration gradients measured by the *in situ* MRI technique for battery mimics are independent of this spacing to lowest order, and in strong agreement with the values predicted from theory and computed using *ex situ* PFG-NMR and electrochemical measurements of the transport

parameters. The measured *in situ* concentration profiles under polarization are therefore applicable to electrochemical model parameterization and validation for real cells, where the inter-electrode spacing is much smaller than is feasible for *in situ* cells amenable to MRI methods.

4.6 References

(1) Ahmed, R.; El Sayed, M.; Arasaratnam, I.; Tjong, J.; Habibi, S. R. Reduced-Order Electrochemical Model Parameters Identification and SOC Estimation for Healthy and Aged Li-Ion Batteries Part I: Parameterization Model Development for Healthy Batteries. *IEEE J. Emerg. Sel. Top. Power Electron.* **2014**, *2* (3), 659–677.

(2) Nyman, A.; Zavalis, T. G.; Elger, R.; Behm, M.; Lindbergh, G. Analysis of the Polarization in a Li-Ion Battery Cell by Numerical Simulations. *J. Electrochem. Soc.* **2010**, *157* (11), A1236.

(3) Mastali Majdabadi, M.; Farhad, S.; Farkhondeh, M.; Fraser, R. A.; Fowler, M. Simplified Electrochemical Multi-Particle Model for LiFePO4 Cathodes in Lithium-Ion Batteries. *J. Power Sources* **2015**, *275*, 633–643.

(4) Ji, Y.; Zhang, Y.; Wang, C.-Y. Li-Ion Cell Operation at Low Temperatures. *J. Electrochem. Soc.* **2013**, *160* (4), A636–A649.

(5) Doyle, M.; Fuller, T. F.; Newman, J. Modeling of Galvanostatic Charge and Discharge of the Lithium/Polymer/Insertion Cell. *J. Electrochem. Soc.* **1993**, *140* (6), 1526.

(6) Harks, P. P. R. M. L.; Mulder, F. M.; Notten, P. H. L. In Situ Methods for Li-Ion Battery Research: A Review of Recent Developments. *J. Power Sources* **2015**, *288*, 92–105.

(7) Yamanaka, T.; Nakagawa, H.; Tsubouchi, S.; Domi, Y.; Doi, T.; Abe, T.; Ogumi, Z. In Situ Raman Spectroscopic Studies on Concentration Change of Electrolyte Salt in a Lithium Ion Model Battery with Closely Faced Graphite Composite and LiCoO 2 Composite Electrodes by Using an Ultrafine Microprobe. *Electrochim. Acta* **2017**, *234*, 93–98.

(8) Forster, J. D.; Harris, S. J.; Urban, J. J. Mapping Li + Concentration and Transport via In Situ Confocal Raman Microscopy. *J. Phys. Chem. Lett.* **2014**, *5* (11), 2007–2011.

(9) Klett, M.; Giesecke, M.; Nyman, A.; Hallberg, F.; Lindström, R. W.; Lindbergh, G.; Furó, I. Quantifying Mass Transport during Polarization in a Li Ion Battery Electrolyte by in Situ 7 Li NMR Imaging. *J. Am. Chem. Soc.* **2012**, *134* (36), 14654–14657.

(10) Chandrashekar, S.; Trease, N. M.; Chang, H. J.; Du, L.-S.; Grey, C. P.; Jerschow, A. 7Li MRI of Li Batteries Reveals Location of Microstructural Lithium. *Nat. Mater.* **2012**, *11* (4), 311–315.

(11) Klamor, S.; Zick, K.; Oerther, T.; Schappacher, F. M.; Winter, M.; Brunklaus, G. 7 Li in Situ 1D NMR Imaging of a Lithium Ion Battery. *Phys. Chem. Chem. Phys.* **2015**, *17* (6), 4458–4465.

(12) Chang, H. J.; Ilott, A. J.; Trease, N. M.; Mohammadi, M.; Jerschow, A.; Grey, C. P. Correlating Microstructural Lithium Metal Growth with Electrolyte Salt Depletion in Lithium Batteries Using 7 Li MRI. *J. Am. Chem. Soc.* **2015**, *137* (48), 15209–15216.

(13) Sethurajan, A. K.; Krachkovskiy, S. A.; Halalay, I. C.; Goward, G. R.; Protas, B. Accurate Characterization of Ion Transport Properties in Binary Symmetric Electrolytes Using In Situ NMR Imaging and Inverse Modeling. *J. Phys. Chem. B* **2015**, *119* (37), 12238–12248.

(14) Krachkovskiy, S. A.; Bazak, J. D.; Werhun, P.; Balcom, B. J.; Halalay, I. C.; Goward, G. R. Visualization of Steady-State Ionic Concentration Profiles Formed in Electrolytes during Li-Ion Battery Operation and Determination of Mass-Transport Properties by in Situ Magnetic Resonance Imaging. *J. Am. Chem. Soc.* **2016**, *138* (25), 7992–7999.

(15) Chandrashekar, S.; Oparaji, O.; Yang, G.; Hallinan, D. Communication— 7 Li MRI Unveils Concentration Dependent Diffusion in Polymer Electrolyte Batteries. *J. Electrochem. Soc.* **2016**, *163* (14), A2988–A2990.

(16) Tang, M.; Sarou-Kanian, V.; Melin, P.; Leriche, J.-B.; Ménétrier, M.; Tarascon, J.-M.; Deschamps, M.; Salager, E. Following Lithiation Fronts in Paramagnetic Electrodes with in Situ Magnetic Resonance Spectroscopic Imaging. *Nat. Commun.* **2016**, *7* (1), 13284.

(17) Ilott, A. J.; Mohammadi, M.; Chang, H. J.; Grey, C. P.; Jerschow, A. Real-Time 3D Imaging of Microstructure Growth in Battery Cells Using Indirect MRI. *Proc. Natl. Acad. Sci.* **2016**, *113* (39), 10779–10784.

(18) Zhang, Z.; Martin, J.; Wu, J.; Wang, H.; Promislow, K.; Balcom, B. J. Magnetic Resonance Imaging of Water Content across the Nafion Membrane in an Operational PEM Fuel Cell. *J. Magn. Reson.* **2008**, *193* (2), 259–266.

(19) Cattaneo, A. S.; Villa, D. C.; Angioni, S.; Ferrara, C.; Melzi, R.; Quartarone, E.; Mustarelli, P. Operando Electrochemical NMR Microscopy of Polymer Fuel Cells. *Energy Environ. Sci.* **2015**, *8* (8), 2383–2388.

(20) Britton, M. M.; Bayley, P. M.; Howlett, P. C.; Davenport, A. J.; Forsyth, M. In Situ, Real-Time Visualization of Electrochemistry Using Magnetic Resonance Imaging. *J. Phys. Chem. Lett.* **2013**, *4* (17), 3019–3023.

(21) Ilott, A. J.; Trease, N. M.; Grey, C. P.; Jerschow, A. Multinuclear in Situ Magnetic Resonance Imaging of Electrochemical Double-Layer Capacitors. *Nat. Commun.* **2014**, *5* (1), 4536.

(22) Hafezi, H.; Newman, J. Verification and Analysis of Transference Number Measurements by the Galvanostatic Polarization Method. *J. Electrochem. Soc.* **2000**, *147* (8), 3036.

(23) Nyman, A.; Behm, M.; Lindbergh, G. Electrochemical Characterisation and Modelling of the Mass Transport Phenomena in LiPF6-EC-EMC Electrolyte. *Electrochim. Acta* **2008**, *53* (22), 6356–6365.

(24) Zugmann, S.; Fleischmann, M.; Amereller, M.; Gschwind, R. M.; Wiemhöfer, H. D.; Gores, H. J. Measurement of Transference Numbers for Lithium Ion Electrolytes via Four Different Methods, a Comparative Study. *Electrochim. Acta* **2011**, *56* (11), 3926–3933.

(25) Wohde, F.; Balabajew, M.; Roling, B. Li + Transference Numbers in Liquid Electrolytes Obtained by Very-Low-Frequency Impedance Spectroscopy at Variable Electrode Distances. *J. Electrochem. Soc.* **2016**, *163* (5), A714–A721.

(26) Ehrl, A.; Landesfeind, J.; Wall, W. A.; Gasteiger, H. A. Determination of Transport Parameters in Liquid Binary Lithium Ion Battery Electrolytes. *J. Electrochem. Soc.* **2017**, *164* (4), A826–A836.

(27) Stewart, S. G.; Newman, J. The Use of UV/Vis Absorption to Measure Diffusion Coefficients in LiPF[Sub 6] Electrolytic Solutions. *J. Electrochem. Soc.* **2008**, *155* (1), F13.

(28) Romanenko, K.; Forsyth, M.; O'Dell, L. A. New Opportunities for Quantitative and Time Efficient 3D MRI of Liquid and Solid Electrochemical Cell Components: Sectoral Fast Spin Echo and SPRITE. *J. Magn. Reson.* **2014**, *248*, 96–104.

(29) Vashaee, S.; Goora, F.; Britton, M. M.; Newling, B.; Balcom, B. J. Mapping B 1 - Induced Eddy Current Effects near Metallic Structures in MR Images: A Comparison of Simulation and Experiment. *J. Magn. Reson.* **2015**, *250*, 17–24.

(30) Gravina, S.; Cory, D. G. Sensitivity and Resolution of Constant-Time Imaging. *J. Magn. Reson. Ser. B* **1994**, *104* (1), 53–61.

(31) Callaghan, P. T.; Forde, L. C.; Rofe, C. J. Correlated Susceptibility and Diffusion Effects in NMR Microscopy Using Both Phase-Frequency Encoding and Phase-Phase Encoding. *J. Magn. Reson. Ser. B* **1994**, *104* (1), 34–52.

(32) Brown, T. R. Chemical Shift Imaging. In *Encyclopedia of Magnetic Resonance*; John Wiley & Sons, Ltd: Chichester, UK, 2007; pp 1–12.

(33) Callaghan, P. T. *Principles of Nuclear Magnetic Resonance Microscopy*; Oxford University Press: Oxford, UK, 1991.

(34) Halse, M.; Goodyear, D. J.; MacMillan, B.; Szomolanyi, P.; Matheson, D.; Balcom, B. J. Centric Scan SPRITE Magnetic Resonance Imaging. *J. Magn. Reson.* **2003**, *165* (2), 219–229.

(35) Krachkovskiy, S. A.; Pauric, A. D.; Halalay, I. C.; Goward, G. R. Slice-Selective

NMR Diffusion Measurements: A Robust and Reliable Tool for In Situ Characterization of Ion-Transport Properties in Lithium-Ion Battery Electrolytes. *J. Phys. Chem. Lett.* **2013**, *4* (22), 3940–3944.

(36) Di Domenico, D.; Fiengo, G.; Stefanopoulou, A. Lithium-Ion Battery State of Charge Estimation with a Kalman Filter Based on a Electrochemical Model. *Control Appl. 2008. CCA 2008. IEEE Int. Conf.* **2008**, 702–707.

(37) Chaturvedi, N. A.; Klein, R.; Christensen, J.; Ahmed, J.; Kojic, A. Modeling, Estimation, and Control Challenges for Lithium-Ion Batteries. In *Proceedings of the 2010 American Control Conference*; IEEE, 2010; pp 1997–2002.

(38) Tanim, T. R.; Rahn, C. D.; Wang, C.-Y. A Temperature Dependent, Single Particle, Lithium Ion Cell Model Including Electrolyte Diffusion. *J. Dyn. Syst. Meas. Control* **2015**, *137* (1), 011005.

(39) Danilov, D.; Notten, P. H. L. Mathematical Modelling of Ionic Transport in the Electrolyte of Li-Ion Batteries. *Electrochim. Acta* **2008**, *53* (17), 5569–5578.

(40) Krachkovskiy, S. A.; Bazak, J. D.; Fraser, S.; Halalay, I. C.; Goward, G. R. Determination of Mass Transfer Parameters and Ionic Association of LiPF 6 : Organic Carbonates Solutions. *J. Electrochem. Soc.* **2017**, *164* (4), A912–A916.

(41) Hall, D. S.; Self, J.; Dahn, J. R. Dielectric Constants for Quantum Chemistry and Li-Ion Batteries: Solvent Blends of Ethylene Carbonate and Ethyl Methyl Carbonate. *J. Phys. Chem. C* **2015**, *119* (39), 22322–22330.

(42) Xu, K. Nonaqueous Liquid Electrolytes for Lithium-Based Rechargeable Batteries. *Chem. Rev.* **2004**, *104* (10), 4303–4418.

(43) Halse, M.; Rioux, J.; Romanzetti, S.; Kaffanke, J.; MacMillan, B.; Mastikhin, I.; Shah, N. J.; Aubanel, E.; Balcom, B. J. Centric Scan SPRITE Magnetic Resonance Imaging: Optimization of SNR, Resolution, and Relaxation Time Mapping. *J. Magn. Reson.* **2004**, *169* (1), 102–117.

(44) Doyle, M.; Newman, J.; Gozdz, A. S.; Schmutz, C. N.; Tarascon, J.-M. Comparison of Modeling Predictions with Experimental Data from Plastic Lithium Ion Cells. *J. Electrochem. Soc.* **1996**, *143* (6), 1890.

(45) Zhang, S. .; Xu, K.; Jow, T. . A New Approach toward Improved Low Temperature Performance of Li-Ion Battery. *Electrochem. commun.* **2002**, *4* (11), 928–932.

(46) Lundgren, H.; Behm, M.; Lindbergh, G. Electrochemical Characterization and Temperature Dependency of Mass-Transport Properties of LiPF6 in EC:DEC. *J. Electrochem. Soc.* **2014**, *162* (3), A413–A420.

Chapter 5 – Mapping of Lithium-Ion Battery Electrolyte Transport Properties and Limiting Currents with *In Situ* MRI

5.1 Introduction and Context in the Thesis

Given the electrochemical modelling and control challenges facing lithium-ion batteries in extreme operating conditions, such as low temperature and high C-rate, it is important to understand the transport dynamics in a polarized cell with large electrolyte concentration gradients. To this end, for the study presented in this chapter, a combination of conventional magnetic resonance imaging (MRI) experiments and MRI experiments coupled with pulsed-field-gradient (PFG) NMR for diffusion measurements were performed on an *in situ* lithium-ion cell operating at a variety of temperatures and current densities. The aim was to quantify the electrolyte transport parameters with spatial resolution. While some progress was attainable towards this aim, and the necessary framework for future studies along this direction was developed, it was determined that in order to accurately quantify the transference number a very accurate measurement of the concentration gradient is necessary when the polarization is large. It was also observed that limiting current behavior in the electrolyte at low temperature arises as a consequence of diffusion limitation on the anodic side, rather than ion depletion on the cathodic side. The framework developed herein has the potential to be useful not only for electrochemical model validation, but potentially also comprehensive electrolyte transport characterization, should the identified experimental limitations be overcome.

This work was performed at McMaster University under the supervision of Prof. Gillian R. Goward. Dr. Sergey A. Krachkovskiy spearheaded the initial implementation of both the *in situ* cell and the pseudo-three-dimensional diffusion imaging pulse sequence. Two undergraduate summer researchers, Ms. J. P. Allen and Mr. Jacob R. Keffer, contributed to data curation; J. Allen made electrolyte solutions, performed mass density measurements, and performed the variable-temperature conductivity measurements (with the author performing the equivalent circuit modelling thereof), while J. Keffer also made electrolyte solutions and performed mass density measurements. All *in situ* MRI experiments were performed by the author, along with all of the data processing and analysis. The text in the remainder of this thesis chapter is being prepared for submission to the *Journal of the Electrochemical Society*, with authorship of J. David Bazak, J. P. Allen, S. A. Krachkovskiy, and G. R. Goward.

5.2 Introduction and Context in the Field

Growth of the electric vehicle (EV) market is continuing at a rapid pace, on account of technological developments, regulatory measures, and cost reductions.[1] Despite this progress, difficulties in the predominant lithium-ion battery energy storage platform of performance loss on low-temperature operation[2,3] and cell degradation at high C-rates, particularly on charging,[4–6] linger on as concerns and potential barriers to furthering adoption. Key to mitigating these performance and degradation issues is robust, accurate battery management and control.[7,8] In order to contend with the inherent complexities of the battery system at the microscopic level, in terms of interdependent charge and mass transport and transfer between electrodes and the electrolyte, described by nonlinear partial

differential equations with intricate boundary conditions, researchers have increasingly turned to sophisticated electrochemical models to estimate the internal state of the battery.[9] However, sound estimation requires accurate parameterization of the model, and a reasonable accounting of all of the many effects that are in play, particularly in the extreme operational regimes of high C-rates and low temperatures. The electrolyte domain becomes central to this process under these circumstances, where the large concentration gradients generated – and associated ramifications for lithium-ion transport rates – must be properly incorporated.[10–12]

Given the complexity and interdependency of the ion transport and reaction processes in electrochemical systems, it is therefore unsurprising that *in situ* and *operando* methods for their study have proliferated and become widely accepted.[13,14] Magnetic Resonance Imaging (MRI), has been at the forefront of this development, with applications to fuel cells,[15,16] metal-air battery electrolytes,[17] electrodeposition,[18–20] supercapacitors,[21,22] lithium insertion[23,24] and plating in lithium-ion batteries,[25–29] lithium distribution heterogeneity in solid-state electrolytes,[30] and transport processes in liquid-state lithium-ion battery electrolytes.[31–36] Specifically, the latter have been used to elucidate the extent and properties of the electrolyte concentration gradients that form under polarization of the cell. Complementary *in situ* approaches to MRI with a similar focus on these gradients include Raman-based approaches[37,38] and x-ray phase imaging,[39] but MRI is unique in its potential for quantitative analysis and visualization of transport and gradient formation under polarization in electrolytes because it can be coupled to the widely-applied[40–49] *ex situ* technique of Pulsed-Field Gradient (PFG) NMR for electrolyte investigations to yield

spatially-resolved diffusivity measurements.[35] Diffusivities – along with other key electrolyte transport parameters such as the ionic conductivity and the transference number – can, of course, be measured via a range of conventional electrochemical techniques with varying degrees of accuracy,[50–58] but these take the form of bulk, cell-wide measurements and do not furnish the additional insight that spatial localization by MRI provides.

The aim of this study is to therefore further extend the *in situ* PFG-MRI approach introduced in Krachkovskiy *et al.*[35] to a quantitative assessment of electrolyte transport parameters with spatial resolution, under a wide range of temperatures and driving currents. This is in service to the goal of gaining increased understanding of the transport processes underway in the electrolyte during extreme operation, elucidating the mechanism that leads to limiting currents in these scenarios, and testing the applicability of the electrolyte-domain equations of the Doyle-Fuller-Newman model[59] conventionally adapted as the core of electrochemical model approaches to battery state estimation. The experiments take the form of a "staircase" of current densities applied to the *in situ* cell, comprising a lithium anode and a graphite cathode with a ternary 1.00M $LiPF_6$ EC/PC/DMC, 5:2:3 (v/v) electrolyte mixture filling the inter-electrode space, until a steady-state concentration gradient is formed at each step, all at a fixed temperature. Chemical Shift (CS) MRI images of the concentration gradient are acquired as the steady-state concentration gradient formation is occurring to monitor the edge change as a result of lithium deposition,[29] and monitor the progress towards the achievement of the steady state. Upon reaching the steady state, a calibration image using the Double-Half-k-Space, Single Point Ramped Imaging with T_1 Enhancement (DHK-SPRITE) technique is acquired for signal calibration

according to previously developed methods,[36] and then both ^{7}Li and ^{19}F Pseudo-Three-Dimensional (P3D) PFG-MRI images are acquired while the concentration profile is stationary, yielding spatial maps of the anion and cation self-diffusivities. The cell is then disassembled and rebuilt, and the process is repeated for the entire series of target temperatures, forming a grid of operating conditions.

The outline of the paper is therefore as follows: the theory necessary to analyze the steady-state ion transport is presented, followed by a detailed discussion of the experimental method outlined above. The raw CS image results for the grid of conditions are then provided, demonstrating limiting current behavior as a function of temperature. Following this, the analysis of the steady-state results begins with an illustration of the alignment and signal calibration procedure of the 40°C current staircase, which was analogous for all of the temperatures considered. Quantitative analysis of the spatially-resolved transport parameters for the 40°C staircase is then presented. This particular data set was chosen to emphasize both the potential and the difficulties inherent in this approach, as it provides an example of results where the quantification can be achieved with reasonable precision, and the conditions under which the high numerical sensitivity of the model equations prevents reliable interpretation. Finally, qualitative observations which could be discerned from the remaining temperature staircases are presented, linked with the quantitative findings from the 40°C case, and then, in turn, linked to the visualization of the limiting current behavior which opens the results section. It will be demonstrated that, particularly at low temperature, it is likely that diffusion limitations on the anodic (concentrated) side of the electrolyte domain ultimately trigger a continual increase in the

electrolyte polarization resistance at high degrees of polarization, and this is what interrupts the current, rather than ion depletion on the cathodic (dilute) side being responsible.

5.3 Theory

The electrolyte domain of many conventional electrochemical models[8,60–63] of lithium-ion batteries based on the Doyle-Fuller-Newman model[59] is derived from Concentrated Solution Theory (CST),[64] with the mass transport governing equation as follows:

$$\frac{\partial c_s}{\partial t} = \frac{\partial}{\partial x}\left[D_s(c_s,T)\left(1-\frac{\partial \ln(c_0)}{\partial \ln(c_s)}\right)\frac{\partial c_s}{\partial x}+\frac{(1-t_+^0)}{F}J\right], \tag{5.1}$$

where $c_s(x,t)$ is the local salt concentration at time t and at position x of the electrolyte domain along the inter-electrode spacing of length L, F is the Faraday constant, and $J = I/A$ is the current density for an applied current of magnitude I from electrode surface area A. D_s is the salt diffusivity of the electrolyte, which is strongly influenced by both the salt concentration and the temperature, T.[47] The term in parentheses involving the solvent concentration, $c_0(x,t)$, is often assumed close to unity in common electrochemical models,[9,59] but given the significant polarizations to be delivered to the cell, this assumption was avoided here. The term involving the cationic transference number with respect to the solvent, t_+^0, represents the compensatory migration of countering anions into a local neighborhood to maintain electroneutrality, $c_+(x,t) = c_-(x,t) \equiv c_s(x,t)$, against the flux of cations. Note that t_+^0 is sometimes simply referred to as "t_+",[35] although this latter notation is more appropriately reserved for dilute solution theory.[64] Also, as previously discussed,[47] the canonical, CST definition of the transference number is often conflated

with the quantity properly identified as the transport number, τ_+, in the electrochemical PFG-NMR literature.

Equation (5.1) is subject to the initial condition that $c_s(0,x) = \text{const.} \forall\, x \in [0,L]$ and the boundary conditions that

$$\left.\frac{\partial c_s}{\partial x}\right|_{x=0,L} = -\frac{(1-t_+^0)}{D_s(c_s,T)F}\left(1-\frac{\partial \ln(c_0)}{\partial \ln(c_s)}\right)^{-1} J, \qquad \forall\, t \in \mathbb{R}^+, \tag{5.2}$$

which specify that the cation flux in the electrolyte at the electrodes equals the exchange current density with the electrode phases. Examination of equation (5.1) readily reveals that there is a tension between diffusive flow of all species against the concentration gradient (mass transport) and migration flow of the charged species against the electrochemical potential gradient (charge transport, represented by the second term in the square brackets). Under constant-current conditions, there exists therefore a steady state of the form:

$$\frac{\overline{\partial c_s}}{\partial x} = -\frac{(1-t_+^0)}{D_s(\bar{c}_s,T)F}\left(1-\frac{\partial \ln(\bar{c}_0)}{\partial \ln(\bar{c}_s)}\right)^{-1} J, \qquad \forall\, x \in (0,L), \tag{5.3}$$

which can be reached by allowing the concentration gradient to evolve under constant current for sufficient time, and, at least in the center of the cell, will be approximately proportional to the applied current density.[36] For all subsequent analysis, overbars denote steady-state spatial distributions of the given parameter or variable.

Under CST, an n-component electrolyte, including the solvent, requires $n(n-1)/2$ parameters to characterize its transport under fixed operating conditions.[64] The origin of this stipulation is its formulation via electrochemical potential gradients driven by mutual drag forces between the components,

$$c_i \vec{\nabla}\mu_i = \sum_j K_{ij}(\vec{\boldsymbol{v}}_j - \vec{\boldsymbol{v}}_i) = RT \sum_j \frac{c_i c_j}{c_T \mathcal{D}_{ij}}(\vec{\boldsymbol{v}}_j - \vec{\boldsymbol{v}}_i), \tag{5.4}$$

where $\vec{\nabla}\mu_i$ are these potential gradients, $\vec{\boldsymbol{v}}_i$ are the average species velocities, the K_{ij} are the drag coefficients, and $\mathcal{D}_{ij}$ are the Onsager-Stefan-Maxwell (OSM) diffusivities (R is the universal gas constant). For a binary, univalent electrolyte, this yields 3 $\vec{\nabla}\mu_i$, with $i = \{+, -, 0\}$, and 3 OSM diffusivities, with the total concentration $c_T = c_+ + c_- + c_0$. The solvent mixture, denoted by $i = 0$, is treated as a uniform entity, even when it is a binary or ternary mixture. However, these OSM diffusivities are not typically accessible to experiment; instead, the three common measurable parameters for a binary, univalent electrolyte are the salt diffusivity $D_s(c_s, T)$ and transference number t_+^0 introduced above, along with the ionic conductivity, $\kappa(c_s, T)$. These are arrived at by applying mass and charge conservation laws to the species fluxes derived from equation (5.4), yielding the following expressions in terms of the OSM diffusivities (again, for a binary, univalent electrolyte):

$$D_s = \mathcal{D}\frac{c_T}{c_0}\left(1 + \frac{\partial \ln(\gamma_\pm)}{\partial \ln(m)}\right), \tag{5.5}$$

$$\mathcal{D} = \frac{2\mathcal{D}_{+0}\mathcal{D}_{-0}}{\mathcal{D}_{+0} + \mathcal{D}_{-0}}, \tag{5.6}$$

$$t_+^0 = \frac{\mathcal{D}_{+0}}{\mathcal{D}_{+0} + \mathcal{D}_{-0}}, \tag{5.7}$$

$$\frac{1}{\kappa} = \frac{RT}{c_T F^2}\left[\frac{1}{\mathcal{D}_{+-}} + \frac{c_0}{c_+}(1 - t_+^0)\frac{1}{\mathcal{D}_{-0}}\right], \tag{5.8}$$

where, in equation (5.5), $\gamma_\pm$ is the specific molal activity coefficient at electrolyte molality m, and the term in parenthesis is commonly denoted "the thermodynamic factor."

A complication arises, however, when attempting to apply diffusivity measurements obtained from PFG-NMR to equations (5.5-8). The self-diffusivities measured by PFG-NMR, D_+^* and D_-^*, include contributions from *both* the charged ions, as well as any transient charged or neutral aggregates which occur in solution.[34,42,44,46,47] Empirical and computational evidence suggests that at even moderate salt concentrations, this aggregation is not moderate for typical aprotic solvent mixtures and electrochemically-relevant lithium salts.[34,45,47,65–68] To disentangle at least the ion pairing contribution from these PFG-NMR self-diffusivities, one approach that has been employed recently is to define so-called "effective diffusivities" which use conductivity measurements obtained under equivalent conditions to separate out the individual contributions:

$$D_+^{\text{eff}} = \frac{1}{2}(D_+^* - D_-^* + D_\kappa), \tag{5.9}$$

$$D_-^{\text{eff}} = \frac{1}{2}(-D_+^* + D_-^* + D_\kappa), \tag{5.10}$$

$$D_p^{\text{eff}} = \frac{1}{2}(D_+^* + D_-^* - D_\kappa), \tag{5.11}$$

with D_p^{eff} as the effective ion pair diffusivity, and

$$D_\kappa = \frac{k_B T}{c_s N_A e^2}\kappa, \tag{5.12}$$

given by the Nernst-Einstein equation (k_B is the Boltzmann constant, N_A is Avogadro's number, and e is the fundamental unit of charge). This then enables the definition of a percentage of ion pairing, α_p, as

$$\alpha_p = \frac{D_p^{\text{eff}}}{D_+^{\text{eff}} + D_p^{\text{eff}}} \times 100\%. \tag{5.13}$$

However, while it is certainly possible to map *ex situ* conductivity measurements onto the local concentration profile *in situ* and compute these diffusivities, they still do not directly connect with OSM diffusivities that define the CST transport properties and consequently, a means of computing κ.

An alternative approach to making this connection between the D_i^* and the $\mathcal{D}_{ij}$ involves the use of the generalized Darken relations.[48,49] These were developed[69] from the original demonstration[70] that the Darken relations could be extended from binary alloys to general mutual diffusion, and have been applied computationally and experimentally in lithium-ion battery electrolytes.[48,49,71] The approximation takes the form

$$\mathcal{D}_{+0} = \frac{x_0}{x_0 + x_+} D_+^* + \frac{x_+}{x_0 + x_+} D_0^*, \tag{5.14}$$

$$\mathcal{D}_{-0} = \frac{x_0}{x_0 + x_-} D_-^* + \frac{x_-}{x_0 + x_-} D_0^*, \tag{5.15}$$

$$\mathcal{D}_{+-} = \frac{x_-}{x_+ + x_-} D_+^* + \frac{x_+}{x_+ + x_-} D_-^*, \tag{5.16}$$

where the x_i are the mole fractions $x_i = c_i/c_T$, and D_0^* is the self-diffusivity of the solvent. Presently available RF coils for NMR diffusion probes are typically only single- or dual-resonance, meaning that only two of the three D_i^* can be probed experimentally at a given time. However, t_+^0 can be directly isolated from a measurement of the concentration gradient at steady state using equation (5.3), which can be measured from CS images taken in the steady state. Combining this with the diffusion dimension of the P3D PFG-MRI experiments for D_+^* and D_-^* provides the three measurable transport parameters necessary to characterize the electrolyte, with spatial resolution. The route to κ is then to eliminate

D_0^* from equations (5.14-15) and use equation (5.7) to write $\mathcal{D}_{0+}$ in terms of $\mathcal{D}_{-0}$ in order to then isolate $\mathcal{D}_{-0}$,

$$\mathcal{D}_{-0} = \frac{\left(\frac{x_0}{x_+}\right) D_+^* - \left(\frac{x_0}{x_-}\right) D_-^*}{\frac{(x_0 + x_+)}{x_+}\frac{t_+^0}{1 - t_+^0} - \frac{(x_0 + x_-)}{x_-}}, \tag{5.17}$$

yielding an expression for $\kappa\left(\overline{\partial c_s}/\partial x\,, D_+^*, D_-^*\right)$ using equation (5.8), where $\overline{\partial c_s}/\partial x$ enters via t_+^0, D_+^* and D_-^* enter via $\mathcal{D}_{+-}$ using equation (5.16), and all three contribute in equation (5.17), along with the salt diffusivity from equation (5.5) expressed in its equivalent definition in terms of the PFG self-diffusivities:

$$D_s = \frac{2D_+^* D_-^*}{D_+^* + D_-^*}, \tag{5.18}$$

that is, it is the harmonic mean of the PFG-NMR self-diffusivities.[35,36,47,72] The solvent concentration at steady state, $\bar{c}_0(x)$, and hence the $\bar{x}_i(x)$ and $\bar{c}_T(x)$, are computed from the $\bar{c}_s(x)$ using the partial molar volumes extracted from fitting *ex situ* mass density measurements $\rho(c_s, T)$ as a function of the mass fraction of salt, and taking $x_+ + x_- + x_0 = 1$ (*i.e.* again treating the solvent as a uniform medium). The net result of the process is then that a spatially-resolved estimate of all electrolyte transport parameters is achievable using the measured concentration gradient at steady state, along with the measured PFG-NMR self-diffusivities from the diffusion dimension of the P3D PFG-MRI experiments for nuclei unique to each ion; for a $LiPF_6$ salt, the natural choices are ^{7}Li and ^{19}F. The process of transformations from the measured quantities to the derived transport parameters is illustrated schematically in **Figure 5.1.**

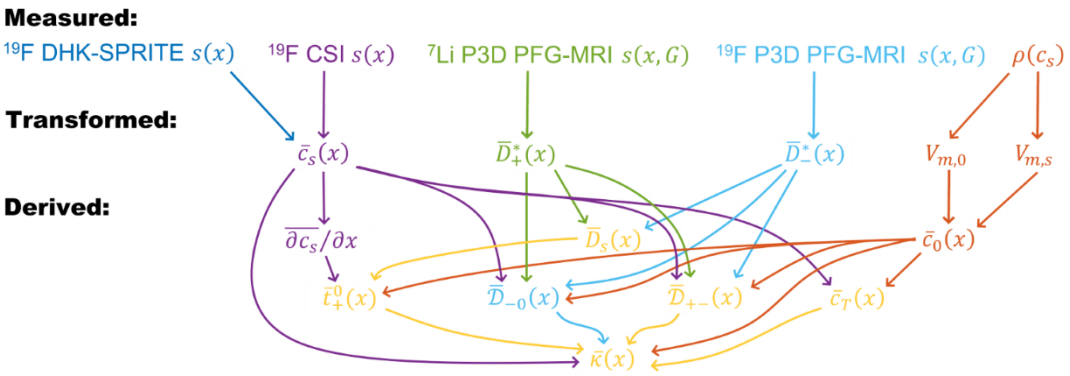

Figure 5.1 – Schematic illustration of the flow of variables, from raw measurements, to transformed electrochemical variables, and finally to derived transport parameters.

One remaining consideration is the form of the transference number, specifically with regard to its temperature- and concentration-dependence. There is no consensus on this in the literature; there are findings of its relative constancy with these variables,[34,35,41,47,51] findings of a clear decreasing trend with concentration and with temperature,[53,55,58] values that sit between ~0.3-0.4 for typical lithium-ion battery electrolyte mixtures at room temperature,[34,35,41,47,48,53] much smaller values,[52] and even negative ones.[58,73] What is clear is that, returning to equation (5.3) for the steady-state condition and applying the variance formula for uncertainty propagation,

$$\Delta f = \pm \sqrt{\sum_i \left(\frac{\partial f}{\partial q_i}\Delta q_i\right)^2}, \tag{5.19}$$

where the q_i are uncertain parameters in a general function f, the sensitivity coefficients will all be identical for the uncertain parameters $(\overline{\partial c_s}/\partial x\,, D_s)$ with non-negligible measurement precision confidence intervals, but the relative error $\Delta\left[\overline{\partial c_s}/\partial x\right]$ in $\overline{\partial c_s}/\partial x$ can be markedly larger than ΔD_s, especially in the center of the cell, and this resulting uncertainty in t^0_+ will propagate through the two subsequent steps in equations (5.17) and

(5.8) to calculating κ. It is therefore important to have a very robust model for fitting the derivative of $\bar{c}_s(x)$.

It is also important to note that extracting the uncertainty in derivatives from analytical fits to data (*i.e.* the uncertainty from fitting $\bar{c}_s(x)$ and then differentiating analytically to obtain $\overline{\partial c_s}/\partial x$) is a non-trivial problem.[74] To this end, one important consideration can be readily arrived at from the steady-state condition in equation (5.3) by differentiating it along the spatial dimension (setting aside the solvent term, because as will be seen below, $\bar{c}_0(x)$ is nearly linearly-varying across the inter-electrode spacing):

$$\left(\frac{\overline{\partial c_s}}{\partial x}\right)^2 \frac{\partial D_s}{\partial c}\bigg|_{c=\bar{c}_s(x)} + D_s\big(\bar{c}_s(x)\big)\frac{\overline{\partial^2 c_s}}{\partial x^2} = \frac{J}{F}\frac{\partial t_0^+}{\partial c}\bigg|_{c=\bar{c}_s(x)} \frac{\overline{\partial c_s}}{\partial x}, \tag{5.20}$$

where the chain-rule was applied to variables that depend directly on concentration, rather than directly on the x-coordinate. Clearly, if t_+^0 is to be approximately independent of c, then $\overline{\partial c_s}/\partial x$ must be concave-up, since D_s is a decreasing function of concentration. A constrained linear regression of this type, with inequality constraints amongst the regression coefficients to enforce the concavity requirement, is also a non-trivial problem.[75] These two non-trivial problems can actually be combined, however, in a way that "weakly enforces" but does not guarantee the concavity constraint if it is a poor fit to the data, by using a Monte Carlo simulated annealing fitting approach[76] to test low-order polynomial fits to the $\bar{c}_s(x)$ profiles with the constraint explicit, and then analytically differentiating the results and tabulating their spread to develop a local confidence interval on the derivative, $\overline{\partial c_s}/\partial x$. In this way, an uncertainty estimate for the derivative is arrived at, but fits to $\bar{c}_s(x)$ which yield the proper concavity for $\overline{\partial c_s}/\partial x$ will be preferentially represented

in the statistical average for $\overline{\partial c_s}/\partial x$ and $\Delta\left[\overline{\partial c_s}/\partial x\right]$. A similar approach was also taken for curve-fitting to the $\overline{D}_+^*(x)$ and $\overline{D}_-^*(x)$ steady-state data to eliminate polynomial fits that were not monotonically increasing near the edges, which could sometimes occur due to the smaller number of diffusion image points and the extrapolation to the edges determined from the other MRI techniques with higher image point densities. Dips in the diffusivity on the anodic side, and equivalently, crests on the cathodic side, would be physically inconsistent with the monotonically *decreasing* (and much smoother) $\bar{c}_s(x)$ profiles.

5.4 Experimental

5.4.1 Electrolyte Mixtures and *In Situ* Cell Preparation

All electrolyte mixtures were prepared in an argon-filled glovebox (0.6 ppm H_2O, 0.6 ppm O_2) using battery grade $LiPF_6$ ($\geq$ 99.99%, trace metals basis), ethylene carbonate (99%), propylene carbonate (99.7%), and dimethyl carbonate (99+%; all Sigma Aldrich). The use of PC was intended to improve low-temperature performance,[77] as it was previously determined that salt precipitation can be a significant problem with even moderate polarizations under this condition.[36] Though the mixture has the design specification EC/PC/DMC 5:2:3 (v/v), the densities of the solvent components measured at glove box temperature were used to prepare it in those fractions with the corresponding masses. All *in situ* MRI experiments were conducted with a 1.00 M $LiPF_6$ concentration, but a range of concentrations from 0.10 M to 2.00 M were prepared from the same solvent mix for the mass density (see Section **3.4.6**) and conductivity measurements. The design of the *in situ* cell has been reported previously,[24,35,36] and the same formation cycle conditions prior to cycling in the magnet as those of a previous investigation were employed here also,

again within the glovebox and using an Arbin BT2000 to deliver the current and monitor the potential.[36] As with the previous investigations, cells were prepared using lithium metal foil (high purity; Chemetall Foote Corporation) pressed onto the copper current collector on the anodic side, with graphite on copper foil (60 g m^{-2} active material loading; MTI) overlaid with a polypropylene separator (Targray) serving as the cathodic side, since this seems to produce more uniform electrodeposition of lithium metal in extreme overcharge conditions than simply cycling Li vs. Li. The inter-electrode spacing of the *in situ* cell varied between current staircases on account of variable compression of the malleable lithium metal electrode used to seal the active electrolyte volume, but is on the order of 2 mm, while the exposed electrode surface area has a diameter of 4.2 mm.

5.4.2 Conductivity Measurements

Ex situ conductivity measurements were made using a range of salt concentrations for the EC/PC/DMC solvent mixture from 0.10 M to 2.00 M. A two-electrode cell provided by Dr. Ion Halalay, of similar construction to that in Halalay, 1999,[78] was outfitted with Ni blocking electrodes and filled with the electrolyte mixtures in the glove box, using overfill Luer ports to ensure complete filling of the measuring volume (electrode diameter of $d = 2.27$ cm and inter-electrode spacing of $L = 2$ mm). Conductivity measurements were conducted using a Gamry Interface 1000 operating in potentiostatic mode about the OCV with an AC amplitude of 3 mV rms covering the 500 kHz to 250 Hz frequency range at 20 points/decade, inside a Dongguan Lixian Scientific HZ2006 environmental test chamber for thermal regulation with a minimum of 30 minutes allowed between measurements. The slope of the OCV as a guideline for when thermal equilibration had been achieved. On

account of the cable inductance at high frequencies for this setup,[79] the low-frequency branch only was fit to an equivalent circuit model appropriate to the cell geometry[80] consisting of a constant-phase element for the double-layer capacitance in series with a resistor, the latter being used to compute the conductivity,

$$\kappa = \frac{L}{\pi(d/2)^2 R_s}, \tag{5.21}$$

where R_s is the solution resistance. In all cases, the CPE behavior was found to be close to ideal. All fits were performed using the Marquardt-Levenberg algorithm package in the Gamry E-Chem Analyst software, with the latter also used to verify Kramers-Kroenig compliance within 1% over the fitting range.

5.4.3 *In Situ* CSI and DHK-SPRITE MRI

All *in situ* MRI experiments, for each current staircase (*i.e.* individual data run, as described in the introduction), were conducted using a Bruker 300WB NMR spectrometer (7 T) operating at 116 MHz for ^{7}Li and 282.3 MHz for ^{19}F, with a Diff50 gradient probe (maximum gradient strength of 2750 G/cm). An 8 mm, dual-tuned RF insert for simultaneous probing of ^{7}Li and ^{19}F was used, with the *in situ* cell designed to fit within this diameter. Current was supplied with an Autolab PGStat 30 potentiostat operating in galvanostatic mode, using shielded coaxial cables to run the current from the potentiostat (operating at a distance removed from the magnet) to the top of the magnet. A separate series of experiments with methanol in the *in situ* cell was used to develop a chemical shift thermometer to accurately calibrate the temperature actually realized within the active volume of the cell.

CS imaging, a pure-phase encode method of MRI,[81,82] was used for relatively rapid (~10 minutes) acquisition of build-up images during the transient evolution to the steady state, and then a series of three CS images at the steady state were averaged to define $\bar{c}_s(x)$, by normalization with another series of three CS images acquired prior to polarization to define the baseline.[35,36] Pure-phase encoding imaging is more robust against both B_0 and B_1 distortions introduced by the conductive surfaces of the electrodes and current collectors.[18,83] By normalizing against a consensus baseline image prior to polarization, relative changes in the signal intensity at each image point can be transformed into concentration data, which also compensates for field inhomogeneity. However, the combination of rapid relaxation for nuclei very near to the paramagnetic electrons on the conductive surfaces and, more significantly, interfacial distortion of B_1 disrupting echo formation,[28] does still result in some "dead space" near the electrodes for CS images,[32,34–36] and since there can also be gradient distortions during the application of the phase-encode pulse from the electrodes, a robust method of field-of-view (FOV) calibration is necessitated. This is achieved via DHK-SPRITE,[84] which makes use of pre-stabilized gradients to mitigate the gradient distortions and small-tip-angle irradiation to minimize the interfacial B_1 distortions. DHK-SPRITE has been demonstrated to generate a very accurate image along the inter-electrode spacing despite the presence of the conductive parts of the cell, thereby providing a high-fidelity image of the concentration gradient which can be reliably used to align the CS images and fulfill this FOV calibration function.[36] The trade-off that justifies using both techniques is that DHK-SPRITE images take relatively longer to acquire than CS images on account of the poorer signal-to-noise, but accurately capture

the edges, while CS images are smoother, enabling more accurate fitting and differentiation of the spatially-resolved concentration profiles obtained.

Owing to electroneutrality, and the previously established equivalence of ^{7}Li and ^{19}F CS images, only ^{19}F CS images and ^{19}F DHK-SPRITE images were used for the concentration profile determinations, since ^{19}F yields much better signal on account of its higher gyromagnetic ratio and higher spin count per ion in $LiPF_6$. CS image gradient strengths varied according to the spatial extent of the electrolyte active volume along the imaging direction in a given construction of the *in situ* cell, but were on the order of $-20\ \mathrm{G}\cdot\mathrm{cm}^{-1}$ to $+20\ \mathrm{G}\cdot\mathrm{cm}^{-1}$ over 32 equally-spaced imaging points using a $1\ \mathrm{ms}$ phase-encode time. Slice-selection for the active volume between the electrodes, to avoid excitation of trapped electrolyte not contributing to concentration gradient formation, was accomplished with a $100\ \mu\mathrm{s}$ slice pulse centred on a slice gradient of $-14.25\ \mathrm{G}\cdot\mathrm{cm}^{-1}$ of duration $300\ \mu\mathrm{s}$. As with previous studies, it was found that excellent signal-to-noise could be achieved using this imaging method with only 2 scans per gradient step. The recycle delay was set to 10 s to allow for optimal recovery of the ^{19}F signal (for ^{19}F on PF_6^- anions in a concentrated solution with an aprotic solvent, $T_1 \sim 2\ \mathrm{s}$). To achieve a complete image profile of the cell along the imaging direction, the frequency dimension of the CSI experiments is integrated over.

The ^{19}F DHK-SPRITE imaging experiments acquired upon reaching the steady state were conducted with a much larger FOV, since slice selection for the active volume is not possible with the ramped imaging gradient, to prevent aliasing of the residual electrolyte trapped behind the current collectors on filling and fold-in of background ^{19}F

signal from the probe. Here, 64 gradient steps for each of the positive and negative ramps were acquired with a maximum gradient strength of $66\ \mathrm{G}\cdot\mathrm{cm}^{-1}$. The excitation was achieved using a $2\ \mu\mathrm{s}$ broadband pulse at each gradient step, corresponding to a tip angle of $\sim 6°$, enabling a much shorter recycle delay of 365 ms between ramps, timed to deliver a total experiment time of 30 minutes with the 2k scans necessary for adequate signal-to-noise. The pre-stabilization delay prior to excitation at each gradient step was set to $500\ \mu\mathrm{s}$. To further boost the signal-to-noise, the multiple-free-induction-decay (FID) point modification[85] to the acquisition was implemented, with 8 FID points collected in quadrature with a dwell time of $1.6\ \mu\mathrm{s}$ atop a base phase-encoding time of $100\ \mu\mathrm{s}$, yielding a range of phase-encoding times up to $122.4\ \mu\mathrm{s}$. A chirp-z transform was then used to composite the image.

5.4.4 DHK-SPRITE Signal Calibration and CS Image Alignment

During the polarization process, substantial amounts of lithium metal are deposited on the graphite anode, since the current densities applied for the duration of the experiment relative to the meagre capacity of the small electrode constitute a massive over-charge. Etching of the metallic lithium anode also becomes noticeable as the experiment progresses. As a result, the edges of the images for all of the MRI techniques shift gradually, which complicates the simple normalization process described above. Since DHK-SPRITE images generate a faithful reproduction of the active volume irrespective of the location of the cell edges, it suffices to simply calibrate the signal for 1.00 M of electrolyte, $s_{1\mathrm{M}}$, from the first steady state image, when the deposition is negligible and the normalization

procedure is sound, and then apply this calibration factor to the signal for all subsequent steps:

$$c_{s,j}(x) = \frac{s_j(x)}{s_{1\mathrm{M}}}(1.00\ \mathrm{M}). \tag{5.22}$$

Matching linear regressions through the steady-state signal and concentration profiles of the first current step yields $s_{1\mathrm{M}}$, and then the signal $s_j(x)$ at each point in the FOV for all current steps $j > 1$ can be converted to the concentration associated with that signal, $c_{s,j}(x)$. The edges of the DHK-SPRITE images at each current step are re-evaluated by differentiating the images, and then applying a criterion that the edge is positively identified when the slope exceeds some multiple of the standard deviation of the differential fluctuations in a sample of the background region of the image, near the edge of the FOV (a multiple of 50 was taken as a very conservative threshold for the ratio of what could be construed as a true edge, versus merely a large fluctuation in the background of the image).

Having positively identified the edges in the DHK-SPRITE images at each current step, the next step in the analysis procedure was to align the CS images to DHK-SPRITE. A linear regression was performed to a suitable fitting region of the calibrated DHK-SPRITE signal centered on the middle of the cell, where the concentration gradient is most approximately linear. A similar region was defined for the steady-state CS images, and then trial FOVs for the CS images from a range of half the "expected" FOV to the full expected FOV were generated. As this alters the spacing between the image points, it provides a mechanism for matching the slopes of the gradients between the two techniques, based on a minimization of the root-mean-square error (RMSE) between them, which compensates for the shortening of the imaged cell length as a result of gradient distortions relative to

what would be expected if the FOV was calculated naively from the nominal gradient strengths.[36] Since both techniques are ultimately generating information about the same physical observable – the steady-state concentration gradient – this is a sound means of correcting for the distortions in the CS images as a result of perturbations to the gradient steps from the conductive parts, particularly to the small gradient steps relative to the large ones. Once the FOV is properly calibrated, an analogous procedure is used, with the RMSE difference to the DHK-SPRITE intercept instead, to compute the correct offset that aligns the CSI FOV to the DHK-SPRITE FOV, side-stepping the uncertainty about the edges of the CS images stemming from the dead space.

Polynomial curve fits to both the concentration gradient and the diffusion coefficient gradient were conducted with a curvature-constraining Monte Carlo regression, to generate fits with the necessary physical properties discussed in the Theory section. A generic simulated annealing approach was used, with the RMSE relative to the raw data used as the objective function. Trial solutions were generated from t-random-distributed combinations of the polynomial coefficients centered on the seed input coefficients (obtained by regular, least-squares regression) with spread determined by the 95% confidence intervals on the input coefficients. The curvature constraints – inequalities on the polynomial coefficients that would guarantee the curvature requirements – were verified prior to the RMSE calculations. A total of 5000 Monte Carlo steps were used for each fit, with the acceptance probability determined from the Boltzmann factor for the difference in RMSE between the trial solution and the previous optimal solution, with the temperature given by the Monte Carlo index raised to the 3/2-th power and scaled by the

characteristic order of magnitude for the quantity under consideration (*i.e.* dividing by 10^{-10} for the diffusivity curve fits).

5.4.5 *In Situ* ^{7}Li and ^{19}F P3D PFG-MRI

The *in situ* coupled PFG-NMR and MRI experiments conducted in the steady-state at each current step are essentially a CSI experiment with a one-shot bipolar pulse pair (BPP) PFG-NMR experiment substituted for the initial excitation.[35] The complete pulse sequence is provided in **Figure 5.2**, but the essential details become manifest by considering it in the individual blocks indicated in the figure. The BPP scheme splits the diffusion-encoding gradient into two oppositely-phased gradient pulses with a π refocusing pulse between them, intended for robust eddy current compensation.[86] By then unbalancing the gradients in the BPP blocks according to the one-shot BPP technique, inherent coherence transfer pathway selection of the gradient pulses is leveraged, substantially

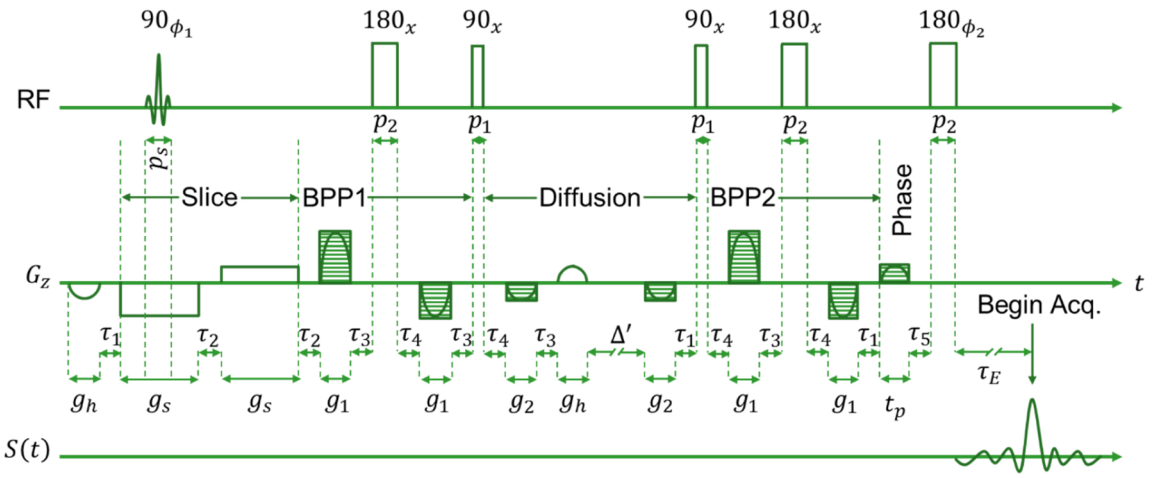

Figure 5.2 – P3D PFG-MRI pulse sequence, constructed by fusing a one-shot BPP stimulated echo PFG-NMR sequence with a CSI experiment, including initial selective excitation. An explanation of the various blocks and salient parameters is provided in the text.

reducing the phase cycle (and hence, the number of necessary scans).[87] The CS imaging experiment then begins where the stimulated echo underlying the one-shot BPP sequence refocuses.

The diffusion-gradient unbalancing requires a modification of the normal Stejskal-Tanner equation[88] for attenuation by diffusion in a PFG-NMR experiment, given by[89]

$$S(g) = S(0)\exp\left\{-D_i^*\gamma_i^2\delta^2 g^2\frac{4}{\pi^2}\left[\Delta - \frac{(5-3\alpha^2)}{16}\delta - \frac{(1-\alpha^2)}{2}\tau\right]\right\}, \quad (5.23)$$

where $S(g)$ is the attenuated signal at gradient strength g, which is the variable parameter for generating attenuation, γ_i is the gyromagnetic ratio of the nucleus i with self-diffusion rate D_i^*, δ is the gradient pulse duration (i.e. twice the length of the oppositely-phased gradient pulses in each BPP block), Δ is the diffusion time, τ is the interval between the two gradient pulses of a given BPP block, and α is the unbalancing factor for the one-shot scheme. The various numerical factors arise from the BPP, one-shot, and sine shaped-pulse modifications to the canonical stimulated-echo formulation of the PFG-NMR experiment to which the original Stejskal-Tanner equation applies. During the analysis of the diffusion dimension of the P3D PFG-MRI experiments, the diffusion coefficient is extracted by regressing the diffusion-gradient values against the signal attenuation in the diffusion dimension, for each of the image points in the spatial dimension.

The slice-selection parameters are the same as for the ^{19}F CSI experiments described above, but with a slightly longer pulse duration for ^{7}Li (150 μs vs. 100 μs) on account of the difference in gyromagnetic ratio. Maximum gradient strengths varied significantly over the temperature range examined, but were typically several hundred

G cm^{-1} for ^{7}Li, with the gradient strength of ^{19}F pegged to that of ^{7}Li by the ratio of the respective gyromagnetic ratios (approximately 30%). Attenuation in the diffusion dimension was observed with 8 diffusion-encoding gradient steps for both nuclei, using (cumulative) 2 ms gradient pulse durations ($2g_1$ in the pulse sequence of **Figure 5.2**), and a total diffusion time of $\Delta = 100$ ms, measured from the beginning of the first diffusion-encoding gradient of the BPP1 block to the first diffusion-encoding gradient of the BPP2 block. The same phase-encoding parameters for ^{19}F were used for the imaging block as for the ^{19}F CSI experiments; for ^{7}Li, correspondingly stronger gradient strengths were used, although the phase-encoding time was 800 µs for ^{7}Li. A total of 16 phase-encoding gradient steps for the imaging dimension were recorded for both nuclei, again with the appropriate 10 s recycle delay and a 4-scan phase cycle at each combination of gradient- and phase-encoding steps, resulting in a total experimental time of 50 minutes. This is why the steady-state condition is an essential feature for performing these experiments. The homospoil gradients were set with recommended Bruker parameters. For both nuclei, the same alignment procedure as discussed above for the ^{19}F CSI experiments was applied. However, because fewer points are available, the loss of one or two points along a sloping edge significantly reduces the size of the fitting region yielded by the imaging dimension, so the same signal calibration approached as applied for DHK-SPRITE was also employed, for both nuclei, prior to the alignment procedure for the PFG-MRI experiments as well.

5.4.6 Mass Density Measurements and Conversion to Partial Molar Volume

The partial molar volumes $V_{m,0}$ and $V_{m,s}$ of the solvent and salt, respectively, are extracted from mass density measurements, ρ, regressed against the mass fraction $y_s =$

$m_s/(m_s + m_0)$ of the added salt, shown in **Figure 5.3**. Under the assumption that the mass density is linear in the salt concentration over the entire concentration range examined, then[53,55]

$$\rho(y_s) = \left(M_s/V_{m,s}\right)y_s + \left(M_0/V_{m,0}\right)(1 - y_s), \tag{5.24}$$

where M_s and M_0 are the molar masses of the $LiPF_6$ and the solvent mixture, respectively. The molar mass of the solvent is arrived at by using the volume weights of the mixture formula, the mass densities of the components, and the total mass of solvent mixture added to the mass of salt for the given concentration. From this approach, the result is that $V_{m,0} = (7.45 \pm 0.02) \times 10^{-5}$ m^3 mol^{-1} and $V_{m,s} = (5.712 \pm 0.008) \times 10^{-5}$ m^3 mol^{-1}. This partial molar volume for $LiPF_6$ is in good accord with previous results,[53,55,94] although the partial molar volume of the solvent mixture is somewhat smaller than other studies. This is attributed to the considerably higher density stemming from the larger fraction of cyclic carbonates used in the mixture relative to those studies. The mass density measurements were carried out in an argon-filled glove box with a mean temperature of 31°C. While this

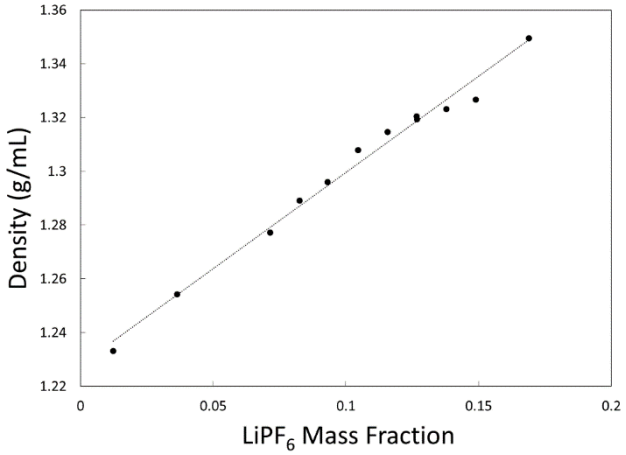

Figure 5.3 – Mass density as a function of salt mass fraction for $LiPF_6$ in EC/PC/DMC, 5:2:3 (v/v) at glove box temperature (31°C).

is lower than the 40°C at which the current staircase transport parameter analysis was carried out, the densities, and hence the partial molar volumes, change negligibly with temperature[95] – certainly insofar as other sources of error in the analysis are concerned.

5.5 Results and Discussion

5.5.1 Concentration Gradient Maps and Limiting Current Density as a Function of Temperature

The complete set of operating conditions under which the current staircases were collected is summarized in **Figure 5.4**, along with raw, interpolated ^{19}F CS images of the steady-state concentration gradients. Several features are apparent from this collection of the most basic results: 1) the limiting current decreases dramatically with decreasing temperature, and 2) the magnitude of the maximum achievable concentration gradient also decreases with decreasing temperature. The signal intensity in **Figure 5.4a** is normalized relative to the baseline signal intensity, and the sharp contrast in magnitude between how polarized the concentration can become at 25°C, where the final achieved steady-state is at a current density close to the limit, and -5°C, where the limiting current is between the final achieved steady-state gradient and one increment of initial staircase step from it. This suggests that at higher temperatures, the limiting current is more influenced by the marked reduction in available ions near cathodic side because of the massive extent of the concentration polarization, slowing the insertion kinetics (or rather, deposition kinetics in this case), while in the low-temperature case, the limiting current is more likely transport-limited on the anodic side, since the concentration polarization is not nearly as great. A phenomenological fit to the limiting current as a function of temperature can be developed,

arrived at by merely splitting the difference between the current staircase multiple at each temperature where the final, achievable steady state was reached and the subsequent step where the current interrupted before the steady state could form. This fits quite well ($R^2 = 0.994$) to an exponential function of temperature:

$$J_{\mathrm{Lim}}(T) \cong (10.1\ \mathrm{A\ m^{-2}})\exp(T/21.8°\mathrm{C}), \tag{5.25}$$

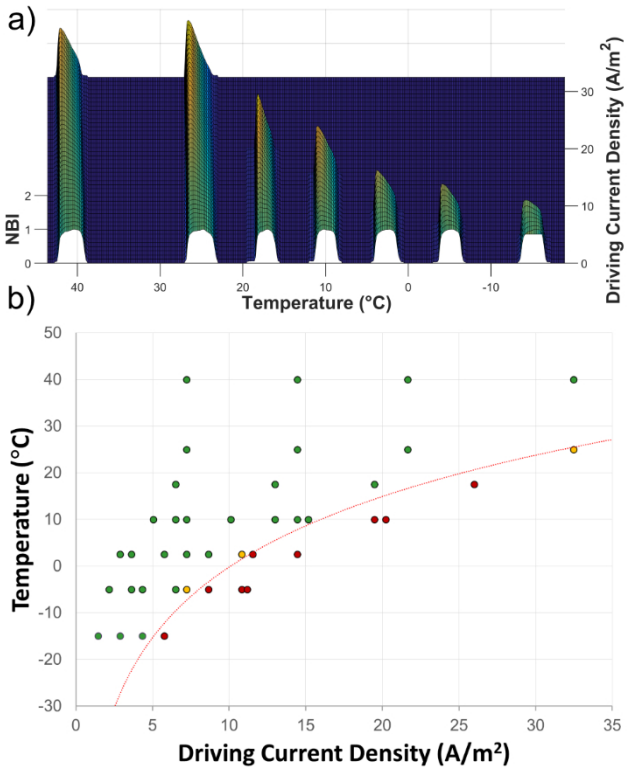

Figure 5.4 – a) Interpolated, baseline-normalized steady-state raw 19F CSI signal intensity profiles illustrating both the reduction in achievable current density with temperature, and the decrease in magnitude of the final formed concentration gradient. b) Schematic of the grid of operating conditions that were attempted, along with the phenomenological fit for the limiting current density. Green dots are successfully formed steady-state gradients, yellow dots were marginally results (*i.e.* the concentration gradient revealed by the images was relatively steady, but the overpotential was steadily increasing over the same time), and red dots indicate current staircase increments where the current interrupted well before steady-state conditions were achieved.

where $J_{\mathrm{Lim}}(T)$ is the limiting current density at temperature T. J_{Lim} was found to range from $\sim 32\ \mathrm{A\,m^{-2}}$ at 25°C down to $< 8\ \mathrm{A\,m^{-2}}$ for -5°C, or a fourfold reduction. While these current densities are certainly lower than what is achievable with state-of-the-art

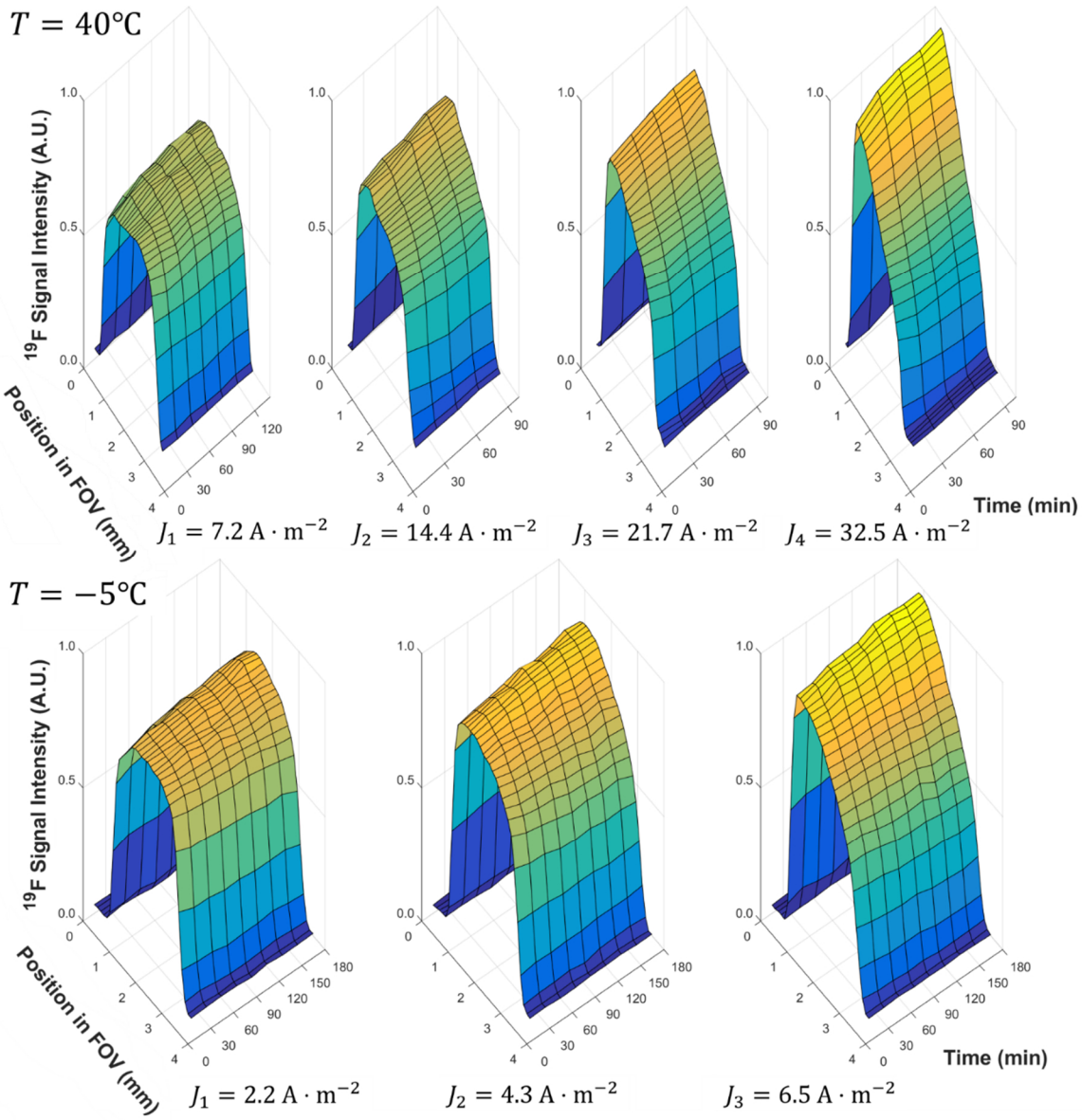

Figure 5.5 – Time series of raw ^{19}F CS images for the evolution to the steady state for 40°C and -5°C. Note the drastic difference in polarization relative to the applied current density.

batteries, it is necessary to point out that this electrolyte formulation was chosen for its potential low-temperature performance, rather than room-temperature rate capability, and indeed, other forms of resistance related to the non-optimal cell geometry will contribute to lowering the magnitude. Nevertheless, the form of the limiting current decrease with temperature, captured as it is by a simple exponential function, is quite interesting, suggesting the predominance of a single effect over this regime. A similar perspective is furnished by **Figure 5.5**, which provides the time series of ^{19}F CS images acquired in the buildup to the steady-state for the 40°C and -5°C current staircases; not only is the evolution slower in the latter, but again, the drastic difference in the extent of the concentration polarization is clear. At -5°C, the final series shows polarization that is not nearly as steep as at 40°C, but the 40°C images are nowhere near the predicted limiting current, whereas at -5°C, the next current increment is not achievable.

It is also instructive at this stage to present the raw ^{19}F DHK-SPRITE images for contrast with the CS images. In **Figure 5.6**, it is clear that the edges of the DHK-SPRITE images are much sharper in comparison to the CS images in **Figure 5.5**, and the shape of the concentration gradient is much more evident, demonstrating their effectiveness as FOV calibration standards for the CS images. **Figure 5.6** also contrasts concentration gradients for 40°C and -5°C, but as with **Figure 5.4**, these are in the steady-state, rather than being a time-lapse of the concentration gradient buildup during the transient regime between steps on the current staircase at the given temperatures. The identified active volume boundaries are marked with closed red dots, and the absolute difference corresponds quite well to the expected inter-electrode spacing, allowing, as mentioned previously, for the slightly

different amounts of protrusion of the malleable lithium metal electrode into the cell active volume marked by the ridge on the cell shaft in the inset of the figure. The marked position on the anodic side, where the concentration is increasing, serves as the zero point at each

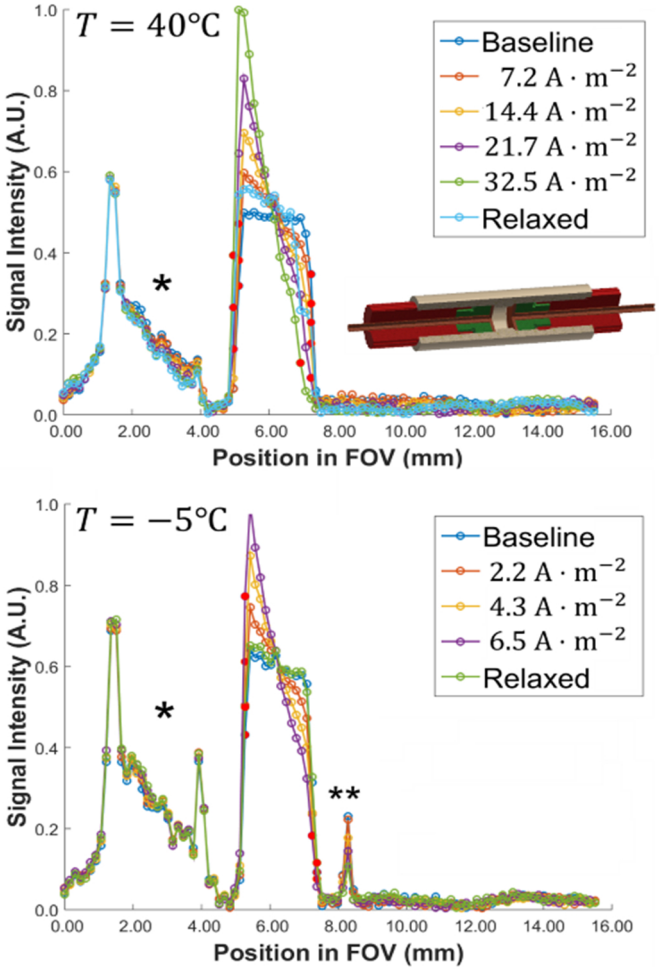

Figure 5.6 – Contrasting the steady-state ^{19}F DHK-SPRITE images for 40°C and -5°C, illustrating the greater edge encroachment in the former (marked by the closed red circles, for the identified edges) and the smaller overall polarization in the latter. The inset provides a design schematic of the *in situ* cell used in the measurements. The feature marked with the single asterisk is leftover electrolyte from the filling process trapped behind the lithium metal electrode (which sits in the ~1 mm region of no signal, between 4-5 mm in the FOV) and surrounding the ferrule (green component in the inset). For the -5°C image series, the double asterisk is excess electrolyte that was squeezed behind the graphite electrode during the refilling process after the formation cycle.

current step for the subsequent analysis. Also evident is the markedly increased amount of deposition in the 40°C case – corresponding to the much greater current densities applied for similar overall experimental durations of the completed current staircase – such that the cell edge has moved several full image points inward by the conclusion, corresponding to 200-300 μm in total length reduction. It is this process that contributes to the need for the extensive signal calibration and alignment between the various techniques in order to generate a commensurate lattice to which all of the results can be accurately mapped.

5.5.2 Attempt at Full Transport Characterization as a Function of Current Density for the 40°C Current Staircase

Having defined the boundaries of the active volume using the DHK-SPRITE results at the steady-state, the signal calibration and alignment procedures can then be carried out. Using equation (5.22), the calibrated concentration is overlaid on the raw image in **Figure 5.7a**, for the example of the 40°C current staircase. The identified edges are marked with red bars, and the fitting region for all subsequent analysis is marked with closed red dots. As can be seen, the slope of the concentration gradient essentially uniformly increases – at least, in terms of a linear approximation about the center of the cell – with the increasing multiples of the staircase current increment. This is consistent with previous findings,[29] and is also consistent with the lowest order approximation of a series expansion of equation (5.3), which can predict this linear region of the concentration gradient from bulk *ex situ* transport measurements, again as demonstrated previously (and verified for the present experiments also).[36] **Figure 5.7b** shows the results of the alignment procedure for all of the images collected at the specified conditions; the ^{19}F CS images used to quantitatively

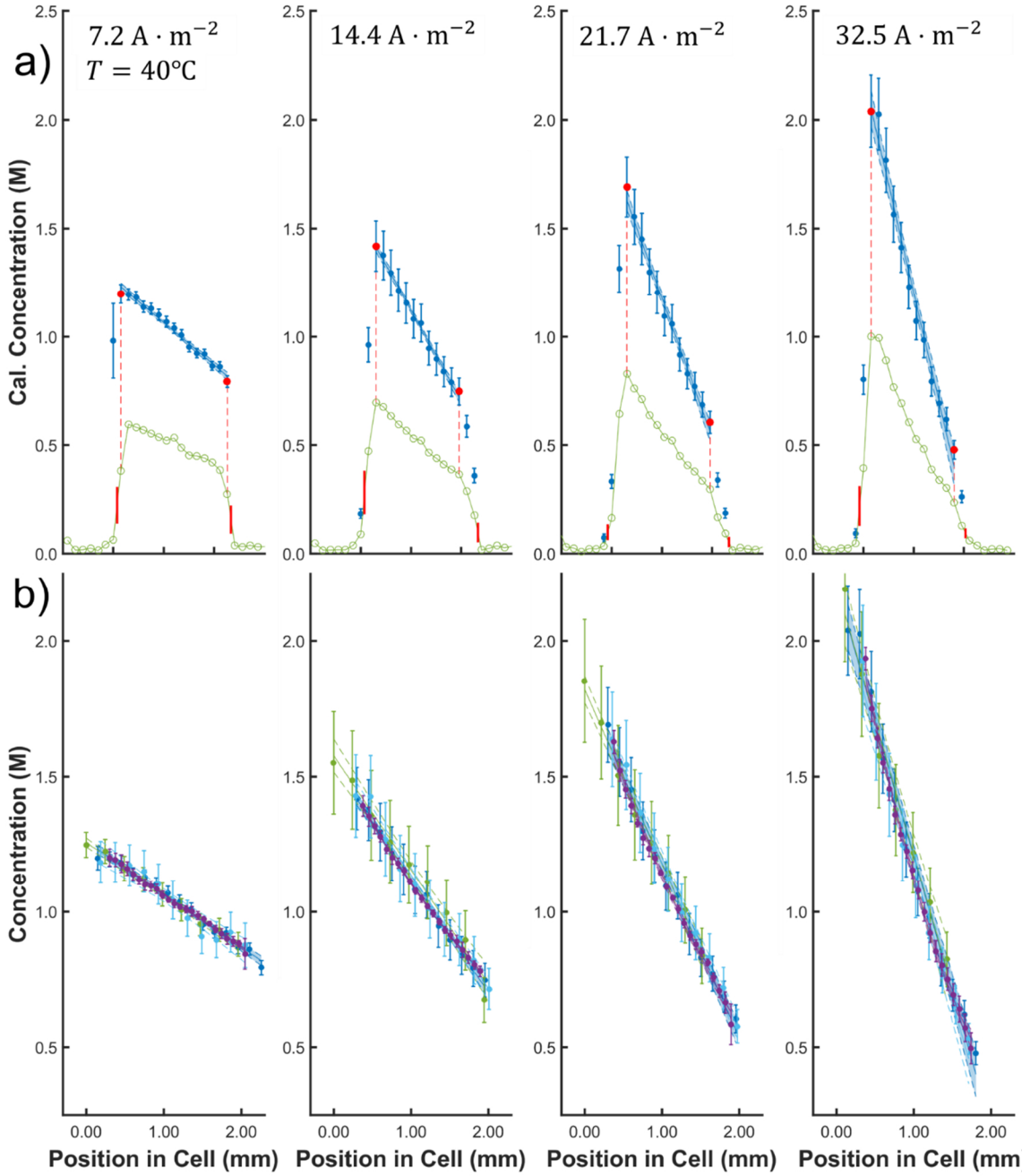

Figure 5.7 – a) The signal calibration and fitting region identification of the steady-state ^{19}F DHK-SPRITE images for the 40°C current staircase used to align all other MRI techniques and properly calibrate their FOVs in light of the gradient distortions to which they are susceptible but DHK-SPRITE is immune. b) The result of the alignment procedure for ^{19}F CSI (purple dots), the imaging dimension for ^{7}Li P3D PFG-MRI (green dots), and the imaging dimension for ^{19}F P3D PFG-MRI (cyan dots).

determine the concentration gradient, and the projected imaging dimensions of the ^{7}Li and ^{19}F P3D PFG-MRI experiments, which are essential for properly positioning the measured self-diffusivities at the correct location across the inter-electrode spacing. Clearly, there is some bandwidth to the results of the alignment procedure; this is inevitable, as it approximates the increasingly nonlinear concentration gradients with straight lines for the purpose of alignment. An obvious future improvement would therefore be to implement a more sophisticated form of shape recognition to accomplish the same end. In particular, this inexact alignment led to a high degree of uncertainty that compromised the quality of the quantitative results that was obtainable for many of the staircase steps for all of the current staircases except for 40°C, so the emphasis of the study now turns to the exclusive analysis of these results, until some general qualitative conclusions are drawn based on the insights gleaned from the 40°C results.

The spatially-resolved diffusion coefficients extracted from the P3D PFG-MRI diffusion dimensions using equation (5.23) are arrayed across the inter-electrode spacing in **Figure 5.8**, using the results of the signal calibration and alignment procedures applied to the imaging dimension. The polynomial fits to the data are, in all cases, of quadratic order to avoid over-fitting the data but still retain the curvature when evident. The curvature-constraining Monte Carlo algorithm discussed in the Theory section in the context of the concentration gradient fitting was used here to disfavor fits which were not monotonically increasing from the anodic to the cathodic side of the cell, on account of the inconsistency with the concentration profiles such a scenario would pose. The aim of the curve fitting is to generate a common series of points to allow measurements based on the

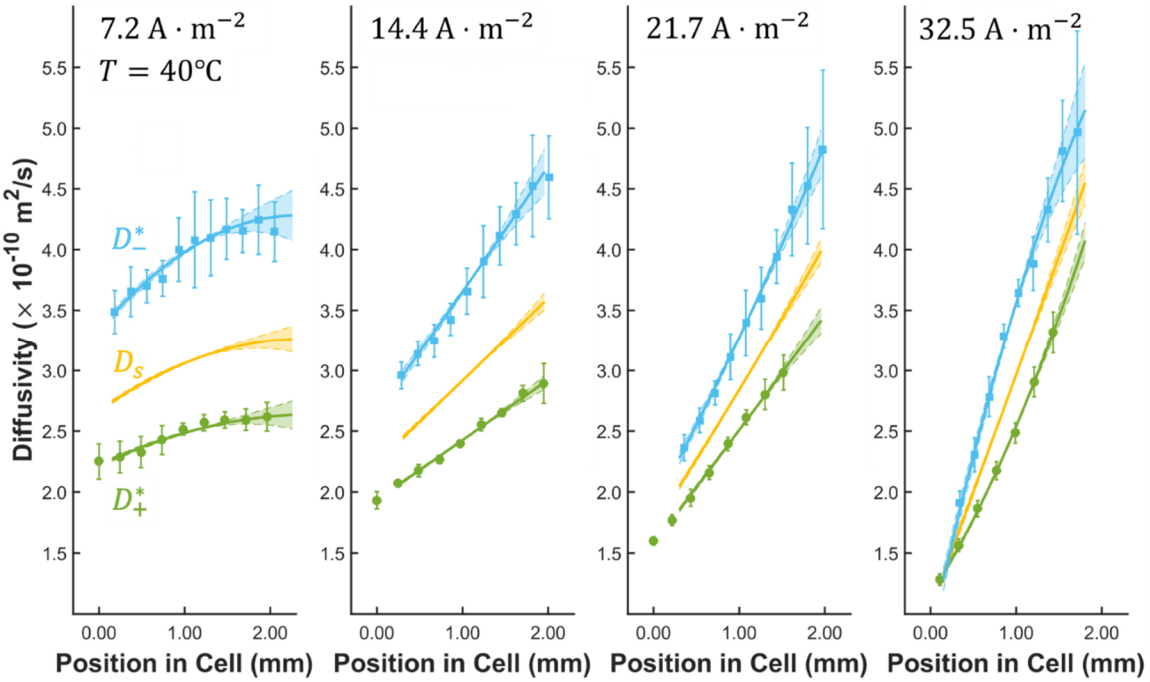

Figure 5.8 – The distribution of cation and anion self-diffusivities, D_+^* and D_-^*, along with the salt diffusivity, across the inter-electrode spacing as a function of driving current density at 40°C. Note the closure of the gap between the higher D_-^* and the lower D_+^* on both sides of the cell at extreme polarization.

incommensurate lattices of image points from the different MRI techniques, with different probed nuclei and resolutions, to be sensibly combined.

At the initial current step, the D_-^* are approximately double those of the D_+^*, consistent with previous results[47] (and indeed, it was verified that the diffusivity measured near the vicinity of the 1.00 M image point was, within uncertainty, consistent with the result of performing the measurements in that study on bulk solutions of the presently employed electrolyte mixture). With increased current densities, the gap between D_-^* and D_+^* gradually diminishes on the anodic side of the cell, along with a general reduction in the magnitudes of both – and therefore the salt diffusivity, computed with equation (5.18)

and entering the steady-state equation, (5.3) – as would be expected on account of the greatly increased salt concentration here as the polarization is increased. The gap between D_-^* and D_+^* also decreases on the cathodic side of the cell; here the increasingly dilute salt concentration is evidently allowing both ions to diffuse more independently.

The polynomial fits to $D_s(x)$ from **Figure 5.8** are then used as inputs to equation (5.3) for a series of fixed values of t_+^0 in the range 0.2-0.4, consistent with previous findings for similar electrolyte mixtures,[34,35,41,47,48,53] to furnish estimate expressions for the concentration gradients (with 30 replicates per t_+^0 value to generate an unbiased estimate). The regression coefficients to these latter expressions are, in turn, taken as the seeds to the curvature-constrained Monte Carlo regression for the actual concentration profiles, in order to contend with extreme sensitivity of t_+^0 to the slope of $\overline{\partial c_s}/\partial x$, particularly in the vicinity of the edges. The algorithm performs a RMSE minimization of cubic regression solutions to $\bar{c}_s(x)$ using t-random distributed combinations of the seed coefficients, plus t-random distributed values of the intercept from the alignment procedure, since the quadratic estimate expression for $\overline{\partial c_s}/\partial x$ leaves the constant of integration unspecified on transferring the regression coefficients to a cubic expression for $\bar{c}_s(x)$. In this way, uncertainty on the precise local value of the derivative, which is crucial for the subsequent transport analysis, is transferred to uncertainty on the fit to $\bar{c}_s(x)$, which has smaller sensitivity coefficients in the uncertainty expressions for $\mathcal{D}_{-_0}$ and κ. However, if these guiding regression coefficients yield poor RMSE relative to the measured data, then obviously they will be, at best, metastable solutions in the Monte Carlo analysis and will be supplanted by more accurate fits as increasing numbers of Monte Carlo runs are

generated. As noted previously, this process also provides a way of obtaining a concrete uncertainty on the derivative, through the spread of the analytically differentiated $\bar{c}_s(x)$ fit coefficients, which is otherwise a non-trivial problem.[74]

The results of this $\overline{\partial c_s}/\partial x$ estimation procedure are presented in **Figure 5.9**, along with the resulting $\bar{c}_s(x)$ fits and associated confidence intervals, compared against the original data. Clearly, the resulting $\overline{\partial c_s}/\partial x$ estimates are very tightly bounded as intended, which is necessary for any reasonable level of precision in estimating t_+^0 and κ from the experimental data. The uncertainty trade-off with the $\bar{c}_s(x)$ fits is also evident, although despite the widened confidence intervals, the consensus fits are still an eminently reasonable match to the data at all current steps. **Figure 5.9** also presents the derived quantities $\bar{c}_0(x)$ and $\bar{c}_T(x)$, with the confidence intervals for these generated from cubic regressions to the original, aligned $\bar{c}_s(x)$ data rather than the Monte Carlo fits to $\bar{c}_s(x)$, in order to avoid propagating unnecessary excess uncertainty (since the Monte Carlo process is primarily intended to get estimates of $\overline{\partial c_s}/\partial x$ with the correct curvature and rigorous confidence intervals). These are computed using partial molar volumes from the salt and solvent extracted from mass density measurements (refer to Section **5.4.6**). The solvent concentrations are similar to those observed in mixtures of EC/EMC[53] and EC/DEC,[55] although this EC/PC/DMC mixture has a considerably higher fraction of the denser cyclic carbonates, so the solvent partial molar volume is lower, and hence, the local solvent concentration is somewhat higher. The effect of the polarization is that solvent mixture is necessarily displaced from the anodic toward the cathodic side of the cell, though the overall increase in the total concentration on the anodic side is faster than the decrease in

the solvent concentration there, potentially modifying the solvation structure of the cations in this region.[67,90,91]

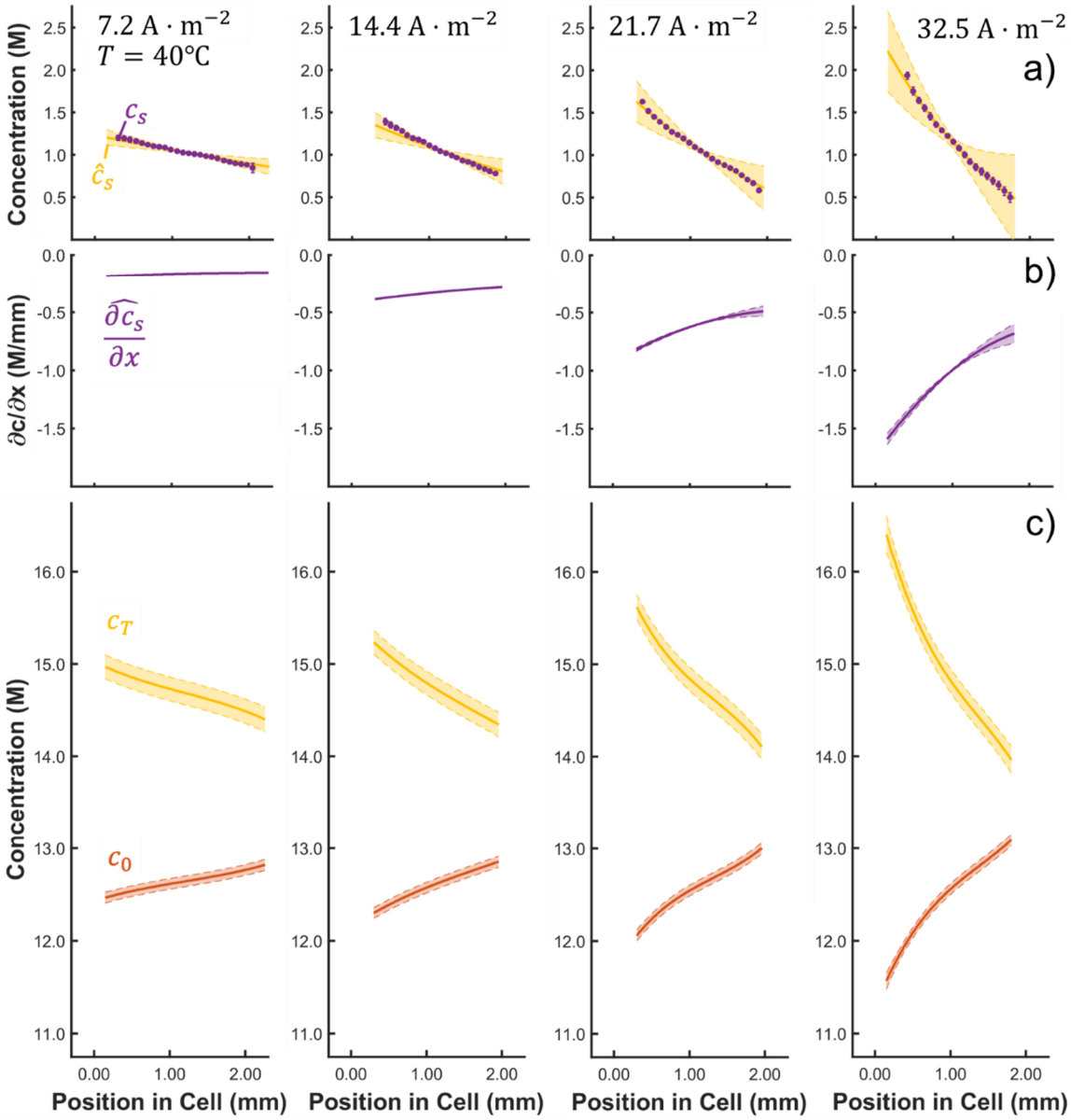

Figure 5.9 – a) Resulting uncertainty on $\bar{c}_s(x)$ from the curvature-constrained Monte Carlo estimation of $\overline{\partial c_s}/\partial x$, at 40°C. b) The curvature-constrained estimates of $\overline{\partial c_s}/\partial x$, computed with the aim of reducing numerical instability in the subsequent estimates of t_+^0 and κ. c) The computed $\bar{c}_0(x)$ and $\bar{c}_T(x)$ profiles, demonstrating modest solvent displacement from the anodic side of the cell, relative to the overall changes in total concentration across the cell due to the salt concentration polarization.

Figure 5.10a presents the t_+^0 estimates derived from the $\overline{\partial c_s}/\partial x$ estimates of **Figure 5.9** and the $\overline{D}_s(x)$ fits from **Figure 5.8**, computed using equation (5.3). As has been previously observed, t_+^0 is relatively constant across the cell (i.e. uniform with salt concentration) at low degrees of concentration polarization. However, as the concentration gradient grows with each increase in the applied current density, t_+^0 increasingly deviates from this behavior, dropping dramatically on the cathodic side of the cell, resulting in a significant reduction of the fraction of the current carried by the cations in this region migrating toward the cathode. Nevertheless, a related measure, the transport number τ_+,

$$\tau_+ = \frac{D_+^*}{D_+^* + D_-^*}, \tag{5.26}$$

remains near its initial steady-state value on this side of the cell. While t_+^0 measures the fraction of positively charged species contributing to the current in a region, τ_+ is a measure of the fraction of total motion of a species – charged and uncharged. If τ_+ remains near its initial value at small concentration polarization while t_+^0 plummets, it signals that the cations are increasingly found in mobile, but on average less- or un-charged, aggregates (*i.e.* ion pairs). This is, however, difficult to reconcile with the increasingly dilute concentrations with increasing current density on the cathodic side of the cell. Conversely, on the anodic side, t_+^0 remains relatively high – in fact, increasing slightly on going from the second to the third current density – despite the increased salt concentration there and the reduction in D_+^* and D_s. This implies that everything is slowing down on the anodic side as the salt concentration increases and the solution becomes more congested, but the relative contribution of the cations to the overall current is still similar. Combined with the

apparent displacement of the solvent (**Figure 5.9c**), the solvation structure – and potentially the conduction mechanism – of the cations is likely changing.[65–67,91]

These processes have a knock-on effect for the estimated ionic conductivity, κ, calculated using the t_+^0 estimate, D_+^*, and D_-^* via equations (5.8), (5.16), and (5.17) and plotted in **Figure 5.10b**. The values fall precipitously across the cell from the anodic to the cathodic side on going from the second to the third current density, and then are small all across the cell on going from the third to the fourth. This progression obviously mirrors what is happening in the t_+^0 distribution, because κ is quite sensitive to t_+^0. The outcome is nevertheless that the ionic conductivity across the cell is heavily depressed, which would lead to significant concentration resistance in these high polarization scenarios – ultimately limiting the current that can be drawn from the cell. Further insight can be gained by mapping *ex situ* bulk measurements of κ made at a variety of concentrations (**Figure 5.11**) onto the measured *in situ* $\bar{c}_s(x)$ profile, using the fitting functions[53,55] which yielded the curves in **Figure 5.10b**:

$$\kappa_{\mathrm{Ex}}(c_s) = A_1 c_s^3 + A_2 c_s^{1.5} + A_3 c_s, \tag{5.27}$$

where κ_{Ex} denotes a bulk measurement of the ionic conductivity. The correspondence between the two measures of the ionic conductivity are in reasonable agreement at the low current density steps, where the concentration polarization is not extreme. However, $\kappa[\bar{c}_s(x)]$ significantly departs from the mapped $\kappa_{\mathrm{Ex}}[\bar{c}_s(x)]$ predictions for the third and fourth current density steps.

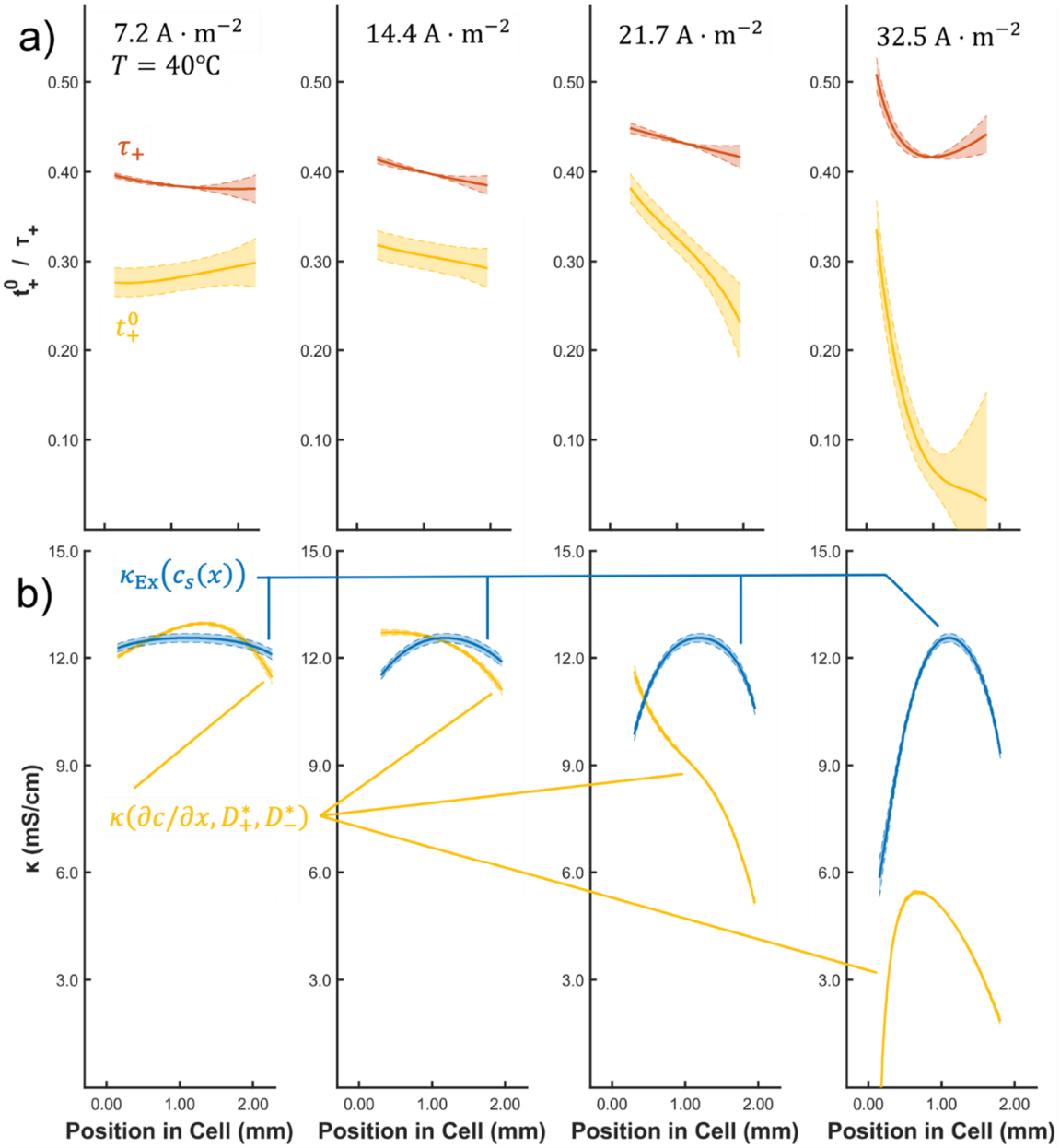

Figure 5.10 – a) The spatial distribution of the transference number, t_+^0, and the transport number, τ_+, across the inter-electrode spacing as a function of applied current density at 40°C, showing a dramatic decrease in t_+^0 at high polarization, with little effect on τ_+. b) Comparison of ionic conductivity values derived from the *in situ* measurements and a mapping of the bulk, *ex situ* values onto the concentration profile, again signaling departure at large concentration polarizations.

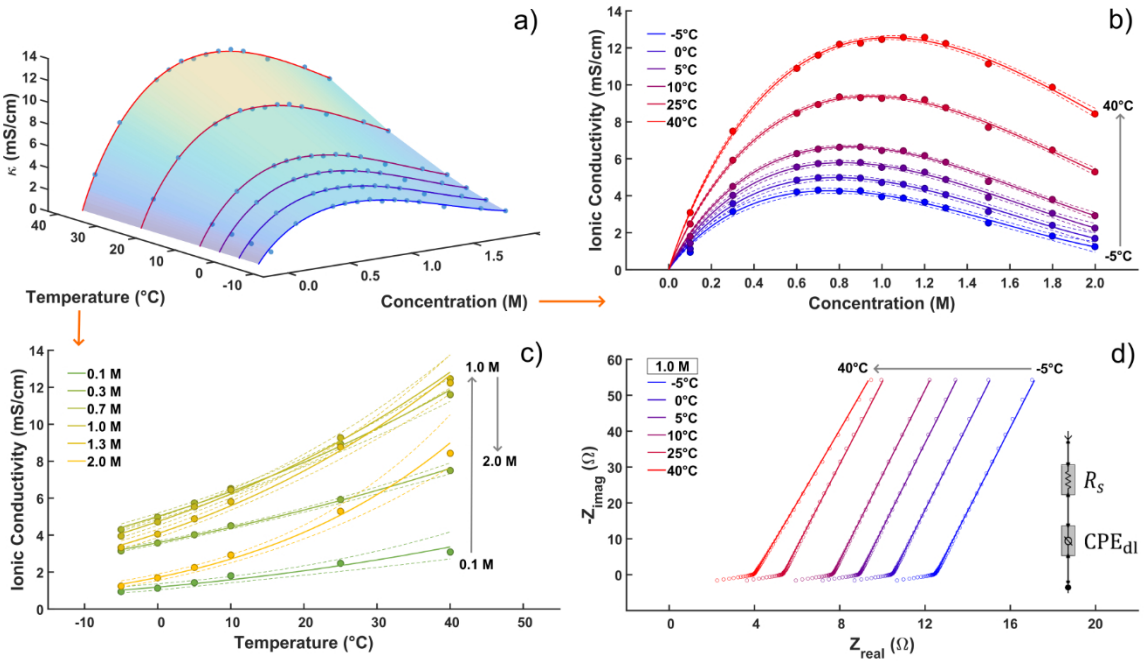

Figure 5.11 – a) Ionic conductivity measurements as a function of both temperature and concentration, with b) concentration fits at each temperature given by equation (5.27), and c) variable-temperature fits at a series of concentrations via an Arrhenius law. d) Nyquist plots at 1.0 M for the entire temperature series, demonstrating the fitting to the equivalent circuit model given in the inset.

To examine one final piece of the puzzle, the mapped *ex situ* ionic conductivities are used in conjunction with the PFG-NMR self-diffusivities to compute profiles of the effective diffusivities, D_i^{eff}, given by equations (5.9-11), across the cell. These explicitly account for ion pairing (although no higher-order aggregates directly), and separate out a diffusivity attributed specifically to it. From these measurements, it is also possible to compute the ion pairing fraction, again mapped into the *in situ* cell electrode domain, via equation (5.13). These findings are provided in **Figure 5.12**, and illustrate that the same trends as **Figure 5.8** for the individual ionic diffusivities are observed, but with considerably reduced magnitudes. Additionally, the effective pair diffusivity, while

between the effective ion diffusivities at all positions (i.e. concentrations) for the initial two moderate current densities, becomes larger than both effective ion diffusivities on the anodic side, again indicative of increased congestion and reduced transport there. However, it actually drops below the cation diffusivity at the highest polarizations. At the same time,

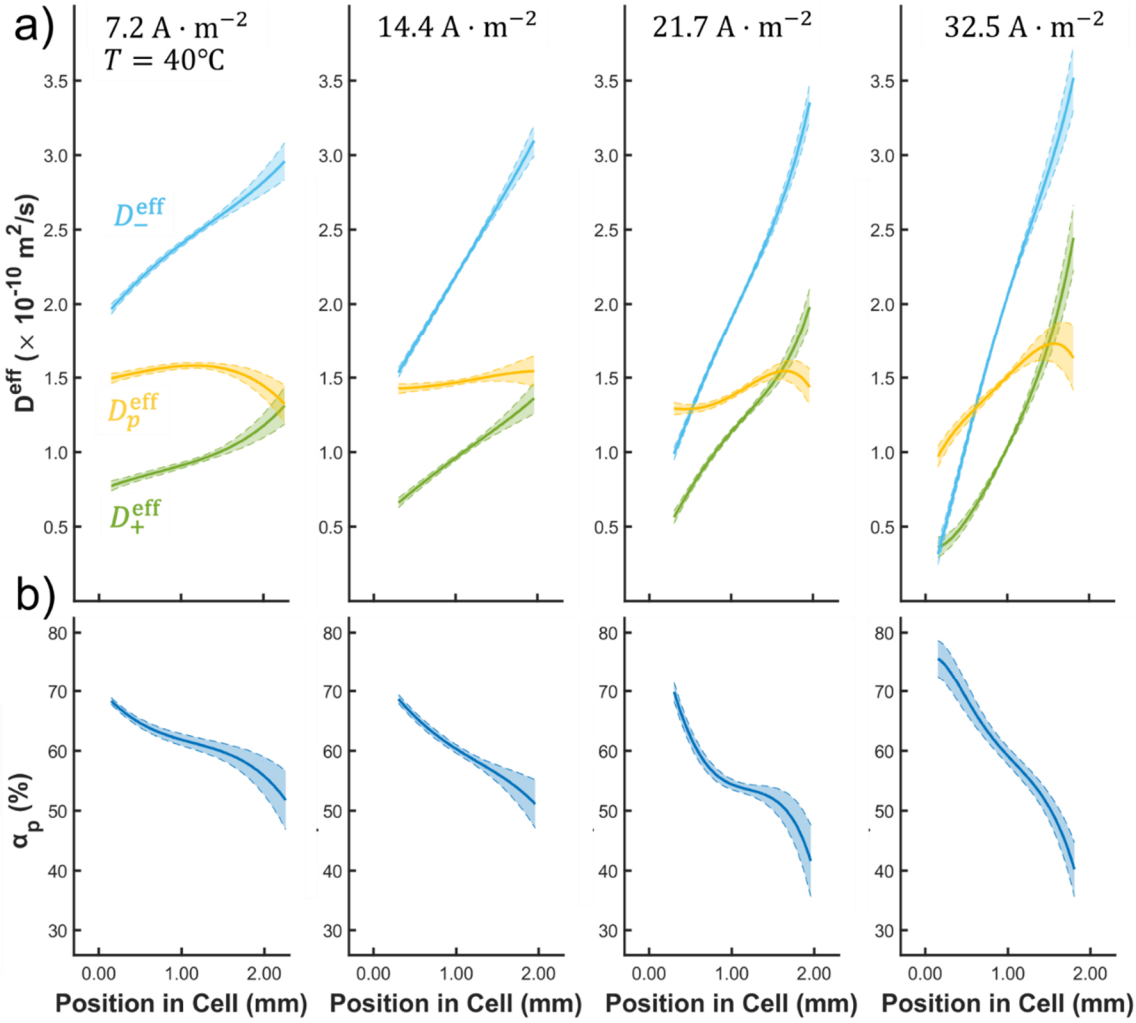

Figure 5.12 – a) Spatial distributions of the effective cationic, anionic, and ion pair diffusivities, D_i^{eff}, as a function of applied current density at 40°C, demonstrating trends consistent with the self-diffusivities and the steady-state concentration profiles. b) The ion pairing fraction, α_p, as a function of salt concentration distribution across the cell, computed, as with the D_i^{eff}, by mapping bulk, *ex situ* ionic conductivity measurements onto the measured concentration profiles. Again, the expected trends are observed.

the pairing fraction is progressing with increasing current density in the way that would be expected; increasing on the concentrated (anodic) side of the cell, and decreasing on the (cathodic) side, with the value in the middle approximately constant at around 60% – which, while seemingly quite large, is actually consistent with previous *ex situ* measurements for this type of electrolyte mixture at elevated temperature.[47]

Combining the insights from **Figures 5.8-5.12**, the inevitable conclusion is that, while the *in situ* approach to calculating spatially-resolved transport parameters for electrolytes with the CST formalism coupled with the generalized Darken relations can make reasonable estimates at low to moderate electrolyte polarizations, an extremely accurate measurement of the local concentration gradient is required for large polarizations. Bereft of this accuracy, quantitative predictions for the transference number will not be consistent with the otherwise qualitatively sound conclusions from the concentration and diffusivity profiles. They will also differ from the qualitative conclusions drawn from the effective diffusivities arrived at by the composite approach of mapping *ex situ* conductivity measurements onto the concentration profile. **Figure 5.13** demonstrates that the transference number predicted via this approach, using

$$t_+^0 = \frac{D_+^{\mathrm{eff}}}{D_\kappa}, \tag{5.28}$$

where D_κ is determined using the Nernst-Einstein equation (which is equation (5.12) above), yields results much more consistent with this qualitative picture. The failure of the prediction at high polarizations cannot be traced to the assumption of the generalized Darken relations, or the assumed constancy of the partial molar volumes under polarization (which would break down in the event that the solvent migration predicted in **Figure 5.9**

leads to partitioning of the ternary mixture, another effect that is important to investigate, and could be readily accomplished with ^{1}H CSI). The fault lies with the application of the steady-state condition in equation (5.3), since this generates the transference number estimate upon which the ionic conductivity measurement clearly hinges, as demonstrated in **Figure 5.10**. Since equation (5.3) uses the directly measured variables $\overline{D}_s(x)$ and $\overline{\partial c_s}/\partial x$, the issue lies with the accuracy of one of these. However, the efficacy of the conductivity mapping strategy for determining the effective diffusivities – and particularly the pairing fraction – demonstrates that the spatial distribution of the PFG-NMR *self*-diffusivities is reasonably sound. Therefore, despite the very careful precautions with curve-fitting $\overline{\partial c_s}/\partial x$, increased accuracy in the highly polarized regime is evidently

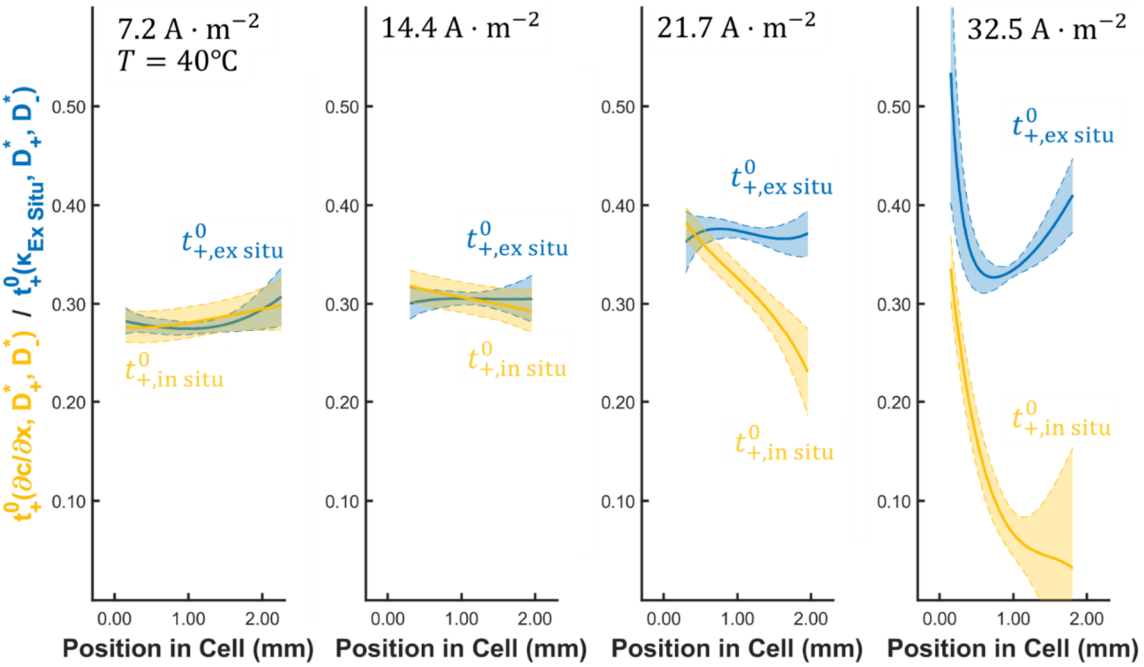

Figure 5.13 – Comparison of the transference number prediction purely from *in situ* diffusivity and concentration gradient measurements with the transference number predicted by combining *ex situ* conductivity measurements solely with the *in situ* diffusivity measurements.

required. This would require a higher imaging point density, and greater fidelity near the edges of the cell, particularly on the cathodic side. With the former, phase-encoding methods will quickly encounter the situation where the imaging is too slow to adequately capture the evolving processes in the cell, even under steady-state conditions. However, the long T_2 values of ions in the electrolyte could be leveraged in conjunction with an approach like Difftrain[92] to potentially circumvent this issue. With a sufficiently high image point density, perhaps more accurate models than simple polynomials for the concentration gradient could be fit with sufficiently high certainty that estimates near the dead spaces in the cell would suitably precise, thereby addressing the latter issue.

5.5.3 Qualitative Conclusions from Variable-Temperature, Spatially-Resolved Diffusivity Measurements

Returning to the analysis of the limiting currents in **Figures 5.4-5.5**, the *in situ* self-diffusivity measurements taken in isolation can provide additional qualitative information regarding the causes, particularly at low temperature. Comparing the evolution of D_+^* in particular across the current staircases at temperatures -5°C, 10°C, 25°C, and 40°C in **Figures 5.14-5.15**, it is clear that in all cases – as would be expected – the diffusivities decrease as the electrolyte polarization increases, leading to greatly increased salt concentration on the anodic side. However, at 40°C and 10°C, consulting **Figure 5.4**, the highest current densities are quite far from the predicted limiting currents from equation (5.25), and the trend in the lowest D_+^* value, nearest the anode, is approximately linear with

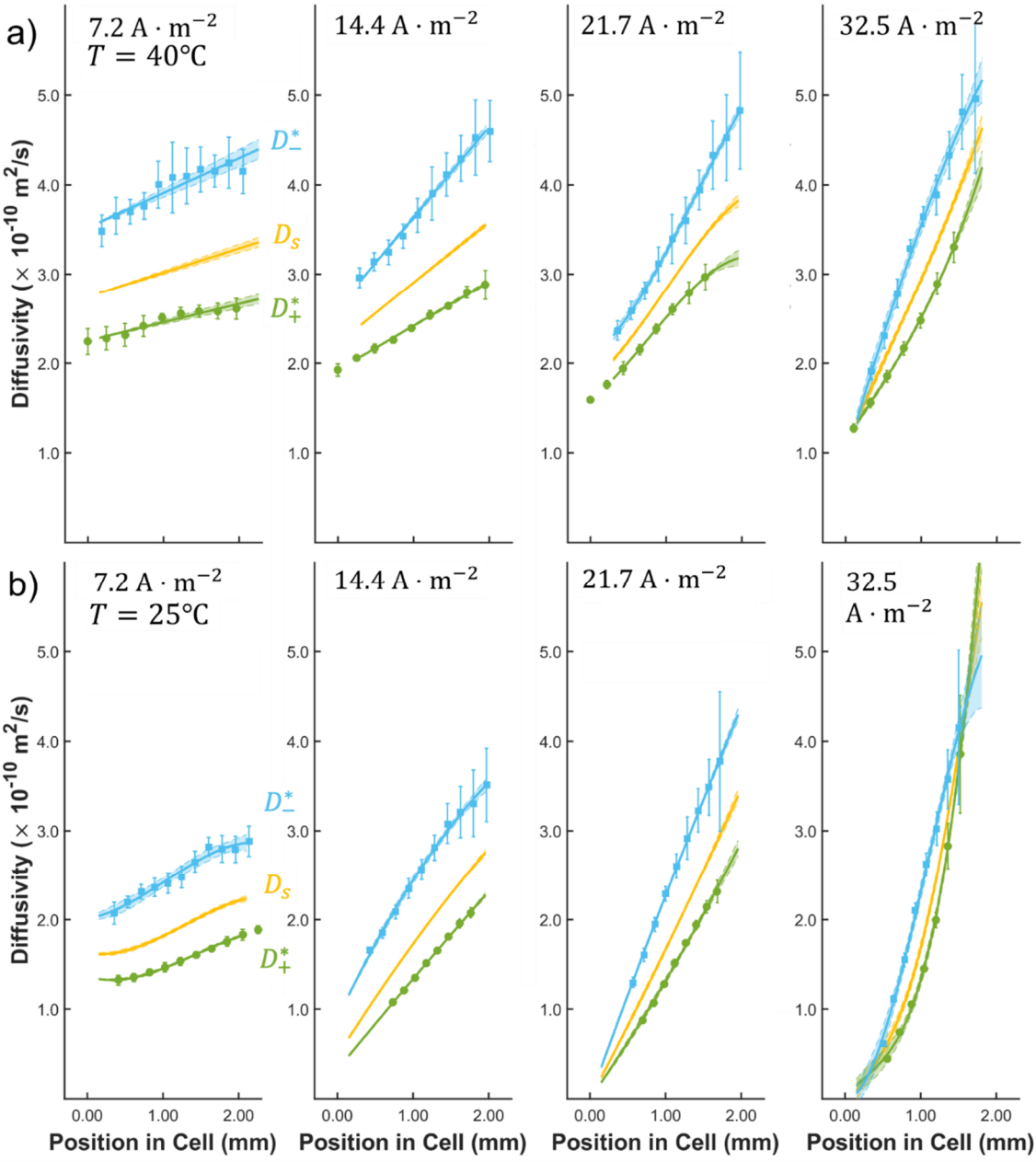

Figure 5.14 – The evolution of the in situ PFG-NMR self-diffusivities at a) 40°C and b) 25°C as a function of applied current density.

current density. For 25°C and -5°C, the final achieved steady states are much closer to the limiting current density, and the downward trend in this anode-proximal D_+^* value exhibits a much more curving approach towards zero. While in the case of 25°C, where the final

current density at which a steady state is realized is very close to the predicted limit, the concentration on the cathodic side is also severely depleted, yet this is clearly not the case at -5°C. It is often assumed that the limiting current arises when the cathodic side has depleted all of the locally available lithium ions,[52] leading to a rapid increase in the charge-transfer resistance, and essentially a "lock-up" of the insertion kinetics. However, **Figures 5.4** and **5.15** demonstrate that at low temperature, it is actually diffusion limitation on the anodic side that seizes up the current, wherein the resistance increase would be due primarily to mass transport failure in the electrolyte. This highlights the importance of careful electrolyte design for lithium-ion battery systems intended to operate in low-

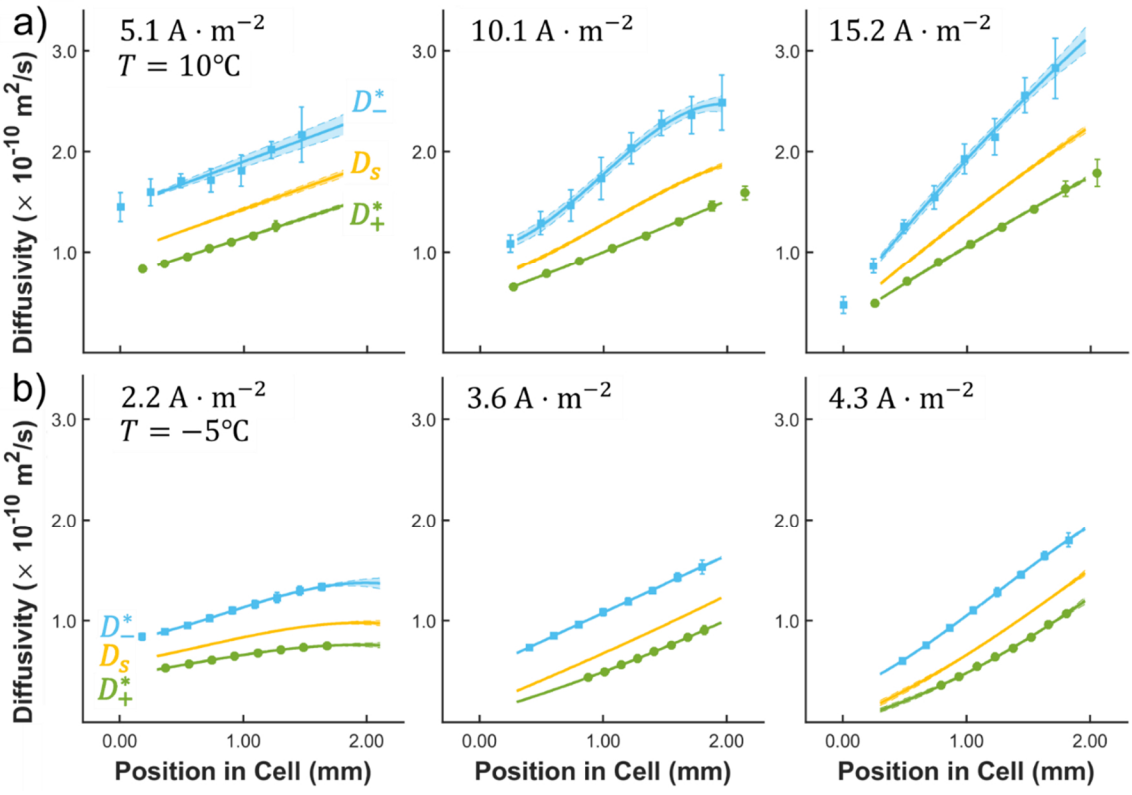

Figure 5.15 – The evolution of the *in situ* PFG-NMR self-diffusivities at a) 10°C and b) -5°C as a function of applied current density.

temperature environments,[93] and demonstrates that bulk measurements of electrolyte properties at low temperature may not provide sufficient information for informed decisions about electrolyte design, without considering how the local electrolyte transport properties will change under even fairly modest concentration polarizations.

5.6 Summary and Conclusions

A series of MRI techniques were applied to an *in situ* lithium-ion cell operating at a variety of temperatures and current densities, in order to quantify the transport parameters for the electrolyte in a CST framework with spatial resolution. Qualitative insights linking the local diffusivity, particularly on the anodic side and at low temperature, to the mechanism of limiting current behavior have been demonstrated. It was determined, however, that for accurate transference number quantification with spatial resolution at extreme electrolyte concentration polarizations, a highly accurate measurement of the local concentration gradient is necessary, particularly on the cathodic side of the cell, where the gradient is less extreme while the concentration becomes quite low at large current densities. Nevertheless, the framework developed herein, with sufficient improvements on the experimental side, could theoretically be used not only for electrochemical model testing and validation, but also potentially comprehensive electrolyte characterization.

5.7 References

(1) IEA. *Global EV Outlook 2019*; Paris, 2019.

(2) Zhu, G.; Wen, K.; Lv, W.; Zhou, X.; Liang, Y.; Yang, F.; Chen, Z.; Zou, M.; Li, J.; Zhang, Y.; et al. Materials Insights into Low-Temperature Performances of Lithium-Ion Batteries. *J. Power Sources* **2015**, *300*, 29–40.

(3) Jaguemont, J.; Boulon, L.; Dubé, Y. A Comprehensive Review of Lithium-Ion Batteries Used in Hybrid and Electric Vehicles at Cold Temperatures. *Appl. Energy* **2016**, *164*, 99–114.

(4) Gallagher, K. G.; Trask, S. E.; Bauer, C.; Woehrle, T.; Lux, S. F.; Tschech, M.; Lamp, P.; Polzin, B. J.; Ha, S.; Long, B.; et al. Optimizing Areal Capacities through Understanding the Limitations of Lithium-Ion Electrodes. *J. Electrochem. Soc.* **2016**, *163* (2), A138–A149.

(5) Waldmann, T.; Hogg, B.-I.; Wohlfahrt-Mehrens, M. Li Plating as Unwanted Side Reaction in Commercial Li-Ion Cells – A Review. *J. Power Sources* **2018**, *384* (November 2017), 107–124.

(6) Shkrob, I. A.; Rodrigues, M.-T. F.; Dees, D. W.; Abraham, D. P. Fast Charging of Li-Ion Cells: Part II. Nonlinear Contributions to Cell and Electrode Polarization. *J. Electrochem. Soc.* **2019**, *166* (14), A3305–A3313.

(7) Tippmann, S.; Walper, D.; Balboa, L.; Spier, B.; Bessler, W. G. Low-Temperature Charging of Lithium-Ion Cells Part I: Electrochemical Modeling and Experimental Investigation of Degradation Behavior. *J. Power Sources* **2014**, *252*, 305–316.

(8) Ahmed, R.; El Sayed, M.; Arasaratnam, I.; Tjong, J.; Habibi, S. R. Reduced-Order Electrochemical Model Parameters Identification and State of Charge Estimation for Healthy and Aged Li-Ion Batteries—Part II: Aged Battery Model and State of Charge Estimation. *IEEE J. Emerg. Sel. Top. Power Electron.* **2014**, *2* (3), 678–690.

(9) Plett, G. L. *Battery Management Systems, Volume I: Battery Modeling*; Artech

House Publishers, 2015.

(10) Nyman, A.; Zavalis, T. G.; Elger, R.; Behm, M.; Lindbergh, G. Analysis of the Polarization in a Li-Ion Battery Cell by Numerical Simulations. *J. Electrochem. Soc.* **2010**, *157* (11), A1236.

(11) Ji, Y.; Zhang, Y.; Wang, C.-Y. Li-Ion Cell Operation at Low Temperatures. *J. Electrochem. Soc.* **2013**, *160* (4), A636–A649.

(12) Mastali Majdabadi, M.; Farhad, S.; Farkhondeh, M.; Fraser, R. A.; Fowler, M. Simplified Electrochemical Multi-Particle Model for LiFePO4 Cathodes in Lithium-Ion Batteries. *J. Power Sources* **2015**, *275*, 633–643.

(13) Harks, P. P. R. M. L.; Mulder, F. M.; Notten, P. H. L. In Situ Methods for Li-Ion Battery Research: A Review of Recent Developments. *J. Power Sources* **2015**, *288*, 92–105.

(14) Tripathi, A. M.; Su, W.-N.; Hwang, B. J. In Situ Analytical Techniques for Battery Interface Analysis. *Chem. Soc. Rev.* **2018**, *47* (3), 736–851.

(15) Zhang, Z.; Martin, J.; Wu, J.; Wang, H.; Promislow, K.; Balcom, B. J. Magnetic Resonance Imaging of Water Content across the Nafion Membrane in an Operational PEM Fuel Cell. *J. Magn. Reson.* **2008**, *193* (2), 259–266.

(16) Cattaneo, A. S.; Villa, D. C.; Angioni, S.; Ferrara, C.; Melzi, R.; Quartarone, E.; Mustarelli, P. Operando Electrochemical NMR Microscopy of Polymer Fuel Cells. *Energy Environ. Sci.* **2015**, *8* (8), 2383–2388.

(17) Britton, M. M.; Bayley, P. M.; Howlett, P. C.; Davenport, A. J.; Forsyth, M. In Situ, Real-Time Visualization of Electrochemistry Using Magnetic Resonance

Imaging. *J. Phys. Chem. Lett.* **2013**, *4* (17), 3019–3023.

(18) Romanenko, K.; Forsyth, M.; O'Dell, L. A. New Opportunities for Quantitative and Time Efficient 3D MRI of Liquid and Solid Electrochemical Cell Components: Sectoral Fast Spin Echo and SPRITE. *J. Magn. Reson.* **2014**, *248*, 96–104.

(19) Bray, J. M.; Davenport, A. J.; Ryder, K. S.; Britton, M. M. Quantitative, In Situ Visualization of Metal-Ion Dissolution and Transport Using 1 H Magnetic Resonance Imaging. *Angew. Chemie Int. Ed.* **2016**, *55* (32), 9394–9397.

(20) Serial, M. R.; Velasco, M. I.; Maldonado Ochoa, S. A.; Zanotto, F. M.; Dassie, S. A.; Acosta, R. H. Magnetic Resonance Imaging in Situ Visualization of an Electrochemical Reaction under Forced Hydrodynamic Conditions. *ACS Omega* **2018**, *3* (12), 18630–18638.

(21) Ilott, A. J.; Trease, N. M.; Grey, C. P.; Jerschow, A. Multinuclear in Situ Magnetic Resonance Imaging of Electrochemical Double-Layer Capacitors. *Nat. Commun.* **2014**, *5* (1), 4536.

(22) Forse, A. C.; Griffin, J. M.; Merlet, C.; Carretero-Gonzalez, J.; Raji, A.-R. O.; Trease, N. M.; Grey, C. P. Direct Observation of Ion Dynamics in Supercapacitor Electrodes Using in Situ Diffusion NMR Spectroscopy. *Nat. Energy* **2017**, *2* (3), 16216.

(23) Tang, M.; Sarou-Kanian, V.; Melin, P.; Leriche, J.-B.; Ménétrier, M.; Tarascon, J.-M.; Deschamps, M.; Salager, E. Following Lithiation Fronts in Paramagnetic Electrodes with in Situ Magnetic Resonance Spectroscopic Imaging. *Nat.*

Commun. **2016**, *7* (1), 13284.

(24) Krachkovskiy, S. A.; Foster, J. M.; Bazak, J. D.; Balcom, B. J.; Goward, G. R. Operando Mapping of Li Concentration Profiles and Phase Transformations in Graphite Electrodes by Magnetic Resonance Imaging and Nuclear Magnetic Resonance Spectroscopy. *J. Phys. Chem. C* **2018**, *122* (38), 21784–21791.

(25) Chandrashekar, S.; Trease, N. M.; Chang, H. J.; Du, L.-S.; Grey, C. P.; Jerschow, A. 7Li MRI of Li Batteries Reveals Location of Microstructural Lithium. *Nat. Mater.* **2012**, *11* (4), 311–315.

(26) Chang, H. J.; Ilott, A. J.; Trease, N. M.; Mohammadi, M.; Jerschow, A.; Grey, C. P. Correlating Microstructural Lithium Metal Growth with Electrolyte Salt Depletion in Lithium Batteries Using 7 Li MRI. *J. Am. Chem. Soc.* **2015**, *137* (48), 15209–15216.

(27) Chandrashekar, S.; Oparaji, O.; Yang, G.; Hallinan, D. Communication— 7 Li MRI Unveils Concentration Dependent Diffusion in Polymer Electrolyte Batteries. *J. Electrochem. Soc.* **2016**, *163* (14), A2988–A2990.

(28) Ilott, A. J.; Mohammadi, M.; Chang, H. J.; Grey, C. P.; Jerschow, A. Real-Time 3D Imaging of Microstructure Growth in Battery Cells Using Indirect MRI. *Proc. Natl. Acad. Sci.* **2016**, *113* (39), 10779–10784.

(29) Sethurajan, A. K.; Foster, J. M.; Richardson, G.; Krachkovskiy, S. A.; Bazak, J. D.; Goward, G. R.; Protas, B. Incorporating Dendrite Growth into Continuum Models of Electrolytes: Insights from NMR Measurements and Inverse Modeling. *J. Electrochem. Soc.* **2019**, *166* (8), A1591–A1602.

(30) Chien, P.-H.; Feng, X.; Tang, M.; Rosenberg, J. T.; O'Neill, S.; Zheng, J.; Grant, S. C.; Hu, Y.-Y. Li Distribution Heterogeneity in Solid Electrolyte Li 10 GeP 2 S 12 upon Electrochemical Cycling Probed by 7 Li MRI. *J. Phys. Chem. Lett.* **2018**, *9* (8), 1990–1998.

(31) Klett, M.; Giesecke, M.; Nyman, A.; Hallberg, F.; Lindström, R. W.; Lindbergh, G.; Furó, I. Quantifying Mass Transport during Polarization in a Li Ion Battery Electrolyte by in Situ 7 Li NMR Imaging. *J. Am. Chem. Soc.* **2012**, *134* (36), 14654–14657.

(32) Krachkovskiy, S. A.; Pauric, A. D.; Halalay, I. C.; Goward, G. R. Slice-Selective NMR Diffusion Measurements: A Robust and Reliable Tool for In Situ Characterization of Ion-Transport Properties in Lithium-Ion Battery Electrolytes. *J. Phys. Chem. Lett.* **2013**, *4* (22), 3940–3944.

(33) Klamor, S.; Zick, K.; Oerther, T.; Schappacher, F. M.; Winter, M.; Brunklaus, G. 7 Li in Situ 1D NMR Imaging of a Lithium Ion Battery. *Phys. Chem. Chem. Phys.* **2015**, *17* (6), 4458–4465.

(34) Sethurajan, A. K.; Krachkovskiy, S. A.; Halalay, I. C.; Goward, G. R.; Protas, B. Accurate Characterization of Ion Transport Properties in Binary Symmetric Electrolytes Using In Situ NMR Imaging and Inverse Modeling. *J. Phys. Chem. B* **2015**, *119* (37), 12238–12248.

(35) Krachkovskiy, S. A.; Bazak, J. D.; Werhun, P.; Balcom, B. J.; Halalay, I. C.; Goward, G. R. Visualization of Steady-State Ionic Concentration Profiles Formed in Electrolytes during Li-Ion Battery Operation and Determination of Mass-

Transport Properties by in Situ Magnetic Resonance Imaging. *J. Am. Chem. Soc.* **2016**, *138* (25), 7992–7999.

(36) Bazak, J. D.; Krachkovskiy, S. A.; Goward, G. R. Multi-Temperature in Situ Magnetic Resonance Imaging of Polarization and Salt Precipitation in Lithium-Ion Battery Electrolytes. *J. Phys. Chem. C* **2017**, *121* (38), 20704–20713.

(37) Forster, J. D.; Harris, S. J.; Urban, J. J. Mapping Li + Concentration and Transport via In Situ Confocal Raman Microscopy. *J. Phys. Chem. Lett.* **2014**, *5* (11), 2007–2011.

(38) Yamanaka, T.; Nakagawa, H.; Tsubouchi, S.; Domi, Y.; Doi, T.; Abe, T.; Ogumi, Z. In Situ Raman Spectroscopic Studies on Concentration Change of Electrolyte Salt in a Lithium Ion Model Battery with Closely Faced Graphite Composite and LiCoO 2 Composite Electrodes by Using an Ultrafine Microprobe. *Electrochim. Acta* **2017**, *234*, 93–98.

(39) Takamatsu, D.; Yoneyama, A.; Asari, Y.; Hirano, T. Quantitative Visualization of Salt Concentration Distributions in Lithium-Ion Battery Electrolytes during Battery Operation Using X-Ray Phase Imaging. *J. Am. Chem. Soc.* **2018**, *140* (5), 1608–1611.

(40) Capiglia, C.; Saito, Y.; Kageyama, H.; Mustarelli, P.; Iwamoto, T.; Tabuchi, T.; Tukamoto, H. 7Li and 19F Diffusion Coefficients and Thermal Properties of Non-Aqueous Electrolyte Solutions for Rechargeable Lithium Batteries. *J. Power Sources* **1999**, *81–82*, 859–862.

(41) Aihara, Y.; Bando, T.; Nakagawa, H.; Yoshida, H.; Hayamizu, K.; Akiba, E.;

Price, W. S. Ion Transport Properties of Six Lithium Salts Dissolved in γ-Butyrolactone Studied by Self-Diffusion and Ionic Conductivity Measurements. *J. Electrochem. Soc.* **2004**, *151* (1), A119.

(42) Stolwijk, N. A.; Wiencierz, M.; Obeidi, S. Self-Diffusion versus Ion Conduction in Polymer Electrolytes: On the Occurrence of Pairs, Triplets, and Higher-Order Clusters. *Electrochim. Acta* **2007**, *53* (4), 1575–1583.

(43) Zhao, J.; Wang, L.; He, X.; Wan, C.; Jiang, C. Determination of Lithium-Ion Transference Numbers in LiPF[Sub 6]–PC Solutions Based on Electrochemical Polarization and NMR Measurements. *J. Electrochem. Soc.* **2008**, *155* (4), A292.

(44) Stolwijk, N. A.; Obeidi, S. Combined Analysis of Self-Diffusion, Conductivity, and Viscosity Data on Room Temperature Ionic Liquids. *Electrochim. Acta* **2009**, *54* (5), 1645–1653.

(45) Hayamizu, K. Temperature Dependence of Self-Diffusion Coefficients of Ions and Solvents in Ethylene Carbonate, Propylene Carbonate, and Diethyl Carbonate Single Solutions and Ethylene Carbonate + Diethyl Carbonate Binary Solutions of LiPF 6 Studied by NMR. *J. Chem. Eng. Data* **2012**, *57* (7), 2012–2017.

(46) Stolwijk, N. A.; Kösters, J.; Wiencierz, M.; Schönhoff, M. On the Extraction of Ion Association Data and Transference Numbers from Ionic Diffusivity and Conductivity Data in Polymer Electrolytes. *Electrochim. Acta* **2013**, *102*, 451–458.

(47) Krachkovskiy, S. A.; Bazak, J. D.; Fraser, S.; Halalay, I. C.; Goward, G. R. Determination of Mass Transfer Parameters and Ionic Association of LiPF 6 : Organic Carbonates Solutions. *J. Electrochem. Soc.* **2017**, *164* (4), A912–A916.

(48) Feng, Z.; Higa, K.; Han, K. S.; Srinivasan, V. Evaluating Transport Properties and Ionic Dissociation of $LiPF_6$ in Concentrated Electrolyte. *J. Electrochem. Soc.* **2017**, *164* (12), A2434–A2440.

(49) Villaluenga, I.; Pesko, D. M.; Timachova, K.; Feng, Z.; Newman, J.; Srinivasan, V.; Balsara, N. P. Negative Stefan-Maxwell Diffusion Coefficients and Complete Electrochemical Transport Characterization of Homopolymer and Block Copolymer Electrolytes. *J. Electrochem. Soc.* **2018**, *165* (11), A2766–A2773.

(50) Hafezi, H.; Newman, J. Verification and Analysis of Transference Number Measurements by the Galvanostatic Polarization Method. *J. Electrochem. Soc.* **2000**, *147* (8), 3036.

(51) Valøen, L. O.; Reimers, J. N. Transport Properties of LiPF[Sub 6]-Based Li-Ion Battery Electrolytes. *J. Electrochem. Soc.* **2005**, *152* (5), A882.

(52) Zhou, J.; Danilov, D.; Notten, P. H. L. A Novel Method for the In Situ Determination of Concentration Gradients in the Electrolyte of Li-Ion Batteries. *Chem. - A Eur. J.* **2006**, *12* (27), 7125–7132.

(53) Nyman, A.; Behm, M.; Lindbergh, G. Electrochemical Characterisation and Modelling of the Mass Transport Phenomena in LiPF6-EC-EMC Electrolyte. *Electrochim. Acta* **2008**, *53* (22), 6356–6365.

(54) Zugmann, S.; Fleischmann, M.; Amereller, M.; Gschwind, R. M.; Wiemhöfer, H. D.; Gores, H. J. Measurement of Transference Numbers for Lithium Ion Electrolytes via Four Different Methods, a Comparative Study. *Electrochim. Acta* **2011**, *56* (11), 3926–3933.

(55) Lundgren, H.; Behm, M.; Lindbergh, G. Electrochemical Characterization and Temperature Dependency of Mass-Transport Properties of LiPF6 in EC:DEC. *J. Electrochem. Soc.* **2014**, *162* (3), A413–A420.

(56) Wohde, F.; Balabajew, M.; Roling, B. Li + Transference Numbers in Liquid Electrolytes Obtained by Very-Low-Frequency Impedance Spectroscopy at Variable Electrode Distances. *J. Electrochem. Soc.* **2016**, *163* (5), A714–A721.

(57) Ehrl, A.; Landesfeind, J.; Wall, W. A.; Gasteiger, H. A. Determination of Transport Parameters in Liquid Binary Lithium Ion Battery Electrolytes. *J. Electrochem. Soc.* **2017**, *164* (4), A826–A836.

(58) Landesfeind, J.; Gasteiger, H. A. Temperature and Concentration Dependence of the Ionic Transport Properties of Lithium-Ion Battery Electrolytes. *J. Electrochem. Soc.* **2019**, *166* (14), A3079–A3097.

(59) Doyle, M.; Fuller, T. F.; Newman, J. Modeling of Galvanostatic Charge and Discharge of the Lithium/Polymer/Insertion Cell. *J. Electrochem. Soc.* **1993**, *140* (6), 1526.

(60) Di Domenico, D.; Stefanopoulou, A.; Fiengo, G. Lithium-Ion Battery State of Charge and Critical Surface Charge Estimation Using an Electrochemical Model-Based Extended Kalman Filter. *J. Dyn. Syst. Meas. Control* **2010**, *132* (6), 061302.

(61) Chaturvedi, N. A.; Klein, R.; Christensen, J.; Ahmed, J.; Kojic, A. Algorithms for Advanced Battery-Management Systems. *IEEE Control Syst.* **2010**, *30* (3), 49–68.

(62) Xue, K.-H.; Plett, G. L. A Convective Transport Theory for High Rate Discharge in Lithium Ion Cells. *Electrochim. Acta* **2013**, *87*, 575–590.

(63) Tanim, T. R.; Rahn, C. D.; Wang, C.-Y. A Temperature Dependent, Single Particle, Lithium Ion Cell Model Including Electrolyte Diffusion. *J. Dyn. Syst. Meas. Control* **2015**, *137* (1), 011005.

(64) Newman, J.; Thomas-Alyea, K. E. *Electrochemical Systems*, 3rd ed.; John Wiley & Sons, 2004.

(65) Borodin, O.; Smith, G. D. Quantum Chemistry and Molecular Dynamics Simulation Study of Dimethyl Carbonate: Ethylene Carbonate Electrolytes Doped with LiPF 6. *J. Phys. Chem. B* **2009**, *113* (6), 1763–1776.

(66) Takeuchi, M.; Kameda, Y.; Umebayashi, Y.; Ogawa, S.; Sonoda, T.; Ishiguro, S.; Fujita, M.; Sano, M. Ion–Ion Interactions of LiPF6 and LiBF4 in Propylene Carbonate Solutions. *J. Mol. Liq.* **2009**, *148* (2–3), 99–108.

(67) Ganesh, P.; Jiang, D.; Kent, P. R. C. Accurate Static and Dynamic Properties of Liquid Electrolytes for Li-Ion Batteries from Ab Initio Molecular Dynamics. *J. Phys. Chem. B* **2011**, *115* (12), 3085–3090.

(68) Maier, J. Salt Concentration Polarization of Liquid Electrolytes and Determination of Transport Properties of Cations, Anions, Ion Pairs and Ion Triples. *Electrochim. Acta* **2014**, *129* (X), 21–27.

(69) Krishna, R.; van Baten, J. M. The Darken Relation for Multicomponent Diffusion in Liquid Mixtures of Linear Alkanes: An Investigation Using Molecular Dynamics (MD) Simulations. *Ind. Eng. Chem. Res.* **2005**, *44* (17), 6939–6947.

(70) Trimble, L. .; Finn, D.; Cosgarea, A. A Mathematical Analysis of Diffusion Coefficients in Binary Systems. *Acta Metall.* **1965**, *13* (5), 501–507.

(71) Kim, S. U.; Srinivasan, V. A Method for Estimating Transport Properties of Concentrated Electrolytes from Self-Diffusion Data. *J. Electrochem. Soc.* **2016**, *163* (14), 2977–2980.

(72) Danilov, D.; Notten, P. H. L. Mathematical Modelling of Ionic Transport in the Electrolyte of Li-Ion Batteries. *Electrochim. Acta* **2008**, *53* (17), 5569–5578.

(73) Gouverneur, M.; Schmidt, F.; Schönhoff, M. Negative Effective Li Transference Numbers in Li Salt/Ionic Liquid Mixtures: Does Li Drift in the "Wrong" Direction? *Phys. Chem. Chem. Phys.* **2018**, *20* (11), 7470–7478.

(74) Cordero, R. R.; Roth, P. On Two Methods to Evaluate the Uncertainty of Derivatives Calculated from Polynomials Fitted to Experimental Data. *Metrologia* **2005**, *42* (1), 39–44.

(75) Wahl, F.; Espinasse, T. Polynomial Regression under Shape Constraints. **2014**.

(76) Birge, J. R.; Louveaux, F. *Introduction to Stochastic Programming*, 2nd ed.; Springer Series in Operations Research and Financial Engineering; Springer New York: New York, NY, 2011.

(77) Zhang, S. .; Xu, K.; Allen, J. .; Jow, T. . Effect of Propylene Carbonate on the Low Temperature Performance of Li-Ion Cells. *J. Power Sources* **2002**, *110* (1), 216–221.

(78) Halalay, I. C. Versatile Cell for Complex Permittivity Measurements on Liquids. *Rev. Sci. Instrum.* **1999**, *70* (8), 3432–3434.

(79) Levi, M. D.; Dargel, V.; Shilina, Y.; Aurbach, D.; Halalay, I. C. Impedance Spectra of Energy-Storage Electrodes Obtained with Commercial Three-Electrode

Cells: Some Sources of Measurement Artefacts. *Electrochim. Acta* **2014**, *149*, 126–135.

(80) Brug, G. J.; van den Eeden, A. L. G.; Sluyters-Rehbach, M.; Sluyters, J. H. The Analysis of Electrode Impedances Complicated by the Presence of a Constant Phase Element. *J. Electroanal. Chem. Interfacial Electrochem.* **1984**, *176* (1–2), 275–295.

(81) Brown, T. R.; Kincaid, B. M.; Ugurbil, K. NMR Chemical Shift Imaging in Three Dimensions. *Proc. Natl. Acad. Sci.* **1982**, *79* (11), 3523–3526.

(82) Brown, T. R. Chemical Shift Imaging. In *Encyclopedia of Magnetic Resonance*; John Wiley & Sons, Ltd: Chichester, UK, 2007; pp 1–12.

(83) Vashaee, S.; Goora, F.; Britton, M. M.; Newling, B.; Balcom, B. J. Mapping B 1 - Induced Eddy Current Effects near Metallic Structures in MR Images: A Comparison of Simulation and Experiment. *J. Magn. Reson.* **2015**, *250*, 17–24.

(84) Halse, M.; Goodyear, D. J.; MacMillan, B.; Szomolanyi, P.; Matheson, D.; Balcom, B. J. Centric Scan SPRITE Magnetic Resonance Imaging. *J. Magn. Reson.* **2003**, *165* (2), 219–229.

(85) Halse, M.; Rioux, J.; Romanzetti, S.; Kaffanke, J.; MacMillan, B.; Mastikhin, I.; Shah, N. J.; Aubanel, E.; Balcom, B. J. Centric Scan SPRITE Magnetic Resonance Imaging: Optimization of SNR, Resolution, and Relaxation Time Mapping. *J. Magn. Reson.* **2004**, *169* (1), 102–117.

(86) Wu, D. H.; Chen, A. D.; Johnson, C. S. An Improved Diffusion-Ordered Spectroscopy Experiment Incorporating Bipolar-Gradient Pulses. *J. Magn. Reson.*

Ser. A **1995**, *115* (2), 260–264.

(87) Pelta, M. D.; Morris, G. A.; Stchedroff, M. J.; Hammond, S. J. A One-Shot Sequence for High-Resolution Diffusion-Ordered Spectroscopy. *Magn. Reson. Chem.* **2002**, *40* (13), S147–S152.

(88) Stejskal, E. O.; Tanner, J. E. Spin Diffusion Measurements: Spin Echoes in the Presence of a Time-Dependent Field Gradient. *J. Chem. Phys.* **1965**, *42* (1), 288–292.

(89) Sinnaeve, D. The Stejskal – Tanner Equation Generalized for Any Gradient Shape — An Overview of Most Pulse Sequences Measuring Free Diffusion. *Concepts Magn. Reson. Part A* **2012**, *40A* (2), 39–65.

(90) Marcus, Y.; Hefter, G. Standard Partial Molar Volumes of Electrolytes and Ions in Nonaqueous Solvents. *Chem. Rev.* **2004**, *104* (7), 3405–3452.

(91) Neuhaus, J.; Forte, E.; Harbou, E. Von; Hasse, H. Electrical Conductivity of Solutions of Lithium Bis(Fl Uorosulfonyl)Imide in Mixed Organic Solvents and Multi-Objective Solvent Optimization for Lithium-Ion Batteries. *J. Power Sources* **2018**, *398* (July), 215–223.

(92) Allen, J. L.; Borodin, O.; Seo, D. M.; Henderson, W. A. Combined Quantum Chemical/Raman Spectroscopic Analyses of Li+ Cation Solvation: Cyclic Carbonate Solvents—Ethylene Carbonate and Propylene Carbonate. *J. Power Sources* **2014**, *267*, 821–830.

(93) Borodin, O.; Olguin, M.; Ganesh, P.; Kent, P. R. C.; Allen, J. L.; Henderson, W. A. Competitive Lithium Solvation of Linear and Cyclic Carbonates from Quantum

Chemistry. *Phys. Chem. Chem. Phys.* **2016**, *18* (1), 164–175.

(94) Mitchell, J.; Johns, M. L. Rapid Measurements of Diffusion Using PFG: Developments and Applications of the Difftrain Pulse Sequence. *Concepts Magn. Reson. Part A* **2009**, *34A* (1), 1–15.

(95) Smart, M. C.; Ratnakumar, B. V.; Surampudi, S. Electrolytes for Low-Temperature Lithium Batteries Based on Ternary Mixtures of Aliphatic Carbonates. *J. Electrochem. Soc.* **1999**, *146* (2), 486.

Chapter 6 – Characterization of Ion Transport in Solid-State Lithium-Ion Electrolytes by PFG-NMR and MAS-NMR

6.1 Outline and Context in the Thesis

The focus of this chapter is on the application of PFG-NMR and MAS-NMR to the quantification and characterization of ion transport in solid-state electrolyte materials. PFG-NMR has been routinely used to measure diffusivity in the solution state,[1] for both pure liquids and mixtures, since its inception[2] over five decades ago. However, the application to solid-state ion conductors has been quite limited until recent advances in ion-conducting material design and synthesis have yielded materials for which the conduction and relaxation properties are within the theoretical lower bound[3] of the technique (which is, of course, also set by the ever-advancing capabilities of the available experimental hardware). Relative to the overall volume of research ongoing in the field of solid-state electrolytes, PFG-NMR transport characterization is infrequent.[4–16] The existing work in the field often uses it to supplement NMR relaxometry measurements of the local ion hopping dynamics, and studies which employ PFG-NMR as the primary characterization technique typically focus on bulk crystalline transport. This work aims to apply the PFG-NMR technique to phases from two families of lithium-sulphide which have emerged as promising candidates for incorporation into fully functioning solid-state lithium-ion batteries (SSLIBs): a series of argyrodite ion conductors derived from two complementary

doping strategies, and a β-phase lithium thiophosphate structurally stabilized at room temperature via aluminum ion doping. When combined with conventional solid-state MAS-NMR characterization, this chapter will demonstrate that solid-state diffusivity measurements bring much additional nuance and insight to the characterization of ion transport in solid-state electrolytes, well beyond what is available from simple electrochemical measurements of the ionic conductivity.

This chapter is based on a series of articles developed in collaboration with the research group of Prof. Linda F. Nazar at the University of Waterloo. The first is a co-first author publication with P. Adeli from the Nazar group which focussed on halide enrichment of the parent argyrodite phase, and combines structural refinement with PFG-NMR and MAS-NMR to ascertain how the halide enrichment impacts the ion transport. The PFG-NMR and MAS-NMR experiments, as well as all subsequent data analyses, were carried out at McMaster University under the supervision of Prof. Gillian R. Goward, while the synthesis and x-ray diffraction was carried out by P. Adeli at Waterloo, along with electrochemical measurements (with contributions from K.-H. Park and I. Kotchetkov), under the supervision of Prof. Nazar. Neutron diffraction was performed by A. Huq at Oak Ridge National Laboratory, with refinement conducted by P. Adeli. This work was published as "Boosting Solid-State Diffusivity and Conductivity in Lithium Superionic Argyrodites by Halide Substitution" in *Angewandte Chemie International Edition* in 2019, with authorship of P. Adeli,[=] J. David Bazak,[=] K.-H. Park, I. Kotchetkov, A. Huq, G. R. Goward, and L. F. Nazar (DOI: 10.1002/anie.201814222).[17]

The second is another co-first author publication with P. Adeli, wherein aliovalent cation substitution of Ca^{2+} for Li^{+} in the argyrodite family and its ramifications for ion transport were explored. The complementarity with the halide substitution approach was also investigated, as well as the influence of sample compression on diffusivity via crystallite grain-boundary modification. Here again, synthesis, x-ray diffraction, and conductivity measurements were carried out by P. Adeli at Waterloo under the supervision of Prof. Nazar, while all PFG-NMR, MAS-NMR and NMR relaxation experiments were conducted at McMaster under the supervision of Prof. Goward. Neutron diffraction was again carried out at Oak Ridge National Laboratory by A. Huq, and refined by P. Adeli. This manuscript is completed, but is currently awaiting clearance for publication by an industrial partner.

The third publication involves the use of Al-doping to stabilize the conductive β-phase of the thiophosphate Li_3PS_4, and characterization of its transport properties. As with the aliovalent cation-doped argyrodites, the influence of macroscopic sample preparation (glass, versus crystalline powder, versus compressed pellet of the crystalline powder) on ion diffusivity was also investigated, along with diffusive exchange between the bulk crystal phase and the amorphous interphase. The synthesis, x-ray diffraction and conductivity measurements were carried out by E. P. Ramos (with contributions from A. Assoud) at Waterloo under the supervision of Prof. Nazar, while all PFG-NMR, MAS-NMR and NMR relaxation measurements were conducted at McMaster under the supervision of Prof. Goward. A manuscript is in preparation, but is not ready for submission at the time of the publication of this dissertation.

This chapter will emphasize only the NMR results from the three aforementioned manuscripts; results from the conductivity measurements and structural characterizations will be drawn from as required to interpret the NMR data, but a full description of those additional methods is beyond the scope of this thesis, and the interested reader is referred instead to the manuscripts themselves. A brief introduction will be provided on the materials themselves and the context of the research, followed by a description of the NMR methods, and then a summary of the NMR results and a discussion of their interpretation for each of the three studies in sequence.

6.2 Introduction and Context in the Field

The recent rise of the Li-sulphide solid-state electrolytes, intended for all-solid-state batteries, has furnished a rich landscape of materials where intricate relationships between structural and dynamical properties are key to improving ionic transport and elucidating its mechanisms. Solid-state electrolytes offer many potential advantages over liquid electrolytes for metal-ion battery systems – lack of flammability in thermal runaway events, higher achievable energy densities, the possibility of incorporating a metallic lithium anode, reduced cost, simplified manufacturing, and the elimination of electrolyte concentration gradients – but also face disadvantages in the form of lower ionic conductivities than liquid electrolytes and interfacing challenges, both with the electrodes and between grain boundaries of the crystallites themselves comprising the electrolyte layer.[18,19] Additionally, as the principles of *ab initio* electrochemical materials design have greatly expanded in recent years,[20–23] with its aim of discovering materials which embody an optimal set of characteristics relative to a given application, it is critical that the factors

which impact the diffusion mechanism – and their relative importance – be well understood.[19,24,25]

A foremost candidate among the new Li-sulphide solid-state electrolyte families is the argyrodites, which yield high room-temperature conductivities, excellent ductility, and good electrochemical stability.[26,27] The argyrodites are defined by the general chemical formula $A^{m+}_{(12-n-x)/m}B^{n+}L^{2-}_{6-x}M^{-}_{x}$ (A = Ag^+, Cu^+, Li^+ etc.; B = Ga^{3+}, Si^{4+}, P^{5+}; L = S, Se, Te; and M = Cl, Br, I).[28] Structurally, they are characterized by a cubic geometry containing PS_4^{3-} tetrahedra with isolated S^{2-} and halide X^- anions in a disordered arrangement, and lithium ions in 48*h* sites forming a "cage-like" structure – known as a Frank-Kasper polyhedra – around these isolated anions, as depicted in **Figure 6.1**.[26,29] Molecular dynamics simulations[30] and NMR relaxometry measurements[31,32] have shown that they should experience rapid intra-cage circulation via 48*h*-24*g*-48*h* "doublet jumps" involving unoccupied 24*g* sites and short-range 48*h*-48*h* hops, whereas long-range ion transport is governed by inter-cage hops, which is enhanced by the anion disorder. This latter point has been underscored in studies of Li_6PS_5I, which demonstrated that the much larger I^- anions preferentially take up an ordered arrangement on the sites outside of the Frank-Kasper polyhedra – to the significant detriment of the ionic conductivity – whereas in Li_6PS_5Cl and Li_6PS_5Br both these positions and the anion positions within the Frank-Kasper polyhedra experience halide substitution for S^{2-} anions.[33] To that end, a halide-enriched version of the Cl-based argyrodite phase, $Li_{6-x}PS_{5-x}Cl_{1+x}$, with $x = \{0, 0.25, 0.375, 0.5\}$, is investigated in this chapter, with particular emphasis on studying the intertwined impacts of the halide-enrichment on the ion transport: i) the altered polarizability of the rigid anion

lattice,[34] which could reduce interactions with the mobile lithium cations and thereby enhance their mobility, and ii) the introduction of vacancies into the lithium cation network owing to the maintenance of electroneutrality, which could increase the likelihood of inter-cage hops by reducing overall congestion within the cages.[30] For the latter case, a related approach is to simply replace a small proportion of the monovalent lithium cations with aliovalent cations, and again rely on charge compensation with the anion lattice to yield vacancy sites.[35] As mentioned above, for this study, Ca^{2+} was used, on account of its comparable ionic radius to Li^{+}. The argyrodite chemical formula given above is then modified with the fraction of Ca^{2+}-doping denoted y: $Li_{6-x-2y}Ca_yPS_{5-x}Cl_{1+x}$, with $z_{Li} = 6 - x - 2y$ as a shorthand for the lithium stoichiometry. Therefore, the first major aim of this chapter is to assess the relative significance of these effects, via their impact on diffusivity measurements by PFG-NMR, and the spectroscopic signature of the doping using MAS-NMR. This investigation culminates in the characterization of a "mixed-phase" sample, featuring both Ca-doping and a significant Cl- excess, resulting in an apparently biphasic material. The influence of compression of the sample into a pellet on the transport was also examined for this mixed-phase sample. Recent work on argyrodite-based, lithium-metal-anode solid-state batteries has shown that stack pressure of the fully fabricated cell plays a crucial role in the electrochemical properties and longevity of the cell,[36] therefore, as device-level optimization of this parameter for cell construction continues, it is important to connect these findings with an understanding of how sample compression manifests in the microscopic ion dynamics of the solid-state electrolyte material.

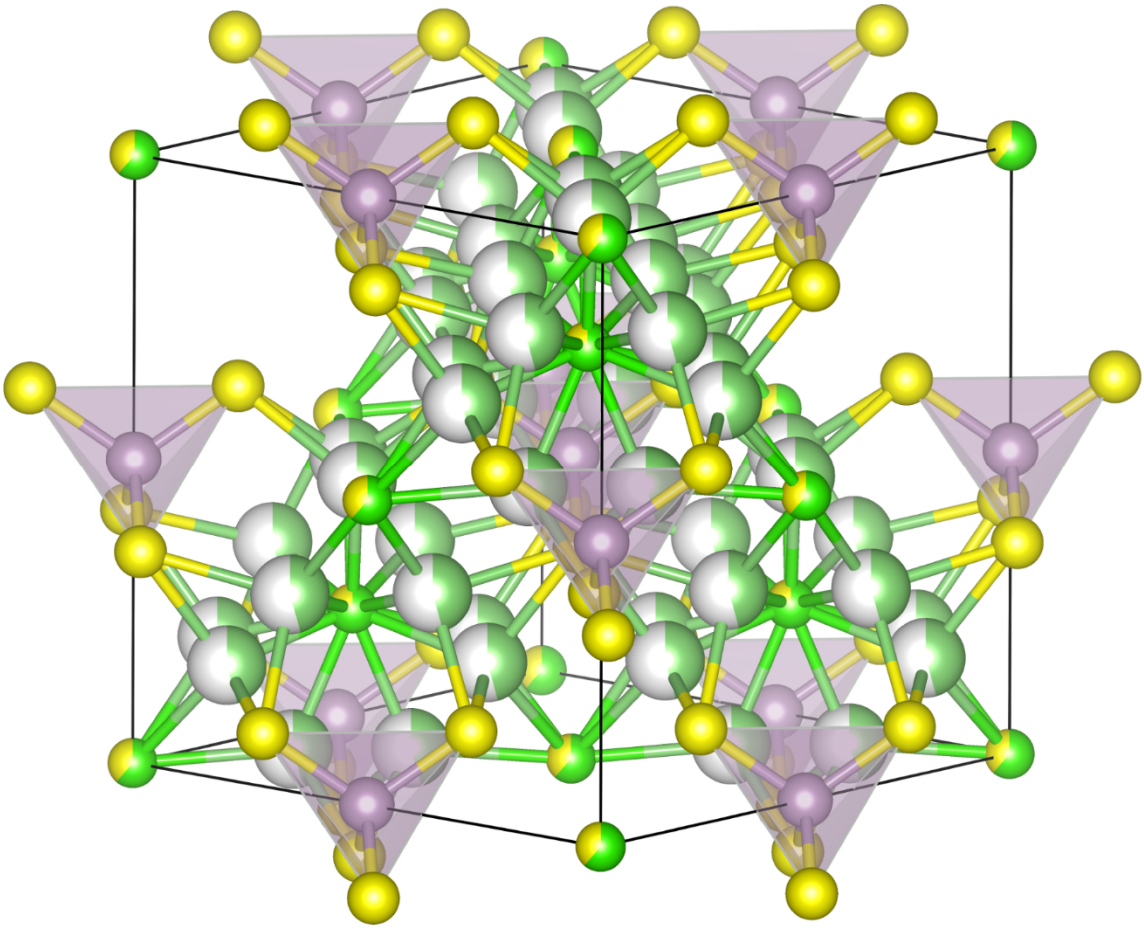

Figure 6.1 – Crystal structure of the Li-Argyrodite family of phases, demonstrating the arrangement of Frank-Kasper polyhedra cages of Li^+ cations coordinating isolated anion positions, embedded in the cubic unit cell geometry. The shaded purple tetrahedra are PS_4^{3-} units (yellow balls are S^{2-}), the yellow/neon green balls are disordered S^{2-}/Cl^- positions, and the grey/dull green balls are partially-occupied Li^+ 48*h* sites. Unoccupied 24*g* sites lie between pairs of adjacent 48*h* sites.

Another facet of the lithium-sulphide ion conductor picture is the thio-LISICON (Lithium Super Ionic CONductor) family, where much recent progress has also been made with phases which are isostructural to β-Li_3PS_4, a high-temperature thiophosphate phase. The initial breakthrough was the discovery that germanium substitution for phosphorus could stabilize this structure at room temperature, and the resulting compound

($Li_{10}GeP_2S_{12}$, commonly termed LGPS) yielded an ionic conductivity competitive with liquid electrolytes.[37] While germanium is expensive, alternative doping strategies with more economical elements rapidly multiplied.[5,10,38] Among the proposed candidates to supplant LGPS as a practical realization of this structural motif for an ion conductor was the aluminum-doped variant, $Li_{11}AlP_2S_{12}$, or LAPS, initially predicted theoretically.[39] This prediction suggested a very large room-temperature ionic conductivity, on the putative increase in aperture for the b-axis primary lithium diffusion tunnels – refer to **Figure 6.2** for the crystal structure. The first synthesis attempt[40] was some distance from achieving the predicted ionic conductivity, and also left undeveloped the description of structure-property relations which could provide insight into the actual workings of the experimentally-

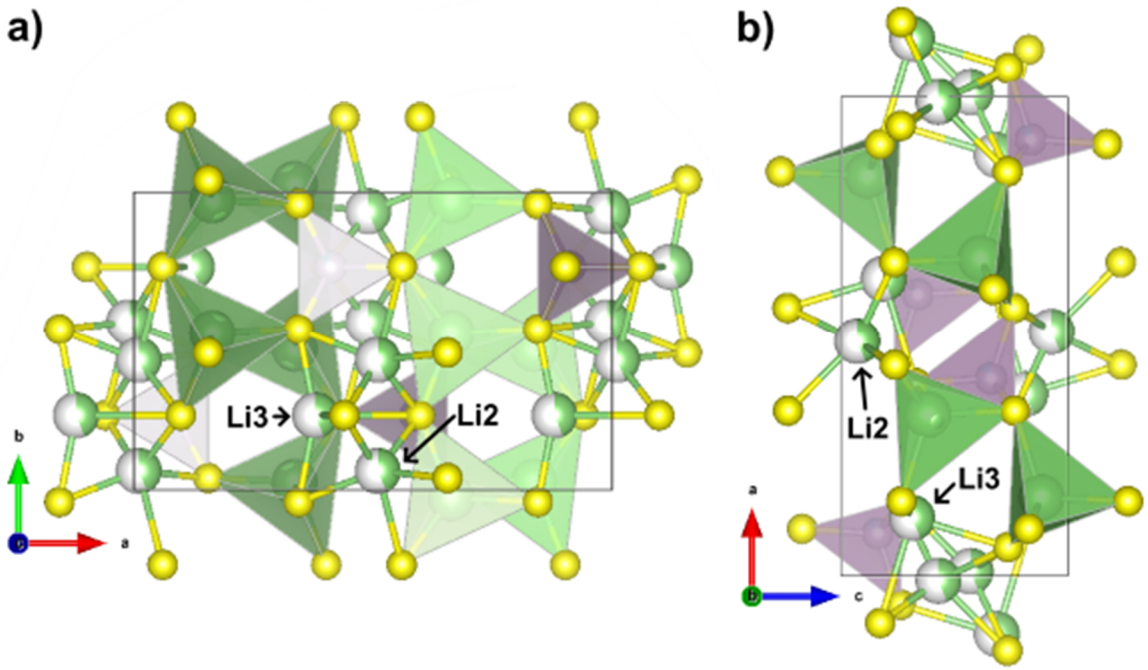

Figure 6.2 – Crystal structure for $Li_{3.3}Al_{0.15}P_{0.85}S_4$, showing the primary conduction channels for lithium ions along the b-axis, viewed along a) the c-axis, and b) the b-axis itself. Also highlighted are the partially occupied Li2 and Li3 sites which comprise this channel. The purple tetrahedral are disordered $[P/Al]S_4^{3-}$ units, while the enclosed, green tetrahedra are the fully-occupied Li1 sites.

realized version of the material. As a result, the second major aim of this chapter is to discuss the PFG-NMR, MAS-NMR and relaxation NMR findings on a related composition, $Li_{3.3}Al_{0.15}P_{0.85}S_4$ (which incidentally, as determined in the pending manuscript on this phase, appears to be the solubility limit for Al in this structure). In particular, the influence of sample preparation – i.e. grain boundary modification and diffusion exchange with the amorphous interphase – will be investigated in detail.

6.3 Methods

6.3.1 Pulsed-Field Gradient NMR

Diffusion measurements by pulsed-field gradient (PFG) NMR were conducted for all phases on a Bruker Avance III 300 MHz (7.0 T) instrument using a Diff50 gradient probe and a 5 mm ^{7}Li coil insert. Powder samples were placed, with a depth of 3-4 mm of sample, in a thoroughly dried 5 mm Shigemi tube. The $\pi/2$ excitation pulse was 8.1 μs at 40 W. For the argyrodite samples, the T_1 relaxation time was 105-186 ms, measured by inversion recovery, while T_2 relaxation was in the range of 9-20 ms. T_2 was measured using the CPMG sequence with a 0.5 ms echo delay, and a series of 2 to 32 echo periods. Diffusion-attenuated spectra for the argyrodite samples were acquired using the bipolar-gradient pulse, stimulated-echo sequence (BPP-STE), with longitudinal eddy current delay (LED).[41] The bipolar gradients, of opposite phase and on either side of a π pulse, act as a means of electronically canceling eddy currents in the gradient coil whilst still delivering a large-magnitude gradient pulse to the sample.[1] Since the experiment is constructed around a stimulated echo, it leverages the fact that T_1 is roughly an order of magnitude longer than T_2 in these materials, with the diffusion time coinciding with a period of magnetization z-

storage. A linear, 16-step gradient ramp was used in each experiment, with the maximum gradient ranging up to 2725 G/cm (99% of the probe capacity), depending on the diffusivity of the material at the temperature being studied. A SINE.100 shape was used for all gradient pulses. Phase-encode times were generally set with δ = 2.4 ms and the diffusion times with Δ = 35 ms as a baseline relative to the typical T_2 and T_1 relaxation times. However, when the primary strategy of varying the gradient strength alone could not generate sufficiently high b-values, particularly at the lower temperatures examined, slightly longer Δ and δ (prioritized in that order) were taken. In all cases, a target attenuation of <5% of the signal intensity for the final step in the ramp relative to the signal intensity in the absence of gradients was used as a metric for setting the gradient strength, δ, and Δ. The linearity of the gradient response was confirmed by performing the same experiment with the gradient strength halved and δ commensurately increased (i.e. with the b-values fixed) for several temperatures with the parent-phase, which required the largest b-values. A simple ^{7}Li frequency-encoding MRI sequence was used to confirm that the sample plug in the Shigemi tube was centred in the gradient coil.

For the LAPS samples, the shorter T_2 values measured – in particular, $\sim$ 4 ms for the glass sample at room temperature – necessitated a PFG-NMR sequence with less total time spent performing spin manipulations on the transverse plane, owing to the rapid intrinsic transverse dephasing. To this end, a regular PGSTE sequence, employing only a single gradient encoding and refocusing period, was used for these diffusivity measurements. The tradeoff of decreased signal-to-noise was somewhat balanced by acquiring additional scans and taking many gradient steps: each experiment entailed 64

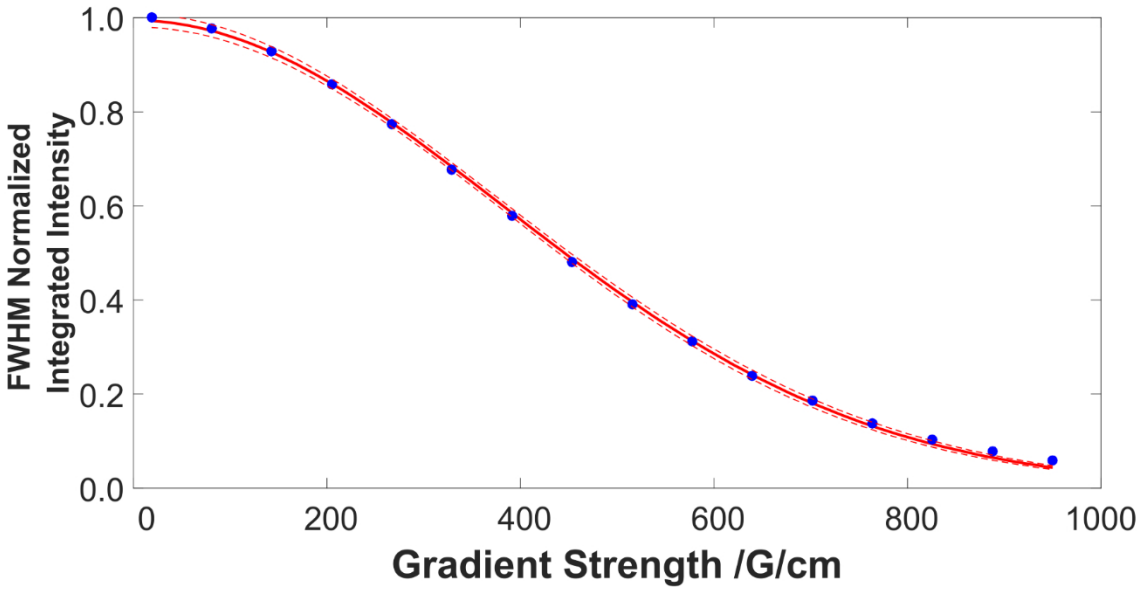

Figure 6.3 – PFG-NMR signal attenuation curve for the $x = 0.5$ argyrodite sample at 300 K, with fit to the modified Stejskal-Tanner equation and $\alpha = 0.95$ confidence interval.

scans at each of the 32 gradient steps, instead of the 16 scans/16 gradient steps template used with the BPP STE sequence for the argyrodite samples. The phase-encoding time was $\delta = 2.4$ ms for the glass samples, and $\delta = 2.8$ ms for the powder and pellet samples, with Δ ranging from 49 ms at the highest temperature to 720 ms for the lowest temperature (only 130 ms was achievable for the glass sample, consequently resulting in a higher low-temperature limit for this experiment series compared with the powder and pellet phases).

Fits to the attenuation curves were performed using the T1/T2 module in TopSpin 3.2 and the Stejskal-Tanner equation,[2] with the necessary modifications for BPP-STE (in the argyrodite case) and the sine-shaped gradient pulses,[42] using the integrated signal intensity at each gradient step taken over the range defined by the FWHM in the non-attenuated spectrum. A typical attenuation curve for the $x = 0.5$ argyrodite sample is presented in **Figure 6.3**. A recycle delay of 3.5 s, while much greater than $5T_1$ for the

argyrodite samples, was imposed by the duty cycle on the gradient coil. In contrast, for the crystalline LAPS samples, the gradient coil duty cycle time of 3.5 s was shorter than the usual $5T_1$ heuristic for setting the recycle delay. However, signal recovery was well in excess of 80% in the T_1 inversion recovery experiments by this point, so a train of 16 dummy scans was appended to the pulse program to equilibrate the signal prior to commencing diffusivity measurements. A 1 ms delay was inserted on either side of the gradient pulses to accommodate eddy current ringdown not compensated by the bipolar gradients in both PFG-NMR pulse sequences, in addition to the 5 ms LED prior to the acquisition. During the z-storage periods, a 2 ms, 143 G/cm spoiler gradient was applied to de-phase any residual transverse magnetization. With this spoiler gradient, the phase cycle can be reduced to 16 steps, which was taken, as mentioned above, as the number of scans utilized for each step in the gradient ramp for the argyrodite samples.

Temperature control was maintained with a BCU II unit, and experiments were conducted over a targeted range of 248.2 K to 358.2 K, with the low-temperature limit for a given sample dictated by whether the exponential reduction in diffusivity with decreasing temperature would still permit reasonable signal acquisition with available gradient strength, taking into account the sample's relaxation properties. A δ ^{1}H chemical shift thermometer was performed with ethylene glycol (298.2 K to 358.2 K) and methanol (248.2 K to 298.2 K) in the Shigemi tube with the same temperature control settings as for the PFG-NMR experiments, using standard Bruker calibration curves, to calibrate the actual temperatures experienced by the samples. The chemical shift measurements were also repeated immediately after transmitting a PFG-NMR sequence to the sample with the RF

pulses blanked to assess sample heating by the gradient coil. The effect was found to be 0.1 K or less. During the PFG-NMR experiments, the temperature was shifted in 5 K increments, with 20 minutes allowed for equilibration at each temperature, which was found to yield reproducible measurements of the diffusivity. For the pelletized samples, the pellet was cold-pressed at 2 tons of applied pressure in a 10 mm dye to an approximate thickness of 2 mm, and was sliced into smaller sections with a dried spatula in an Ar-filled glovebox. The resulting sections were then carefully stacked in the Shigemi tube to retain a roughly cylindrical sample geometry.

6.3.2 Magic-Angle Spinning NMR

Fast magic-angle spinning (MAS) NMR was performed on the materials using a Bruker 850 MHz HD spectrometer, with ^{7}Li possessing a Larmor resonance frequency of 330 MHz in the 20 T field of this instrument, and ^{31}P resonating at 343 MHz. Samples were packed in 1.9 mm zirconia rotors spinning at 30 kHz. The $\pi/2$ excitation pulse for ^{7}Li was 3.5 µs at 110 W, while it was 6 µs at 80 W for ^{31}P. Referencing for ^{7}Li was nominally achieved relative to a static sample of 1 M LiCl (aq) in a sealed capillary tube. The 850HD is a pumped magnet, and the resulting longitudinal field drift is discernible, in particular, for the narrow lineshapes of the diamagnetic, extreme motionally-narrowed argyrodite samples, which complicates chemical shift referencing between different samples on account of the relatively small degree of shift encountered in samples of this nature. However, these samples invariably contain a trace impurity, which was directly confirmed as LiCl by performing MAS-NMR on a sample of the pure compound on the basis of its chemical shift (-1.18 ppm) and T_1 (approximately 60 s). This signal was

therefore used as a fortuitous internal reference to directly compare the shifts between the various argyrodite samples and counteract the magnet drift in the absence of a lock. The broader ^{7}Li LAPS signals were less effected by this phenomenon, and ^{31}P shifts for both types of samples were essentially unaffected by it. The ^{31}P referencing was accomplished with 85% H_3PO_4 sealed in a capillary.

2D exchange spectroscopy (EXSY) was also performed for ^{7}Li with the $y = 0.10$, $y = 0.15$, and $(x = 0.25, y = 0.10)$ argyrodite compositions, which exhibited a secondary signal. A 12 ppm spectral width in the indirect dimension digitized with 650 points was used to acquire the 2D EXSY spectra, with a 4.5 s recycle delay and an 8-step phase cycle (using States-TPPI as the acquisition mode in the indirect dimension), which was sufficient to eliminate any ringing in the indirect dimension, and resulted in an approximately 7-hour experiment time (depending on mixing time). Mixing times ranged from 10 μs to 500 ms, but owing to the imbalance in spectral volumes between the primary and secondary signals, and the long Lorentzian tails of the primary signal, volumetric deconvolution of the cross-peaks was not reliable. Consequently, the 2D EXSY results presented below are only interpreted qualitatively to demonstrate that the secondary signal is in exchange with the primary signal.

6.3.3 NMR Lineshape Deconvolution and Quadrupolar Fitting

Deconvolution and fitting of lineshapes was performed using ssNake v1.1,[43] which can interpret Bruker TopSpin output files. Simple Lorentzian/Gaussian fitting was performed for the crystalline powder LAPS ^{7}Li MAS-NMR lineshape, and the secondary signals in the $y = 0.10$, $y = 0.15$, and $(x = 0.25, y = 0.10)$ ^{7}Li argyrodite MAS-NMR

lineshapes, in order to recover the component signal contributions, including the amorphous portion for the LAPS sample. Additionally, for the crystalline powder LAPS sample, static ^{7}Li quadrupolar fits were performed to lineshapes at 300 MHz, 500 MHz, and 850 MHz to extract the C_Q and η_Q parameters, again using ssNake v1.1. The amorphous background was also fit with a single, broad Gaussian line, so that the relative proportion of the total signal from the amorphous contribution could be compared with that determined from the MAS-NMR lineshape. The ^{7}Li C_Q and η_Q parameters for LAPS were then used to generate a library for a Czjzek fit in ssNake to its ^{7}Li MAS-NMR lineshape, to assess

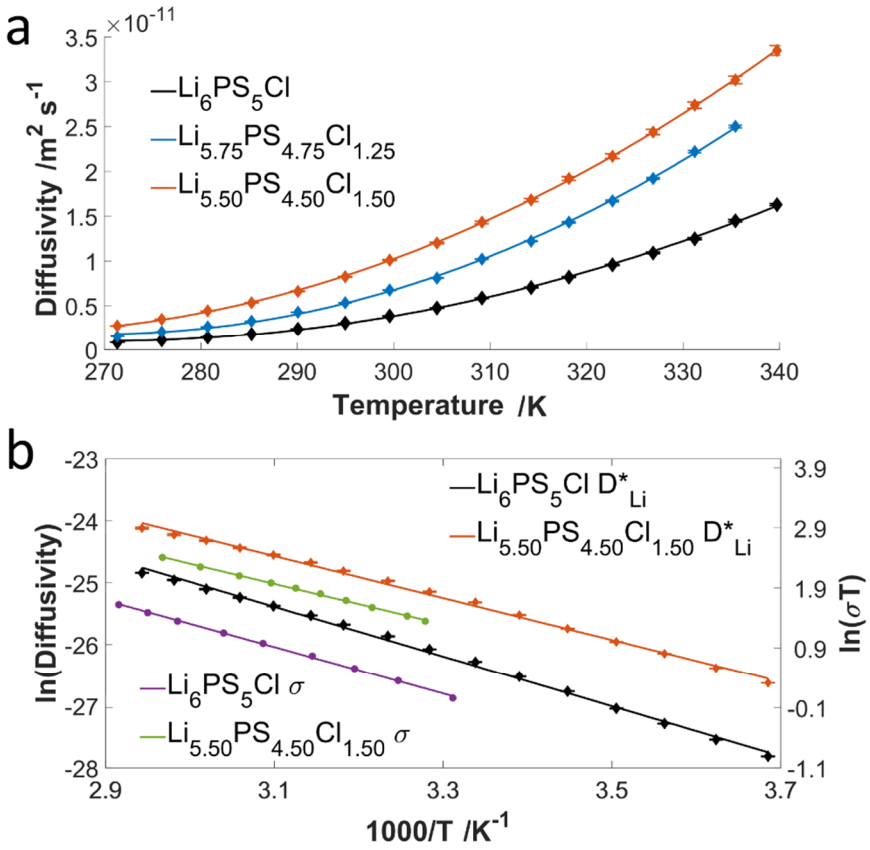

Figure 6.4 – a) Li^+-ion diffusivity in $Li_{6-x}PS_{5-x}Cl_{1-x}$ obtained from ^{7}Li PFG-NMR measurements for x = 0, 0.25 and 0.5; b) Arrhenius plots of the diffusivity and conductivity values for x = 0 and x = 0.5 from PFG-NMR and EIS.

whether a disordered quadrupolar model for the MAS-NMR lineshape was a better fit than a pure Lorentzian/Gaussian deconvolution.

6.4 Results and Discussion

6.4.1 Factors Affecting Halide-Enriched Argyrodite Transport

The "headline" finding from the study of the halide-enrichment of the argyrodite phase comes in the form of three values corresponding to the room-temperature ion transport of the $x = 0.5$ phase: an ionic conductivity of (9.4 ± 0.1) mS/cm, a lithium ion self-diffusivity of $(1.005 \pm 0.007) \times 10^{-11}$ m^2/s, and an activation energy of (0.29 ± 0.01) eV (from the diffusivity measurements). Such an ionic conductivity is competitive with the common benchmark liquid electrolyte LP30 (*i.e.* 1.0 M $LiPF_6$ in EC/DMC, 1:1 (v/v)),[44] and the activation energy is comparable to what has been measured for the benchmark solid-state electrolyte LGPS.[45] Owing to the relative paucity of diffusion measurements for solid-state electrolytes discussed in **6.1**, diffusivity is a less common metric for the evaluation of ion transport in these materials, but remarkably, the room-temperature diffusivity for the $x = 0.5$ phase is several times that of LGPS (2.2×10^{-12} m^2/s)[9] and the related ultrafast $Li_{11}SiP_2S_{12}$ (3.25×10^{-12} m^2/s).[5] Variable-temperature plots of the diffusivity and the Arrhenius fits to both the diffusivity and conductivity, measured by EIS, for several levels of halide-enrichment are presented in **Figure 6.4**. There is a marked increase in diffusivity upon adding a moderate amount of dopant Cl^-; further additions up to $x = 0.5$ continue this increase, but the synthesis efforts ultimately demonstrated a solubility limit of $x < 0.55$ for the lattice, after which appreciable LiCl exsolvation was observed. As can be observed from **Figure 6.4b**, the

thermal activation behaviour of both the diffusivity and the conductivity are nearly in parallel, demonstrating that they are indeed measuring the same transport processes and length scales. It is well-known that ^{7}Li NMR relaxometry measurements generate considerably lower activation energies in similar phases;[32,46–49] however, these measurements are restricted to highly local dynamical processes, and are less reflective of the long-range transport behaviour, particularly as the influence of grain boundaries is concerned. This latter effect is likely the reason for the slightly elevated values of the activation energies derived from variable-temperature PFG-NMR measurements,

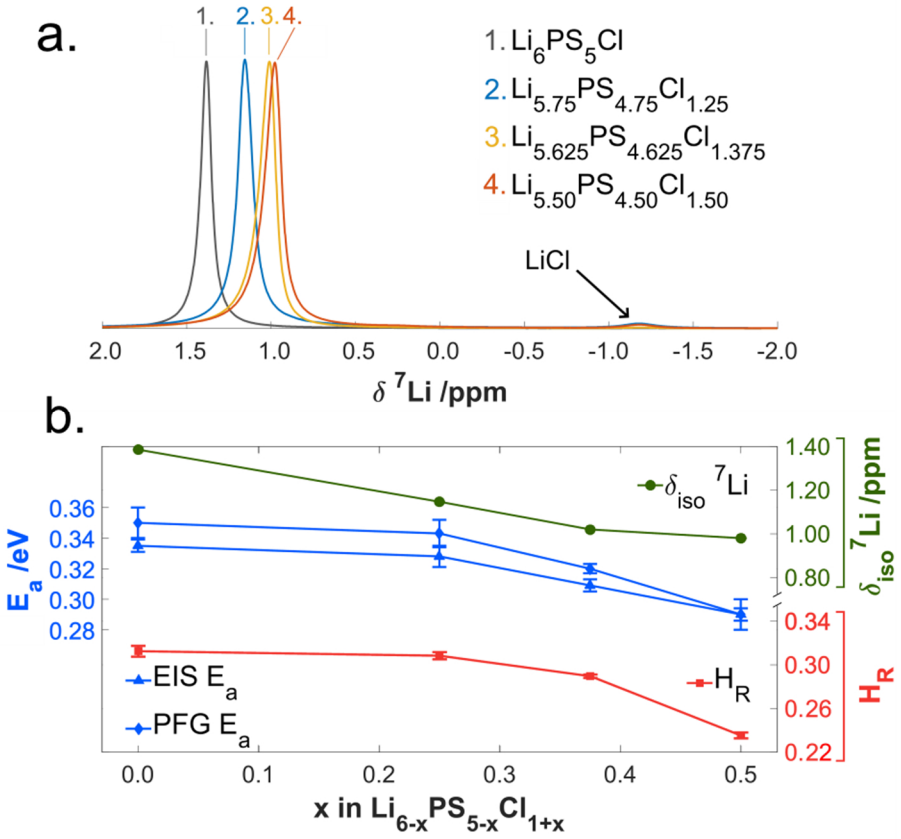

Figure 6.5 – a) ^{7}Li MAS-NMR for $Li_{6-x}PS_{5-x}Cl_{1-x}$ $(x = 0, 0.25, 0.375, 0.5)$; b) correlation of the activation energies from both techniques with the ^{7}Li isotropic chemical shift and the Haven ratio for all values of x under study.

compared with those from the conductivities in **Table 6.1**, which will be explored further in sections **6.4.3** and **6.4.5**.

Table 6.1 – Comparison of room-temperature transport properties and activation energies for the halide-enriched argyrodite series.

$Li_{6-x}PS_{5-x}Cl_{1+x}$	$D^*_{Li}(300\ K), (m^2/s)$	$\kappa_{Li}(300\ K), (mS/cm)$	$E_a(D^*_{Li}), (eV)$	$E_a(\kappa_{Li}), (eV)$
Li_6PS_5Cl	$3.25(2) \times 10^{-12}$	2.5(1)	0.35(1)	0.335(4)
$Li_{5.75}PS_{4.75}Cl_{1.25}$	$6.73(3) \times 10^{-12}$	4.2(2)	0.343(9)	0.328(7)
$Li_{5.625}PS_{4.625}Cl_{1.375}$	$7.97(6) \times 10^{-12}$	5.6(2)	0.320(3)	0.309(4)
$Li_{5.50}PS_{4.50}Cl_{1.50}$	$1.005(7) \times 10^{-11}$	9.4(1)	0.29(1)	0.290(4)

Figure 6.5a shows the ^{7}Li MAS-NMR data for $Li_{6-x}PS_{5-x}Cl_{1-x}$, at all four studied levels of halide enrichment. As expected from the Li site symmetry, one primary resonance is observed, with the small broad resonance at -1.18 ppm corresponding to the LiCl impurity used for internal shift referencing. Increasing the halide substitution shifts the isotropic resonance to much lower frequency. The substitution of Cl^- should withdraw electron density from the Li environments relative to S^{2-}, decreasing the paramagnetic component of the chemical shift, in accord with the principle that the lower ionic charge of the halogen will decrease the electrostatic attraction of the mobile Li^+ ions to the rigid framework. Alternately, this can be viewed as a gradual progression toward a more ionic, "LiCl-like" environment with increasing x, since as noted above, LiCl resonates at a much lower frequency than the parent-phase. However, this effect is not linear with the value of x; in particular the change from $x = 0.375$ to $x = 0.5$ is much lessened. Moreover, the symmetric, Lorentzian character of the resonances for $x = 0$ and $x = 0.25$ gives way to a lineshape with much more pronounced chemical shift dispersion, which is a symptom of the greater halide disorder. The fact that this shift trend is not linear in x points toward a

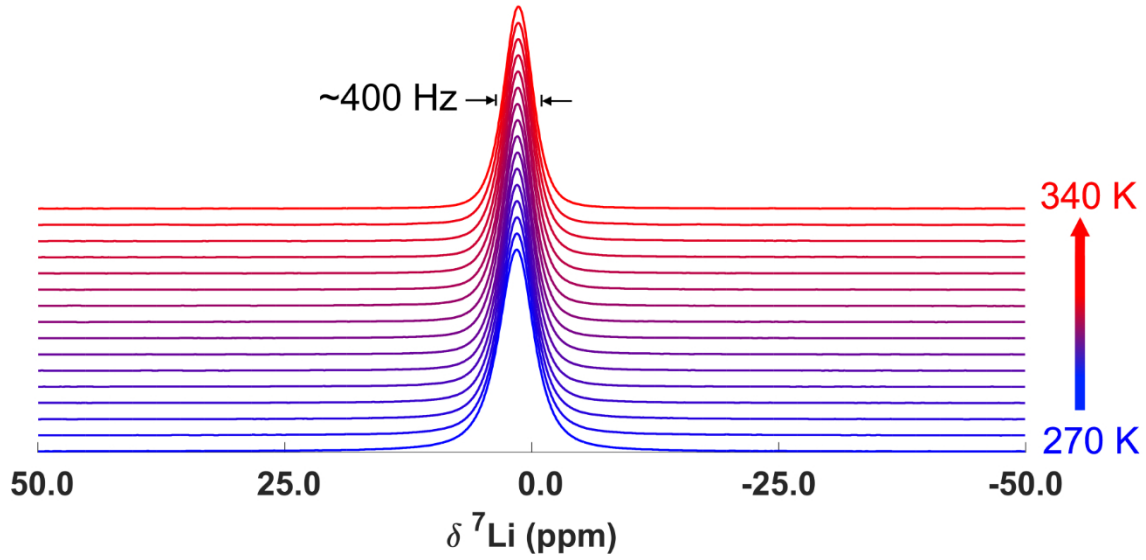

Figure 6.6 – Variable-temperature stack plot of static ^{7}Li spectra for the $x = 0$ argyrodite at 300 MHz, demonstrating the absence of significant quadrupole coupling, in terms of the lack of satellite transitions, broadening of the central transition, and a shift in its position over the entire temperature range, which points to a change in the shielding properties as the primary source of the shift trend in **Figure 6.5a**.

decreased interaction with the anion framework, and therefore the magnitude of the shift cannot be attributed to the changing statistical distribution of the anions alone. **Figure 6.6** demonstrates that, at 300 MHz and static conditions, these materials are well within the extreme motional narrowing regime for all temperatures studied and exhibit no significant quadrupole coupling, in the form of either resolved satellite transitions or shifting of the isotropic resonance. Hence, the shift trend observed in **Figure 6.5a** under high-field, MAS conditions is too large to be generated by a 2nd-order quadrupole-induced isotropic shift (especially given that the quadrupole-induced isotropic shift is inversely proportional to the Larmor frequency). This region of x levels where the shift trend saturates, between $x = 0.375$ and $x = 0.5$, also shows the most pronounced decrease in the activation energy with increasing halide substitution (**Figure 6.5b**).

Here, the increase in Li vacancy content, which is one of the factors contributing to the lowered activation energy, is demonstrated through the Haven ratios, $H_R = D^*/D_\kappa$, in **Figure 6.5b**, where D^* is the self-diffusivity of the mobile ions measured via PFG-NMR and D_κ is defined by rescaling the ionic conductivity measured by EIS, κ_{Li}, into diffusivity via the Nernst-Einstein equation:[3,11]

$$D_\kappa = \kappa_{Li}\frac{k_B T}{cq^2} \tag{6.1}$$

Here, k_B is the Boltzmann constant, T is the temperature, c is the concentration of charge-carriers in units of particle number per unit volume, and q is the charge of the carriers. The form of H_R stated above is the IUPAC-recommended definition,[50] but while other conventions exist, it is important to distinguish H_R from the correlation factor, f, which describes deviation from the Einstein-Smoluchowski equation for the Fickian diffusion coefficient on account of inter-particle interactions. Determining the appropriate number of charge-carriers per unit volume is somewhat subtle. The number of Li in the stoichiometric formula corresponds to the number of ions within a particular cage, with the cages themselves forming a tetrahedral motif within the unit cell. As such, the hops which determine the long-range transport are strictly those between the 4 cages; irrespective of the rapid intra-cage circulation, the number of mobile ions in the unit cell from the perspective of long-range transport is the number which can make a 48*h*-48*h* inter-cage jump. The approach to setting the correct number of carriers for c is therefore to multiply the average cage occupation – *i.e.* the Li stoichiometry – by four cages/unit cell and 1/6 potential carriers/ions in the cage. In order to match the diffusivities at the shift-thermometer-calibrated PFG-NMR temperatures to the oven temperatures used for the

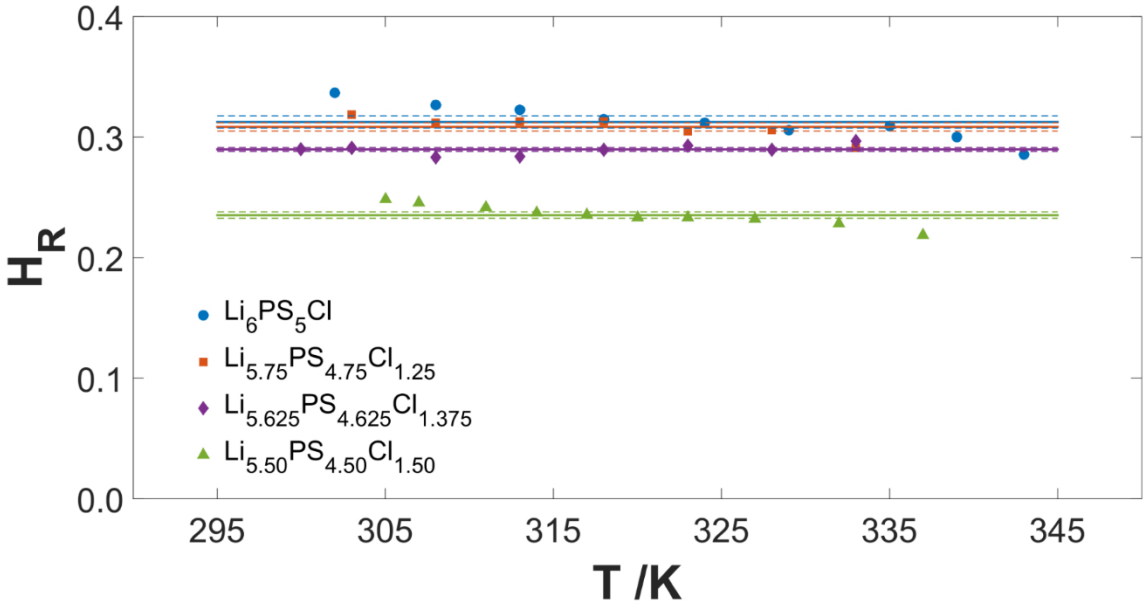

Figure 6.7 – Haven ratios versus temperature, for all four halide-enriched phases examined in the study, demonstrating the relative temperature insensitivity. The flat lines are the average values, and dashed lines indicate the standard error interval.

conductivity measurements, the former were quadratically interpolated to the oven temperatures.

The raw variable-temperature data and the associated averages for H_R of the halide-enriched argyrodites are plotted in **Figure 6.7**. The Haven ratio is relatively insensitive to temperature,[51] but is known to be primarily influenced by, and is a complicated function of, the concentration of mobile charge carriers in theoretical studies of lattice-gas models for Na conduction in β-alumina.[52] Indeed, a temperature-independent Haven ratio implies that there is no change in the diffusion mechanism over the investigated temperature range.[53] This justifies the use of taking the average over all temperatures to compute a singular H_R value for each phase, as in **Figure 6.7**, to compensate for the systematic error stemming from the different pressure levels of the samples in the diffusion and conductivity

experiments (*i.e.* the activation energy offset in **Table 6.1**) in order to draw general conclusions. The $x = 0.375$ phase exhibits this temperature-invariant H_R behaviour most directly. Considering all of the halide-enriched phases in **Figure 6.7**, H_R clusters around 0.3, similar to recent experimental findings for the Li-ion conductors LLZTO and $Li_{10}SnP_2S_{12}$ – studies that also employed EIS and PFG-NMR measurements.[10,15] Molecular dynamics simulations similarly point to values of H_R of this magnitude for superionic conductors: 0.3-0.4 for $Li_{10}GeP_2S_{12}$,[45,54] 0.43 for LLZO,[45] 0.62 for LATP,[45] and 0.56 in the analogous chalcogenide sodium-ion conductor $Na_{10}SnP_2S_{12}$.[55] While the Haven ratio is relatively unchanged from $x = 0$ to $x = 0.25$, it decreases slightly thereafter, reaching 0.23 at $x = 0.5$. A Haven ratio $H_R = 1$ corresponds to purely random ion motion, and is only realizable in extremely dilute systems, while lower values of H_R indicate strong correlation of the ion hops via cooperative mechanisms mediated by the presence of vacancies,[52] an effect that has also been directly observed in systems as diverse as Ag-chalcogenide and alkali-oxide glasses as the modifier concentration is steadily tuned from the dilute regime (in the modifier-controlled regime, $H_R \sim 0.3$ for both systems).[56,57] In the more extreme scenario of the fluoride ion conductor LaF_3, only one site is mobile and the transport is entirely vacancy-mediated, yielding $H_R \sim 0.1$.[58]

As noted above, the onset of decrease in H_R (**Figure 6.5b**) is coincident with the largest decrease in the activation energy with increasing x, and also with the smallest change in the isotropic chemical shift. This points toward a synergy in the complementary effects of performing Cl^-/S^{2-} substitution: namely, for relatively low substitution levels, the most pronounced effect on the ionic transport is likely from the reduced electrostatic

interaction with the framework, while at higher substitution levels the much higher vacancy content (and hence more correlated ion mobility)[21] further drives the increased diffusivity. Statistically, there will be a greater chance of an empty doublet of 48*h* sites near the Cl^- ions, which will facilitate intercage jumps. Moreover, the decrease in the intercage jump distance from 2.88 Å ($x = 0$) to 2.81 Å ($x = 0.5$) (determined from the diffraction data) owing to the shrinkage of the unit cell will also favour higher jump rates, although this effect is anticipated to be much less significant.[34]

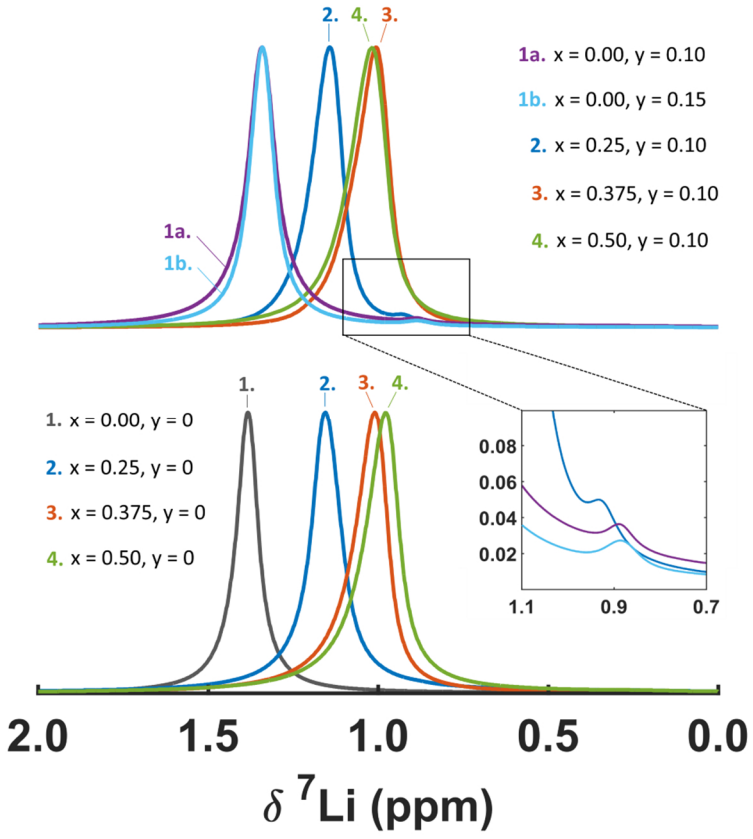

Figure 6.8 – Comparison of ^{7}Li MAS-NMR spectra for the *y*-series and dual-doped series (upper panel), demonstrating the strong halide-enrichment shift trend (which is paralleled in the lower panel with the original *x*-series covered in **6.4.1**), and no major change in chemical shift associated with Ca^{2+}-doping. The inset reveals the secondary peak associated with a Ca^{2+} dopant modifying the local electronic environment of a subset of the Li ions, confirming the proximity of the two cation species.

6.4.2 The Effect of Ca^{2+} Substitution

The introduction of vacancy populations in the conduction sublattice for an ion conductor is a well-known mechanism for boosting the conductivity,[59] and the results of section **6.4.1** from the H_R analysis again underscore this principle with the largest halide-enrichment levels evidently gaining the bulk of their ion transport boost relative to moderate levels from this increased vacancy population. A complementary strategy for introducing vacancies into the conduction sublattice is aliovalent cation doping; for the argyrodites, Ca^{2+} was a natural choice on the grounds of ionic radius, although other possibilities were also explored in the full manuscript by P. Adeli at Waterloo. Nevertheless, Ca^{2+} doping was found to be the most effective on conductivity measurement grounds, and degree of achievable solvation. It was, however, also found that a "dual-doping" strategy of combining the halide enrichment with Ca^{2+} substitution placed a limit of $y = 0.10$ on the latter.

Initial neutron powder diffraction (NPD) results had confirmed that the Ca^{2+} dopants did indeed occupy Li^+ 48*h* sites, but given the relatively small amounts of doping studied ($y = 0.1 - 0.15$) and the complexities of NPD refinement, it was important to support this finding with solid-state NMR. ^{7}Li MAS-NMR measurements for several of the Ca^{2+}-containing compositions established the presence of Ca^{2+} in the vicinity of Li^+ on account of the appearance of a small secondary peak (**Figure 6.8**), along with the expected main resonance. Deconvolution of the lineshapes for $y = 0.1$, $y = 0.15$, and $(x = 0.25, y = 0.1)$, for which the secondary peak was not obscured by the larger, halide-enrichment-induced chemical shift trend discussed in **6.4.1**, yielded peak areas with ratios

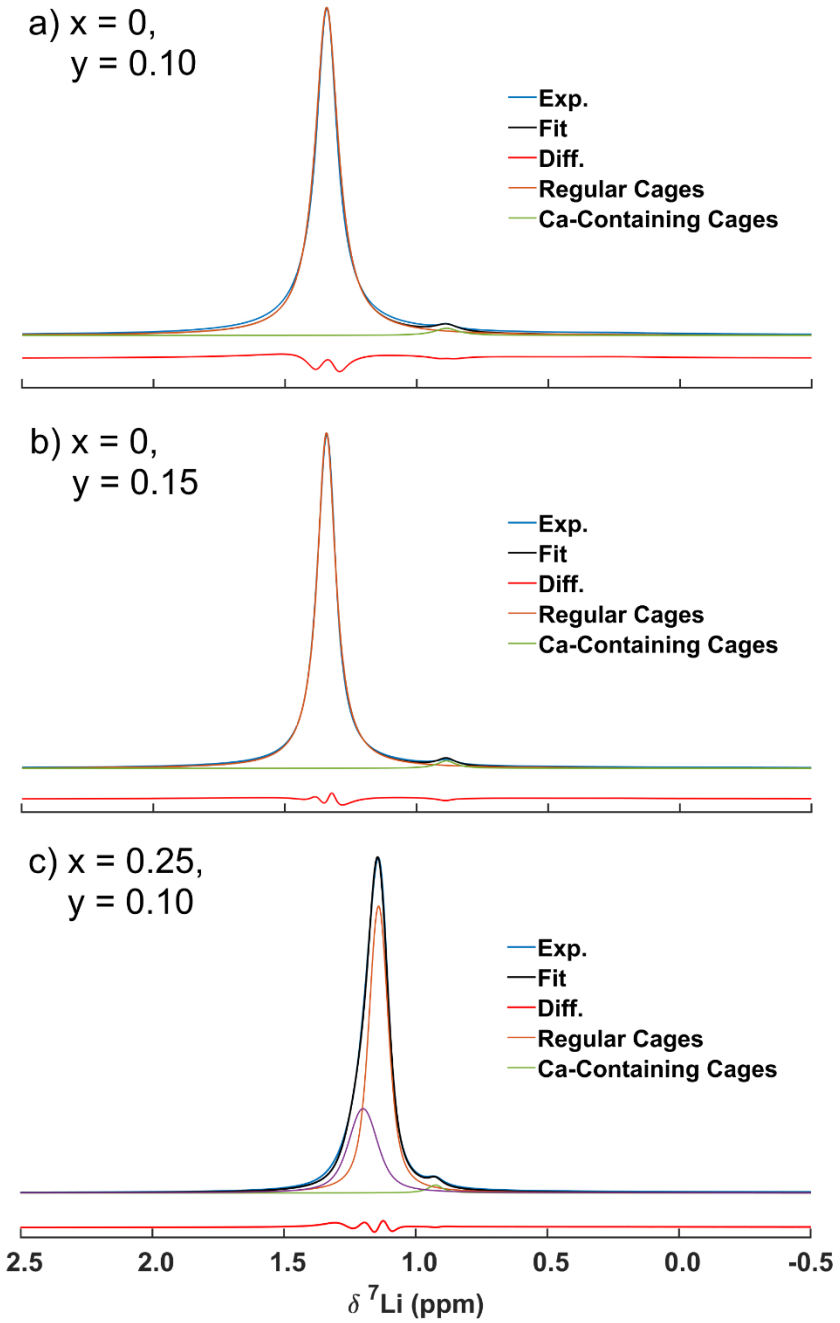

Figure 6.9 – Secondary peak deconvolutions of ^{7}Li MAS-NMR spectra for the compositions where the halide-enrichment shift trend did not obscure them. In all cases, the blue lineshape is the spectrum, the orange lineshape is the primary resonance, the green lineshape is the secondary resonance, and the black lineshape is the fit sum (the additional purple lineshape for $(x = 0.25, y = 0.10)$ is to account for the halide disorder chemical shift dispersion).

corresponding to the Ca^{2+}/Li^{+} stoichiometric ratio in each case (**Figure 6.9**). These secondary signals in the one-dimensional ^{7}Li MAS-NMR spectra were deconvoluted using Lorentzian lineshapes to fit both the primary and secondary peaks; the primary peak was fit in isolation first and then the secondary peak was fit using the same line-broadening as determined for the first peak. Owing to the chemical shift dispersion for the $(x = 0.25, y = 0.10)$ composition – the appearance of asymmetry in the halide-enriched lineshapes discussed in section **6.4.1** – a second Lorentzian was added and fit in conjunction with the primary Lorentzian to account for the full primary peak. The secondary-to-primary peak ratios are 1.8%, 2.2%, and 1.4% from top to bottom in **Figure 6.9**. With $z_{\mathrm{Li}} = \{5.7,5.8,5.55\}$ and $y = \{0.10,0.15,0.10\}$, the targeted stoichiometric ratios of Ca^{2+}/Li^{+} are 1.7%, 2.6%, and 1.8%, respectively. **Figure 6.8** also demonstrates that the same shift trend exhibited by the purely halide-enriched series of argyrodite compositions carries over to the dual-doped series (*i.e.* $= 0.10, x > 0$).

Additionally, ^{7}Li 2D exchange spectroscopy (EXSY), while not quantitative in this case owing to the difficulty in deconvoluting overlapping spectral volumes, indicates that lithium species generating these secondary peaks are in close proximity to those producing the primary peaks – that is, within the same phase, and not due to a contaminant impurity – since the cross peaks in an EXSY experiment can only form directly via chemical exchange or because of (short-range) homonuclear dipolar coupling (i.e. spin diffusion).[60] The cross peaks in these EXSY spectra (**Figure 6.10**) indicate that the Li^{+} ions corresponding to the two peaks are more than likely undergoing chemical exchange given the short mixing times involved, although variable-temperature experiments to test the

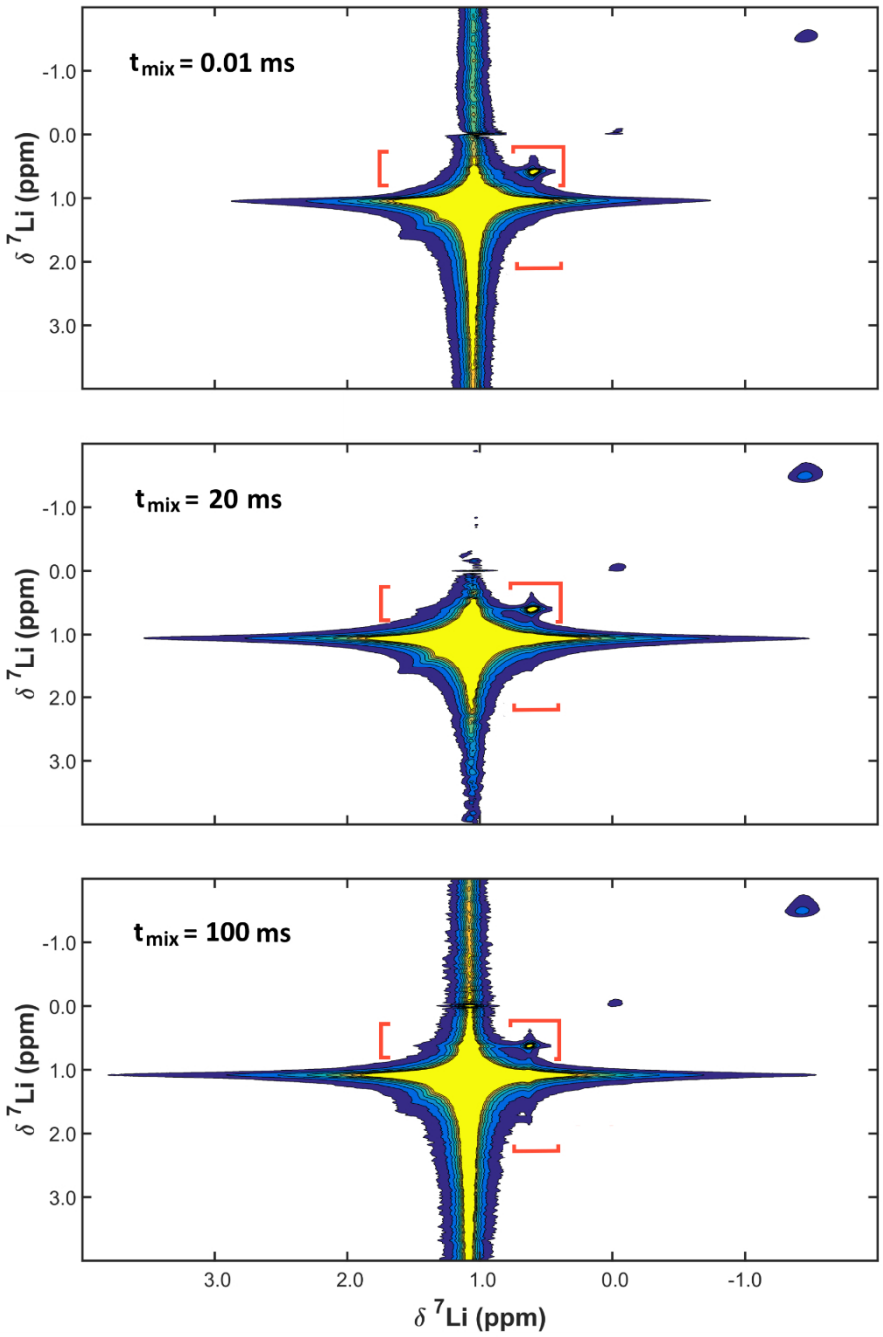

Figure 6.10 – Selected ^{7}Li 2D EXSY spectra for $y = 0.10$ at 20℃, at 850 MHz field strength and 30 kHz MAS rate. Red brackets indicate cross-peak regions for secondary signals associated with the presence of Ca^{2+} dopants in the Li^{+} cages. The 100 ms mixing time is on the order of T_1 for this sample.

thermal activation of the cross-peak onset were not attempted. Further to this point, the secondary peak for the much faster diffusing ($x = 0.25,\ y = 0.1$) composition is closer to the main resonance than it is for the $y = 0.1$ and $y = 0.15$ compositions, indicating a greater degree of averaging of the signals on the NMR timescale.

Temperature-dependent EIS and PFG-NMR measurements were then carried out to assess changes to the ion transport as a result of Ca^{2+} substitution in both y-series and dual-doped series samples. The diffusivities and impedance responses with the respective fits for selected compositions are shown in **Figure 6.11**; the diffusivities and conductivities at room temperature, as well as the activation energies for compositions varying in both Ca^{2+} and Cl^{-} content are displayed in **Table 3**. For the y-series $Li_{6-2y}Ca_yPS_5Cl$, the stepwise introduction of Ca^{2+} in the Li^{+} 48*h* site is accompanied by a gradual increase in vacancy concentration, which is the main contributor to the enhancement in the conductivity given that NPD results demonstrated that the anion disorder is not significantly changed *vis a vis* the parent-phase Li_6PS_5Cl. The effect of Ca^{2+} incorporation on the intracage or doublet jumps should be negligible at this small level of doping (one Ca per ~ 10 and ~ 6 cages for $y = 0.1$, $y = 0.15$ respectively), as it is the long-range transport between the cages which dictates the macroscopic conductivity in Li-argyrodites, as demonstrated by ab initio molecular dynamics simulations;[61] these studies showed that the intercage jump rate has the lowest jump frequency of all. The fact that the Ca^{2+} does not disrupt transport is further supported by the activation energies of the solely Ca^{2+}-substituted phases (**Table 6.2**), which are effectively the same as Li_6PS_5Cl.

Table 6.2 – Comparison of room-temperature transport properties and activation energies for the y-series and the dual-doped series.

$Li_zCa_yPS_{5-x}Cl_{1+x}$	D^*_{Li}(300 K), (m^2/s)	κ_{Li}(300 K), (mS/cm)	$E_a(D^*_{Li})$, (eV)	$E_a(\kappa_{Li})$, (eV)
Li_6PS_5Cl	$3.25(2) \times 10^{-12}$	2.5	0.35(1)	0.335(4)
$Li_{5.80}Ca_{0.10}PS_5Cl$	$4.15(3) \times 10^{-12}$	4.3	0.337(4)	0.35(1)
$Li_{5.70}Ca_{0.10}PS_5Cl$	$4.44(3) \times 10^{-12}$	5.2	0.334(3)	0.34(1)
$Li_{5.55}Ca_{0.10}PS_{4.25}Cl_{1.25}$	$8.23(8) \times 10^{-12}$	6.8	0.317(6)	0.33(1)
$Li_{5.425}Ca_{0.10}PS_{4.625}Cl_{1.375}$	$9.8(1) \times 10^{-12}$	7.2	0.307(7)	0.31(1)
$Li_{5.30}Ca_{0.10}PS_{4.50}Cl_{1.50}$	$9.10(9) \times 10^{-12}$	7.7	0.302(5)	0.31(1)
$Li_{5.35}Ca_{0.10}PS_{4.50}Cl_{1.55}$ Powder	$1.209(5) \times 10^{-11}$	10.2	0.287(4)	0.30(1)
$Li_{5.35}Ca_{0.10}PS_{4.50}Cl_{1.55}$ Pellet	$1.02(1) \times 10^{-11}$		0.301(4)	

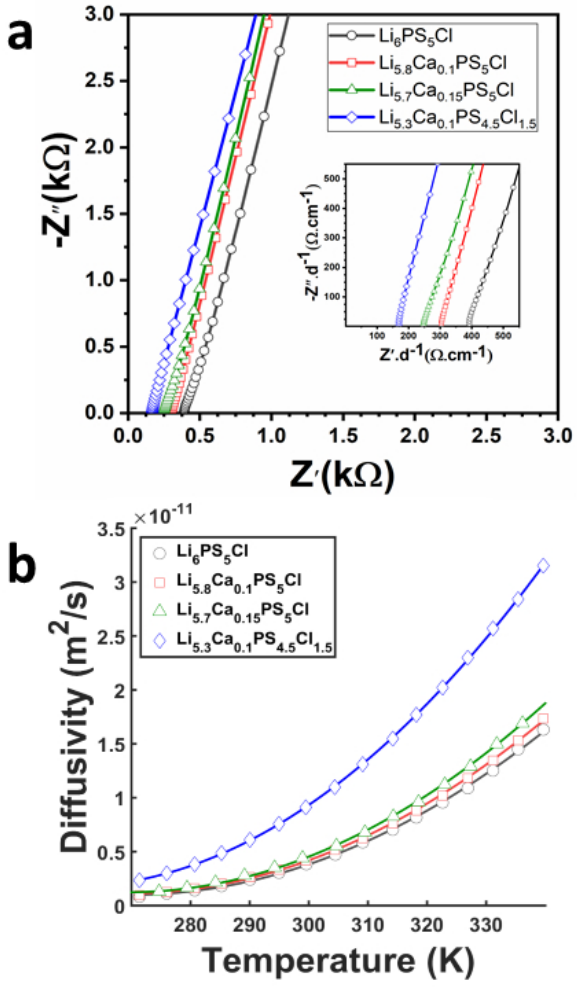

Figure 6.11 – a) Nyquist impedance plots of $y = 0$, 0.1, 0.15, and ($x = 0.5$, $y = 0.1$) at 298 K, normalized to the pellet thickness. Figure inset illustrates the enlarged view at high frequencies. b) Diffusivity plots for the same samples, from the PFG-NMR data, illustrating the significantly different effects on the two types of transport measurement from the two doping strategies.

Room temperature Li^+ diffusivities exhibited by the $y = 0.1$ and $y = 0.15$ phases are 4.15×10^{-12} m^2/s and 4.44×10^{-12} m^2/s respectively, compared with 3.85×10^{-12} m^2/s for $y = 0$ (parent phase), which reflects a respective 8% and 15% increase. On the other hand, the dual-doped argyrodite ($x = 0.5, y = 0.1$) exhibited a high diffusivity of 9.10×10^{-12} m^2/s, which is about 2.5 times that of the parent phase, but nevertheless still lower than that of the solely Cl-enriched phase ($Li_{5.5}PS_{4.5}Cl_{1.5}$); the interplay between the two doping mechanisms clearly becomes quite complex when both are simultaneously applied to their maximum extent. NPD results demonstrated that the additional vacancies contract the lattice, resulting in a progressive decrease in the intercage hop distance as the vacancy population is increased, coupled with the increase in the site disorder. These factors, conjointly with the weakened electrostatic interactions between the mobile Li^+ ions and surrounding framework anions (induced by substitution of divalent S^{2-} for monovalent Cl^-), are the key contributors to the high ionic conductivities for the dual-doped compositions, similar to what was found for the purely Cl-enriched argyrodites. However, it is possible that this contraction of the lattice might at some point reach a tipping point where defects are increasingly common, which explains the lower diffusivities of the ($x = 0.50$, $y = 0.10$) phase compared with ($x = 0.375$, $y = 0.10$). Indeed, this scenario might even lead to an altogether different macroscopic composition, which will be explored further in section **6.4.3**. It is also important to note that ionic conductivities for the soft argyrodites can be further improved by hot pressing the powder or sintering and modifying the grain boundaries. Indeed, the effect of purely cold-pressing the sample on the diffusivity

constitutes a key component of this study, and is described subsequently in section **6.4.3** as well.

Low activation energy is another structure factor for exhibiting excellent ionic conduction. E_a values obtained from ^{7}Li PFG-NMR are in good accord with the values obtained from impedance spectroscopy, as compared in **Table 6.2**. As with the purely halide-enriched x-series, there is a general downward trend with increasing substitution, but it is with E_a that the contrasting roles of the cation and anion doping is most telling. As noted above in conjunction with **Figure 6.8**, for each dual-doped composition, the chemical shift was virtually identical to that of the equivalent x-only series. Combined with the relatively small ^{7}Li chemical shift of the y-series relative to the parent phase Li_6PS_5Cl (again from **Figure 6.8**), this suggests that the Ca^{2+} dopants are not significantly modifying the electronic environment of Li^+ within the cages where the Ca^{2+} reside; their primary contribution to improving the transport is via the excess vacancies that they introduce to the Li^+ cage network.

This correlation is elaborated in **Figure 6.12**, which tracks the activation energy trends from both EIS and PFG-NMR, along with the isotropic ^{7}Li chemical shift under MAS, as a function of lithium stoichiometry, $z_{\mathrm{Li}} = x + 2y$. This enables comparisons to be made between the y-series and the dual-doped series ($y = 0.1$). Increasing x lowers the ^{7}Li chemical shift toward a more ionic, "LiCl-like" environment, but this effect eventually saturates, indicating that there is a limit to which disordering of S^{2-} sites with Cl^- can decrease Li^+ attraction to the anion framework. Nevertheless, the activation energy continues decreasing as x is increased, which stems from the impact of the additional

vacancies on Li^+ sites, as discussed above. Conversely, the lack of shift decrease on going from $y = 0$ to $y = 0.1$ opposes the associated activation energy drop, which can therefore be attributed strictly to the increased vacancy population. **Figure 6.12** also demonstrates that the most significant incremental lowering of the activation energy can be achieved by incorporating moderate Cl^- enrichment with a small amount of Ca^{2+} doping. The two effects act in concert to both lower the activation energy and boost the magnitudes of the conductivity and diffusivity to a greater amount than performing one or the other, when the solubility limit of the lattice with respect to either dopant is not exceeded.

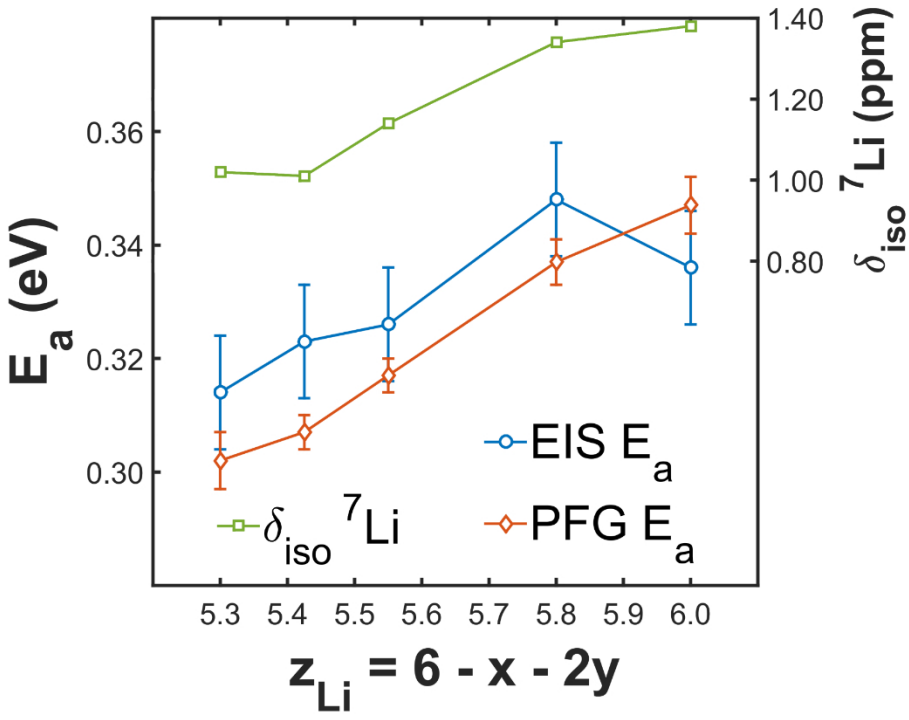

Figure 6.12 – Correlation of activation energies from both EIS and PFG-NMR, as well as ^{7}Li isotropic chemical shift, with lithium vacancy concentration ($x + 2y$).

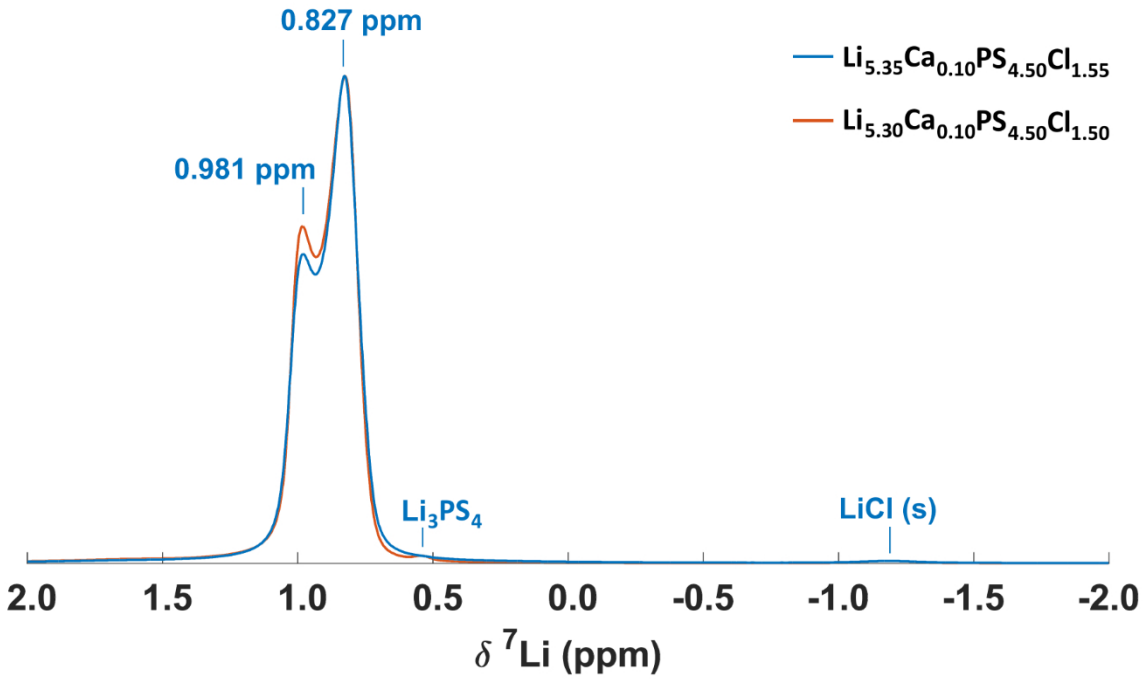

Figure 6.13 – ^{7}Li MAS-NMR spectrum for the so-called mixed-phase sample, $Li_{5.35}Ca_{0.10}PS_{4.50}Cl_{1.55}$. The resonance at 0.98 ppm is consistent with $x = 0.5$, as determined in **6.4.1**, and consistent with the minimal shift modification of the Ca^{2+}-doping relative to that of Cl^- (**Figure 6.8**), while the resonance at 0.83 ppm appears to be a much more halide-rich environment as per the established shift trend for increased Cl^- substitution. An example of a $(x = 0.5, y = 0.1)$ sample that also exhibited mixed-phase behaviour, which prompted the synthesis of the $Li_{5.35}Ca_{0.10}PS_{4.50}Cl_{1.55}$ mixed-phase sample with a deliberate LiCl excess, is overlaid for comparison. There is negligible (< 0.5% of integrated signal intensity) LiCl (s) in both samples.

6.4.3 The "Mixed-Phase" Sample and the Influence of Pellet Compression

For several nominally targeted $(x = 0.5,\ y = 0.1)$ samples that were synthesized, more than one primary peak appeared in the ^{7}Li MAS-NMR (**Figure 6.13**). Although there was no indication of more than one main phase in the XRD pattern, these samples interestingly exhibited higher diffusivity, which prompted further investigation. In particular, the diffusivity of the "mixed-phase" $Li_{5.35}Ca_{0.10}PS_{4.50}Cl_{1.55}$ sample, which

includes some intentional added LiCl excess, is 33% higher than ($x = 0.5,\ y = 0.1$), with an outstanding value of 1.21×10^{-11} m^2/s. The resulting mixed-phase sample is possibly a biphasic mixture of the ($x = 0.5,\ y = 0.1$) phase with domains in which $x > 0.5$ can exist, as evidenced by the ^{7}Li MAS-NMR spectrum for this sample in **Figure 6.13**, which exhibits a peak at 0.98 ppm consistent with $x = 0.5$ and an additional peak further shifted towards an even more "LiCl-like" environment at 0.83 ppm. The ^{31}P MAS-NMR for this same sample, **Figure 6.14**, also exhibits a series of shifts with cascading intensities,

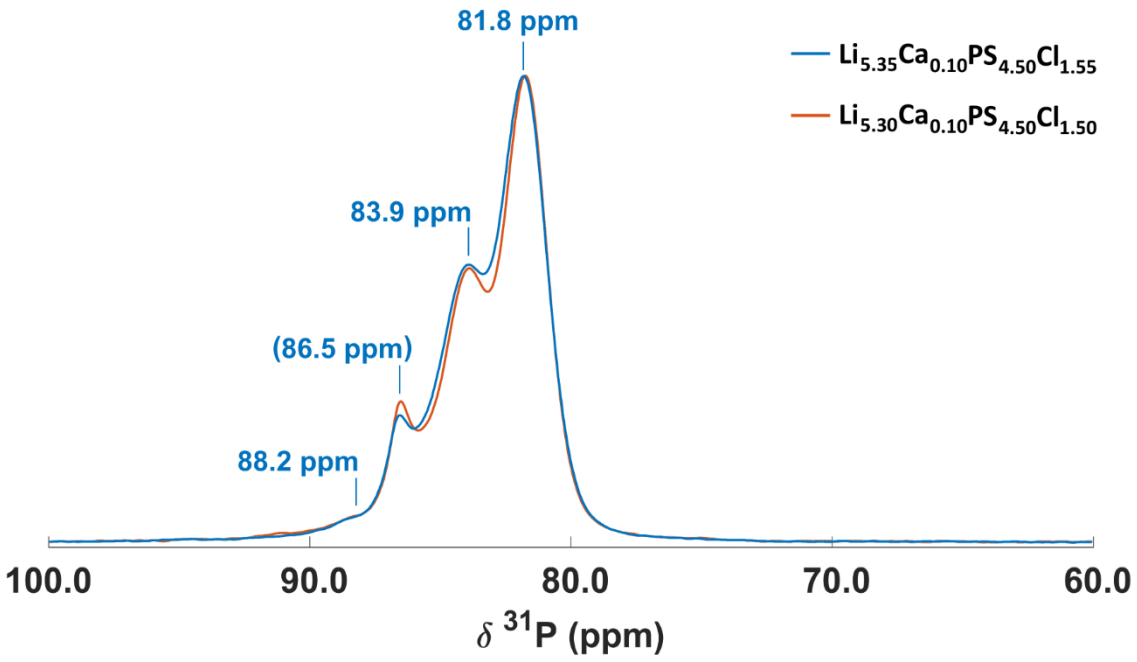

Figure 6.14 – ^{31}P MAS-NMR spectrum for the so-called mixed-phase sample, $Li_{5.35}Ca_{0.10}PS_{4.50}Cl_{1.55}$. The cascading pattern of nearly evenly-spaced resonances is indicative of a distribution of phosphorus environments with progressively increasing Cl^- substitution in the surrounding anion shells. Note that the resonance at 86.5 ppm is indicative of isolated $[PS_4]^{3-}$ tetrahedra, and overlays the shift distribution pattern (with the peak in this region expected, from the remainder of the pattern, to appear at ~86 ppm). It potentially arises from a small amount of Li_3PS_4-like impurity, which would appear in the tail of the ^{7}Li MAS-NMR spectrum at 0.5-0.6 ppm (and is definitely present in the sample ($x = 0.5, y = 0.1$) sample provided there, as well as here, for comparison).

indicative of a series of Cl^- substitution levels in the surrounding anion shells, as would be expected from the NPD results on the anion disorder.

Further insight into the activation energy magnitudes was obtained by performing ^{7}Li PFG-NMR on both powder and pellet-pressed versions of the mixed-phase sample, $Li_{5.35}Ca_{0.10}PS_{4.50}Cl_{1.55}$. Over the temperature range of 243 K to 358 K, the Arrhenius plots exhibit non-ideal behaviour, with curvature appearing in the lower temperature region of this range (**Figure 6.15**). This type of behaviour has been previously observed in variable-temperature EIS measurements for $Li_{10}SnP_2S_{12}$,[10] where it was established as being a cross-over from domination of grain-boundary contributions in the lower temperature regime to predominantly bulk grain contributions by careful equivalent-circuit modelling of the Nyquist plots. The magnitude of activation energy difference for the mixed-phase sample obtained by performing a two-component, limiting-slope fit of the PFG-NMR Arrhenius plots (**Figure 6.16**) is evidently not as extreme as in $Li_{10}SnP_2S_{12}$ (grain versus grain boundary difference of 0.27 eV to 0.60 eV for $Li_{10}SnP_2S_{12}$, compared with (0.383 ± 0.004) eV to (0.257 ± 0.007) eV for the uncompressed mixed-phase $Li_{5.35}Ca_{0.10}PS_{4.50}Cl_{1.55}$ sample). However, the temperature range achievable with the PFG-NMR setup may not have been sufficiently low as to fully avoid fitting to some of the cross-over curvature between the grain- and grain-boundary-dominated regimes. Nevertheless, the primary conclusion from comparing the activation energies between the powder and pellet-pressed samples is that in the "high temperature" regime associated with the grain contribution (as defined by the range of temperatures fit to the upper limiting slope – see **Figure 6.15**), the Arrhenius slopes are essentially parallel.

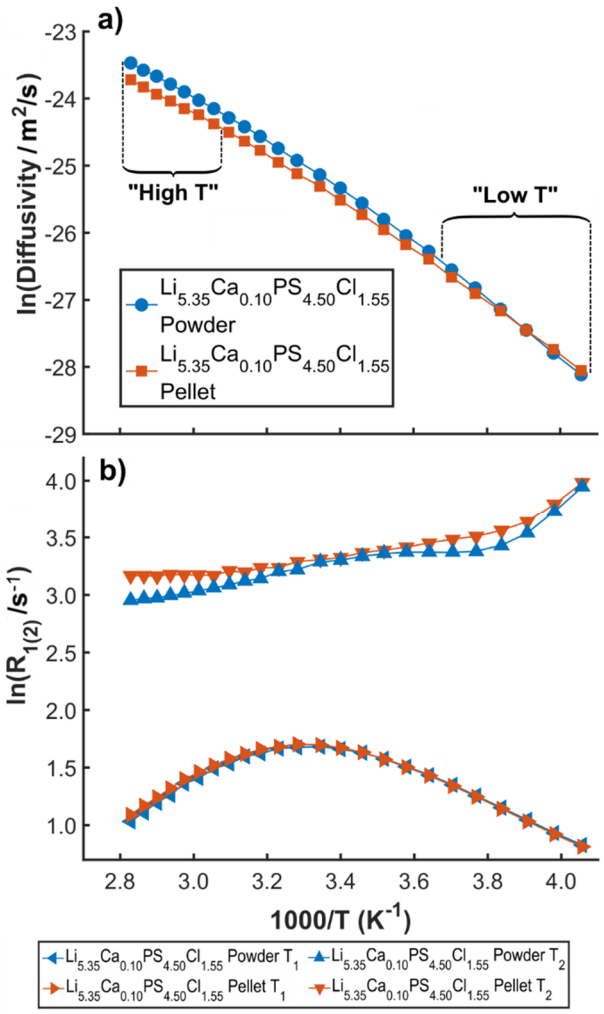

Figure 6.15 – a) Diffusivity Arrhenius plot from variable-temperature ^{7}Li PFG-NMR measurements on powder and pellet-pressed versions of the mixed-phase $Li_{5.35}Ca_{0.10}PS_{4.50}Cl_{1.55}$ sample, showing non-ideal Arrhenius behaviour with a cross-over in slopes from low to high temperature which is significantly reduced in the pellet version of the sample. b) NMR relaxation rates compared between the powder and pellet mixed-phase samples. Note the presence of two inflection points in the T_2 curve, indicating the presence of two distinct motional correlation times.

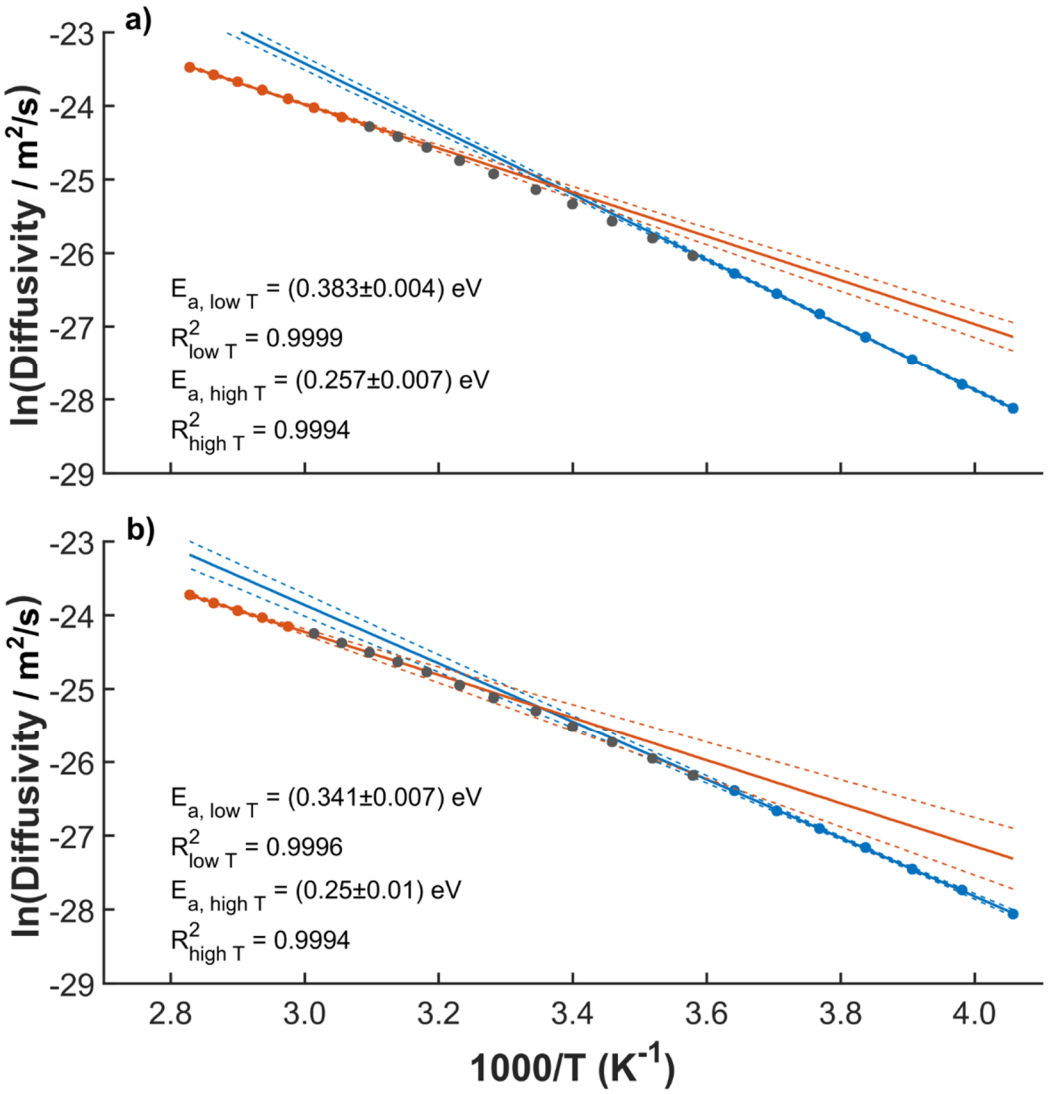

Figure 6.16 – Two-component activation energy fits to the Arrhenius plots for the ^{7}Li PFG-NMR data for the powder (a) and pellet (b) versions of the mixed-phase sample $Li_{5.35}Ca_{0.10}PS_{4.50}Cl_{1.55}$. The non-ideal Arrhenius behaviour is indicative of competing grain and grain-boundary contributions to the overall lithium-ion transport, with the latter having greater influence at lower temperature. That influence is reduced by the compression of the sample into a pellet (**Figure 6.15**).

On the other hand, in the "low temperature" regime, there is a distinct reduction in slope between the pellet-pressed and powder samples, which can be attributed to a reduction in the difficulty of hops over grain dislocations in multi-crystallite particles when the spatial extent of these gaps is presumably reduced by the macroscopic compression of the sample. The relative magnitudes of the activation energies for these regimes are summarized in **Figure 6.17**. Note that, for the sake of uniform comparison between the compositions, the PFG-NMR activation energies for all compositions listed in **Table 3** are single-component fits over the same temperature range of 268 K to 343 K, though even within this more restricted temperature range, there is still evidence of curvature in the Arrhenius plots (**Figure 6.18**).

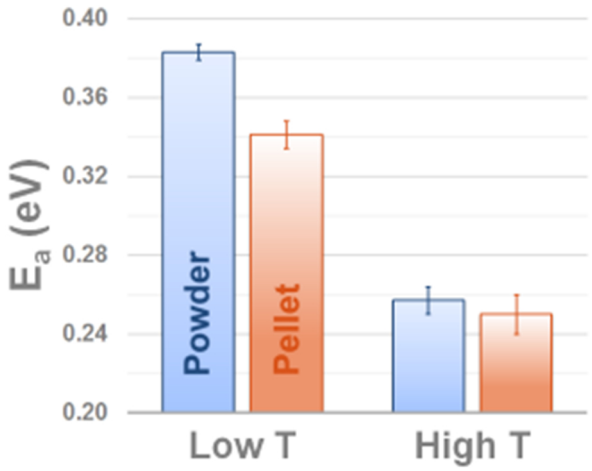

Figure 6.17 – Comparison of powder and pellet activation energies in the "low"- and "high-temperature" regions of the ^{7}Li PFG-NMR diffusivity Arrhenius plots from **Figure 6.15** for the mixed-phase sample $Li_{5.35}Ca_{0.10}PS_{4.50}Cl_{1.55}$. (See **Figure 6.16** for explicit delineations for the limiting slopes.) The high-temperature region is the same between samples and is associated with grain contributions, while the compression to form the pellet enhances transport across grain dislocations in multi-crystallite particles, which is the source of the lower activation energy in the pellet sample for the low-temperature region, associated with grain boundary contributions.

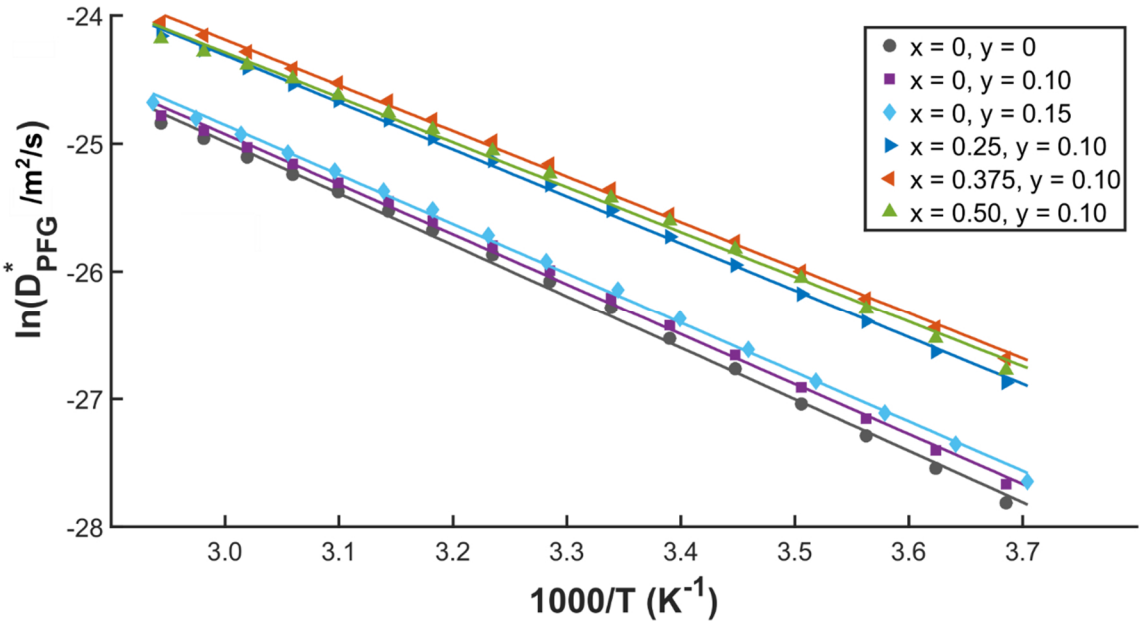

Figure 6.18 – Comparison of ^{7}Li PFG-NMR Arrhenius plots for the main y-series and (x, y)-series of compositions. Evident is the small amount of non-ideal behaviour – the slight curvature – even over the relatively restricted temperature range (268 K – 343 K) from which the activation energies in **Table 6.2** were calculated.

As demonstrated in **Figure 6.15**, variable-temperature T_2 relaxation measurements clearly show the presence of two motional correlation times in the form of inflection points in the Eyring plot; one associated with the T_1 minimum, and a separate one in the low-temperature flank which has no associated local minimum in the T_1 rate curve. The pairing of a T_1 minimum with an inflection point in the T_2 rate curve is a generic feature of Bloembergen-Purcell-Pound relaxation theory, irrespective of the type of fluctuating interaction which is the source of the relaxation.[62] This buttresses the assignment, in the diffusivity Arrhenius plot, of two distinct regimes of motion, as opposed to a significant difference in the ion transport between the two lithium environments known to exist in this mixed-phase sample (**Figure 6.13**). The same interaction must be driving the longitudinal relaxation in both (and is evidently not significantly modified by the mechanical

compression), but there is an additional timescale purely associated with the motion that is influencing the T_2 rate curve in the lower-temperature region. It is also interesting to note that T_2 is slightly reduced in the pellet sample relative to the powder at each temperature, and the diffusivity is also smaller, which is again indicative of some extent of compression in the lattice within the grains itself, consistent with the oft-touted thio-LISICON ductility. The detection of this difference in activation energies between the powder and pellet-pressed versions of the mixed-phase sample indicates that the efficacy of particle-scale, materials engineering modifications of fast-diffusing solid electrolytes can be interrogated with the use of PFG-NMR. It further indicates that careful analysis over a wide range of temperatures is necessary for fitting PFG-NMR Arrhenius plots in these materials in order to be able to compare macroscopic measurements with transport coefficients indirectly extrapolated from microscopic measurements, such as NMR relaxometry techniques,[11,32,46,47] or molecular dynamics simulations.[39,45,48,63]

6.4.4 LAPS Structural Insights from MAS-NMR and Quadrupolar NMR

In contrast to the argyrodite phases, where there is a single lithium site and most of the structural complexity pertains to the disorder in the anion framework, the structure of LAPS, $Li_{3.30}Al_{0.15}P_{0.85}S_4$, has proved much more difficult to nail down from XRD and NPD measurements. The most likely candidate, depicted in **Figure 6.2**, exhibits 3 lithium sites, with Li1 fully occupied and situated in highly symmetric tetrahedral positions, while Li2 and Li3 are less than 50% occupied, and are in highly distorted octahedral and tetrahedral sites, respectively, which form the primary, unidimensional ion conduction channels oriented along the b-axis. It is also common for syntheses of this phase to yield

10-20% amorphous product by weight percentage, even after heat treatment to form ordered crystal grains from the freshly synthesized glass. As a result, any compositional insights which can be gained from solid-state NMR analysis will help bolster the structural assignment, and will prove important in interpreting the diffusivity measurements also, as will be demonstrated in section **6.4.5**.

Beginning with the high-field, 30 kHz ^{7}Li MAS-NMR, **Figure 6.19** illustrates that there is a relatively sharp, dominating signal at 0.861 ppm, along with smaller inflection points to either side, at 0.471 ppm and 1.540 ppm. This general pattern is consistent with other β-Li_3PS_4-derived phases which have been examined; the example of β-Li_3PS_4 itself is provided in **Figure 6.20**, along with the LAPS glass sample for comparison. Comparing

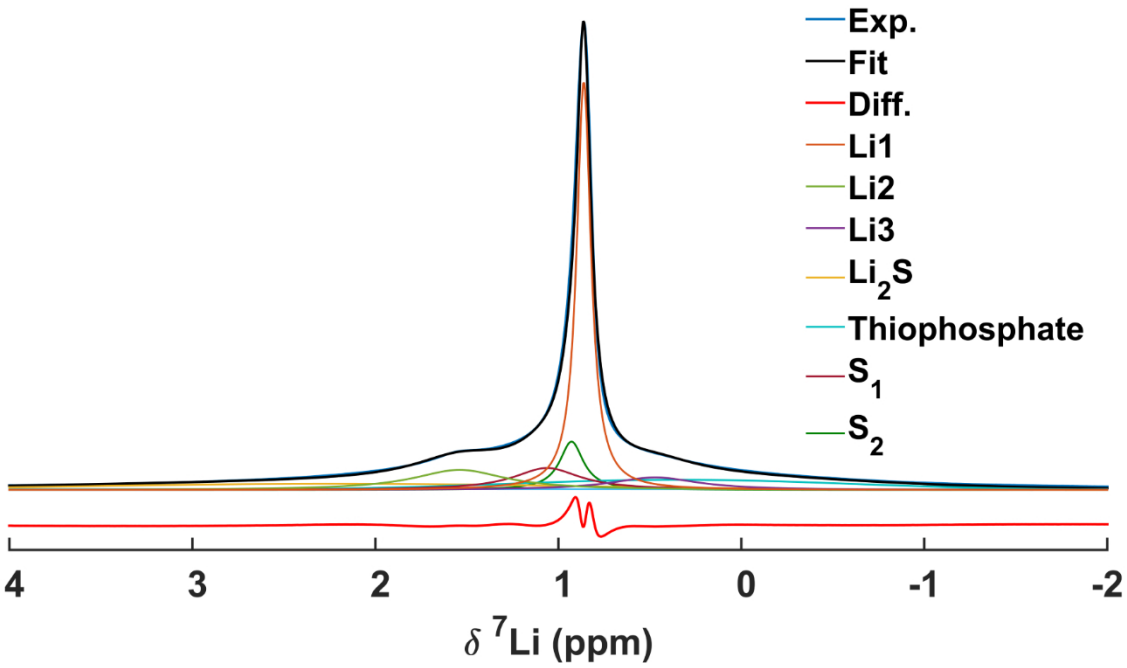

Figure 6.19 – ^{7}Li MAS-NMR of crystalline LAPS, $Li_{3.30}Al_{0.15}P_{0.85}S_4$, at 850 MHz and 30 kHz MAS rate, with deconvolution under the assumption of complete MAS averaging of the quadrupolar broadening.

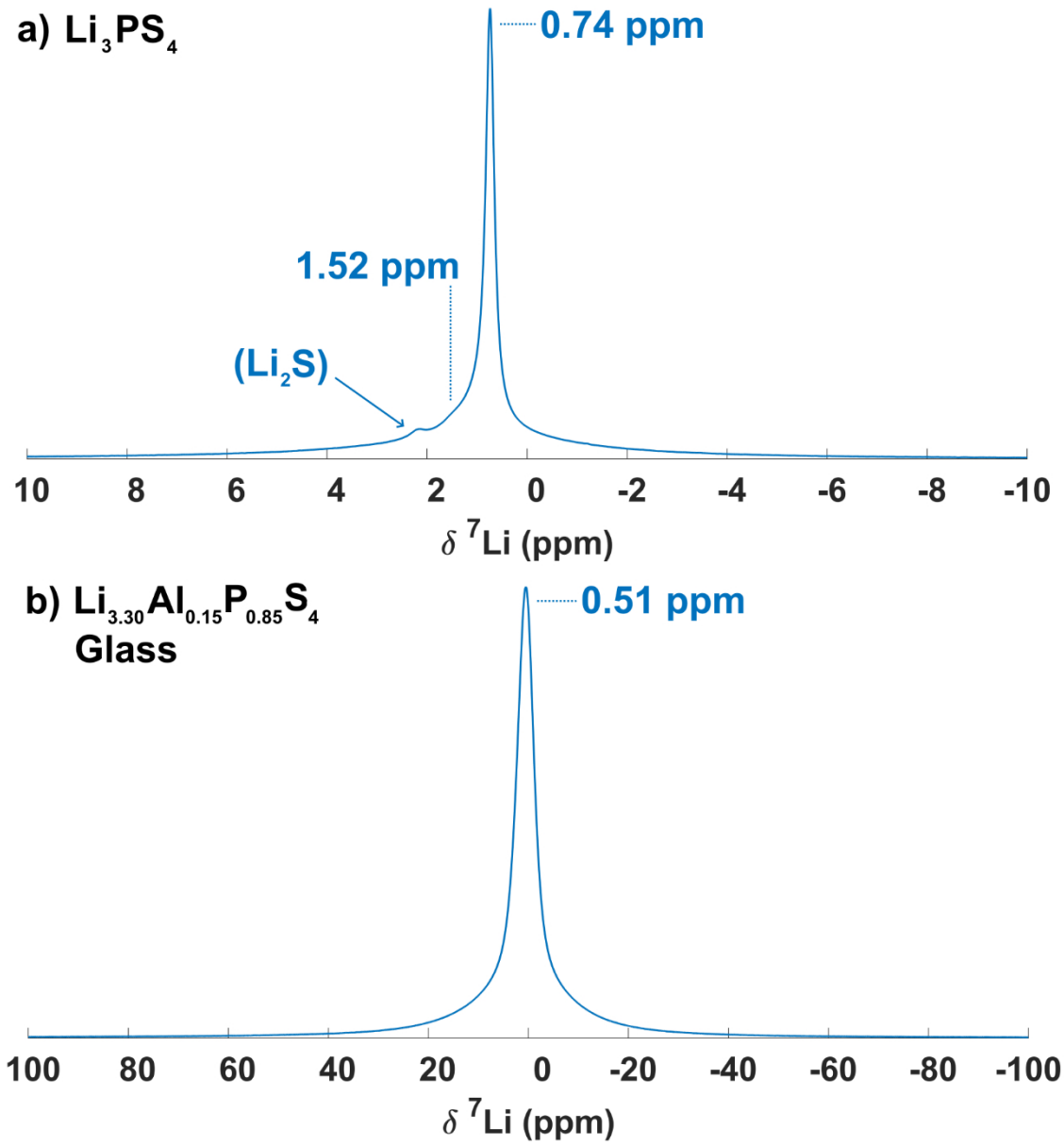

Figure 6.20 – ^{7}Li MAS-NMR of a) β-Li_3PS_4, and b) glass-phase LAPS, both at 850 MHz and 30 kHz MAS rate, to contrast with **Figure 6.19** for the crystalline LAPS. Note that the chemical shift scale is a factor of ten larger in b).

all three spectra, it is evident that the dominant signal in LAPS is shifted to slightly higher frequency than β-Li_3PS_4, but that the centre-of-mass for the glass sample is lower – in fact, resonating at a similar frequency to the lowest-frequency peak for the crystalline LAPS

sample. The β-Li_3PS_4 sample also evidently exhibits some Li_2S impurity (which is, after all, a precursor), which resonates at 2.22 ppm. The lineshape in **Figure 6.19** was deconvoluted with these observations in mind, under the assumption that all quadrupolar broadening was sufficiently averaged by the 30 kHz MAS rate (to be verified below, in the discussion of the static NMR lineshapes).

To obtain a very high-fidelity fit with only Lorentzian-Gaussian lineshapes, it was necessary to introduce five sharp resonances, and two broad ones in the tails of the spectrum. The latter are attributed to the amorphous phase – with Li_2S being highly consistent with the higher frequency resonance. Considering the position of the other impurity resonance in **Figure 6.19**, it is likely either residual glass, or some other type of thiophosphate phase. Collectively, the two impurity phases account for approximately 28% of the total ^{7}Li signal; while this is greater than the weight percentage of the amorphous phase, it is important to recognize that lithium is light and monovalent – often appearing in inorganic compounds at higher than unit stoichiometry – so it is unsurprising that this amorphous signal fraction exceeds the weight percentage. The results, and comparison with the NPD refinement in **Table 6.3**, are summarized in **Table 6.4**. The ^{31}P MAS-NMR spectrum, on the other hand, only reveals one relatively small secondary signal at 89.3 ppm, which is likely consistent with some sort of thiophosphate again,[64] but the broad signal centred at 81.5 ppm may mask additional contributions, and there is a shoulder at ~84 ppm. Primarily, the conclusions from the ^{31}P spectrum are that there is an absence of signal at 86.5 ppm consistent with isolated $[PS_4]^{3-}$ tetrahedra and related $[PS_4]^{3-}$-containing phases, and that the centre-of-mass is shifted to lower frequency, suggesting a modification

of the electronic band structure which implies the successful introduction of the Al into the anion lattice.

Table 6.3 – LAPS NPD Refinement Site Identification and Populations

Site	Symmetry	Multiplicity	Occupation	Expected Signal Fraction
Li1	Tetrahedral	8a	1.00	0.60
Li2	Dist. Octahedral	8a	0.44	0.27
Li3	Dist. Tetrahedral	4c	0.44	0.13

Table 6.4 – LAPS ^{7}Li MAS-NMR Lorentzian* Deconvolution

Resonance (ppm)	Fit Width (Hz)	Fraction of Crystalline Signal	Fraction of Total Signal	Putative Attribution
0.471	189	0.09	0.07	Li3
0.861	31.3	0.51	0.37	Li1
0.928	52	0.10	0.07	(Li1?)
1.062	146	0.13	0.09	(Li2?)
1.540	203	0.16	0.12	Li2
0.345	726 (G)		0.15	(Thiophosphate?)
2.220	1050 (G)		0.13	Li_2S

*Impurity peaks were fit with Gaussian lineshapes, under the assumption that amorphous signal would not exhibit Lorentzian tails; indicated in the column with a (G).

Since the static ^{7}Li lineshapes of LAPS exhibit pronounced quadrupolar satellite transitions, illustrated in **Figure 6.22**, it is also necessary to investigate whether the "extra" Lorentzian signals in the deconvolution of **Figure 6.19** may arise instead from a Czjzek lineshape, a phenomenon which arises in disordered quadrupolar systems under MAS, despite the nominal averaging of quadrupolar broadening. In particular, a Czjzek distribution can have an almost "trapezoidal" centre-of-mass extending to lower frequencies from the isotropic shift, which would potentially "fill in" some of the extra signals in the ^{7}Li MAS-NMR deconvolution between the 1.52 ppm signal and the main

resonance at 0.861 ppm. However, in order to perform this fit, it is necessary to have a reasonable estimate of the quadrupole parameters for each site – C_Q and η_Q – to parameterize the fit. These can be obtained from quadrupolar fitting to the static satellite transitions in **Figure 6.22**, in the process also furnishing an additional estimate for the fraction of amorphous ^{7}Li signal from the "remainder" of the quadrupole fits not accounted for under the 3-site model suggested by **Figure 6.2**.

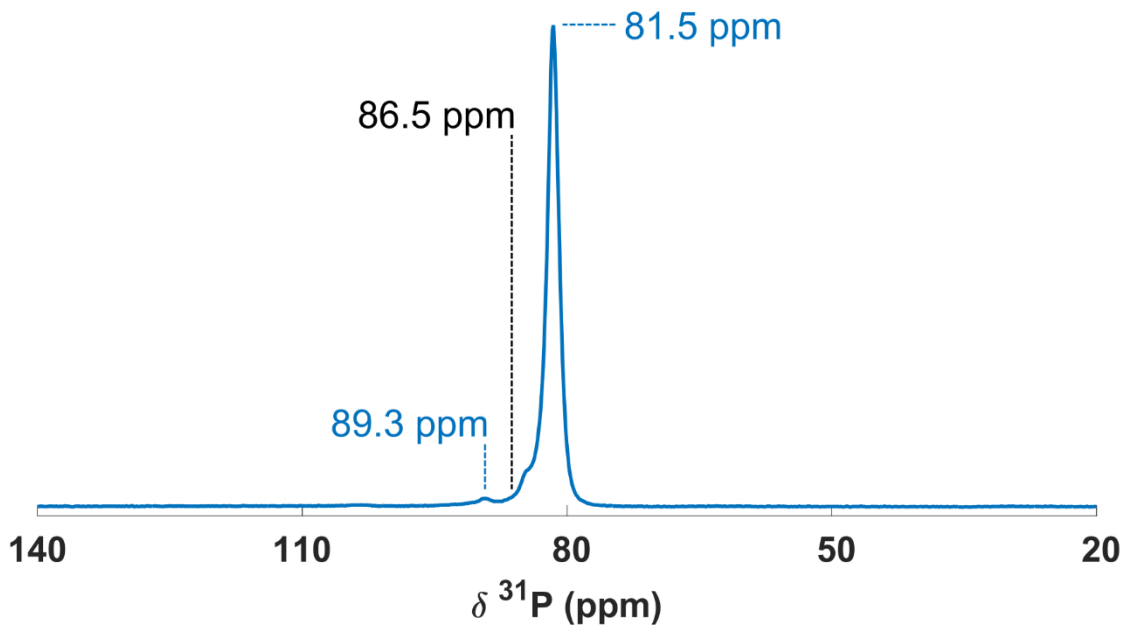

Figure 6.21 – ^{31}P MAS-NMR spectrum of crystalline LAPS at 850 MHz and 30 kHz MAS rate. The primary signal is at 81.5 ppm, with a shoulder centred at ~84 ppm and a secondary signal at 89.3 ppm.

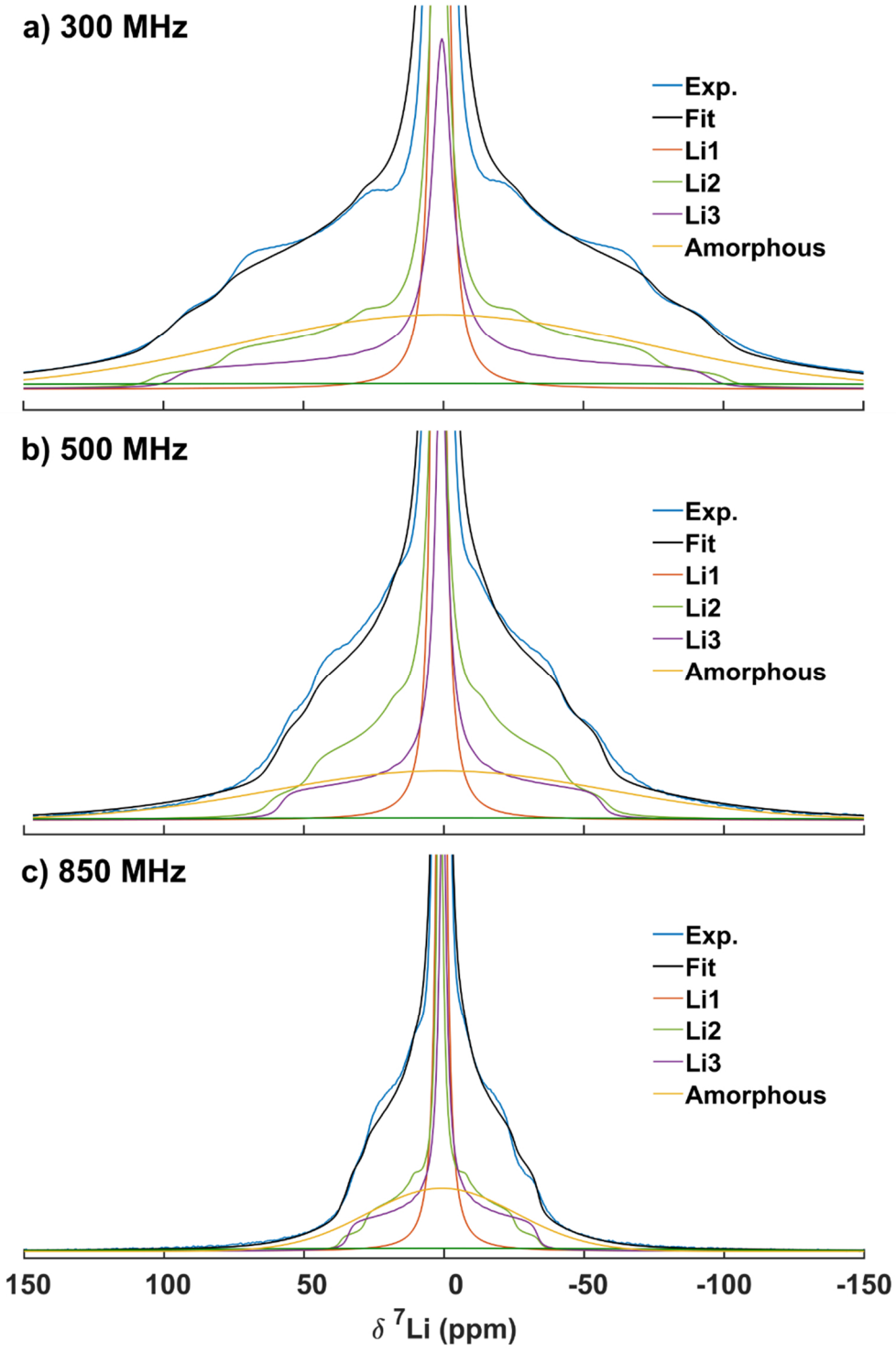

Figure 6.22 – Static ^{7}Li quadrupolar NMR spectra collected at 300 MHz, 500 MHz, and 850 MHz for crystalline LAPS, to obtain estimates of the quadrupole parameters and residual amorphous phase signal content.

The quadrupolar deconvolutions in **Figure 6.22** were performed under the assumption that $\eta_Q(\mathrm{Li1}) \ll \eta_Q(\mathrm{Li2}) < \eta_Q(\mathrm{Li3})$, on the basis of the site symmetries and relative populations from the NPD refinement. The fits were replicated at three field strengths: 300 MHz, 500 MHz, and 850 MHz, in order to ensure consistency. Exact quantitative fitting of the static quadrupolar lineshapes is difficult because of the interplay between the nutation rate of quadrupolar signals and the applied RF power,[65] which makes it difficult to guarantee uniform excitation of the entire lineshape. However, as stated, the primary objective of these fits was simply to extract the lineshape parameters and estimate the size of the residual contribution from the amorphous phase. It was found that $C_Q \cong 23.5$ kHz for Li2 and $C_Q \cong 22.5$ kHz for Li3, but more diagnostically, $\eta_Q = 0.495$ for the former and $\eta_Q = 0.96$ for the latter. From the three fits, the residual amorphous

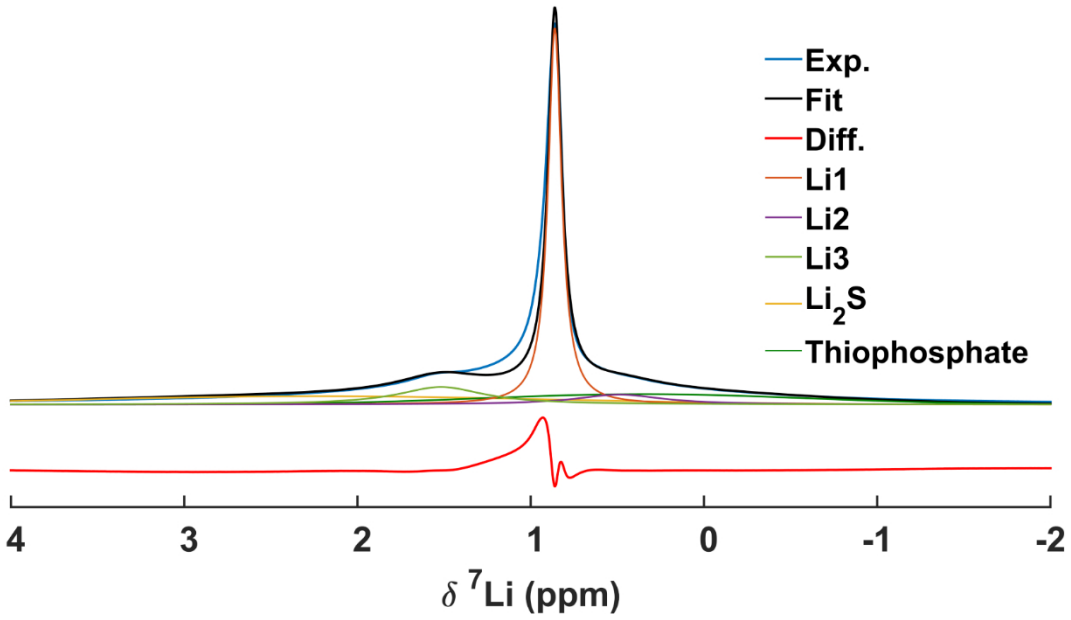

Figure 6.23 – Czjzek fit to the ^{7}Li MAS-NMR lineshape at 850 MHz and 30 kHz, originally presented as a Lorentzian deconvolution in **Figure 6.19**. The Czjzek model evidently cannot explain the lineshape on the basis of 3 sites + amorphous content.

contribution to the total signal fraction was estimated to be 0.28 ± 0.02, with a low of 0.25 for 300 MHz and a high of 0.31 for 500 MHz, consistent with the sum of the two impurity peak signal fractions identified in the MAS-NMR deconvolution.

The values for the quadrupole parameters were then used to generate a fit library for the Czjzek fit in ssNake v1.0, using the isotropic shift positions identified from the Lorentzian deconvolution. The results are presented in **Figure 6.23**, and indicate that the C_Q of the two asymmetric lithium sites are simply not large enough to generate significant Czjzek broadening, despite the large asymmetry parameters of the signals; the 5-signal Lorentzian fit model is therefore the most suitable representation of the MAS-NMR lineshape. Given this conclusion, it is necessary to reconcile the two extra Lorentzian signals in the MAS-NMR deconvolution with the NPD refinement. Since the unassigned signal S_2 (0.928 ppm) is entirely encompassed by the significantly larger Li1 signal, it is reasonable to suppose that this may simply be chemical shift dispersion from the combinatorics of Al-containing P1 sites nearby, versus the (majority) of Li1 tetrahedra which would not have a nearby Al-containing P1 site, based on the relatively small amount of Al doping, and in analogy with the same phenomenon observed with the $x > 0$ argyrodite ^{7}Li MAS-NMR spectra (refer to **Figure 6.9**). If this supposition is taken at face value, then by comparing the signal fractions in **Table 6.4**, it must be that the remaining Lorentzian signal at 1.062 ppm, S_1 in **Figure 6.19**, is somehow associated with Li2, or perhaps more likely should be split between the Li1 and Li2 resonances, again with some sort of chemical shift dispersion. However, lacking a model which could accurately account

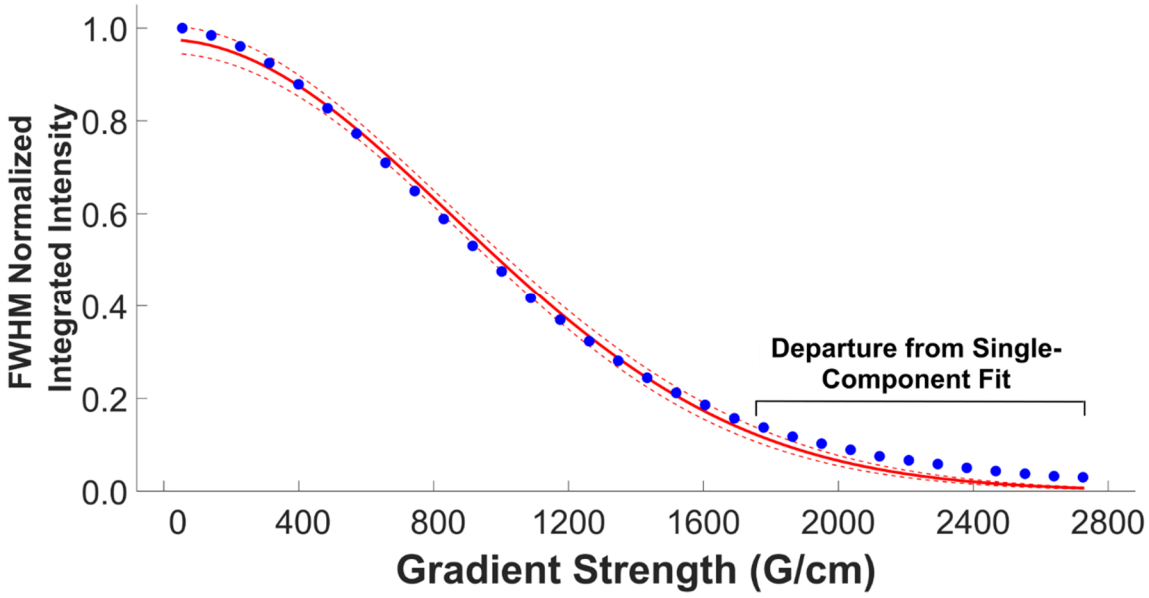

Figure 6.24 – Attempted single-component diffusivity fit to the crystalline powder LAPS sample PFG-NMR attenuation curve at 358 K, showing that slower diffusion at high gradient values is not well captured. (Note that the confidence interval for the fit decreases at high gradient strength because the model approaches zero asymptotically here.)

for this disorder-induced chemical shift dispersion, this final piece of attribution is not pursued further.

6.4.5 LAPS Transport and the Influence of Sample Preparation

The importance of determining the fraction of amorphous content in the sample becomes critical upon turning to the analysis of the PFG-NMR results for the crystalline powder and crystalline pellet LAPS samples. As with the mixed-phase argyrodite sample in section **6.4.4**, it is very desirable to quantify the impact of sample preparation on the macroscopic transport – whether the sample is prepared as a glass, a crystalline powder, or a compressed pellet of the crystalline powder. However, inspection of the PFG-NMR signal attenuation curves readily reveals that a single-component diffusivity fit via the usual

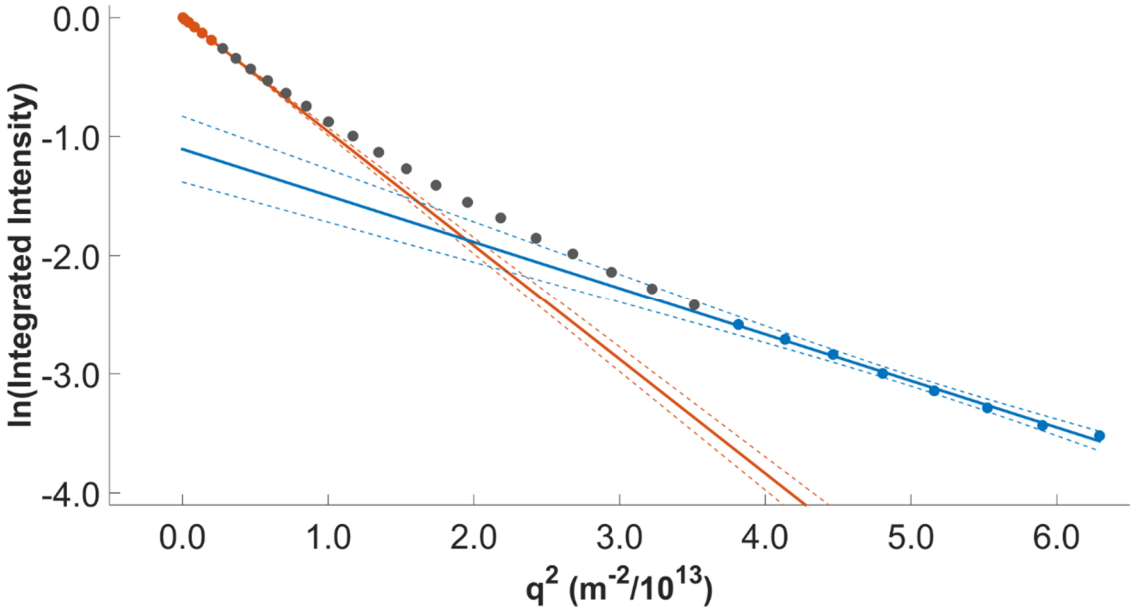

Figure 6.25 – Two-component, limiting-slope fit under the intermediate-time approximation to the linearized version of the attenuation curve in **Figure 6.24**, with $q = \gamma\delta g$.

Stejskal-Tanner equation does not adequately capture the attenuation, as demonstrated in **Figure 6.24**. It is therefore necessary to explore the possibility of diffusive exchange between the amorphous phase, as it would exist within grain boundaries and adhered to the surface of the individual crystallites. Tellingly, the glass-phase LAPS sample PFG-NMR attenuation curves are well fit by a single diffusivity component, resembling the attenuation curve for the $x = 0.5$ argyrodite sample in **Figure 6.3**.

A simple, signal-fraction-weighted two-component fit to the diffusivity (known as the "long-time approximation"),[62] does not resemble the linearized attenuation curve, which shows that the two components must be somewhat similar in magnitude (**Figure 6.25**). Therefore, the so-called "intermediate-time approximation" to the Kärger equations,[66] describing multi-compartment diffusion with exchange between compartments

having residence times τ_i and occupation fractions p_i, was adopted (refer to **Section 2.3** for additional details). In this formalism, when there is a two-compartment scenario with $p_1 \ll p_2$ and the diffusion rate is higher for p_1, the limiting slopes of the attenuation curve have simple relations to the diffusivities, residence times, and occupation fractions. The compartment with the smaller fraction and higher diffusivity will be identified with the amorphous phase here, while the other is "the bulk phase." Note that "higher" in the context of diffusivity does not necessarily mean "faster moving" (diffusivity is not a speed), or that there is not a significant energy barrier to a particle entering the amorphous phase; it simply refers to the fact that particles which exchange into this amorphous phase will possess a larger diffusion sphere over the duration of the experiment, relative to the more confined "bulk" particles.

The fitting approach is to cycle through combinations of the attenuation data points, split at the so-called "breakpoints," and find the minimum combined correlation coefficient, as an approximation to the limiting slope case. This balances the precision of the fit, by including sufficient numbers of data points at each limit, against the accuracy of the limiting slopes, to avoid fitting an outsized proportion of the curvature between the limits. The fitting output is demonstrated, again for the crystalline powder LAPS sample at 358 K, in **Figure 6.26**. This is where the crucial importance of an accurate estimation of the fraction of total signal attributable to the amorphous phase enters: there are too many parameters to extract two τ_i, two p_i, and two D_i^* from two limiting slopes. From the simple intermediate-time approximation, only combinations of these parameters can be determined from the

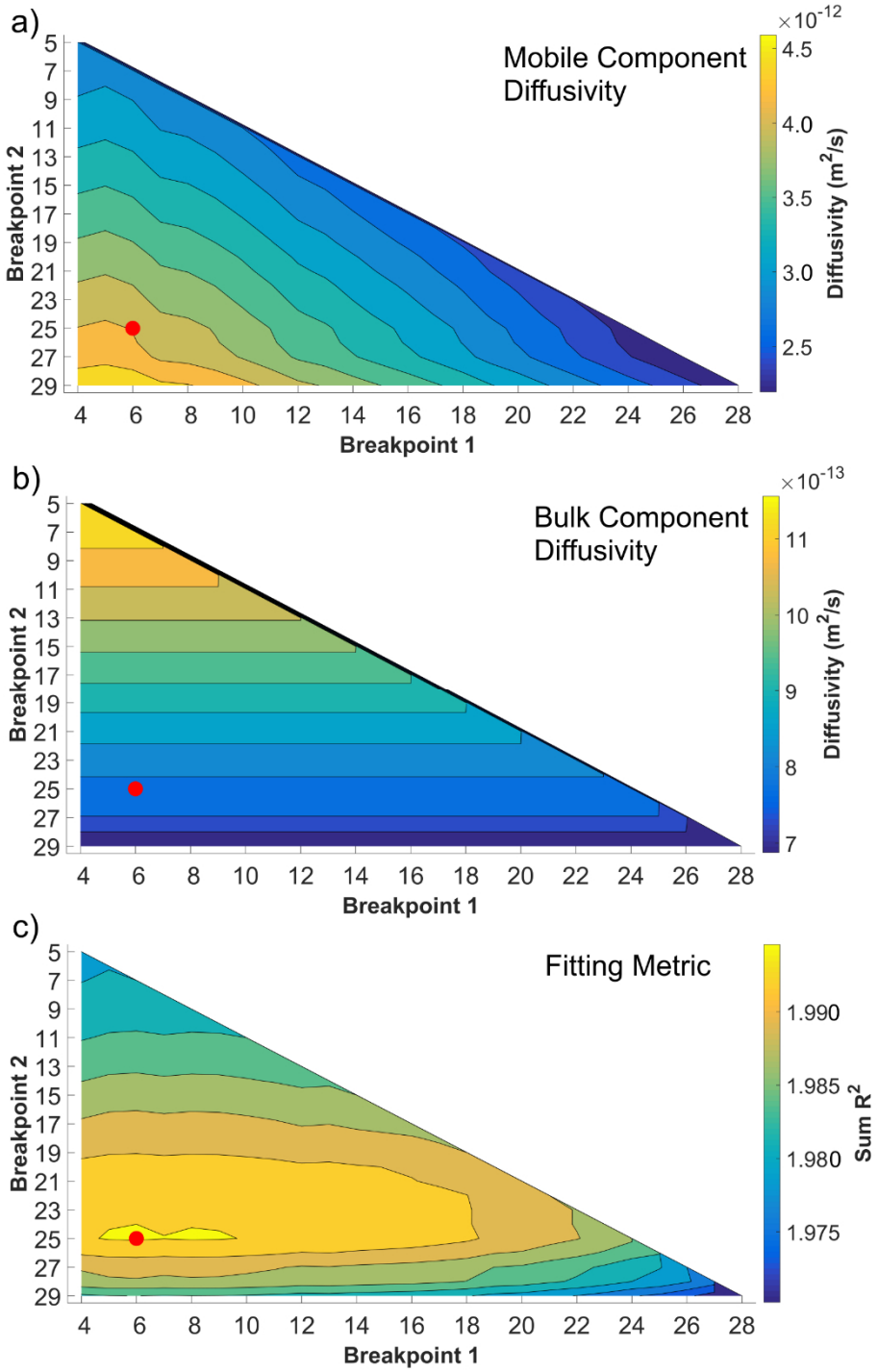

Figure 6.26 – The breakpoint-dependence of the component diffusivities from the limiting-slope intermediate-time approximation to the two-component diffusivity fit of the crystalline powder LAPS sample for a) the amorphous, and b) the bulk component. c) The combined correlation coefficient – the fitting metric – as a function of the location of the two breakpoints along the attenuation curve.

slopes, and bulk component intercept, and the intersection of the limiting slopes. However, since the p_i can be independently estimated from the deconvolutions in section **6.4.4**, they can be used to parameterize the fit, and every unknown can be resolved. This approach was then repeated for each of the temperatures studied, for both the crystalline powder and crystalline pellet samples, in order to separate out the amorphous and bulk components of the diffusivity and assess the impact of the sample preparation on each.

The two-component Arrhenius plots for each of the LAPS samples – glass-phase, crystalline powder, and crystalline pellet – along with the single-component Arrhenius plot for comparison, are presented in **Figure 6.27**. From the single-component plot, the hierarchy of the diffusivities is already apparent: the glass-phase is the smallest at every temperature, while the crystalline powder is the largest, as would be expected from a variant of the material with greater long-range order. Interestingly, the crystalline pellet diffusivity, while more similar to the crystalline powder in magnitude, is slightly lower. It can be surmised that, as a result of the compression, there is some deformation in the bulk of this ductile material which induces some constriction on the long-range ion transport. However, when comparing the fully-resolved two-component Arrhenius plots between the crystalline powder and the crystalline pellet, while the slope of the amorphous phase (*i.e.* the larger magnitude of the two diffusivity components) is approximately equivalent, there is a significant reduction in the slope of the bulk phase for the pellet sample. This is directly attributable to the modification of the spatial extent of the grain boundary voids, and the improved contact between the crystallites, in exact analogy with the findings for the compressed pellet sample of the mixed-phase argyrodite in section **6.4.3**. The activation

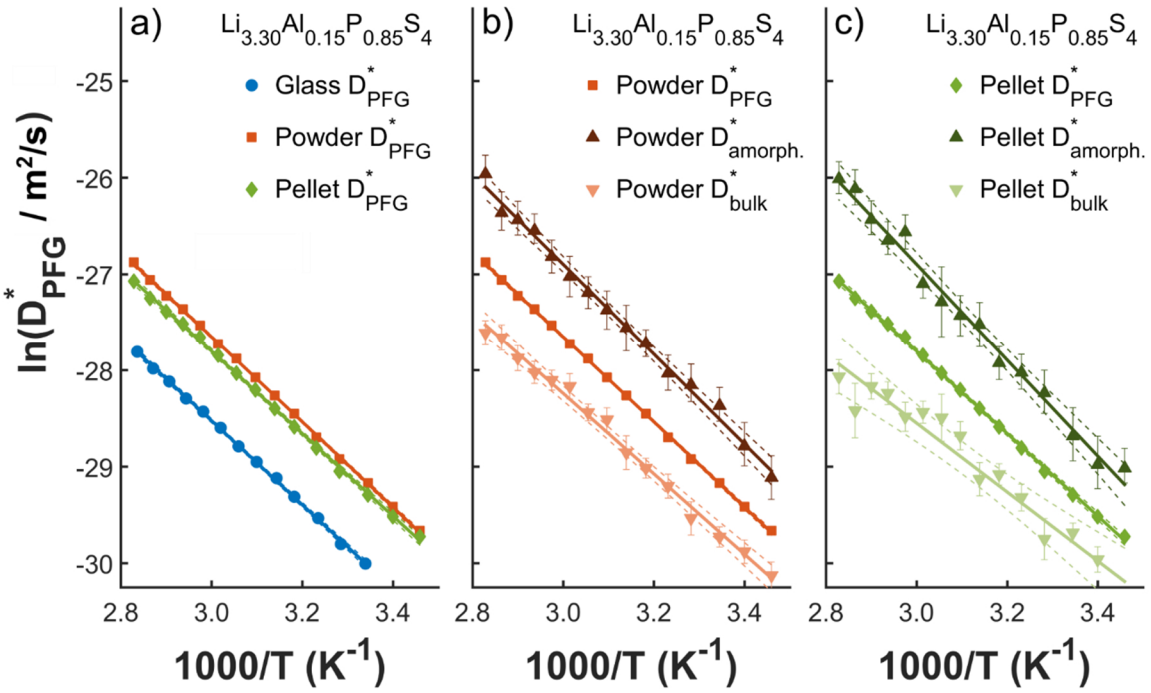

Figure 6.27 – Comparison of the single-component diffusivity Arrhenius plot (a) for the glass-phase, crystalline powder, and crystalline pellet LAPS samples with the two-component Arrhenius plots for (b) the powder, and (c) the pellet. The amorphous components of the powder and pellet samples are approximately similar, but the slope of the bulk component in the pellet sample is significantly reduced, indicating a reduced activation energy for the long-range transport.

energies obtained for each sample preparation from the Arrhenius plots are summarized graphically in **Figure 6.28**. Along with the trends discussed above, the additional salient point is that the bulk-compartment activation energy of the pellet sample agrees within uncertainty with the activation energy derived from variable-temperature ionic conductivity measurements for LAPS: $E_a(\kappa_{\mathrm{Li}}) = (0.302 \pm 0.003)$ eV versus $E_a\left(D^*_{\mathrm{Li,bulk}}\right) = (0.31 \pm 0.02)$ eV. Without a careful analysis of the multi-component diffusivity for this sample, factoring in the preparation method, it would not have been apparent that this agreement was latent within the diffusivity data.

The residence times, $\tau_{\text{amorph.}}$ and τ_{bulk}, were also extracted from the two-component limiting-slope fitting process, and are displayed in **Figure 6.29**. Since the determination of these parameters hinges on the intercept of the limiting slope for the smaller bulk component, the precision is not as high as for the diffusivity determination. Within this approximation, the ratio of the residence times is constant (colloquially, "if an ion is not in the bulk compartment, then it is in the amorphous compartment"), and they exhibit exponential increase with decreasing temperature, ranging from milliseconds in the amorphous phase at 358 K to over one second in the bulk phase at 288 K. Since the proportions of amorphous and crystalline phase are assumed to be consistent between the

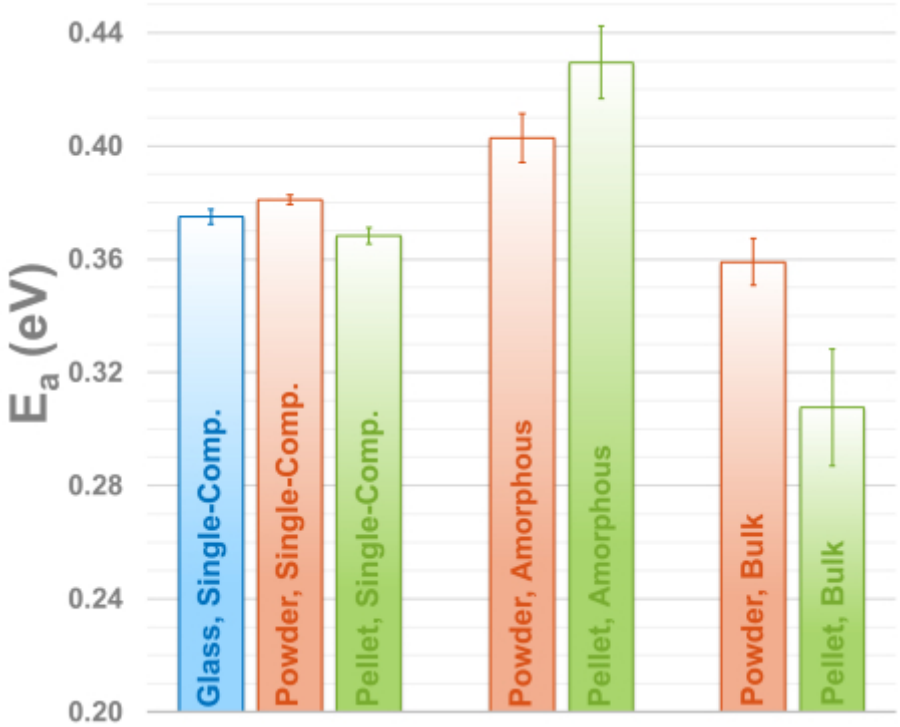

Figure 6.28 – Summary of the activation energies obtained from the Arrhenius plots of **Figure 6.27** for all sample treatments, with the amorphous and bulk compartment contributions for the crystalline samples separately extracted by the two-component fitting method.

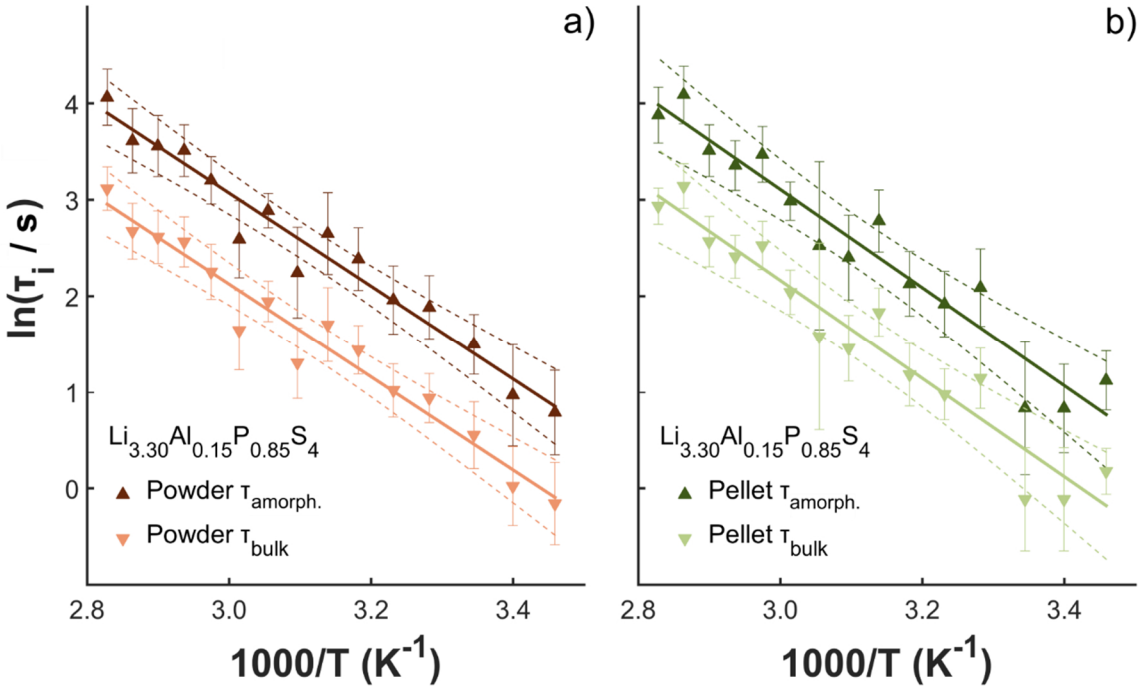

Figure 6.29 – The extracted bulk and amorphous residence times for the two-component diffusivity fits for the crystalline powder and crystalline pellet LAPS samples, demonstrating the exponential decrease in residence time with increasing temperature.

two samples (the pellet was made from the same batch that the sample for the powder was obtained from), the fits were parameterized with the same relative occupations, which is why the slopes are quite similar. Subtle differences in the relative residence times in the amorphous phase between the powder and pellet samples on account of the lower activation energy for the bulk diffusivity in the latter are, unfortunately, not discernible with the precision that was obtainable from the limiting slope analysis. It would be interesting to more carefully quantify this – potentially simply via the use of a denser gradient step ramp – as it would furnish an additional metric that could quantify the impact of sample treatment modifications on the long-range macroscopic transport.

Further support for the conclusions drawn from the two-component diffusivity analysis comes from the NMR relaxation measurements conducted at each temperature, for all of the sample treatments (**Figure 6.30**). As with the diffusivity measurements, the variable-temperature T_2 curves readily split into two branches for the crystalline sample treatments. The T_1 values were essentially consistent across temperatures between the three sample treatments, suggesting that the local magnetization transfer dynamics that generate longitudinal relaxation are unaffected by the macroscopic condition of the sample, as would be expected. However, the T_2 curves for the amorphous components – based, again, on the relative signal fractions – are very similar in magnitude to what is found for the glass

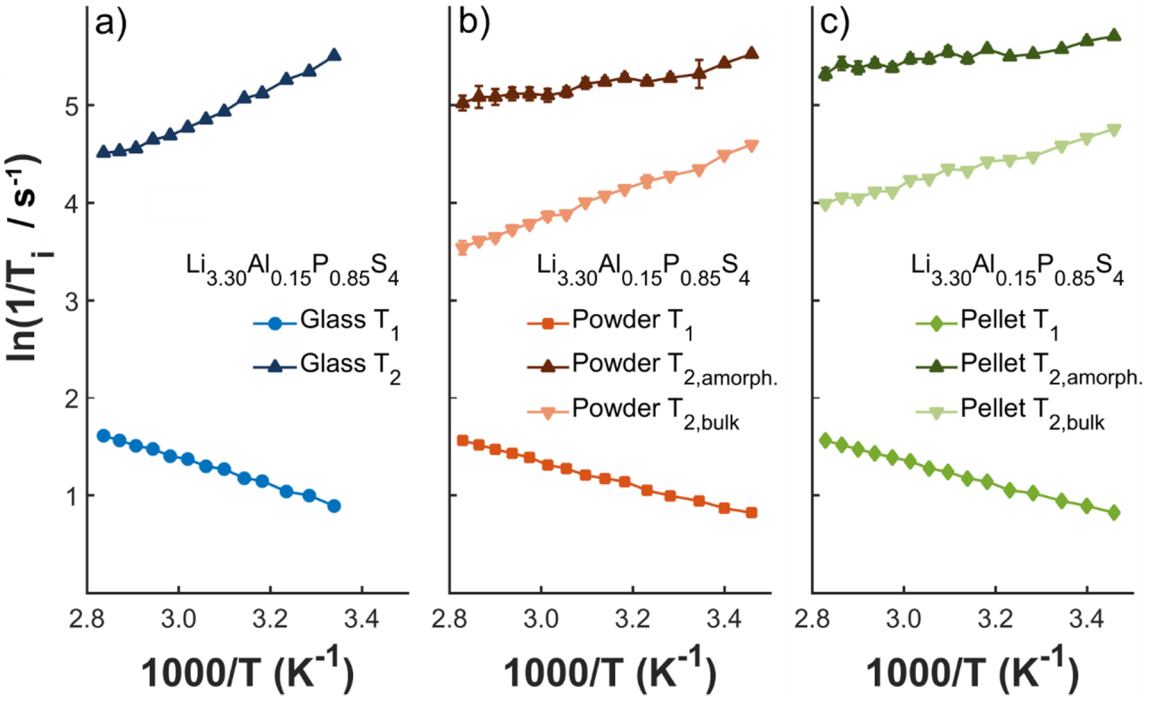

Figure 6.30 – Comparison of the NMR relaxation times as a function of temperature for all three sample preparations of LAPS: a) the glass-phase, b) the crystalline powder, and c) the crystalline pellet. In particular, note the similarity of the magnitude of the amorphous compartment branch in the crystalline samples to the glass-phase, and the shorter magnitude of the bulk compartment branch for the pellet sample compared with the powder sample.

sample, again suggesting that this compartment in the two-component fits indeed is the amorphous phase of the sample. Comparing the bulk compartment T_2 branches, a similar trend is observed as with the single-component diffusivities: the T_2 of the pellet bulk compartment is shorter than the uncompressed powder bulk compartment. Given that T_2 relaxation is predominantly governed by quadrupolar and dipolar coupling interactions in a diamagnetic system, both of which are distance-mediated,[62] it stands to reason that the compression has, to some extent, reduced the relevant length-scales for these interactions, thereby increasing their rate (the former via the steeper electric field gradient that induces quadrupolar coupling).

6.5 Summary and Conclusions

This chapter provided a survey of results in applying PFG-NMR and MAS-NMR, along with NMR relaxometry measurements, to two families of lithium-sulphide ion conductor, the argyrodites and a β-Li_3PS_4 derivative, $Li_{3.30}Al_{0.15}P_{0.85}S_4$. The aim of all three studies was to try to generate insight into the ion transport of these materials beyond simple quantification. The first study examined the impact of halide-enrichment on the argyrodites, looking at a series of compositions of the form $Li_{6-x}PS_{4-x}Cl_{1+x}$. Correlation of activation energies and Haven ratios obtained from PFG-NMR measurements with the shift trend as a function of x revealed by ^{7}Li MAS-NMR was able to explain the observed activation energy trend, and elucidate how the dominant mechanistic contribution to the ion transport boost from increasing x varied with the magnitude of x. Building on this approach, the effect of aliovalent doping with calcium ions in the argyodites, of the form $Li_{6-x-2y}Ca_yPS_{4-x}Cl_{1+x}$, was examined for a series of compositions. The role of the

calcium ions in increasing the vacancy population to boost ion transport was confirmed, and the relative magnitude of the enhancements from halide-enrichment and aliovalent doping was contrasted. Additionally, the ion transport of an unusual mixed-phase argyrodite composition was explored, and the effect of sample preparation on the diffusivity – in the form of a loose powder sample versus a compressed pellet sample – was examined. It was confirmed that PFG-NMR could detect subtle changes in the ion transport as a result of grain-boundary interfacing modification by the applied pressure during pellet fabrication. This concept was then transferred to the LAPS sample, with the diffusivity differences between glass-phase, crystalline powder, and crystalline pellet preparations quantified. The added complication of diffusive exchange with the amorphous phase in this sample was addressed with the novel application of a two-compartment diffusivity model, based on the Kärger equations, to separate out contributions to the PFG-NMR attenuation curves from the amorphous and the bulk, crystalline phase. The activation energy determined from the bulk compartment of the compressed pellet sample thus determined was consistent with the activation energy derived from macroscopic conductivity measurements.

6.6 References

(1) Price, W. S. *NMR Studies of Translational Motion*; 2009.

(2) Stejskal, E. O.; Tanner, J. E. Spin Diffusion Measurements: Spin Echoes in the Presence of a Time-Dependent Field Gradient. *J. Chem. Phys.* **1965**, *42* (1), 288–292.

(3) Heitjans, P.; Indris, S. Diffusion and Ionic Conduction in Nanocrystalline Ceramics. *J. Phys. Condens. Matter* **2003**, *15* (30), R1257–R1289.

(4) Chowdhury, M. T.; Takekawa, R.; Iwai, Y.; Kuwata, N.; Kawamura, J. Lithium Ion

Diffusion in Li β-Alumina Single Crystals Measured by Pulsed Field Gradient NMR Spectroscopy. *J. Chem. Phys.* **2014**, *140* (12), 124509.

(5) Kuhn, A.; Gerbig, O.; Zhu, C.; Falkenberg, F.; Maier, J.; Lotsch, B. V. A New Ultrafast Superionic Li-Conductor: Ion Dynamics in Li11Si2PS12and Comparison with Other Tetragonal LGPS-Type Electrolytes. *Phys. Chem. Chem. Phys.* **2014**, *16* (28), 14669–14674.

(6) Hayamizu, K.; Seki, S. Long-Range Li Ion Diffusion in NASICON-Type Li $_{1.5}$ Al $_{0.5}$ Ge $_{1.5}$ (PO $_{4}$) $_{3}$ (LAGP) Studied by ^{7} Li Pulsed-Gradient Spin-Echo NMR. *Phys. Chem. Chem. Phys.* **2017**, *19* (34), 23483–23491.

(7) Hayamizu, K.; Aihara, Y.; Watanabe, T.; Yamada, T.; Ito, S.; Machida, N. NMR Studies on Lithium Ion Migration in Sulfide-Based Conductors, Amorphous and Crystalline Li 3 PS 4. *Solid State Ionics* **2016**, *285*, 51–58.

(8) Chowdhury, M. T.; Takekawa, R.; Iwai, Y.; Kuwata, N.; Kawamura, J. Lithium Ion Diffusion in Li β-Alumina Single Crystals Measured by Pulsed Field Gradient NMR Spectroscopy. *J. Chem. Phys.* **2014**, *140* (12), 124509.

(9) Kuhn, A.; Duppel, V.; Lotsch, B. V. Tetragonal Li10GeP2S12 and Li 7GePS8-Exploring the Li Ion Dynamics in LGPS Li Electrolytes. *Energy Environ. Sci.* **2013**, *6* (12), 3548–3552.

(10) Bron, P.; Johansson, S.; Zick, K.; Schmedt auf der Günne, J.; Dehnen, S.; Roling, B. Li 10 SnP 2 S 12 : An Affordable Lithium Superionic Conductor. *J. Am. Chem. Soc.* **2013**, *135* (42), 15694–15697.

(11) Stöffler, H.; Zinkevich, T.; Yavuz, M.; Senyshyn, A.; Kulisch, J.; Hartmann, P.; Adermann, T.; Randau, S.; Richter, F. H.; Janek, J.; et al. Li + -Ion Dynamics in β-Li 3 PS 4 Observed by NMR: Local Hopping and Long-Range Transport. *J. Phys. Chem. C* **2018**, *122* (28), 15954–15965.

(12) Harm, S.; Hatz, A.-K.; Moudrakovski, I.; Eger, R.; Kuhn, A.; Hoch, C.; Lotsch, B. V. Lesson Learned from NMR: Characterization and Ionic Conductivity of LGPS-like Li 7 SiPS 8. *Chem. Mater.* **2019**, *31* (4), 1280–1288.

(13) Griffith, K. J.; Wiaderek, K. M.; Cibin, G.; Marbella, L. E.; Grey, C. P. Niobium

Tungsten Oxides for High-Rate Lithium-Ion Energy Storage. *Nature* **2018**, *559* (7715), 556–563.

(14) Hayamizu, K.; Seki, S.; Haishi, T. Non-Uniform Lithium-Ion Migration on Micrometre Scale for Garnet- and NASICON-Type Solid Electrolytes Studied By7Li PGSE-NMR Diffusion Spectroscopy. *Phys. Chem. Chem. Phys.* **2018**, *20* (26), 17615–17623.

(15) Dorai, A.; Kuwata, N.; Takekawa, R.; Kawamura, J.; Kataoka, K.; Akimoto, J. Diffusion Coefficient of Lithium Ions in Garnet-Type Li6.5La3Zr1.5Ta0.5O12 Single Crystal Probed by 7Li Pulsed Field Gradient-NMR Spectroscopy. *Solid State Ionics* **2018**, *327* (1 December 2018), 18–26.

(16) Kaus, M.; Stöffler, H.; Yavuz, M.; Zinkevich, T.; Knapp, M.; Ehrenberg, H.; Indris, S. Local Structures and Li Ion Dynamics in a Li10SnP2S12-Based Composite Observed by Multinuclear Solid-State NMR Spectroscopy. *J. Phys. Chem. C* **2017**, *121* (42), 23370–23376.

(17) Adeli, P.; Bazak, J. D.; Park, K. H.; Kochetkov, I.; Huq, A.; Goward, G. R.; Nazar, L. F. Boosting Solid-State Diffusivity and Conductivity in Lithium Superionic Argyrodites by Halide Substitution. *Angew. Chemie* **2019**, ange.201814222.

(18) Janek, J.; Zeier, W. G. A Solid Future for Battery Development. *Nat. Energy* **2016**, *1* (9), 16141.

(19) Zhang, Z.; Shao, Y.; Lotsch, B.; Hu, Y.-S.; Li, H.; Janek, J.; Nazar, L. F.; Nan, C.-W.; Maier, J.; Armand, M.; et al. New Horizons for Inorganic Solid State Ion Conductors. *Energy Environ. Sci.* **2018**, *11* (8), 1945–1976.

(20) Meng, Y. S.; Arroyo-de Dompablo, M. E. First Principles Computational Materials Design for Energy Storage Materials in Lithium Ion Batteries. *Energy Environ. Sci.* **2009**, *2* (6), 589.

(21) Wang, Y.; Richards, W. D.; Ong, S. P.; Miara, L. J.; Kim, J. C.; Mo, Y.; Ceder, G. Design Principles for Solid-State Lithium Superionic Conductors. *Nat. Mater.* **2015**, *14* (10), 1026–1031.

(22) Deng, Z.; Zhu, Z.; Chu, I.-H.; Ong, S. P. Data-Driven First-Principles Methods for

the Study and Design of Alkali Superionic Conductors. *Chem. Mater.* **2017**, *29* (1), 281–288.

(23) Park, K. H.; Bai, Q.; Kim, D. H.; Oh, D. Y.; Zhu, Y.; Mo, Y.; Jung, Y. S. Design Strategies, Practical Considerations, and New Solution Processes of Sulfide Solid Electrolytes for All-Solid-State Batteries. *Adv. Energy Mater.* **2018**, *8* (18), 1800035.

(24) Dawson, J. A.; Canepa, P.; Famprikis, T.; Masquelier, C.; Islam, M. S. Atomic-Scale Influence of Grain Boundaries on Li-Ion Conduction in Solid Electrolytes for All-Solid-State Batteries. *J. Am. Chem. Soc.* **2018**, *140*, 362–368.

(25) Culver, S. P.; Koerver, R.; Krauskopf, T.; Zeier, W. G. Designing Ionic Conductors: The Interplay between Structural Phenomena and Interfaces in Thiophosphate-Based Solid-State Batteries. *Chem. Mater.* **2018**, *30* (13), 4179–4192.

(26) Deiseroth, H.-J.; Kong, S.-T.; Eckert, H.; Vannahme, J.; Reiner, C.; Zaiß, T.; Schlosser, M. Li6PS5X: A Class of Crystalline Li-Rich Solids With an Unusually High Li+ Mobility. *Angew. Chemie Int. Ed.* **2008**, *47* (4), 755–758.

(27) Wang, S.; Zhang, Y.; Zhang, X.; Liu, T.; Lin, Y.-H.; Shen, Y.; Li, L.; Nan, C.-W. High-Conductivity Argyrodite Li 6 PS 5 Cl Solid Electrolytes Prepared via Optimized Sintering Processes for All-Solid-State Lithium–Sulfur Batteries. *ACS Appl. Mater. Interfaces* **2018**, *10* (49), 42279–42285.

(28) Evain, M.; Gaudin, E.; Boucher, F.; Petricek, V.; Taulelle, F. Structures and Phase Transitions of the A7PSe6 (A = Ag, Cu) Argyrodite-Type Ionic Conductors. I. Ag7PSe6. *Acta Crystallogr. Sect. B Struct. Sci.* **1998**, *54* (4), 376–383.

(29) Pecher, O.; Kong, S.-T.; Goebel, T.; Nickel, V.; Weichert, K.; Reiner, C.; Deiseroth, H.-J.; Maier, J.; Haarmann, F.; Zahn, D. Atomistic Characterisation of Li+ Mobility and Conductivity in Li7−xPS6−xIx Argyrodites from Molecular Dynamics Simulations, Solid-State NMR, and Impedance Spectroscopy. *Chem. - A Eur. J.* **2010**, *16* (28), 8347–8354.

(30) de Klerk, N. J. J.; Rosłoń, I.; Wagemaker, M. Diffusion Mechanism of Li Argyrodite Solid Electrolytes for Li-Ion Batteries and Prediction of Optimized Halogen Doping:

The Effect of Li Vacancies, Halogens, and Halogen Disorder. *Chem. Mater.* **2016**, *28* (21), 7955–7963.

(31) Yu, C.; Ganapathy, S.; de Klerk, N. J. J.; Roslon, I.; van Eck, E. R. H.; Kentgens, A. P. M.; Wagemaker, M. Unravelling Li-Ion Transport from Picoseconds to Seconds: Bulk versus Interfaces in an Argyrodite Li 6 PS 5 Cl–Li 2 S All-Solid-State Li-Ion Battery. *J. Am. Chem. Soc.* **2016**, *138* (35), 11192–11201.

(32) Hanghofer, I.; Brinek, M.; Eisbacher, S. L.; Bitschnau, B.; Volck, M.; Hennige, V.; Hanzu, I.; Rettenwander, D.; Wilkening, M. Substitutional Disorder: Structure and Ion Dynamics of the Argyrodites Li 6 PS 5 Cl, Li 6 PS 5 Br and Li 6 PS 5 I. *Phys. Chem. Chem. Phys.* **2019**, *12* (i), 8–10.

(33) Rayavarapu, P. R.; Sharma, N.; Peterson, V. K.; Adams, S. Variation in Structure and Li+-Ion Migration in Argyrodite-Type Li6PS5X (X = Cl, Br, I) Solid Electrolytes. *J. Solid State Electrochem.* **2012**, *16* (5), 1807–1813.

(34) Kraft, M. A.; Culver, S. P.; Calderon, M.; Böcher, F.; Krauskopf, T.; Senyshyn, A.; Dietrich, C.; Zevalkink, A.; Janek, J.; Zeier, W. G. Influence of Lattice Polarizability on the Ionic Conductivity in the Lithium Superionic Argyrodites Li6PS5X (X = Cl, Br, I). *J. Am. Chem. Soc.* **2017**, *139* (31), 10909–10918.

(35) Schneider, H.; Sedlmaier, S. J.; Du, H.; Kelley, T.; Leitner, K.; ter Maat, J.; Scordilis-Kelley, C.; Mudalige, A.; Kulisch, J.; Schneider, L. Stabilization of Highly Conductive Lithium Argyrodites by Means of Lithium Substitution: The Case of Li 6 Fe 0.5 PS 6. *ChemistrySelect* **2019**, *4* (12), 3351–3354.

(36) Doux, J.-M.; Nguyen, H.; Tan, D. H. S.; Banerjee, A.; Wang, X.; Wu, E. A.; Jo, C.; Yang, H.; Meng, Y. S. Stack Pressure Considerations for Room-Temperature All-Solid-State Lithium Metal Batteries. *Adv. Energy Mater.* **2019**, *1903253*, 1903253.

(37) Kamaya, N.; Homma, K.; Yamakawa, Y.; Hirayama, M.; Kanno, R.; Yonemura, M.; Kamiyama, T.; Kato, Y.; Hama, S.; Kawamoto, K.; et al. A Lithium Superionic Conductor. *Nat. Mater.* **2011**, *10* (9), 682–686.

(38) Zhou, L.; Assoud, A.; Shyamsunder, A.; Huq, A.; Zhang, Q.; Hartmann, P.; Kulisch, J.; Nazar, L. F. An Entropically Stabilized Fast-Ion Conductor: Li 3.25 [Si 0.25 P

0.75]S 4. *Chem. Mater.* **2019**, *31* (19), 7801–7811.

(39) Ong, S. P.; Mo, Y.; Richards, W. D.; Miara, L. J.; Lee, H. S.; Ceder, G. Phase Stability, Electrochemical Stability and Ionic Conductivity of the Li 10±1 MP 2 X 12 (M = Ge, Si, Sn, Al or P, and X = O, S or Se) Family of Superionic Conductors. *Energy Environ. Sci.* **2013**, *6* (1), 148–156.

(40) Zhou, P.; Wang, J.; Cheng, F.; Li, F.; Chen, J. A Solid Lithium Superionic Conductor Li 11 AlP 2 S 12 with a Thio-LISICON Analogous Structure. *Chem. Commun.* **2016**, *52* (36), 6091–6094.

(41) Wu, D. H.; Chen, A. D.; Johnson, C. S. An Improved Diffusion-Ordered Spectroscopy Experiment Incorporating Bipolar-Gradient Pulses. *J. Magn. Reson. Ser. A* **1995**, *115* (2), 260–264.

(42) Sinnaeve, D. The Stejskal – Tanner Equation Generalized for Any Gradient Shape — An Overview of Most Pulse Sequences Measuring Free Diffusion. *Concepts Magn. Reson. Part A* **2012**, *40A* (2), 39–65.

(43) van Meerten, S. G. J.; Franssen, W. M. J.; Kentgens, A. P. M. SsNake: A Cross-Platform Open-Source NMR Data Processing and Fitting Application. *J. Magn. Reson.* **2019**, *301*, 56–66.

(44) Goodenough, J. B.; Kim, Y. Challenges for Rechargeable Li Batteries †. *Chem. Mater.* **2010**, *22* (3), 587–603.

(45) He, X.; Zhu, Y.; Mo, Y. Origin of Fast Ion Diffusion in Super-Ionic Conductors. *Nat. Commun.* **2017**, *8* (May), 15893.

(46) Epp, V.; Gün, Ö.; Deiseroth, H.-J.; Wilkening, H. M. R. Long-Range Li+ Dynamics in the Lithium Argyrodite Li7PSe6 as Probed by Rotating-Frame Spin–Lattice Relaxation NMR. **2013**, 7123–7132.

(47) Bottke, P.; Rettenwander, D.; Schmidt, W.; Amthauer, G.; Wilkening, M. Ion Dynamics in Solid Electrolytes: NMR Reveals the Elementary Steps of Li + Hopping in the Garnet Li 6.5 La 3 Zr 1.75 Mo 0.25 O 12. *Chem. Mater.* **2015**, *27* (19), 6571–6582.

(48) Liang, X.; Wang, L.; Jiang, Y.; Wang, J.; Luo, H.; Liu, C.; Feng, J. In-Channel and

In-Plane Li Ion Diffusions in the Superionic Conductor Li 10 GeP 2 S 12 Probed by Solid-State NMR. *Chem. Mater.* **2015**, *27* (16), 5503–5510.

(49) Xiang, Y.; Zheng, G.; Zhong, G.; Wang, D.; Fu, R.; Yang, Y. Toward Understanding of Ion Dynamics in Highly Conductive Lithium Ion Conductors: Some Perspectives by Solid State NMR Techniques. *Solid State Ionics* **2018**, *318* (July 2017), 19–26.

(50) Kizilyalli, M.; Corish, J.; Metselaar, R. Definitions of Terms for Diffusion in the Solid State. *Pure Appl. Chem.* **1999**, *71* (7), 1307–1325.

(51) Roling, B.; Martiny, C.; Brückner, S. Ion Transport in Glass: Influence of Glassy Structure on Spatial Extent of Nonrandom Ion Hopping. *Phys. Rev. B* **2001**, *63* (21), 214203.

(52) Murch, G. E. The Haven Ratio in Fast Ionic Conductors. *Solid State Ionics* **1982**, *7*, 177–198.

(53) Imre, Á. W.; Staesche, H.; Voss, S.; Ingram, M. D.; Funke, K.; Mehrer, H. Pressure-Dependent Diffusion Coefficients and Haven Ratios in Cation-Conducting Glasses. *J. Phys. Chem. B* **2007**, *111* (19), 5301–5307.

(54) Marcolongo, A.; Marzari, N. Ionic Correlations and Failure of Nernst-Einstein Relation in Solid-State Electrolytes. *Phys. Rev. Mater.* **2017**, *1* (2), 025402.

(55) Richards, W. D.; Tsujimura, T.; Miara, L. J.; Wang, Y.; Kim, J. C.; Ong, S. P.; Uechi, I.; Suzuki, N.; Ceder, G. Design and Synthesis of the Superionic Conductor Na 10 SnP 2 S 12. *Nat. Commun.* **2016**, *7*, 1–8.

(56) Bychkov, E. Superionic and Ion-Conducting Chalcogenide Glasses: Transport Regimes and Structural Features. *Solid State Ionics* **2009**, *180* (6–8), 510–516.

(57) Thomas, M. P.; Peterson, N. L. Electrical Conductivity and Tracer Diffusion in Sodium Germanate Glasses. *Solid State Ionics* **1984**, *14*, 297–307.

(58) Sinitsyn, V. V.; Lips, O.; Privalov, A. F.; Fujara, F.; Murin, I. V. Transport Properties of LaF3 Fast Ionic Conductor Studied by Field Gradient NMR and Impedance Spectroscopy. *J. Phys. Chem. Solids* **2003**, *64* (7), 1201–1205.

(59) Knauth, P. Inorganic Solid Li Ion Conductors: An Overview. *Solid State Ionics* **2009**, *180* (14–16), 911–916.

(60) Bain, A. D. Chemical Exchange in NMR. *Prog. Nucl. Magn. Reson. Spectrosc.* **2003**, *43* (3–4), 63–103.

(61) Chen, H. M.; Maohua, C.; Adams, S. Stability and Ionic Mobility in Argyrodite-Related Lithium-Ion Solid Electrolytes. *Phys. Chem. Chem. Phys.* **2015**, *17* (25), 16494–16506.

(62) Callaghan, P. T. *Principles of Nuclear Magnetic Resonance Microscopy*; Oxford University Press: Oxford, UK, 1991.

(63) de Klerk, N. J. J.; Maas, E. van der; Wagemaker, M. Analysis of Diffusion in Solid-State Electrolytes through MD Simulations, Improvement of the Li-Ion Conductivity in B‑Li3PS4 as an Example. *ACS Appl. Energy Mater.* **2018**, *1*, 3230–3242.

(64) Gobet, M.; Greenbaum, S. G.; Sahu, G.; Liang, C. Structural Evolution and Li Dynamics in Nanophase Li3PS 4 by Solid-State and Pulsed-Field Gradient NMR. *Chem. Mater.* **2014**, *26* (11), 3558–3564.

(65) Leigh Spencer, T.; Goward, G. R.; Bain, A. D. Complete Description of the Interactions of a Quadrupolar Nucleus with a Radiofrequency Field. Implications for Data Fitting. *Solid State Nucl. Magn. Reson.* **2013**, *53*, 20–26.

(66) Karger, J.; Pfeifer, H.; Heink, W. Principles and Application of Self-Diffusion Measurements by Nuclear Magnetic Resonance. In *Advances in Magnetic Resonance*; Waugh, J. S., Ed.; Academic Press, Inc.: San Diego, 1988; p 438.

Chapter 7 – Conclusions and Future Work

7.1 Transport Phenomena in Liquid-State Lithium-Ion Battery Electrolytes

The bulk of the results presented in this thesis concern the characterization and quantitative measurement of ion transport in lithium-ion battery electrolytes in the conventional liquid-state form. The results in **Chapters 3-5** exhibit a progression in the sophistication and scope of the investigation of the transport properties. This begins in **Chapter 3** with bulk, *ex situ* measurements of the electrolyte cation and anion self-diffusivities by PFG-NMR and ionic conductivities by EIS over a series of temperatures, combined to yield the full set of transport parameters necessary to characterize a binary electrolyte at a given temperature within the CST paradigm: the salt diffusivity D_s, the ionic conductivity κ, and the cationic transference number t_+^0. **Chapter 4** then considers the effect of temperature on the steady-state concentration gradient formed during constant-current polarization of an electrochemical cell, directly imaged *in situ* with MRI.[1] The magnitude of this concentration gradient is shaped by the two CST transport parameters which govern mass transport: D_s and t_+^0. **Chapter 5** is the culmination of this progression, as it attempts to move one step further still, by combining not only *in situ* MRI measurements of the concentration gradient, but also spatially-resolved diffusivity measurements, with the aim of obtaining the variation of the complete set $\{D_s, t_+^0, \kappa\}$ of transport parameters across the breadth of the polarized electrolyte, over a wide range of temperature and applied current operating conditions.

The findings of **Chapter 3** are centred on contrasting the temperature performance of the ion transport in different electrolyte mixtures; first, a high cyclic-carbonate-fraction solvent mixture, which would be viscous but have a favourable permittivity for cation solvation, was contrasted against a mixture where the linear carbonate fraction was largest, corresponding to higher solvent mobility (the salt and its concentration was the same between the two mixtures). Indeed, cation and anion diffusivity measurements bore these hypotheses out, and the transport number also reflected higher mass transport in the high-mobility solvent mixture. However, in terms of charge transport, the ionic conductivity was uniformly higher in the high-permittivity mixture, and its transference number in the low-temperature regime was significantly greater also – with a diametrically opposed temperature-dependence relative to the high-mobility mixture. A corollary of the coupled PFG-NMR and EIS analysis method employed for these experiments is that information about the temperature-dependence of the contact ion pairing is also extractable. This clarified the reason for the charge and mass transport disparities between the two mixtures – despite the higher solvent mobility, ion pairing was considerably higher in the high linear-carbonate-fraction mixture – and facilitated a correlation with the Bjerrum critical distance, which is a form of effective radius for ion pairing which is a function of solvent permittivity.

The results for these more conventional electrolytes were then compared with mixtures which involved the replacement of the cyclic carbonate EC with its fluorinated variant, FEC (prized for its higher electrochemical stability[2] at the potentials which next-generation cathode materials are intended to operate at), and the utilization of higher salt

concentrations. The temperature performance of the transport properties of these mixtures largely fell between the two contrasting poles of the first two electrolyte mixtures, although one of the mixtures, which had a $1.20\ \mathrm{M}\ \mathrm{Li}^+$ concentration, but realized with $0.20\ \mathrm{M}$ LiFSI and $1.00\ \mathrm{M}\ \mathrm{LiPF}_6$ (as opposed to just increasing the concentration of LiPF_6 from the standard $1.00\ \mathrm{M}$), surpassed the charge transport of the conventional high-permittivity mixture in the high-temperature regime, and exhibited mass transport nearly as large as the high-mobility electrolyte, though its charge transport performance did drop off with decreasing temperature. It would be interesting, therefore, to study the influence of the LiFSI, and determine what the concentration range is, relative to the LiPF_6, that it is helpful to the charge transport in this secondary-salt capacity, as well as how this depends on the temperature of the mixture. The lack of permittivity data for FEC prevented an analysis of the Bjerrum critical distance for these mixtures – but this also highlights an opening to potentially expand the analysis. There are straightforward methods for permittivity measurements,[3] as well as for viscosity and mass density,[4] which could be performed in order to have more measurables available for inter-correlation; combined with cation and anion diffusivity measurements and ionic conductivities, this could potentially be used in several ways. First, to attempt to develop and parameterize a more extensive model of ion aggregation than simple contact pairing in the vein of the PFG-NMR + EIS approach used here (for a linear construction like this one, more measurables means more identifiable parameters), or could alternately potentially be harnessed to measure some of the additional parameters which appear in the CST formalism when the electrolyte is no longer simply a binary mixture (*i.e.* it contains a secondary salt).

Ex situ, bulk measurements of transport parameters certainly offer a useful set of metrics for evaluating electrolytes and optimizing their design, but as the results of **Chapter 4** and **Chapter 5** illustrate, they are not the only important consideration. In **Chapter 4**, *in situ* MRI of electrolyte polarization under constant-current conditions was investigated as a function of temperature, and it was found that a 1.00 M $LiPF_6$ in EC/DEC, 1:1 (v/v) electrolyte could not reach the steady-state at even the moderately low temperature of 10℃, with a current density of $7.2\,\mathrm{A}\cdot\mathrm{m}^{-2}$ (roughly, $C/3$). The voltage would eventually start to rise precipitously, and then the concentration gradient would begin to *decrease* on the anodic side of the cell. Once fully relaxed, a comparison of the total signal profile compared with the initial signal profile revealed missing intensity; combined with the retention of the original shape of the active volume, this signals that salt precipitation had occurred on the anodic side as the concentration gradient increased. Since a less concentrated version of the same electrolyte could reach the steady-state at the same temperature and current rate, and a 1.00 M $LiPF_6$ electrolyte with an EC/PC/DMC, 5:2:3 (v/v) solvent mixture could also reach the steady-state, it implies that the EC/DEC electrolyte is completely unsuitable to polarization at low temperature.

Chapter 5 furnished conclusions reminiscent to this. Here, both the temperature and current density dependence of the steady-state concentration gradient for the 1.00 M $LiPF_6$ in EC/PC/DMC, 5:2:3 (v/v) electrolyte was investigated, using both *in situ* MRI, and a P3D spatially-resolved diffusivity measurement. The limiting current behaviour as a function of temperature was investigated, and correlated to the diffusivity measurements on the anodic side of the cell. For the $25℃ - 40℃$ temperature range, the

decrease in the anodic side diffusivities with increasing concentration there, as a function of applied current density, occurred in concert with the depletion of the ions from the cathodic side. The limiting current was encountered as the polarization resistance from both of these factors increased, as both tended toward zero at the largest current densities. On the other hand, for lower temperatures such as $-5℃ - 10℃$, the ion depletion on the cathodic side was nowhere near the same extent as in the $25℃ - 40℃$ temperature regime, but the anodic side diffusivities tended toward zero much more rapidly as a function of current density than in the $25℃ - 40℃$ range, demonstrating that mass transport limitations are actually responsible for the limiting current behaviour at low temperature. Both of these factors – the salt precipitation at low temperature, and the anodic side mass transport deficiency leading to limiting current behaviour in the form of a polarization resistance rather than high charge-transfer resistance on the ion-poor cathodic side causing it – would not be apparent simply from performing bulk *ex situ* measurements. Certainly, electrochemical cycling under these conditions would reveal that there was a problem, but the *in situ* MRI and P3D PFG-NMR measurements are able to *diagnose* it, via quasi-real-time monitoring of the concentration gradient build-up and steady-state stability.

The study presented in **Chapter 4** also included a quantitative comparison of the measured steady-state concentration gradient magnitudes, for a range of temperatures, to the predictions from CST parameterized via *ex situ* measurements of the type performed in **Chapter 3**. A calibration method was developed between two different phase-encoding MRI approaches – CSI and DHK-SPRITE – which enabled the robustness of the latter to ensure the accuracy of the former and facilitate this quantitative experiment-to-model

concentration gradient comparison. It was found that the concentration gradients were consistent with the predicted values at all temperatures, and independent of the inter-electrode spacing of the cell, verifying that the large electrolyte active volumes used in this *in situ* cell design did not produce steady-state concentration gradients inconsistent with the CST framework, as these gradients are necessary for transport parameter extraction – particularly of the transference number – in the *in situ* cell.

This provided the platform for the quantitative and comprehensive transport parameter determination attempt, with spatial resolution, that was detailed in **Chapter 5**. Here, the steady-state concentration gradients and P3D PFG-NMR measurements of the steady-state diffusivity profiles for both the anion and the cation were combined to evaluate the set $\{D_s, t_+^0, \kappa\}$ across the cell. This proved formidably challenging; while the data were qualitatively sound, exhibiting the general behaviour that would be surmised from basic considerations of the influence of temperature and applied current density on the charge and mass transport across the cell, the quantitative determination ran aground. Despite calibration of the steady-state images using the method developed in **Chapter 4**, it appears that the concentration gradient slope determination is not sufficiently accurate to reliably calculate the transference number – particularly at high current densities, where the slope on the cathodic side is very small and difficult to determine accurately with a limited number of image points, and in light of the extreme numerical sensitivity of the model for computing κ from the measured set $\left\{\overline{\partial c}/\partial x\,, D_+^*(x), D_-^*(x)\right\}$ to the value of t_+^0. Using *ex situ* ionic conductivity measurements over a wide range of temperatures and salt concentrations, it was possible to map the *ex situ* conductivities across the cell as a function

of the local concentration measured by MRI, which then facilitated a determination of the transference number using the methods of **Chapter 3**. The significant disparity between the predictions for t_+^0 from the mapped *ex situ* conductivities and the *in situ* measurements of $\{\overline{\partial c}/\partial x\,, D_+^*(x), D_-^*(x)\}$ confirmed the problem.

While this *in situ* approach to comprehensive electrolyte transport parameter characterization shows promise, the MRI methods will require improvement in order to achieve the necessary level of both accuracy and precision for local concentration gradient slope estimation, and to attain a highly reliable alignment of the steady-state measurements from the 4 different types of MRI experiments that provide inputs to the calculations. This will involve careful management of the trade-off between the longer acquisition times for higher-resolution, better signal-to-noise experiments, and image alignment accuracy as a function of the total time for which the current is applied (since, with the present *in situ* cell geometry, large amounts of lithium deposition are an inevitable consequence of lengthy experimental runtimes). One potential approach is to alter the MRI strategy, such as by using RARE (Rapid Acquisition with Relaxation Enhancement)[5] to take advantage of the relatively long T_2 times for the cation and anion in solution possess, which has shown promise for *in situ* MRI of other electrochemical systems with conductive parts,[6,7] albeit with much larger active volumes from which signal was acquired. Additionally, it may be possible to acquire the diffusion dimension at each image point along the spatial dimension by using a Difftrain approach[8,9] coupled to a regular phase-encoding imaging strategy, which would again leverage the long T_2 times, rather than collecting a single point of $(\vec{k}, \vec{q})$-space at a time, as is done with the current P3D PFG-NMR strategy. Alternately, it

may simply be better to switch to a different *in situ* cell geometry with larger electrode surface area – such as a parallel-plate resonator design[10] – which will obviate the lithium deposition problem (at least for moderate applied current densities). Nevertheless, the analysis methods developed in **Chapter 5** provide a platform for future investigations along this direction to build from, and the results yield key insights that will streamline future investigations aimed toward the goal of comprehensive *in situ* MRI characterization of lithium-ion battery electrolyte transport parameters with spatial resolution.

7.2 Solid-State Lithium-Ion Battery Electrolyte Transport Measurement

The results of **Chapter 6** comprise a series of PFG-NMR and MAS-NMR characterization studies of lithium-sulphide ion conductors, in collaboration with the Nazar group at University of Waterloo. The first of these[11] examined the role of halide-enrichment of argyrodite lithium-ion conductors. The PFG-NMR method used in **Chapters 3-5** was adapted for solid-state measurements, with the resulting variable-temperature diffusivity measurements used to extract activation energies for the ion hopping, which were compared with the same obtained from conductivity measurements using EIS at Waterloo. The two transport measurements were then used to evaluate Haven ratios, a measure of the degree of correlation in the ion hopping, and the Haven ratios were, in turn, correlated with the activation energies and the isotropic chemical shift from MAS-NMR measurements as a function of chloride enrichment to discern the mechanism by which the chloride enrichment was boosting the ion transport, and how this varied with composition.

The effect of aliovalent doping for lithium sites in the argyrodites – via the introduction of Ca^{2+} – was then examined, again with PFG-NMR and MAS-NMR. Activation energies from the diffusivity measurements and the conductivity measurements were again correlated, along with the isotropic shifts, as a function of vacancy level in order to assess the impact of the Ca^{2+}-doping. The relative impacts of the Ca^{2+}-doping and halide-enrichment were compared with the same methods, applied to a dual-doped series of compositions. The impact of pellet compression on the ion transport was then assessed for a "mixed-phase" version of a highly-chloride-enriched sample, which exhibited multiple phases under ^{7}Li MAS-NMR, using a combination of PFG-NMR and NMR relaxometry methods. A lowering of the activation energy for ion hopping was correlated with the appearance of a second time-scale in the T_2 measurements, and the two observations were linked to the grain boundary modification that would occur as a result of the macroscopic compression. This illustrates the utility of PFG-NMR in quantifying micro-scale impacts to the ion transport as a function of macro-scale sample modification.

The final study focused on a thio-LISICON ion conductor synthesized at Waterloo by aluminum doping of the β-Li_3PS_4 structural motif. Carrying on from the PFG-NMR studies of the impact of macroscopic sample modification implemented for the mixed-phase argyrodite sample, glass, crystalline powder, and compressed crystalline pellet samples were investigated with PFG-NMR. A combination of ^{7}Li MAS-NMR and ^{7}Li static solid-state NMR lineshape fitting methods were used to estimate and partially identify the proportion of amorphous content in the crystalline samples. With this proportion, a two-compartment analysis of the PFG-NMR signal attenuation curves for the

crystalline samples based on the Kärger equations was conducted, in order to separate out components from the bulk ion transport and diffusion into and from the amorphous content. The activation energy from the bulk crystalline component of the compressed pellet sample was consistent within uncertainty with the activation energy obtained from conductivity measurements, also performed with a compressed sample, while the other activation energies (associated with the crystalline powder and pellet amorphous compartments, and the crystalline powder bulk compartment) were not. This was buttressed with relaxometry measurements, which again showed two components for the crystalline sample formats but not the glass sample. The shorter T_2 components from the crystalline sample formats were consistent with the single T_2 of the glass sample, implying that they originated from the amorphous content in the crystalline samples, while the longer T_2 component was similar in magnitude for the crystalline powder and pellet samples, but exhibited a shortening in the pellet sample (with the two sample formats otherwise identical in composition, being fashioned from the same batch of synthesized product). This study again underscored the utility of PFG-NMR as a tool for the characterization of macroscopic sample modification, despite being a microscopic measurement, and also developed an approach for probing ion transport into the amorphous content in a sample of mixed composition.

This latter outcome could be of great utility as the emphasis in solid-state ion conductors switches from discovery and understanding structure-property relations to operationalizing them in energy storage devices. A key problem to be addressed is the ion transport into and from interphases which are necessary to produce electrochemically stable interfaces between solid-electrolyte crystallites and electrode particles.[12,13] There is a large

supply of candidate solid-electrolyte materials in various stages of development for which this is a relevant question. There have been some NMR-based studies of this interfacial transport problem,[14,15] but the type of extended PFG-NMR analysis employed in **Chapter 6** could be a valuable contributor in terms of correlating effect magnitudes with micro-scale transport impacts, which could, in turn, also improve mechanistic understanding and help suggest alternative strategies for interface optimization. The related issue of grain-boundary conduction in crystalline solid-state electrolytes is also a subject of intense research and optimization at present.[16] As the results on the mixed-phase argyrodite sample demonstrate, PFG-NMR can also be a useful probe of ion transport in this context as well, and could complement studies where applied pressure on the solid-state electrolyte is correlated with cycling performance.[17]

7.3 Concluding Summary

Taken together, the results in this thesis demonstrate the utility of magnetic resonance measurements in the investigation of ion transport in lithium-ion battery electrolyte materials of a variety of compositions, sample preparations, and even states of matter. *Ex situ* PFG-NMR, *in situ* MRI, and then a combination of *in situ* MRI and spatially-resolved PFG-NMR has been used to address increasingly complex questions about the transport dynamics of liquid-state electrolytes. Further, several different applications of solid-state PFG-NMR measurements, operating as they do at a length-scale intermediate to relaxometry on the atomic scale and EIS on the bulk scale, have demonstrated a unique window for the investigation of transport phenomena in the presently blossoming field of solid-state ion conduction.

7.4 References

(1) Bazak, J. D.; Krachkovskiy, S. A.; Goward, G. R. Multi-Temperature in Situ Magnetic Resonance Imaging of Polarization and Salt Precipitation in Lithium-Ion Battery Electrolytes. *J. Phys. Chem. C* **2017**, *121* (38), 20704–20713.

(2) Glazier, S. L.; Downie, L. E.; Xia, J.; Louli, A. J.; Dahn, J. R. Effects of Fluorinated Carbonate Solvent Blends on High Voltage Parasitic Reactions in Lithium Ion Cells Using OCV Isothermal Microcalorimetry. *J. Electrochem. Soc.* **2016**, *163* (10), A2131–A2138.

(3) Hall, D. S.; Self, J.; Dahn, J. R. Dielectric Constants for Quantum Chemistry and Li-Ion Batteries: Solvent Blends of Ethylene Carbonate and Ethyl Methyl Carbonate. *J. Phys. Chem. C* **2015**, *119* (39), 22322–22330.

(4) Lundgren, H.; Behm, M.; Lindbergh, G. Electrochemical Characterization and Temperature Dependency of Mass-Transport Properties of LiPF6 in EC:DEC. *J. Electrochem. Soc.* **2014**, *162* (3), A413–A420.

(5) Hennig, J.; Nauerth, A.; Friedburg, H. RARE Imaging: A Fast Imaging Method for Clinical MR. *Magn. Reson. Med.* **1986**, *3* (6), 823–833.

(6) Romanenko, K.; Forsyth, M.; O'Dell, L. A. New Opportunities for Quantitative and Time Efficient 3D MRI of Liquid and Solid Electrochemical Cell Components: Sectoral Fast Spin Echo and SPRITE. *J. Magn. Reson.* **2014**, *248*, 96–104.

(7) Bray, J. M.; Davenport, A. J.; Ryder, K. S.; Britton, M. M. Quantitative, In Situ Visualization of Metal-Ion Dissolution and Transport Using 1 H Magnetic Resonance Imaging. *Angew. Chemie Int. Ed.* **2016**, *55* (32), 9394–9397.

(8) Stamps, J. P.; Ottink, B.; Visser, J. M.; van Duynhoven, J. P. M.; Hulst, R. Difftrain: A Novel Approach to a True Spectroscopic Single-Scan Diffusion Measurement. *J. Magn. Reson.* **2001**, *151* (1), 28–31.

(9) Mitchell, J.; Johns, M. L. Rapid Measurements of Diffusion Using PFG: Developments and Applications of the Difftrain Pulse Sequence. *Concepts Magn. Reson. Part A* **2009**, *34A* (1), 1–15.

(10) Ramírez Aguilera, A.; MacMillan, B.; Goward, G. R.; Balcom, B. J. Optimization of a Parallelplate RF Probe for High Resolution Thin Film Imaging. *Concepts Magn. Reson. Part A* **2018**, *47A* (1), e21465.

(11) Adeli, P.; Bazak, J. D.; Park, K. H.; Kochetkov, I.; Huq, A.; Goward, G. R.; Nazar, L. F. Boosting Solid□State Diffusivity and Conductivity in Lithium Superionic Argyrodites by Halide Substitution. *Angew. Chemie* **2019**, ange.201814222.

(12) Hou, W.; Guo, X.; Shen, X.; Amine, K.; Yu, H.; Lu, J. Solid Electrolytes and Interfaces in All-Solid-State Sodium Batteries: Progress and Perspective. *Nano Energy* **2018**, *52*, 279–291.

(13) Culver, S. P.; Koerver, R.; Krauskopf, T.; Zeier, W. G. Designing Ionic Conductors: The Interplay between Structural Phenomena and Interfaces in Thiophosphate-Based Solid-State Batteries. *Chem. Mater.* **2018**, *30* (13), 4179–4192.

(14) Yu, C.; Ganapathy, S.; de Klerk, N. J. J.; Roslon, I.; van Eck, E. R. H.; Kentgens, A. P. M.; Wagemaker, M. Unravelling Li-Ion Transport from Picoseconds to Seconds: Bulk versus Interfaces in an Argyrodite Li 6 PS 5 Cl–Li 2 S All-Solid-State Li-Ion Battery. *J. Am. Chem. Soc.* **2016**, *138* (35), 11192–11201.

(15) Yu, C.; Ganapathy, S.; Eck, E. R. H. van; Wang, H.; Basak, S.; Li, Z.; Wagemaker, M. Accessing the Bottleneck in All-Solid State Batteries, Lithium-Ion Transport over the Solid-Electrolyte-Electrode Interface. *Nat. Commun.* **2017**, *8* (1), 1086.

(16) Dawson, J. A.; Canepa, P.; Famprikis, T.; Masquelier, C.; Islam, M. S. Atomic-Scale Influence of Grain Boundaries on Li-Ion Conduction in Solid Electrolytes for All-Solid-State Batteries. *J. Am. Chem. Soc.* **2018**, *140*, 362–368.

(17) Doux, J.-M.; Nguyen, H.; Tan, D. H. S.; Banerjee, A.; Wang, X.; Wu, E. A.; Jo, C.; Yang, H.; Meng, Y. S. Stack Pressure Considerations for Room□Temperature All-Solid-State Lithium Metal Batteries. *Adv. Energy Mater.* **2019**, *1903253*, 1903253.